Experiments and Modelling Studies of Producer Gas based Spark-Ignited Reciprocating Engines

A Thesis

Submitted for the Degree of

Doctor of Philosophy

In the Faculty of Engineering

by

SRIDHAR GURURAJA RAO

Department of Aerospace Engineering

Indian Institute of Science

Bangalore – 560 012, India

February 2003

Acknowledgements

I convey my deepest gratitude to Research Supervisors Prof. H S Mukunda and Prof. P J Paul for their constant encouragement, help and guidance through out my research work. I am indebted to them for the skills, computational and analytical, acquired during my association with them.

I am grateful to the Secretary and Executive Secretary of Karnataka State Council for Science and Technology (KSCST) for enrolling me as an external registrant at the Institute. Similarly, I express my gratitude to Dr. T S Channesh, who was my organization Supervisor. I thank him for all the necessary support extended. I am also grateful to Prof. B Dattaguru, Chairman, Department of Aerospace Engineering, IISc for extending necessary support during my studentship at the Institute. My deepest thanks go to Dr. N K S Rajan and Dr. S Dasappa for their useful suggestions relating to the experimental work. I learnt quite a bit relating to reciprocating engines from their vast experience.

I thank my friends and well-wishers at Combustion Gasification and Propulsion Laboratory (CGPL), Sridhar H V, Nagaraj Upadyaya, Bhaskar Dixit, Nikhil Patel, Ramakrishna P V, Sudarshan Kumar, Subbukrishna D, Gayathri V, Girish Belandur, Shankarlingam, Sheshagiri, Paul Raj, Jaytheertha, Sachin, Avinash, Anand, Prashanth, Nisha and Anusuya who provided useful inputs and supported me in this endeavour. I specially thank Srinivas for helping me with neat sketches. Similarly, I also thank to my other colleagues Venu, Mallaiah, Parmesh, Ramesh Acharya, Sridhar T C, Anil kumar, Thirupathaiah, Shankar, Anantha, Channakeshava, Muniraju, Suresh and Narasamma who have immensely helped in the experimental work.

I am grateful to M/s Greaves, Pune for having spared their 250 kW gas engine for experiments with the producer gas, M/s Apex Innovations for the timely help in the area of engine instrumentation and M/s AEA Technologies for all the guidance on CFD computational work. I also thank the undergraduate engineering students who helped me during the various phases of my research activity. I am also thankful to my brother Giridhar for proof reading my thesis.

Finally, I express my gratitude to my elders, in particular to my parents and parents-in-law, to my dearest wife Vidya and my little son Rajat who provided inspiration and constant support all along. I am indebted to them for all the sacrifices made to make my effort a success.

G.Sridhar

Publications Arising Out of the Present Work

1. Sridhar G., Paul P.J. and Mukunda H.S. (2001): "Biomass Derived Producer Gas as a Reciprocating Engine Fuel – An Experimental Analysis", Biomass & Bioenergy, Vol. 21, pp. 61-72.

2. Sridhar G., Paul P.J. and Mukunda H.S. (2002): "Experiments and Modelling of Producer Gas based Reciprocating Engines", Proceedings of the 2002 Fall Technical Conference of the ASME Internal Combustion Engines Division, held at New Orleans, Louisiana, USA, Paper No. ICEF2002-520, ICE-Vol. 39, pp. 377-388,

---

The primary concepts of the open top, re-burn, down draft gasifier had been developed by the time the author of this thesis became a part of the development team. He participated in the major gasifier tests of Dec 1994 to Jan 1995 performed in Bangalore and from Dec 1995 to Jan 1996 tests held at Chatel-St-Denis, Switzerland. He has been involved in other developments related to gasifier reactor, cooling and cleaning system as a part of the development team, subsequently through the specific tests performed for this work. The other published work related to the gasifier in which the present author of the thesis is a co-author is as follows:

1. Report on the Gasifier Tests by Indian Institute of Science-Swiss Team, Internal Report 1994.

2. Technology for Gasifying Pulverised Bio-fuels Including Agricultural Residues, Journal of Energy for Sustainable Development, No.2 Vol. III, July 1996.

3. Experience on Testing of IISc-DASAG Open Top Wood Gasifier in Switzerland, Bun-India Newsletter, Vol. 1.2, December 1996.

4. Fixed Bed Gasification for Electricity Generation, Biomass Gasification and Pyrolysis, State of the Art and Future Prospects, pp. 105 -116, CPL Press, 1997.

5. Tar Characterization in New Generation Agro-residue Gasifier-Cyclone Down Draft Open Twin Air Entry Systems, Proceedings of Biomass Gasification and Pyrolysis Conference held at Stuttgart, Germany in Feb 1997.

Contents

List of Tables

List of Figures

List of Plates

Nomenclature

Abbreviations

ABC	After Bottom Centre
ATC	After Top Centre
BBC	Before Bottom Centre
BC	Bottom Centre
BP	Brake Power
bsfc	Brake Specific Fuel Consumption
BTC	Before Top Centre
CA	Crank Angle
CFD	Computational Fluid Dynamics
CFR	Cooperative Fuel Research
CGPL	Combustion Gasification and Propulsion Laboratory
CI	Compression Ignition
COV	Coefficient of Variation
CPCB	Central Pollution Control Board
CR	Compression Ratio
DNS	Direct Numerical Simulation
EELB	Eddy Entrainment and Laminar Burn-Up
FET	Filling and Emptying Technique
FIP	Fuel Injection Pump
FSR	Flame Speed Ratio
GHG	Green House Gas
HUCR	Highest Useful Compression Ratio
IGN	Ignition Timing
IISc	Indian Institute of Science
IMEP	Indicated Mean Effective Pressure
INJ	Injection Timing
IP	Indicated Power
LCV	Lower Calorific Value
LES	Large Eddy Simulation
MBT	Minimum Advance for Brake Torque
MPE	Medium Power level Engine
NG	Natural Gas
P & T	Particulate and Tar
PG	Producer Gas
PIV	Particle Image Velocimetry
p-v	Pressure-Volume
p-θ	Pressure-Crank Angle
RG	Recycled Gas
RSF	Reverse Squish Flame
RSV	Reverse Squish Velocity
S	Separation Zone
SI	Spark Ignition

SPE	Small Power level Engine
T	Torroidal structure
TC	Top Centre
TKE	Turbulence Kinetic Energy
0-D	Zero –Dimension

Symbols

A	Area
A_f	Frequency Factor
a,b	Heat transfer Coefficients
B	Body Force
C	Concentration
C_d	Discharge Coefficient
c	Specific Heat of Gas
D	Bore
Da	Damkohler Number
dQ	Heat loss
E	Internal Energy
e	Specific Internal Energy
F_A	Power Consumed by Accessories
F_L	Pumping Loss
F_R	Frictional Loss
g	Accounts for Expansion/Contraction of Grid
H	Total Enthalpy
h	Specific Enthalpy
J	Mass Flux
k, λ	Thermal Conductivity
L_T	Total Losses
l_I	Integral Length Scale
l_k	Kolmogorov Length Scale
l_M	Taylor Micro Scale
ℓ_T	Characteristic Length
m	Mass
$\dot{m}_b$	Mass Burn Rate
p	Pressure
R	Characteristic Gas Constant
Re	Reynolds Number
S	Burning Velocity
T	Temperature
t	Time
U	Velocity
x	Co-ordinate
α	Crank Angle

μ	Parametric/Entrained Mass
ε	Turbulence Dissipation Rate
Φ	Fuel-Air Equivalence Ratio
k	Turbulence Kinetic Energy
ψ	Recycled Gas
r	Radius
τ_b	Characteristic Time
u'	Turbulence Intensity
u_T	Characteristic Speed
V	Volume
δ_L	Reaction Sheet Thickness
Y	Mass Fraction of Species
δ_L	Laminar Flame Thickness
η	Efficiency
ρ	Density
τ_b	Characteristic Time
$\dot{\omega}'''$	Volumetric Production/Consumption Rate
σ	Stress Tensor
μ	Viscosity

Subscripts

G	Gross
N	Net
p	Pressure, Products
v	Volume
f	Flame
b	Burned Gas
L	Laminar
m	Mixture, Mean
u	Unburned Gas
w	Wall
i	Species
mech	Mechanical
T	Turbulent
o	Reference

ABSTRACT

This thesis is concerned with the experimental and modelling aspects relating to the operation of high compression ratio (CR) spark-ignition engine using a high-octane, low energy density gaseous fuel known as producer gas (PG). The work also reemphasizes the potential of biomass-derived producer gas as the future fuel for power generation application. The thesis is arranged in two parts. The first part discusses the experimental work conducted on a small power level (20 kW) spark-ignited engine at varying compression ratios (CR) and a medium power level engine (250 kW) at a fixed CR. The 20 kW, naturally aspirated spark-ignition engine is locally converted from a production diesel engine of 24 kW delivered capacity (Kirloskar make), by retaining the original feature of bowl-in-piston combustion chamber. The CR is varied between 17.0 and 11.5 by changing the thickness of the cylinder head gasket. The 250 kW is a factory-converted Greaves turbo-charged spark-ignition engine at a reduced CR of 12.0, with a bowl-in-piston combustion chamber. The producer gas for the experimental work is derived from the well-established open top, re-burn, down draft gasification system, which is proven to generate consistent quality, ultra-clean producer gas. The engine – alternator system is characterized for its performance by the simultaneous measurement of gas and airflow rates, gas composition (on-line), in-cylinder pressure, emission levels and power delivered. Typical producer gas composition is about 19 $\pm$ 1% H_2, 20 $\pm$ 1% CO, 2 $\pm$ 0.5% CH_4 and rest being inert like CO_2 and N_2, with lower calorific value being 5.2 $\pm$ 0.2 MJ/Nm^3. The stoichiometry air to fuel ratio is about 1.30 $\pm$ 0.1 on mass basis, with laminar burning velocity being 0.5 m/s at ambient conditions.

The engine operation is found to be smooth at the highest CR of 17.0 without any undesirable effects of knock as discerned, in part, from the pressure-crank angle (p-θ) curve, which shows smooth rise in pressure without any pressure oscillations. The pressure-crank angle (p-θ) curves are in turn used in the modelling section for comparing with the zero-dimensional (0-D) predictions.

In the case of Small Power level Engine (SPE) category, the de-rating in terms of power is about 16.7% at the CR of 17.0 and increases to 26% at a CR of 11.5. Maximum net power (excluding power consumed by fan and accessories) is recorded at a fuel-air equivalence ratio of 1.08 $\pm$ 0.2, with gas to useful shaft power conversion efficiency being 30.7 and 27.5% respectively for the highest and lowest CR. The reduction in power with producer gas is attributed to reduction in the net calorific value of the fuel gas and air mixture, and to the net reduction in number of molecules as the mixture goes to product gases.

Small Power level gas Engine (SPE)		
CR	INJ/IGN, ° BTC	Max Power, kW
17.0 - Diesel	*34*	*24.0**
17.0 - PG	06 -12	20.0 + 0/-0.2
14.5 - PG	08 -12	18.6 - 0/+0.2
13.5 - PG	08 -14	18.2 - 0/+0.4
11.5 - PG	06 -17	17.0 - 0/+0.6

*INJ: Injection timing; IGN: Ignition timing; BTC: Before Top Centre; * reference*

The choice of optimum ignition timing and its occurrence close to Top Center (TC) is due to laminar burning velocity being high for producer gas fuel (at ambient conditions laminar burning velocity for PG and Natural gas is 0.5 and 0.35 m/s respectively). The high laminar burning velocity contributes to faster combustion with a result that there is a low cycle-to-cycle variation in the indicated mean effective pressure (IMEP) at all CRs and ignition timings.

In the Medium Power level Engine (MPE) category, the optimum ignition timing is found to be between 12° and 14° BTC, the small retardation in the ignition timing is related higher turbulence intensity on account of higher mean piston speed. There is a de-rating of power to an extent of 21% in producer gas mode compared to diluted natural gas operation and this is attributed to the reduction in the mixture calorific value. The producer gas engine operation is found to be environmentally benign in terms of emissions; in case of MPE, nitric oxide level is found to be much lower (< 0.7 g/MJ) than the stipulated norm for diesel engine powered vehicles (2.22 g/MJ) specified by Central Pollution Control Board (CPCB), India. The carbon monoxide levels are lower (< 1.20 g/MJ) than CPCB norm of (1.25 g/MJ).

Medium Power level gas Engine (MPE)		
CR	IGN, BTC	Max Power, kW
12.0 – Diluted natural gas (75% CH_4)	28 - 30	270 #
12.0 - PG	12 - 14	212 #

IGN: Ignition timing; BTC: Before Top Centre; # with fan power

The second part of the thesis is devoted to the modelling aspect, where in a zero-dimensional (0-D) model is constructed to simulate the processes of a spark-ignition engine operation. The heat release part, which is key to the modelling, is based on the well-postulated Eddy Break-up and Laminar Burn-up (EELB) model meant for turbulent pre-mixed wrinkled flames. The two key input parameter sets for the heat release sub-model are derived from further computations. The parameter set required is the laminar burning velocity data, at pressures and temperatures encountered in an engine combustion chamber. These data are obtained from computations based on one dimensional flame code. The other set is the turbulent parameter, namely, turbulent intensity and integral length scale. These are obtained from three-dimensional CFD computations for engine combustion chamber geometry, involving bowl-in piston arrangement at CR of 17.0 and 11.5. Turbulence is modelled using standard k-ε model with compressibility effect being accounted. The calculation simulating the motored condition is run through two complete cycles to arrive at the flow field conditions required for the 0-D calculations (at the time of initiation of ignition). The data on turbulent intensity extracted from the 3-D flow calculations match reasonably well with experiments from literature till compression stroke but are in contradiction with trends close to TC. This is reasoned to be due to limitation of the k-ε model in capturing transient effects due to reverse squish phenomenon. The CFD results revealed spatial variations in turbulent intensity and integral length scale across the combustion chamber. However, mass-averaged values across a 3-D zone passing through the bowl

center have been used in heat release model of 0-D study.

The in-cylinder pressure predictions are made by using the data on laminar burning velocity and turbulence parameters from the above-mentioned computations. The turbulence parameters are further modified using simple rapid distortion process cited in the literature as the flow undergoes variations under reacting conditions. The displacement of the flame kernel subsequent to its point of formation is appropriately accounted in the 0-D model. This is obtained from the motored CFD results by tracking the velocity (normal component) of a particle along a streak line, in and around the point of ignition. The enhancement in velocity under reacting conditions is accounted by considering the density changes occurring due to combustion (proportional to the ratio of T_{burned} to $T_{unburned}$).

One experimental firing case is used as a test case in tuning the 0-D model in terms of constants required for computation of heat loss. Subsequently, keeping these parameters fixed 0-D predications are made for twelve test cases involving combustion chambers of SPE and MPE at varying CRs and ignition settings. These are further categorized under three sub-groups, namely Simple, Complex I and Complex II depending upon the intricacy involved in the predictions. Under the Simple sub-group, four test cases of SPE are dealt with, wherein the predictions match very well with the experimental p-θ curve. These computations are attempted assuming simple spherical flame propagation model. Whereas, under Complex-I sub-group, six cases of SPE are dealt, wherein the cylinder pressures are under-predicted with simple spherical flame propagation model. It is observed that in most of the cases, major part of the combustion occurs during the reverse squish period. A careful analysis of the motored CFD results indicated increased movement of the fluid out of the bowl during the reverse squish period. This fluid movement could modify the normal combustion process. The velocity vectors of the fluid indicate to a 'Flat' shape flame beyond the spherical flame engulfing the bowl. The change in the flame shape could enhance the effective burning area and thereby contribute to higher burn rate. These effects are termed, as 'Reverse Squish Flame' (RSF) hypothesis in this thesis and when these effects are accounted in the 0-D model the predictions are much better. Under Complex-II category, two test cases belonging to MPE are addressed. For these cases higher turbulence intensity is accounted due to higher mean speed of the piston (7.0 m/s) compared to SPE (5.8 m/s). Also additional flame kernel displacement is considered due to eccentric location of the ignition source. Even in these cases the predictions are better with RSF hypothesis.

The thesis is set out in eight chapters. Chapter I provide a brief introduction along with review of the earlier literature. Chapter II discusses the aspects of producer gas generation through gasification process. Chapter III deals with the experimental work conducted on two spark-ignition engines and their results. Chapter IV discusses the overview of the zero-dimensional modelling. Chapter V presents the laminar burning velocity calculation procedure and results at higher pressure and temperatures (along with recycled gas) encountered in an engine operation. Chapter VI deals with the detailed three-dimensional CFD computations. Chapter VII discusses the predictions at various ignition timings and CR for two combustion chamber geometries. Chapter VIII presents an overview of the work.

Nomenclature

Abbreviations

ABC	After Bottom Centre
ATC	After Top Centre
BBC	Before Bottom Centre
BC	Bottom Centre
BP	Brake Power
bsfc	Brake Specific Fuel Consumption
BTC	Before Top Centre
CA	Crank Angle
CFD	Computational Fluid Dynamics
CFR	Cooperative Fuel Research
CGPL	Combustion Gasification and Propulsion Laboratory
CI	Compression Ignition
COV	Coefficient of Variation
CPCB	Central Pollution Control Board
CR	Compression Ratio
DNS	Direct Numerical Simulation
EELB	Eddy Entrainment and Laminar Burn-Up
FET	Filling and Emptying Technique
FIP	Fuel Injection Pump
FSR	Flame Speed Ratio
GHG	Green House Gas
HUCR	Highest Useful Compression Ratio
IGN	Ignition Timing
IISc	Indian Institute of Science
IMEP	Indicated Mean Effective Pressure
INJ	Injection Timing
IP	Indicated Power
LCV	Lower Calorific Value
LES	Large Eddy Simulation
MBT	Minimum Advance for Brake Torque
MPE	Medium Power level Engine
NG	Natural Gas
P & T	Particulate and Tar
PG	Producer Gas
PIV	Particle Image Velocimetry
p-v	Pressure-Volume
p-θ	Pressure-Crank Angle
RG	Recycled Gas
RSF	Reverse Squish Flame
RSV	Reverse Squish Velocity
S	Separation Zone
SI	Spark Ignition
SPE	Small Power level Engine

T	Torroidal structure
TC	Top Centre
TKE	Turbulence Kinetic Energy
0-D	Zero –Dimension

Symbols

A	Area
A_f	Frequency Factor
a,b	Heat transfer Coefficients
B	Body Force
C	Concentration
C_d	Discharge Coefficient
c	Specific Heat of Gas
D	Bore
Da	Damkohler Number
dQ	Heat loss
E	Internal Energy
e	Specific Internal Energy
F_A	Power Consumed by Accessories
F_L	Pumping Loss
F_R	Frictional Loss
g	Term Accounting for Expansion/Contraction of Grid
H	Total Enthalpy
h	Specific Enthalpy
J	Mass Flux
k, λ	Thermal Conductivity
L_T	Total Losses
l_I	Integral Length Scale
l_k	Kolmogorov Length Scale
l_M	Taylor Micro Scale
ℓ_T	Characteristic Length
m	Mass
$\dot{m}_b$	Mass Burn Rate
p	Pressure
R	Characteristic Gas Constant
Re	Reynolds Number
S	Burning Velocity
T	Temperature
t	Time
U	Velocity
x	Co-ordinate
α	Crank Angle
μ	Parametric/Entrained Mass
ε	Turbulence Dissipation Rate
Φ	Fuel-Air Equivalence Ratio

k	Turbulence Kinetic Energy
ψ	Recycled Gas
r	Radius
u'	Turbulence Intensity
u_T	Characteristic Speed
V	Volume
Y	Mass Fraction of Species
δ_L	Laminar Flame Thickness
η	Efficiency
ρ	Density
τ_b	Characteristic Time
$\dot{\omega}'''$	Volumetric Production/Consumption Rate
σ	Stress Tensor
μ	Viscosity

Subscripts

G	Gross
N	Net
p	Pressure, Products
v	Volume
f	Flame
b	Burned Gas
L	Laminar
m	Mixture, Mean
u	Unburned Gas
w	Wall
i	Species
mech	Mechanical
T	Turbulent
o	Reference

Chapter I

Introduction and Literature Review

In the recent times, gaseous fuels are gaining prominence as cleaner fuels for power generation via internal combustion engine route, the power generation package including both reciprocating engines and gas turbine machinery. Complete combustion with minimal emission is the key feature of gaseous fuels and this feature is currently being exploited the world-over for power generation purposes. Producer gas derived from biomass is one such eco-friendly gaseous fuel. While natural gas is the most used one, next one being the land fill gas or biogas, which is diluted natural gas (with 20-30% CO_2) biomass based producer gas is perhaps the least used fuel, hence the literature in the area is scant. The literature review is categorized into three sub-topics, namely producer gas engines addressing the experimental part, fluid flow in reciprocating engines and combustion studies in spark ignition engines the modeling aspect.

1.1 Introduction

Internal combustion reciprocating engines have integrated into societal service in the last century. Their use has improved the quality of life substantially, but at the cost of degradation to the environment, certainly in several countries with insufficient environmental consciousness. Therefore, large impetus is being given to improve the efficiency and thereby reduce the emissions by using two approaches namely, improvement in engine design and use of alternate fuels in place of fossil fuels.

In the domain of engine design, the complex fluid dynamics and thermo-chemical interaction occurring in the combustion chamber play an important role in the eventual efficiency and emissions released. One way to reduce the emissions is to adopt leaner combustion for which understanding fluid dynamics inside the combustion chamber becomes pertinent. Many tools in the form of computational modelling have been used both in the past and the present to understand these phenomena. These range from simple zero-dimensional phenomenological modelling to full-fledged three-dimensional modelling.

In the domain of alternate fuels, oxygenated liquid and gaseous fuels receive more prominence because of the possibilities of cleaner combustion. Among the gaseous fuels, producer gas, a low-energy density gas derived from biomass holds a large promise as an environment friendly fuel. This fuel gas in addition to being CO_2 neutral generates lesser quantum of undesirable emissions. Even though these merits of biomass have been recognized widely, the technological capitalization has remained in infancy largely.

The thermo-chemical conversion of biomass leads to a gas generally termed as producer gas. The process is termed gasification implying that a solid fuel is converted to a gaseous fuel. Gasification is not a new technology but is known ever since World War II. During this period a number of vehicles in Europe were powered with charcoal gasifiers. It is estimated that over seven million vehicles in Europe, Australia, South America and Pacific Islands were converted to run on producer gas during World War II. These engines were spark ignition (SI) engines, mostly in the lower compression ratio (CR) bracket operating either on charcoal or biomass derived gas. It is appropriate to mention here the contribution of National Swedish Testing Institute of Agricultural Machinery, Sweden whose extensive fieldwork conducted by mounting gas generator and engine set on truck and tractors has provided an important demonstration of the enormous possibilities.

In the recent times, there is a renewed interest in biomass gasification technology, which has stimulated interest in producer gas operated engines. Whatever work has been attempted in this area has been limited to lower CR (less than 12.0) engine due to perceived limitation of knock at higher CR. A review of some of earlier studies relevant to this thesis, namely producer gas engine, fluid flow in reciprocating engines and combustion studies in SI engines are presented now.

1.2 Literature Review

1.2.1 Producer Gas Engine

Literature survey in the field of producer gas based engines reveals modest research work accomplished since the inception of biomass/charcoal gasification systems. This could be attributed to two reasons, namely non-availability of standard gasification system that could generate consistent quality producer gas and the other relating to misconceptions about producer gas fuel. These issues are addressed in Chapter II, which contains the description of biomass gasification process along with application of producer gas in reciprocating engines. The literature survey on this particular topic addresses some of research activities conducted in Europe, America and the Indian sub-continent.

It is reported that Europe exploited the most of gasification technology during petroleum oil crisis of World War II. Among the European nations, Sweden accounts for a large amount of work in the area of wood and charcoal gasification. National Swedish Testing Institute of Agricultural Machinery, Sweden [ANON-FAO Report, 1986] has

reported extensive work on the design and development of closed top charcoal and wood gasifiers for use with the reciprocating engines. These reciprocating engines were mostly diesel engines mounted on trucks and tractors for operation in dual-fuel mode. Many finer aspects relating to dual-fuel operation have been extensively reported, with cumulative operational experience exceeding a few thousand hours. However, whatever work was conducted on the producer gas alone operation is either proprietary to the engine manufacturers or is not adequately reported in the public domain literature. These engines were however in the lower CR – 10 either adapted from petrol engines or modified diesel engine. In the recent times, Martin et al [1981] have reported work using charcoal gas and biomass based producer gas on a SI engine with a de-rating of 50% and 40% respectively at a CR of 7. However, the same authors claim 20% de-rating when worked with producer gas at a CR of 11. They indicate an upper limit of CR of 14 and 11 for charcoal and biomass based producer gas respectively. However, there is no presentation of experimental evidence in favour of these results

American sub-continent also claims experimental work relating to producer gas engines. Tatom et al [1976] have reported working on a gasoline truck engine with a simulated pyrolysis gas at a de-rating of 60-65%. The authors have also identified the optimum ignition timings as a function of speed. Parke et al [1981] have worked on both naturally aspirated and super charged gas engines. The authors claim a de-rating of 34%, compared to gasoline operation and a lesser de-rating in a supercharged mode. The authors discuss aspects relating to fuel-air mixture ratio, flame speed and its relation to the ignition timing for producer gas operation. They have also identified the best possible mixture for maximum power and efficiency along with ignition timing at various speeds.

In the Indian sub-continent, work in the area of producer gas engine has been reported by the biomass gasification group of Indian Institute of Technology, Mumbai. Shashikantha et al [1993, 1999] and Parikh et al [1995] have reported work on a gas engine converted from a naturally aspirated diesel engine at CR of 11.5. The reason for limiting the CR is cited to be the knocking tendency; however, no experimental evidence is provided in support of it. The work is reported on a gas engine converted from a diesel engine with a modified combustion chamber. The modified combustion chamber of Hesselman (shallow W) shape is claimed to enhance the in-cylinder turbulence by suppression of swirl and promotion of squish effect. With the above modification, a power output of 16 kW is reported in gas mode against a rated output of 17 kW in diesel mode. The maximum thermal efficiency is claimed at 32%, which is close to the results in compression ignition (with diesel) mode at an output of 15 kW. It is quite surprising to note the conversion efficiencies to be same, when the CRs are widely different. The authors also claim an optimum ignition timing of 35° BTC compared to 22° BTC for natural gas on the same engine. With the producer gas claiming to contain about 24.1% H_2, 21.5% CO and 2.1% CH_4 the burning velocities ought to be higher than natural gas. In contradiction to the reported ignition timing, the claimed gas composition would require the ignition timing to be located close to TC. Therefore, it is not clear as to how such a large output was obtained at an advanced ignition timing when all logics point towards retarded ignition timing (as also demonstrated in this work).

The only earlier experimental work in the higher CR range is reported by Ramachandra [1993] on a single cylinder diesel engine (CR=16.5) coupled to a water pump. A power de-rating of 20% was reported at an overall efficiency of 19% without any signs of detonation. This work does not report of detailed measurements like the gas composition, pressure-crank angle diagram and emissions, which are essential for systematic investigation and scientific understanding.

If one were to summarize the findings of earlier studies, it becomes evident that no systematic investigation has been attempted so far in identifying if limitation of knock exists with producer gas operation at CR comparable with the diesel engine operation. This topic is worth analyzing since producer gas contains a large fraction of inert (> 50%) and with laminar burning velocity being high (due to the presence of H_2), smooth operation at higher CR does not seem impossible. These aspects are very vital in establishing the fact that close to comparable power (with a lesser extent of de-rating ~ 15-20%) could be achieved with producer gas by operating in engines at higher CR.

1.2.2 Fluid Flow in Reciprocating Engines

Fluid dynamics inside the engine combustion chamber plays a predominant role in the operation of an internal combustion engine. Fluid flow governs mixing, combustion and heat transfer processes in reciprocating engines. The in-cylinder swirl and turbulence affect the burn rate depending upon the combustion chamber design and intake port configuration. Studies have established in-cylinder flow to be extremely complex and three-dimensional in nature. Due to their highly turbulent nature, the in-cylinder flows are not easily quantified. But to improve the combustion process and thereby economy and emission, a better understanding of the relationship between the in-cylinder flow field and combustion process becomes necessary. In an attempt to do this, a number of experimental studies have been conducted including the flow visualization by researchers like Ekchian et al [1979], Hirotomi et al [1981] and Namazian et al [1980]. Similarly, researchers like Acroumanis et al [1987] and Bicen et al [1985] have studied flow past valves of different configurations and their effect on the subsequent in-cylinder flow field. All these aspects have been subsequently brought out in the review paper by Acrounamis et al [1987].

The emergence of various laser anemometry techniques over the last few decades has given researchers a non-intrusive method of measuring velocities in combustion chamber. Amongst the large number of workers Fanslar [1985], Ikegami et al [1987], Corcione et al [1994], Floch et al [1995], Yoo et al [1995] and Catania et al [1996], Einewall et al [1997]. Corcione et al [1994] have studied the in-cylinder turbulent flow field in a modern diesel engine – with a re-entrant geometry, motored over a wide range of speeds (1000 to 3000 rev/min). They highlight the jet character of the intake flow that generates large-scale rotating flow structures during intake and compression process. The large-scale rotating structure is observed to be highly turbulent and unstable, and is indicated to achieve greater stability during the compression process. In case of the re-entrant geometry, the authors observe that turbulence intensity tends to increase in the early stages of the expansion process, unlike the falling trend with the conventional

cylindrical geometry. This increase in turbulence intensity is attributed to higher shear zones with re-entrant geometries.

Similar behaviour has been observed by Catania et al [1996], who has measured turbulence quantities using hot wire anemometer in combustion chamber of an automotive diesel engine with a slightly re-entrant geometry at varying speeds from 600 to 3000 rev/min. The variation of turbulence intensity with time as a function of engine speed is clearly brought out.

In another work, Einewall et al [1997] have studied six combustion chambers namely, Nebula, Turbine, Reentrant square and Reentrant cylindrical, Quartette and Fair top in a supercharged natural gas engine. Results pertaining to turbulence intensity and burn rate for each of the combustion chamber are discussed. Quartette chamber is reported to have a favourable turbulence intensity peak, with a positive influence on the performance in terms of higher efficiency and lower emissions with lean mixtures.

In parallel with the experimentation, a detailed modelling of engine flow processes has become a new-found tool in generating a wealth of information. A number of researchers, namely Schapertons et al [1986], Wakisaka et al [1986], Jennings [1992], Trigui et al [1994], Han et al [1995], Bauer et al [1996], Jones et al [1995], and Lebrere et al [1996], have worked on 3-D computational studies with respect to the fluid flow in engine cylinder, simulating the motored or non-fired condition. CFD studies focusing on engine related work, address either the complete flow, encompassing the manifold and the engine cylinder or in part. Majority of the studies addresses geometries formed by a moving piston either flat or bowl and without or with moving intake valve. For cases not involving the intake valve, the initial condition for the compression process is taken as spatially uniform based either on empirical correlations or on single point experimental measurements. In the case of geometry with moving valve, suitable boundary condition is considered upstream of the intake valve or manifold.

The Study by Schapertons et al [1986] on bowl-in piston geometry reveals higher turbulence levels compared to the flat piston geometry due to enhanced swirl and squish effect. This study has been conducted on eccentric, reentrant bowls using standard k-ε model. The prediction depicts strong radial inward squish flow at the lip of the bowl near Top Centre (TC). The bowl-axis offset also seems to produce complex flow field in the bowl resulting in substantial spatial variation in turbulence intensity within the bowl. Trigui et al [1994] have checked the feasibility of using experimentally determined flow field at the intake valve closure as the initial condition for the compression process. The authors observe the study to be feasible, and that with adequate vector field data from the 3-D Particle Image Velocimetry (PIV) as the initial condition the overall error in prediction of subsequent flow field is modest. Han et al [1995] have proposed a high Reynolds-number RNG k-ε model for variable-density flows by including the effects of velocity dilatation and kinematic viscosity variation in the turbulence dissipation rate. Computations have been made of compressing/expanding flows in a production diesel engine consisting of a piston with

bowl arrangement. The computation does not account for intake flow and therefore a uniform initial condition is assumed at the beginning of computation. The predicted trend of increasing turbulence intensity due to squish late in the compression process and the magnitude of the integral length scale near TC seems to compare well with that of single point PIV measurements.

The ability of k-ε model in predicting turbulence quantities under engine like conditions has been examined by Lebrere et al [1996] by comparing with higher order Reynolds stress model on simple flat piston geometry. The Reynolds stress model predicts the presence of anisotropy during compression and it is attributed to be the reason for higher u' values with k-ε mode1 (~ 20% higher).

Summarizing findings from the above studies, the predictions using simpler turbulence models (k-ε model) seem to compare well with the available experimental results. Therefore using CFD to generate necessary flow field data for further modelling seems to be feasible.

1.2.3 Combustion Studies in Spark-Ignition Engine

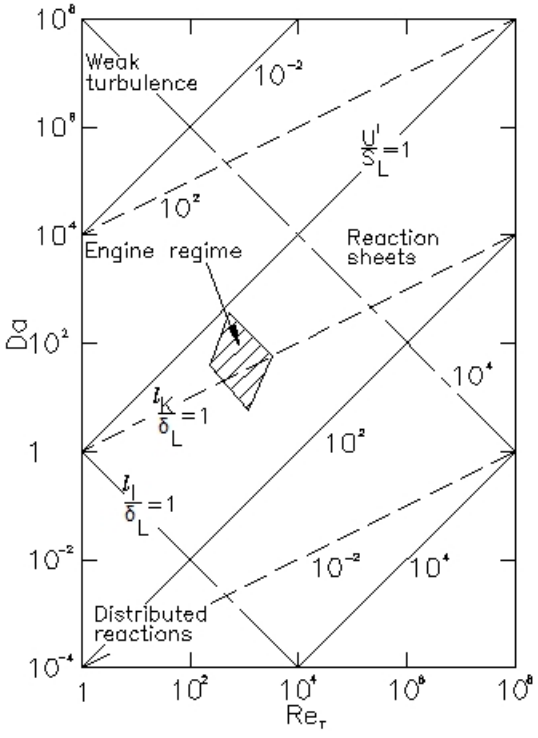

Fig. 1.1 Engine Flame Regime Shown on Da vs. Re_T Plot, From Abraham et al [1985].

Combustion in a SI engine has been observed to be turbulent in nature, governed by the physical and chemical processes and the complex interaction between them. Turbulent premixed combustion is essentially characterized by dimensionless parameters, namely turbulent Reynolds number (Re_T), a ratio of turbulence inertial to viscous force and Damkohler number (Da), a ratio of characteristic flow time to characteristic chemical time. The other parameter of interest is the ratio of Kolmogorov length scale l_k to laminar flame thickness δ_L, which provides a measure of distortion of a laminar flame front by the turbulent flow. Turbulent flames are primarily classified into two regimes; namely, the wrinkled flame and the distributed reaction zone, the above-mentioned parameters identify the regime of a flame. Many researchers have addressed the question of identifying the regime of engine flames. These studies have indicated the value of Da and Re_T for a typical SI engine to lie in the wrinkled flame regime as shown in Fig 1.1 - identifying the engine flame among different turbulent flame regimes [Abraham et al, 1985]. A sufficient condition for the wrinkled flame regime is $l_k >> \delta_L$. Abraham et al [1985] has observed the ratio of l_k/δ_L to be more than

unity based on engines of different configurations. In this case, one definition for laminar flame thickness is the ratio of thermal diffusivity in the reactants to the laminar burning velocity Abraham et al [1985].

The fact that engine flame is wrinkled [Keck, 1982; Heywood 1988] has been established based on experimental evidence, largely from Schlieren photographs and studies of flame structure using laser diagnostics. It is observed that early in the burning process the flame is a thin, moderately wrinkled but simply connected front or reaction sheet between unburned and burned gas. The thickness is reported to be about 0.1 mm, which is comparable to the thickness of a laminar flame under the prevailing engine conditions. The scale of wrinkles is about 2 mm at engine speeds of 1000 to 2000 rev/min. As the flame propagates across the chamber, the flame front is observed to become more convoluted, with the scale of wrinkles tending to decrease with time. Further evidence that a thin reaction sheet front becomes highly wrinkled and convoluted by the turbulent flow field into a thick turbulent flame "brush" is provided from the Schlieren studies conducted by Heywood et al [1984]. Experiments with propane–air mixture and hydrogen-air mixture indicate a turbulent flame thickness of 4 to 5 mm and 1.5 mm respectively. The lower flame thickness with hydrogen-air mixture is attributed its higher laminar burning velocity, whereby the increase in *Da* shifts the flame toward the wrinkled flame regime. Similar wrinkled structure has been observed by Namazian et al [1980] and Gatowski et al [1984] using Schlieren photography. The laser shadowgraphs acquired by Witze [1982] effectively captures the effect of spark location on the turbulent flame structure. Laser scattering experiments conducted by Smith [1982] reveal similar such wrinkled structure with the flame becoming increasingly finely wrinkled due to increase in engine speed on account of enhanced turbulence intensity and reduction in turbulence scale. The concept of wrinkled flame is shown in Fig 1.2. A thin laminar flame front of thickness (δ_L) is seen propagating into the unburned mixture, which is highly turbulent. The flame becomes increasingly distorted by the turbulent flow field through which it is propagating and develops a highly wrinkled and probably multiply-connected structure as shown to the left in Fig. 1.2, where δ_T is the thickness of the flame brush.

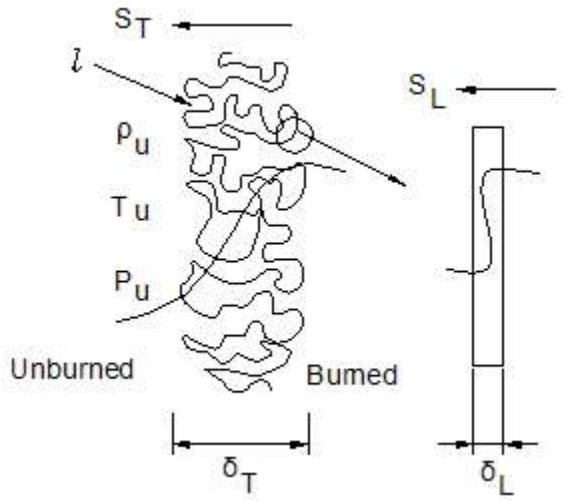

Fig. 1.2 Concept of Wrinked/Flamelet Regime in the Premixed Turbulent Flame.

The above stated experimental evidence indicates that the developed turbulent flames in SI engines, under normal operating conditions are highly wrinkled and probably multiply connected thin reaction sheets [Keck, 1982; see Heywood 1988]. The overall thickness of the turbulence flame brush is reported to be of the order 10 mm, with the reaction sheet thickness being 0.1 mm. The scale of wrinkles is reported to be 1

mm. This, therefore, establishes the engine flame to lie above l_k/δ_L=1 line, within the wrinkled flame or flamelet combustion regime.

Modelling of engine cyclic processes has been addressed extensively covering a wide range of fuels including liquid and gaseous fuels. In the area of gaseous fuels, propane and natural gas have received sufficient attention including multi-dimensional combustion modelling. The ability to utilize experimental data in new situations and conditions other than those where experiments are conducted is truly enhanced by using mathematical modelling. Mathematical modelling involves a combination of appropriate assumptions and equations describing a process under consideration and thereby allows critical features of a process to be analyzed. Modelling is being seriously pursued to acquire physical insight of the critical processes and thereof suggest suitable improvements based on the derived understanding. These are expected to become more robust with improvements in physical understanding over a period of time. Mathematical modeling calibrated with experimental data can provide a powerful predictive tool to decide on new designs as well make good predictions for new and complex situations. Modelling is classified as thermodynamic or fluid dynamic based on the equations that provide the model its predominant structure are either based on energy conversation or on a complete analysis of fluid flow [Heywood, 1988]. The thermodynamic models are more popularly known as zero-dimensional (0-D), phenomenological or quasi-dimensional models. The fluid-dynamic based models are often multidimensional due to their inherent ability to provide detailed information of the flow field and these involve solving of governing conservation equations.

In the recent times, detailed 3-D modelling of engine combustion using Computational Fluid Dynamics (CFD) has been investigated by Jennings [1992], Khalighi et al [1995] and Watkins et al [1996]. Jennings has simulated combustion using a fully turbulent combustion process, represented essentially as a two-zone model as represented in 0-D combustion models. However, unlike what has been observed experimentally in engine flames, the combustion is assumed to occur at multiple burning sites within the flame front. Khalighi et al [1995] have worked on flow visualization studies and simulations using flamelet combustion model on a four-valve-per cylinder SI engine. The authors have addressed issues relating to the application of CFD to engine modelling, which includes that of numerical inaccuracies. The authors discuss the technique adopted for near-wall combustion and the merits of flamelet model vis-à-vis the Arrhenius and turbulence-mixing-controlled model in predicting the mass burn. The authors also identify a mesh density of 1 million grid points for obtaining grid-independent solution for cold flows, with errors estimated at 10 to 15% at lower mesh densities. Watkins et al [1996] have simulated combustion and turbulence using flamelet and second order-moment closure models respectively. The authors claim turbulence anisotropy to be better represented by the second order-closure approach. Also the superiority of flamelet model as compared to eddy-burn-up model in predicting burn rate along the wall has been demonstrated.

Similarly, simpler models like the 0-D modelling have been addressed by a number of researchers due to their advantage that they could be put to immediate use till better understanding prevails in the complex-turbulent combustion process. The

phenomenological models are structured from the first law of thermodynamics formalism in which the only real independent variable is crank angle or time. Different approaches are used in modelling some of the important processes or phenomena occurring in the complex thermo-fluid dynamic environment in the engine cylinder. The in-cylinder phenomenon modelled could be either burn rate, boundary layer heat transfer or pollutant formation depending upon the focus of the study. Since 'burn rate' phenomenon is of interest in this work, it has been dealt with in the following paragraphs.

The burn rate in reciprocating SI engine is specified by some functional relationship where the start of combustion and combustion duration are related to the crank angle. Two examples of such functions are the Cosine burning law and Wiebe function [see Heywood, 1988]. The burn rate modelling is deficient because there is no physics involved in such an approach. In an attempt to alleviate such inadequacy, several researchers have proposed models to predict the burn rate in SI engines. Such models are based on fundamental quantities such as turbulence intensity and the turbulence length scales with specified kinetics. These models are required to predict the burn rate for a wide range of operation conditions like spark timing, equivalence ratio and engine speed. Burn rate is often expressed as:

$$\frac{dm_b}{dt} = \rho_u A_f S_T \tag{1.1}$$

Where ρ_u is the unburned gas density, A_f is the flame front area and S_T the turbulent flame speed or the burning velocity. Mechanistically S_T has been related to laminar burning velocity, S_L by the expression known as the Flame Speed Ratio (FSR), which is the ratio of S_T to S_L. There are a number of correlations available for calculation of FSR. Lancaster et al [1976] correlated the FSR with the turbulence intensity. A diagnostic combustion model, based on the assumption that flame propagates from the spark plug as a sphere, was used to determine burning velocities from the cylinder pressure-time data measured on a Cooperative Fuels Research (CFR) engine operating with propane. Similar correlation exhibiting FSR as a linear function of u'/S_L emerged from the studies of Mattavi et al [1978], Abel-Gayed et al [1976] and Ballal et al [1974]. Most of these correlations assume the following form

$$FSR = C_1 + C_2 \frac{u'}{S_L} \tag{1.2}$$

Where C_1 and C_2 are constants. In one such work by Groff [1987] on a constant volume vessel the value of C_1 and C_2 are found to be 2.273 and 1.681 respectively.

Another approach to model the turbulent flame propagation is entrainment and subsequent laminar burn-up of discrete, coherent, turbulent eddies; Blizard and Keck [1974, 1982] used this concept to calculate the burn rate in SI engines. This model has been formulated based on a series of experimental investigations that include Schlieren photographs, Shadowgraph and laser scattering measurements. The model postulates a

wrinkled turbulent flame formed by the distortion of a thin reaction sheet (δ_L) due to surrounding turbulent flow field. The flame propagation is modelled as a two-zone model, where the wrinkled multi-connected laminar flame separates the burned and the unburned mixture. They assumed that the entrainment front moves with respect to the unburned mixture at a constant velocity u_T that is proportional to turbulence intensity. Upon entrainment, each eddy burns in a characteristic time τ_b, which depends on the eddy size ℓ_T and laminar burning velocity S_L. This model can be summarized by the following two equations.

$$\frac{dm_b}{dt} = \rho_u A_f S_L + \frac{\mu}{\tau_b} \tag{1.3}$$

$$\frac{d\mu}{dt} = \rho_u A_f u_T + \frac{\mu}{\tau_b} \tag{1.4}$$

where $\mu = \rho_u \ell_T (A_\ell - A_f)$. A_l and A_f are laminar and spherical flame area respectively. Equation 1.3 represents the mass burn rate; Equation 1.4 represents the rate of change of unburned mixture within the flame front. For the two quantities namely the characteristic speed, u_T and characteristic length, ℓ_T in equations 1.3 and 1.4, Keck [1982] has provided an empirical relationship by coupling with a few variables relating to engine of simple geometry. The author concludes that the burning equations for complicated engine geometry with squish and swirl needs further examination. This model is discussed in detail in section 4.1.2 of Chapter IV.

Tabaczynski et al [1977] worked on the eddy entrainment concept and postulated the following theory. The vorticity in the turbulent flow field is concentrated in vortex sheets that are of a size comparable to Kolmogorov scale l_k. These vortex sheets are assumed to have a characteristic spacing that is of the order of the Taylor micro scale l_M related to integral length scale l_I and turbulent Reynolds number Re_T. Based on these assumptions it is argued that ignition sites propagate along the vortex sheets with a velocity $u'+S_L$, where u' is the local turbulence intensity. The propagation of the reaction front between the vortex sheets is assumed to be laminar.

In the recent work reported by James [1990] on an engine with flat piston geometry, the author has compared the experimental pressure-time data with the 0-D results. The predictions are made with an assumption of 'thin' and 'elliptical' turbulent flame instead of the 'thick' and 'spherical' flame up to a certain point, beyond which a thick and spherical flame is assumed. The point of transition is related to increased heat loss on account of higher surface-to-volume ratio at the time of completion of combustion. The author observes that thick turbulent flame could well be valid for the complete flame propagation, with flame shape tending towards ellipsoid at higher CR from that of spherical at lower CR.

If one were to summarize the findings of the above studies, the entrainment and laminar burn-up model seems to be an established model for predicting burn rate provided parameters related to turbulence are properly accounted for a given engine

geometry. However, there are open questions concerning the uniformity of the turbulence flow field for complex geometries involving swirl or squish, spherical flame assumption and flame movement subsequent to kernel formation. Detailed modelling of the fluid dynamics needs to be pursued to assess the validity of the model.

1.3 Approach of the Present Thesis

Based on the review of the earlier work, it is clear that there is no positive evidence for the presence of knock with producer gas fuel in spark ignition (SI) engines at high CR. This restriction in CR appears to be simply a matter of presumption rather than fact. Therefore, one of the primary objectives of this work is to attempt to operate a SI engine at the highest possible CR and establish the performance of the engine. This has called for a systematic investigation where all parameters relevant to engine characterization, namely gas and airflow rates, gas composition (on-line), emission levels and power delivered are recorded simultaneously. For combustion diagnosis, the cylinder pressure history data is also acquired and it later provides a basis to assess the thermodynamic behaviour of the engine. The producer gas fuel is generated from the well-established open top re-burn down draft gasifier system using Casuarina wood pieces as fuel.

It is evident from the literature that in-cylinder processes in a reciprocating engine are extremely complex in nature. While much is known about these processes, they are not adequately understood at a fundamental level. Therefore at present, constructing a model to predict the engine operation from the governing equations alone is difficult. Nevertheless, simpler models like the 0-D are helpful in analyzing the thermodynamic behaviour and identifying key parameters responsible for such behaviour. One such approach based on the above lines has been adopted in this work. The objective of the current modeling effort is to simulate the burn rate in a producer gas fuelled SI engine under the influence of varying ignition timing and CRs. Therefore, heat release forms the critical part of the model, with simpler gas exchange model to complete the thermodynamic cycle. Eddy entrainment and laminar burn-up (EELB) postulated by Keck is adopted to compute burn rate with parameters of turbulence properly accounted for engine geometry under study. This called for a detailed three-dimensional CFD modelling of the actual engine geometry to obtain relevant parameters of turbulence under non-firing conditions. The data on laminar burning velocity have also been generated at pressures and temperature relevant to engine operation. Using these data, the cylinder pressure-time histories are predicted for two combustion chamber geometries at various CR and ignition timings. The limitations of the EELB model have been examined.

1.4 Summary

From the literature survey in the field of producer gas engine it clear that no attempt has been made to understand whether knock occurs with producer gas operation. The existence of knock appears more of a presumption. In the field of modelling of SI engines, Eddy Entrainment and Laminar Burn-up model proposed by

Keck [1982] appears to be validated model to be used as a predictive tool for simple geometries. In order to implement the model on complex geometries (piston with bowl) requires apriori information on the turbulence level in the geometry. This could be quantified by experiments or through further computations. Use of CFD for computation of turbulence parameters appears to be rational based on the validation of the results with turbulence models such as $k-\varepsilon$ in most cases.

Chapter II

Biomass Gasification Process

This chapter provides details of biomass gasification process. Technological aspects relating to clean and consistent quality gas generation are discussed along with a few results related to gasifier performance. Also, the properties of producer gas fuel relevant to spark-ignition engine operation are discussed.

2.1 Introduction

Among the clean sources of fuels for power generation, natural gas has been exploited largely due to significant availability in specific locations. Similarly, there is also an impetus on using gas generated from industrial and municipal wastes, namely diluted natural gas - biogas and land-fill gas. As distinct from gas generation from biological/organic wastes by biological conversion process, which is limited to non-lignaceous matter, the thermo-chemical conversion route (also termed gasification) can process any solid organic matter. The range of biomass includes agro-residues like rice husk, sugarcane trash and bagasse in compact or briquetted form. The resultant gas known as 'Producer gas' can be used for fuelling a compression ignition engine in dual-fuel mode or a spark-ignition (SI) engine in gas alone mode. Harnessing of energy from biomass via gasification route is not only proving to be economical but also environmentally benign [Mukunda et al, 1993]. In fact, renewable energy is gaining popularity in Europe and the West, referred commonly as the 'Green Energy' and its harnessing is encouraged through attractive incentives on the tariff by the governments.

As mentioned in the earlier chapter, the technology of gasification has existed for more than seventy years. Some of the work done during World War II is well documented in SERI [1979]. Subsequent to World War II, the technology did not gain popularity on two counts, the first reason being unrestricted availability of petroleum fuels the world over at a low cost. The other reason being technological problems

relating to the presence of high level of tar content in the product gas, which posed a threat to engine operations.

Though there has been a sporadic interest in biomass gasifiers whenever there has been an oil crisis, sustained global interest developed only in the recent times for reasons like Green House Gas (GHG) emission reduction and carbon-trading through clean development mechanisms. In addition, a steep rise in the oil prices has had a severe impact on the industrial economy and this has forced many oil-importing countries to reconsider gasification technology and initiate improvements in them. Combustion, Gasification and Propulsion Laboratory (CGPL) at the Indian Institute of Science (IISc) has been addressing issues related to biomass gasification for over two decades. There has been extensive work carried out in this field involving more than 300 man-years. The outcome of this sustained effort is the design of open top, twin air entry, re-burn gasifier and its uniqueness in terms of generating superior quality producer gas provides a definite edge over other gasification technologies [Mukunda et al, 1994].

2.2 The Gasification Process

Biomass is basically composed of carbon, hydrogen and oxygen represented approximately by $CH_{1.4}O_{0.6}$. A proximate analysis of biomass indicates the volatile matter to be between 60% - 80% and 20% – 25% carbon and rest, ash. Gasification is a two-stage reaction consisting of oxidation and reduction processes. These processes occur under sub-stoichiometric conditions of air with biomass. The first part of sub-stoichiometric oxidation leads to the loss of volatiles from biomass and is exothermic; it results in peak temperatures of 1400 to 1500 K and generation of gaseous products like carbon monoxide, hydrogen in some proportions and carbon dioxide and water vapor which in turn are reduced in part to carbon monoxide and hydrogen by the hot bed of charcoal generated during the process of gasification. Reduction reaction is an endothermic reaction to generate combustible products like CO, H_2 and CH_4 as indicated below.

$$C + CO_2 \longrightarrow 2CO$$
$$C + H_2O \longrightarrow CO + H_2$$
$$C + 2H_2 \longrightarrow CH_4$$

Since char is generated during the gasification process the entire operation is self-sustaining. The temperature of gas exiting the reactor is about 600 – 900 K. Typical composition of the gas after cooling to ambient temperature is about 18-20% H_2, 18-20% CO, 2-3% CH_4, 12% CO_2, 2.5% H_2O and rest, N_2. The lower calorific value of the gas ranges is about 5.3 ± 0.3 MJ/Nm^3, with a stoichiometry requirement of 1.2 to 1.4 kg of air for every kg of producer gas.

One of the pre-requisites for the producer gas to be suitable for internal combustion application is the cleanliness of the gas apart from the composition. Conventionally, the gas purity is specified by quantifying the contaminant levels in

terms of particulate and tar matter. The permissible levels of gas quality also differ with the nature of the engine's induction process. The permissible level for a naturally aspirated engine is around 50 mg/Nm^3, whereas the level for a turbo-charged engine or a gas turbine is below a few mg/ Nm^3.

Producer gas can either be used in mono or dual-fuel mode in reciprocating engines. In case of mono-fuel mode of operation, the gas is fuelled to a SI engine, whereas in the dual-fuel mode it is operated along with small quantity of liquid fuel (high-speed diesel, furnace oil or bio-diesel) in a compression ignition (CI) engine. The choice of mode of operation is entirely dictated by the economics of operation, and of course on the availability of appropriate engines.

Conventionally, gasifiers can be classified as fixed bed and fluidized bed gasifiers. In a fixed bed gasifier, the charge is held statically on a grate and the air moving through the fuel bed leads to gasification in the presence of heat. In a fluidized bed system, the charge is suspended using air as the fluidizing media. The fluidized bed system generates excessively large tar-laden gas and external cracking using dolomite bed is necessary to bring down the tar to acceptable levels and hence the approach is limited to large power level systems (in MWe class). There are again variations in fluidized bed system known as the circulating fluidized bed system designed to make the system more compact. It is well recognized that for power levels of 1 MWe or less, fixed bed systems offer excellent performance at lower capital costs.

Fixed bed gasifiers are classified depending upon the flow path of feedstock (biomass) and the generated gas (producer gas) as updraft, crossdraft and downdraft systems. The updraft system is of counter current design, wherein the biomass and resultant gas flow path are in opposing directions as shown in Fig. 2.1a. In this case, the volatiles released from biomass in the upper region of the reactor do not pass through the hot char bed and therefore exit the reactor without cracking along with the producer gas. This gas is therefore less amenable for engine operation than thermal applications. In a crossdraft system the flow path of biomass and resultant gas are normal to each other as shown in Fig. 2.1b. Even this system produces tar-laden gas and is therefore not amenable for engine operations.

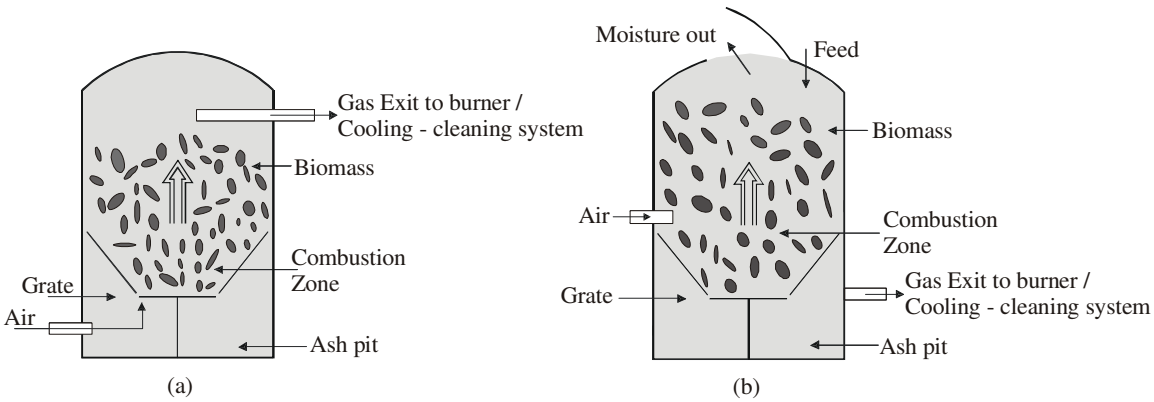

Fig 2.1 Gasifier Types – (a) Updraft, (b) Crossdraft

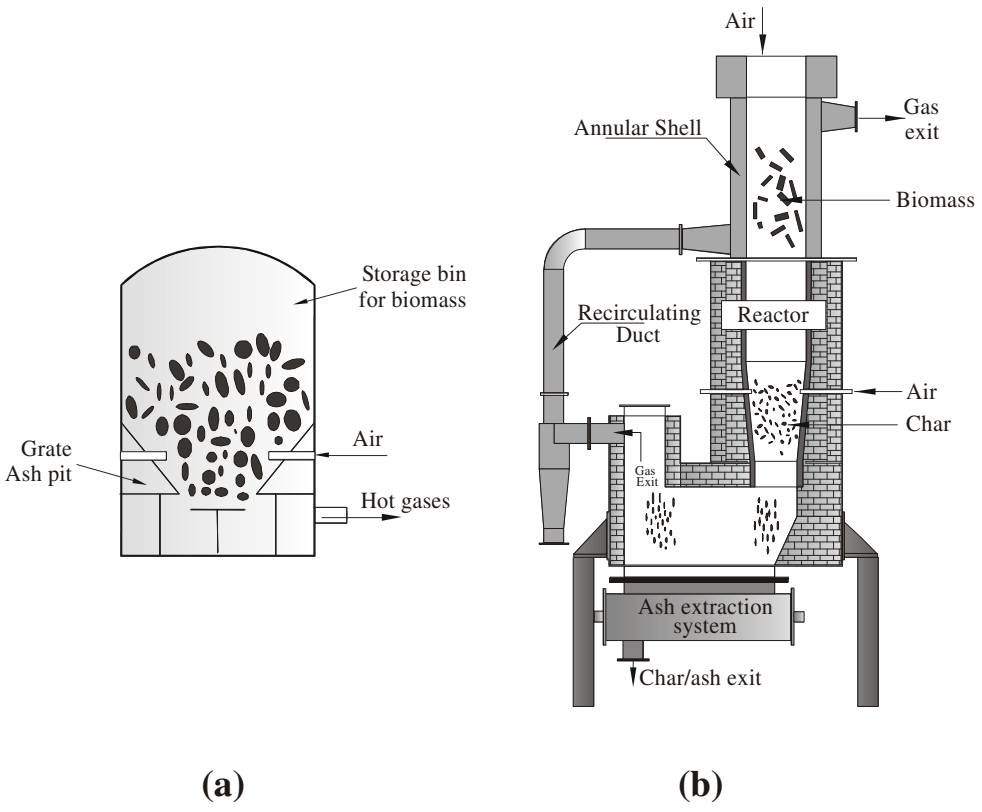

Fig 2.2 Downdraft Gasifier – (a) Closed Top, (b) Open Top Re-burn

The downdraft system shown in Fig. 2.2 is a co-current design wherein biomass and the resultant gas flow path are in the same (downward) direction. It is known from literature that among the fixed bed gasifiers, the downdraft design generates less of tar-laden gas and is amenable for thermal and engine applications. This happens by design wherein tar cracking occurs within the reactor (the gases generated in the upper regions of the reactor pass through the hot bed char). These allow for simpler gas clean-up system for usage of gas in internal combustion engines.

The downdraft design was the one that was employed as charcoal gasifiers during the World War II and is conventionally used for biomass (wood chips). In the design shown in Fig. 2.2a, the reactor top is normally kept closed and hence referred as 'closed top'. This design has a barrel shaped reactor with a provision for opening the top for feedstock charging and a narrow region called the 'throat' for tar cracking, a feature very vital for wood based systems. The gasification media i.e. air is drawn through the air nozzles/tuyures located at the oxidation zone.

The open top re-burn design (shown in Fig. 2.2b) pursued at IISc has concepts that can be argued to be helpful in reducing the tar levels in the resultant gas. This design has a long cylindrical reactor with air entry both from the top and the oxidation zone. The principal feature of the design is related to residence time of the reacting mixture in the reactor so as to generate a combustible gas with low tar content at different throughputs. This is achieved by the combustible gases generated in the

combustion zone located around the side air nozzles to be reburnt before passing though a bottom section of hot char. Also the reacting mixture is allowed to stay in the high temperature environment along with reactive char for such duration that ensures cracking of higher molecular weight molecules. Other relevant aspects pertaining to open top concept are presented – Appendix I.

2.3 Open Top Re-burn Gasifier

The open top, re-burn down draft gasifier consists of reactor, cooling and cleaning system. The producer gas exits the reactor at about 600 to 900 K, and is laden with contaminants in form of particulate matter (1000 mg/Nm^3) and tar (150 mg/Nm^3). The hot dust laden gas is further processed in the gas cooling and cleaning system in order to condition the gas to a level that is acceptable for engine operations. The elements of the system are as shown in Fig. 2.3.

2.3.1 Reactor

The reactor is the component wherein the thermo-chemical reactions occur and producer gas is generated. This sub-system is composed of two elements namely the ceramic shell and the ash extraction unit. However, for systems with throughput up to 75 kg/hr, the reactor has additional two elements in the form of annular shell and a re-circulating duct as shown in Fig 2.2(a). These additional elements are required at lower throughputs, as they have been found to be beneficial in terms of performance. The manner in this is achieved is as follows. The hot gas exiting at the reactor bottom is passed through the stainless steel annular shell, which is essentially a double wall shell isolating the charge (biomass) and the producer gas. A part of the heat recovered during the hot gas flow through the annular shell is pumped into the reactor – essentially utilized for drying of biomass. The estimated heat recovery is of the order of 5-10% of the input energy. The re-circulating duct forms the conduit between the reactor bottom and the annular shell. However, for system throughput >75 kg/hr the benefit of system simplicity and life far outweigh the heat recovery, and therefore the reactor is built as a single integral shell. The ceramic shell/part of the reactor is built of refractory bricks with an innermost lining of high alumina tiles. This part of the reactor is exposed to highest temperatures and includes both oxidizing and reducing environment. The ash extraction system consists of a screw that is intermittently operated to discharge ash from the reactor bottom into a container, for later disposal.

Air, which is the gasification medium, enters the reactor at two levels. The first level of air entry is provided at the reactor top, wherein the feedstock i.e. biomass is charged into the reactor. The second level of air entry occurs at the oxidation zone level, wherein the volatiles released in the upper zone of the reactor oxidize along with some char. The gasification process occurs along the lines indicated in the earlier section.

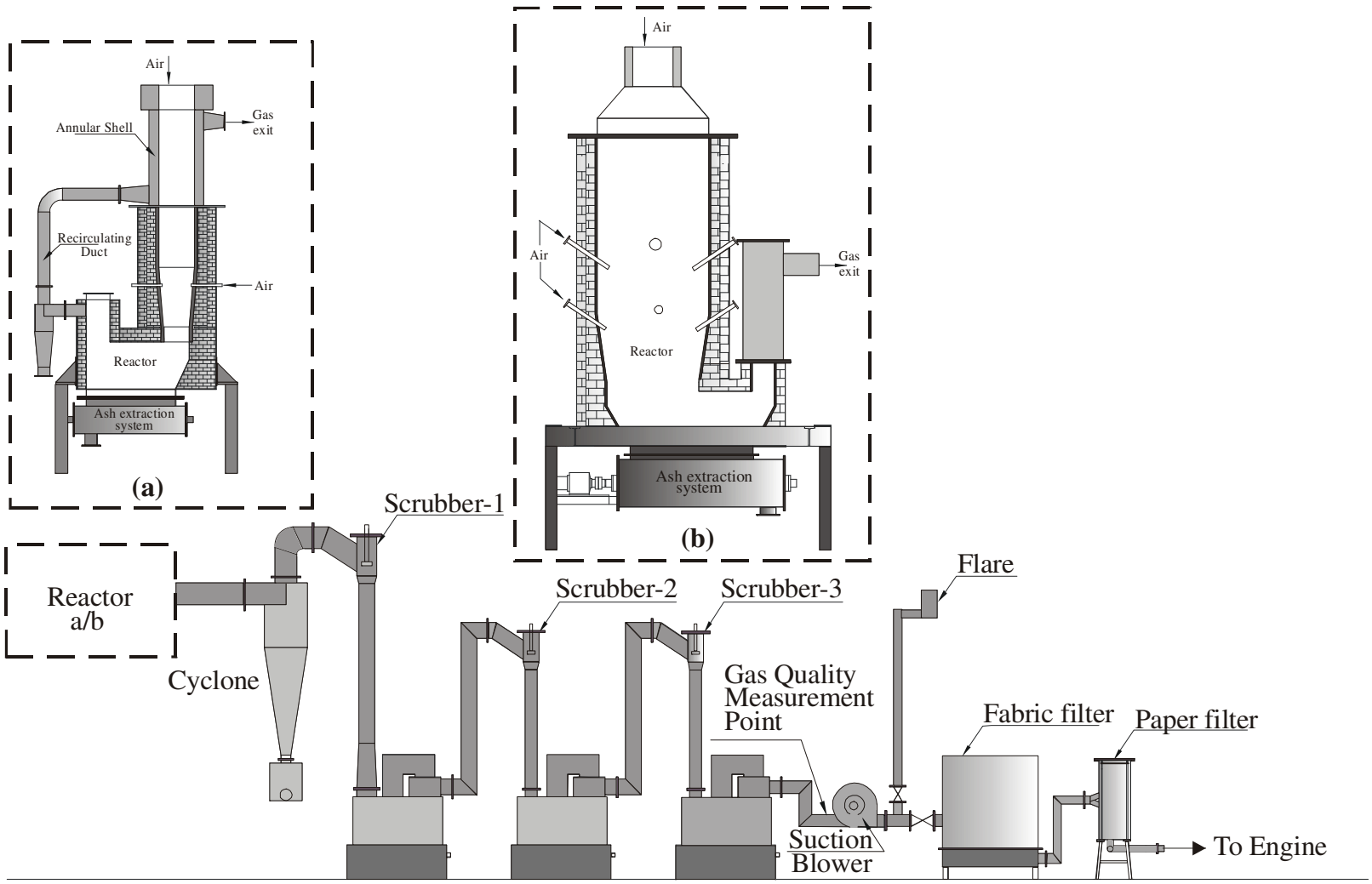

Fig 2.2 General Schematic of Open Top Re-burn Gasifier System with Reactor of Configuration (a) ≤ 75 kg/hr Capacity, (b) > 75 kg/hr Capacity. The Gas Scrubbing/Cooling and Cleaning Train are Identical but Scaled-down Accordingly.

2.3.2 Gas Clean-Up Systems

2.3.2.1 Cyclone

Large part of contaminant, mainly the particulate matter is separated in the hot cyclone. Nearly 80% of the particulate matter is separated from the hot producer gas in this unit.

2.3.2.2 Gas Scrubbers

This section consists of a series of scrubbers wherein the gas is brought into intimate contact with finely distributed scrubbing medium. In the first and second scrubber, water at ambient temperature is used as the scrubbing medium; wherein the gas is not only cooled to ambient condition but also cleaned to a reasonable extent. Water-soluble tar along with some particulate matter is separated from the gas stream in this section and the gas is led further to the chilled water scrubber. The chilled water scrubber uses cold water and separates fine sized particulate matter from the gas by the process of agglomeration. The gas at the exit of the chilled water scrubber would be at 10° C and has P & T matter lesser than about 2.0 mg/Nm^3. The gas is finally passed through a security filter, which is essentially a fabric filter with filtering cloth of 5.0-micron pore size. The tar and particulate laden wash water are led to the water treatment plant for processing prior to re-circulation.

2.3.3 Flare

A swirl design flare is provided with a central opening at the bottom for air intake. The initial quality of the flame is established by flaring the gas prior to supplying the gas to end device namely, engine etc.

2.3.4 Gas Quality Indicator

This on-line device provides a qualitative indication regarding the quality of the producer gas supplied to the engine. This is made possible by sampling small quantity of gas from the main gas stream and bubbling in the solvent (methoxy-benzene). In case the gas contains contaminants in excess of few mg/Nm^3 it dissolves into the solvent and the color of the solvent changes from transparent clear to yellow or greenish.

2.3.5 Safety Indicator

An on-line oxygen-measuring instrument provides a means for ensuring the safety of the gasifier plant. This is accomplished by monitoring the oxygen level at all times in the main gas stream connected to the end device. This is mandatory during events such as flaring of the gas in order to prevent flame flash back. An upper limit of 2% oxygen by volume (beyond lean flammability limit) in the producer gas is regarded as safe operation.

2.4 Gasifier Testing Protocol

The IISc gasifier design has undergone long duration testing with a wide variety of biomass ranging from low ash content biomass like wood to high ash content fuels like rice husk, in briquetted form. A typical testing protocol at the laboratory involved operating the gasifier continuously in excess of twelve hours duration. The testing procedure involved operating the system for about three hours at the rated power level in order establish steady state conditions for commencement of measurements. Measurements are made of those parameters which assess the overall mass and energy balance and thereby the gasification efficiency. The parameters measured towards that are gas composition, gas quality – particulate and tar matter, gas flow rates and biomass consumption.

The gas composition measurements involved use of on-line gas analyzers to record H_2, CO, CH_4 and CO_2 on a continuous basis. Whereas, the gas quality measurement involved sampling the gas under iso-kinetic conditions and passing it through a sampling train. An overview of this procedure is given here and the details are given in the gasification test report [Mukunda et al, 1994]. The sampling train consists of a series of bubblers containing distilled water and a solvent, methoxy-benzene (also called Anisole). The bubbler containing water separates the particulate matter present in the sampled gas and similarly methoxy-benzene dissolves the tar. Finally, the gas is passed through a cellulose filter to trap residual particulate matter prior to igniting the sampled gas in a swirl burner. The entire sampling train is placed in an ice bath to prevent evaporative losses. The actual quantity of gas sampled is metered using an integrating flow meter. Once the gas sampling is complete for a specified duration, the aqueous and solvent phase is separately collected and a gravimetric analysis is conducted in order to quantify the particulate and tar level separately. The details of the analytical procedure are outlined in the gasification test report [Mukunda et al, 1994].

Other parameters, namely the reactor wall temperatures, gas exit temperatures, gas flow rate and static pressure across different sub-systems are continuously monitored and data acquired on to a computer. The gas flow rate is continuously monitored any changes in pressure drop across various elements are corrected by adjusting the valves to maintain the gas flow rate. Similarly the rate of biomass charging into the reactor and the ash/char extracted are noted for mass and energy balance calculations.

2.5 Gasifier Performance

The parameter that quantifies the over-all efficiency of the gasification system is termed 'Gasification efficiency'. Gasification efficiency refers to the efficacy with which the energy content present in solid biomass is captured or transformed into the gaseous form. Depending upon the condition of the gas either 'hot' or 'cold' the gasification efficiency term is suitably pre-fixed. Typical values of gasification efficiencies at the hot and cold ends (reactor exit and gas-clean-up exit) are 82 ± 2 and $78 \pm 2\%$ respectively.

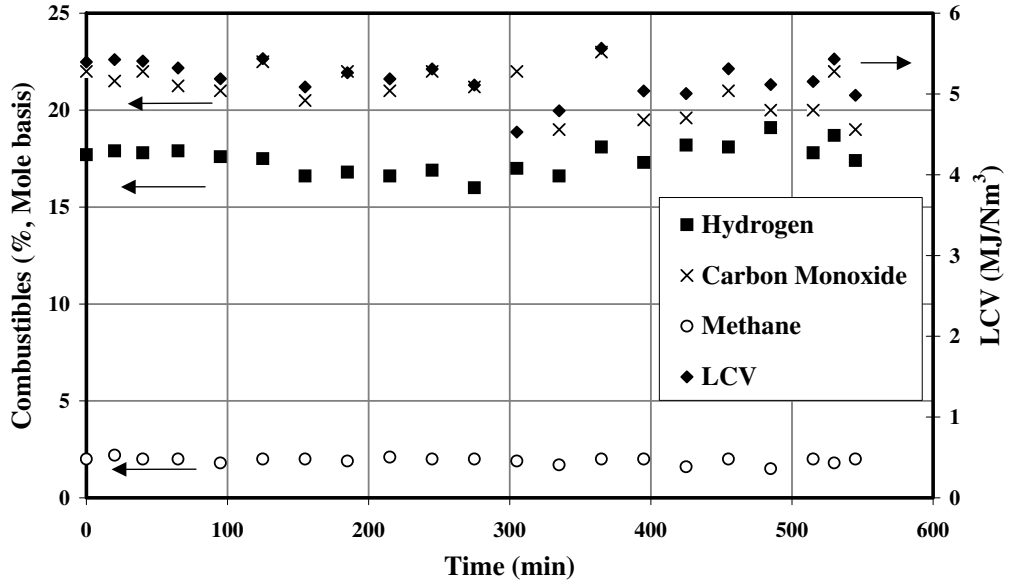

Fig 2.4 Trace of Producer Gas Composition (Combustibles) and Lower Calorific Value (LCV) During Steady State Operation of Gasifier.

The variation in the producer gas composition (combustibles) with time is shown in Fig. 2.4, the mean lower calorific value (LCV) works out to about 5.3± 0.3 MJ/Nm^3. The small variation in gas composition with time is caused due to inherent working of the gasifier. The amount of hydrogen content influences significantly the laminar burning velocity of the producer gas + air mixture. These have significant effect on the selection of optimum ignition timing for reciprocating engine operation in SI mode. The influence of moisture content in the biomass on the LCV is shown in Fig. 2.5. It is evident from this figure that moisture exerts a major influence on the end producer gas LCV. The increase in moisture content by 1% has resulted in reduction in LCV by about 1.2 to 1.4%. However, with the exception is rice husk, wherein the mean calorific value is as low as 3.8 MJ/Nm^3, even though its inherent moisture content is less than 12%. This is on account of higher ash content (20%) that inhibits the carbon conversion process and thereby the char conversion/reduction process of gasification. The gas generated from rice husk as the feedstock contains about 12-14% each of H_2 and CO and about 3% CH_4. The higher methane content with rice husk as the feedstock somewhat offsets the lowering of LCV due to reduction in hydrogen and carbon monoxide. The particulate and tar (P and T) level reflect the adoptability of the gas for engine related application. The data on P and T level in the cold gas is shown in Fig 2.6. These values have been achieved with gas cleaning system comprising of water-impinged coolers and sand filters [Mukunda et al, 1994]. The mean value (P and T combined) is about 70 + 20 mg/Nm^3 and meets the norms for naturally aspirated reciprocating engines. However, with the fair amount of data gathered from a number of field-installed systems, the limit is understood to be more stringent for turbo-charged engines. The upper limit for this kind of engine could be less than few mg/Nm^3. This limit has been achieved with the new gas clean-up system as described earlier.

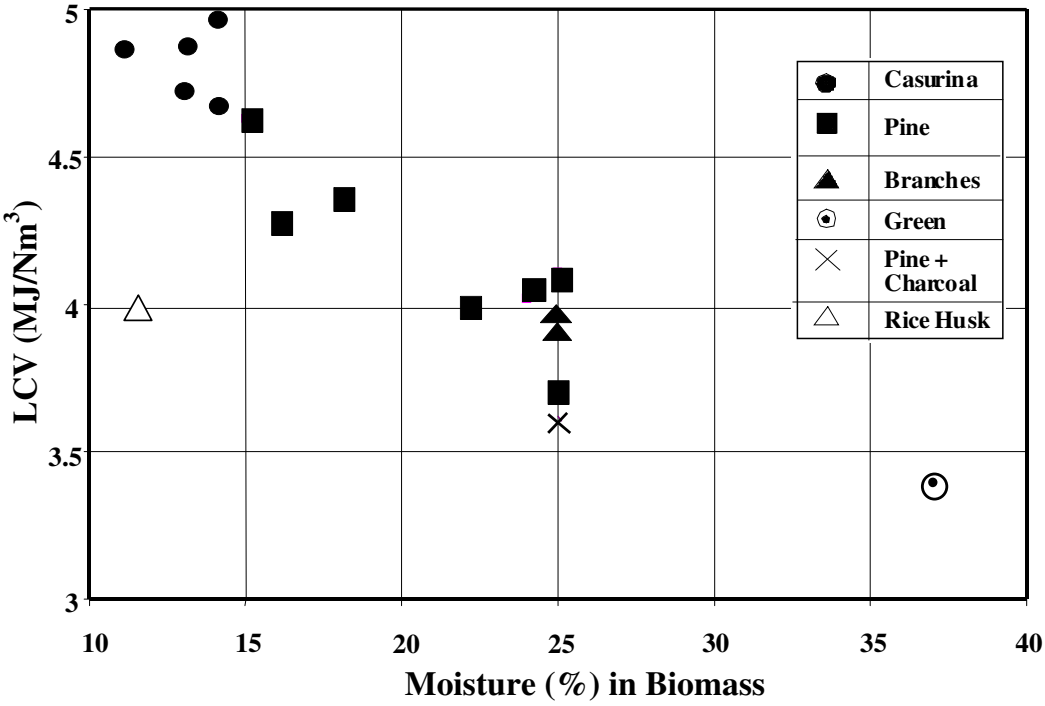

Fig 2.5 Variation in Producer Gas Lower Calorific Value (LCV) with Different Biomass.

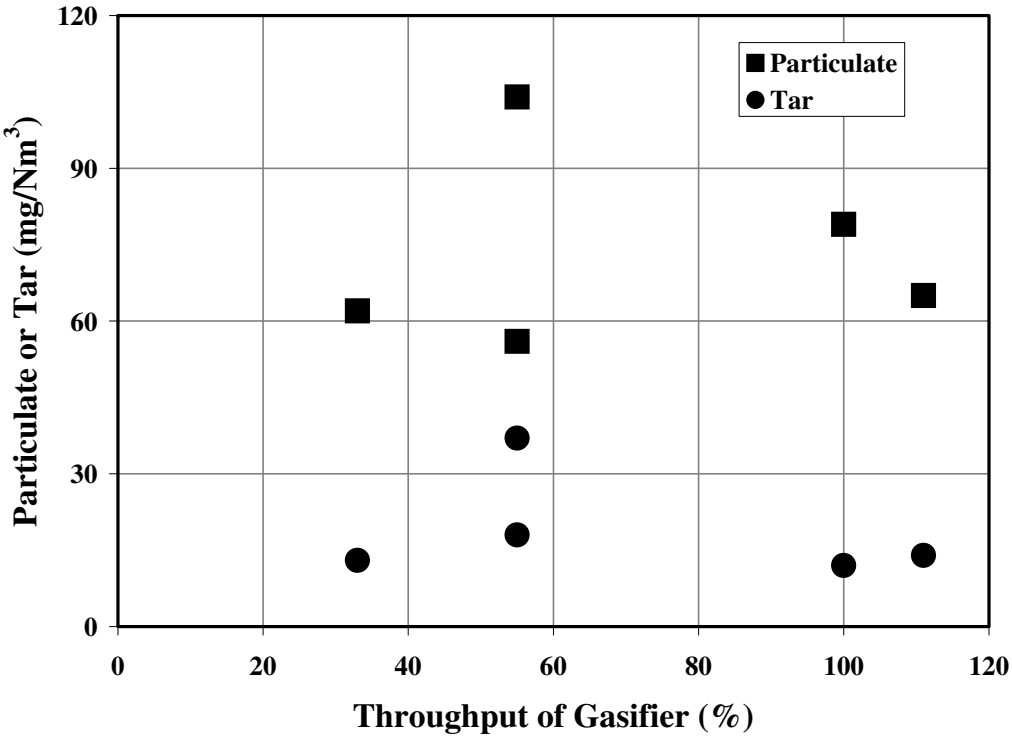

Fig 2.6 Particulate and Tar Content in Producer Gas at the Exit of Gas Clean-Up System

2.6 Properties of Producer Gas

Some of the fundamental data relating to producer gas are compared with pure gases in Table - 2.1. The comparison of producer gas with methane is more vital with regard to the internal combustion engine operation. This is because most of the engines operating on gaseous fuels are either close to pure methane (natural gas) or diluted methane (bio-gas, land-fill gas). The fuel-air equivalence ratio (actual fuel to air ratio)/(stoichiometric fuel to air ratio) at the flammability limits [Kanitkar et al, 1993] compares closely for both the gases, but the laminar burning velocity for producer gas at the lean limits is much higher. The laminar burning velocity for producer gas (at 0.1MPa, 300K) is about 0.5 m/sec [Kanitkar et al, 1993], which is about 30% higher than methane. This feature is argued to demand lower advancement in the ignition timing and needs consideration while arriving at the optimum ignition timing for the producer gas fuel.

Like any other gaseous fuel, producer gas can be used for internal combustion engine operation provided the gas is sufficiently clean such that contaminant does not accumulate in the intermediary passages to the engine cylinder. But this fuel has largely been left unexploited due to additional perceptions, namely (1) auto-ignition tendency at higher CR, (2) large de-rating in power due to energy density being low.

However, these perceptions need re-examination and clarification. The arguments against the classical view in favour of better knock resistivity are as follows. Firstly, with the laminar burning velocity being high due to the presence of hydrogen (more so, with the gasifier system adapted in this thesis work) might reduce the tendency for the knock. Secondly, the presence of inert in the raw gas (CO_2 and N_2) might suppress the pre-flame reactions that are responsible for knocking on account of increased dilution. Also the maximum flame temperature attainable with the producer gas being lower compared to conventional fuels like methane, one could expect better knock resistivity. An examination of literature shows that producer gas has not been subjected to study on knock behaviour.

Further, there is a general perception that producer gas being a low-density energy fuel, the extent of de-rating in power would be large when compared to high-energy density fuels like natural gas and Liquefied petroleum gas. This could be misleading because what needs to be accounted for comparison is the mixture energy density [Fleischer et al, 1981] and not the fuel energy density per se. On comparison with CH_4, the mixture energy density for producer gas is lower by 23% as reflected in Table 2.1. The product to reactant mole ratio for producer gas is less than one. These two parameters could contribute to de-rating of engine output. However, it might be possible to reduce de-rating by working with engines of higher CR, perhaps higher than what has been examined using natural gas (CR=15.8) by Das et al [1997].

Table - 2.1: Properties of Producer Gas (PG) Compared with Pure Combustible Gases

Fuel + Air	Fuel LCV, MJ/kg	Air/Fuel @ (Φ =1)	Mixture, MJ/kg	Φ, Limit		S_L (Limit), cm/s		S_L Φ =1, cm/s	Peak Flame Temp, K	Product/ Reactant Mole Ratio
				Lean	Rich	Lean	Rich			
H_2	121	34.4	3.41	0.01	7.17	65	75	270	2400	0.67
CO	10.2	2.46	2.92	0.34	6.80	12	23	45	2400	0.67
CH_4	50.2	17.2	2.76	0.54	1.69	2.5	14	35	2210	1.00
C_3H_8	46.5	15.6	2.80	0.52	2.26	-	-	44	2250	1.17
C_4H_{10}	45.5	15.4	2.77	0.59	2.63	-	-	44	2250	1.20
PG	5.00	1.35	2.12	0.47 a	1.60 b	10.3	12	50 c	1800 d	0.87

PG: H_2 - 20%, CO - 20%, CH_4 - 2%; a: $\pm$0.01, b: $\pm$0.05, c: $\pm$5.0, d: $\pm$50 ; Source: Lewis et a l [1987], Mukunda [1989], Kanitkar et al [1993]

2.7 Summary

Technological aspects relating to biomass gasification technology have been discussed. The performance of IISc open top re-burn downdraft gasification in terms of generating reasonably clean gas has been brought out. The potential of producer gas as an engine fuel vis-à-vis other pure gaseous fuels has been highlighted.

Chapter III

The Experimental Work

This chapter discusses the experimental work conducted on spark-ignited gas engines fuelled with biomass-derived producer gas. The experimental work is presented in two parts. The first part discusses experiments on a Small Power level Engine (SPE), converted from a diesel engine and tested at varying compression ratio. The second part deals with experiments on a Medium Power level Engine (MPE) at a fixed compression ratio of 12. The results of performance are compared with baseline results obtained with diesel fuel in compression ignition mode of operation.

3.1 Introduction

This experimental work is considered in the background of the weak information base on producer gas engines in the literature. However, with the perceptions of the author being different from that quoted in the literature relating to operations at high compression ratio (CR), a thorough scientific investigation was launched for the first time. The primary investigation is conducted on an engine of 24 kW nominal capacity. For this purpose, a commercially available production diesel engine of CR = 17 is chosen for conversion to a spark-ignition (SI) engine. The engine operations have been found to be challenging with respect to data acquisition of engine cylinder pressure history due to severe electro-magnetic interference from the mechanical ignition system, which seriously hampered the working of the computer, a part of the data acquisition system in the initial stages. This was resolved subsequently through electrical circuit changes.

3.2 Small Power level Experiments

3.2.1 Description of the Engine

Small power level engine (SPE) experiments were conducted on a spark ignition (SI) engine converted from a naturally aspirated, three-cylinder, direct injection diesel engine (RB 33 model) of compression ratio (CR) 17. The reason for choosing this particular CR diesel engine is explained as follows. It is known from fundamental thermodynamics that it is beneficial to operate an internal combustion engine at as high a CR as possible in order to attain high overall efficiencies. But the gain in efficiency beyond a certain CR can be expected to be marginal due to the other counter influencing factors such as increased heat loss and friction. But in the case of a SI engine the limitation of CR comes from a supplementary factor namely, 'knock'. It is to be noted that knock sensitivity identifies the Highest Useful Compression Ratio (HUCR) for most of the fuels. However, for higher-octane fuels, it has been experimentally established that the upper limit of CR is 17 beyond which there is a fall in efficiency [Caris et al, 1959]. The inference drawn by Caris et al [1959] is based on extensive tests conducted on a multi-cylinder engine at varying CRs up to 20, using iso-octane doped with anti-knock agent. The variation of thermal efficiency with CR from the work of Caris et al [1959] is shown in Fig. 3.1. The decline in efficiency beyond CR of 17.0 is attributed to delayed or late burning leading to increased heat loss. If one were to consider this as the upper limit and since no other work has been reported at higher CR for SI engines, choosing a production engine in CR = 17 for the current study appeared to be meaningful.

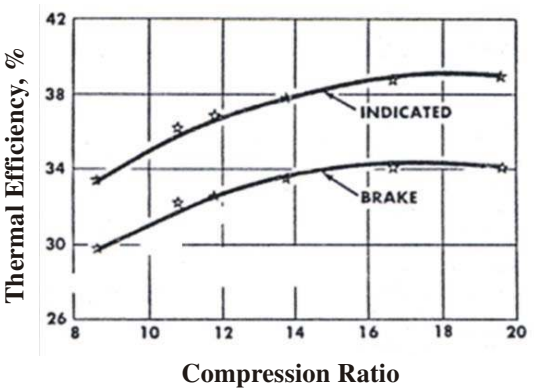

Fig. 3.1 Full Throttle Thermal Efficiency in SI Engine - 2000 rev/min, From - Caris et al [1959].

The salient features of the diesel engine chosen for conversion to SI engine are shown in Table 3.1. The naturally aspirated engine of 3.3 Litre capacity is designed at a CR =17, to operate at an air-to-fuel ratio of 20 - 21 (with diesel) at a rated conditions. The engine employs an in-line fuel injection system along with multi-hole injectors to atomize diesel at a pressure of 180 bar. The air intake system is comprised of an air filter, manifold and runner to each cylinder head. The intake port is of a simple design – directed type with air entering into the cylinder all around its periphery. The engine is designed with a valve overlap of 64° CA (refer Fig. 6.2 Chapter VI). The combustion chamber of the engine is formed of a flat cylinder head and slightly offset bowl-in piston as shown in Plate 3.1 and in Fig. 7.1 of Chapter VII. The bowl is hemispherical in shape and has a squish area of 70% (percentage of piston area closely approaching the cylinder head). The engine was characterized using diesel fuel prior to conversion.

Table 3.1: Small Power level Engine Configuration Details

Parameter	Specification
Make and Model	Kirloskar, RB-33 Coupled to a 25kVA Alternator
Engine Type	In-Line, 3 Cylinder, 4-Stroke, Naturally Aspirated
Rated Output - Diesel	28 kW @ 1500 rev/min
Net Output - Diesel	24 kW (21kWe) @ 1500 rev/min
Type of Cooling	Water Cooled with Radiator
Bore x Stroke	110 x 116 mm
Swept Volume	1.1 Litre
Compression Ratio	17:1
Bumping Clearance	1.5 mm
Combustion Chamber	Flat Cylinder Head and Hemispherical Bowl-in Piston Type
Squish Area	70%
Ignition System - Gas	Battery Based Distributor Type with Ignition Advance/Retard Facility
Spark Plug Type & Location - Gas Mode	Cold, Offset from the Axis of Cylinder by 8mm (Refer Fig. 7.1)
Intake Port	Directed Type
Valve Timing	Inlet Valve Opening – 26 ° BTC Inlet Valve Closing – 66 ° ABC Exhaust Valve Opening – 64 ° BBC Exhaust Valve Closing – 38 ° ATC
Firing Order	1-2-3
SFC, g/kWh - Diesel	280 - 290
Air-to-Fuel Ratio - Diesel Mode at Peak Load	20 to 21:1 at 24 kW
Alternator Efficiency	87%

BTC: Before Top Center, ABC: After Bottom Centre, BBC: Before Bottom Centre, ATC: After Top Centre

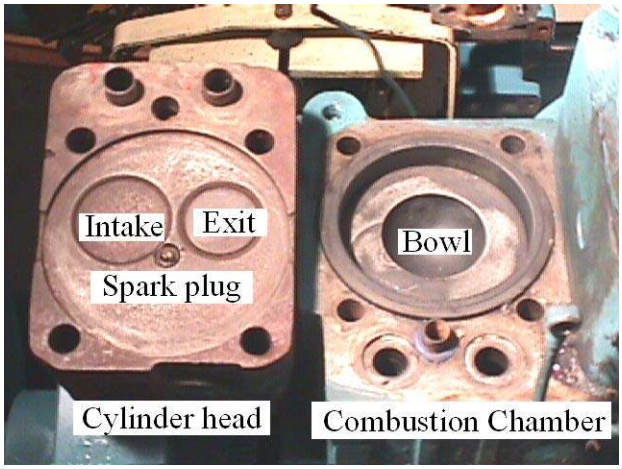

Plate - 3.1: SPE Combustion Chamber

Cylinder Head with Centrally Located Injector or Spark Plug Shown on the Left. Location of Intake and Exit Valve also Shown; on the Right is the Bowl-in-Piston combustion chamber.

The database obtained included in-cylinder pressure, and the specific fuel consumption at the rated speed of 1500 rev/min. The engine delivered a peak power of 21 kWe, which is equivalent to a net brake (shaft) output of 24.0 kW against the rated output of 28.0 kW (at sea level). The loss in power is attributed to lower air density at Bangalore, due to its elevation (~1000 m above sea level). Details of power output calculations of the diesel engine are illustrated in Table 3.2.

Table 3.2: Diesel Engine Net Output Calculations

A	Rated shaft output at sea level. The rated output includes power consumed by the accessories namely, water pump with fan, dynamo, fuel injection pump (FIP).	28.0 kW
B	Air pressure at Bangalore is 690 mm HG. De-rating on account of elevation is 9.3%	2.60 kW
C	Power consumed by accessories like water pump with fan and dynamo. This was measured by external motoring and is exclusive of power consumed by the FIP.	1.30 kW
D	Net shaft output available = A - (B+C)	24.1 kW
E	Net shaft output (Inclusive of the power consumed by FIP, which is assumed)	24.0 kW

3.2.2 Conversion Methodology

Modifications carried on the diesel engine in order for it to work as a SI engine are as follows.

- Insertion of spark plug in place of fuel injector as shown in Plate 3.2. This called for enlarging the diameter of the recess and tapping of appropriate thread (M10) in the cylinder head to receive the spark plug. Modification was done in such a way that the tip of spark plug was in flush with the cylinder head. The location of the spark plug was retained at central position with respect to the combustion chamber. At the time of conversion, hot spark plugs (Product No. W8DC, MICO make) were chosen with an intention of avoiding frequent fouling of spark plugs,

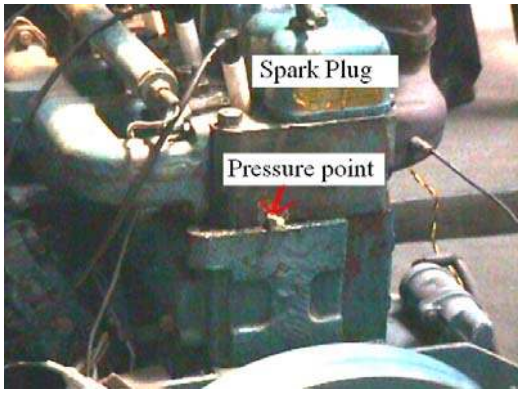

Plate - 3.2: Instrumentation on SPE

Fuel Injector Replaced with Spark Plug; Provision Made for Pressure Measurement on the Cylinder Head Shown by the Red Arrow.

but this led to problem of backfiring into the intake manifold at higher power output. It took sometime to identify the cause for the backfire and was later traced to the malfunctioning of the hot spark plug (acting like a hot spot) beyond a certain load (> 16 kW). The problem was subsequently resolved by installing cold spark plugs (Product No. W5DC, MICO make).

- Adaptation of a three-cylinder distributor type battery based ignition system. The fuel injection pump was left intact with an intention of reserving the possibility of modifying back to a diesel engine in a short span of time (less than one hour). This called for additional provision whereby a gearbox was specifically designed to drive the mechanical ignition system's distributor at camshaft speed. Also provision was made to advance/retard the ignition timing. The diesel fuel injection pump had no role in the operation of gas engine. These details are depicted in Plate 3.3.

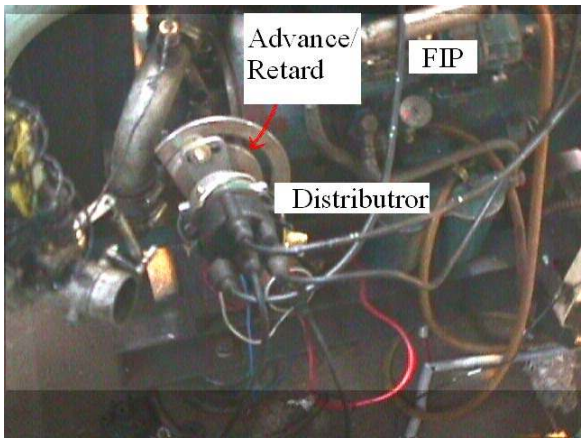

Plate - 3.3: Ignition system on SPE

Battery Based Mechanical Ignition System Fitted on the Camshaft Drive; Red Arrow Pointing Towards Provision for Manual Advance/Retard of Ignition Timing. Diesel Fuel Injection Pump (FIP) is also Evident (Right).

- The combustion chamber design comprising of a flat cylinder head and slightly offset bowl-in-piston was retained. Changing the thickness of cylinder head gasket altered the clearance volume and hence different CRs were simulated. The combustion chamber along with the cylinder head showing the location of valve and spark plug is shown in Plate 3.1.

3.2.3 Instrumentation on the Engine

3.2.3.1 p-θ Measurements

Fig. 3.2 depicts the instrumentation scheme adopted for the experiments. For combustion diagnostics, the in-cylinder pressure was measured using a Piezo sensor (PCB make) mounted on the cylinder No. 1 of the engine. The sensor is hermitically sealed (model No. HS 111A22) with a built-in charge amplifier, the other specifications

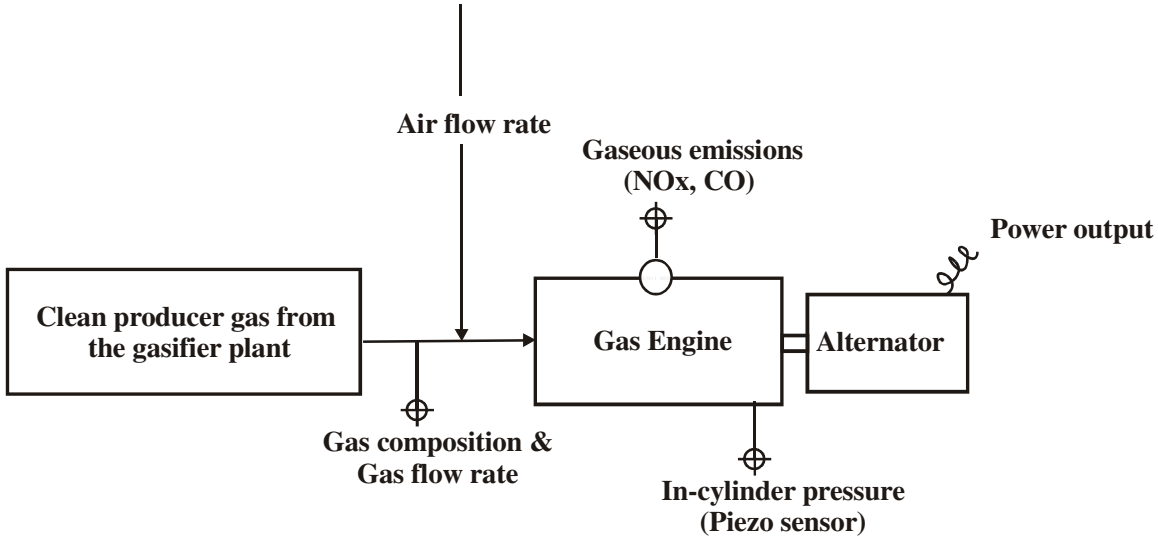

Fig. 3.2 Scheme for Instrumentation

being: resolution - 0.69 kPa, rise time < 1 micro second, discharge time constant > 500 second, natural frequency of the crystal = 550 kHz. The in-cylinder pressure measurement synchronized with the crank angle measurement (sensed using an optical sensor) was acquired on a PC (Personal Computer, 600 MHz processor) at time intervals of one-degree crank angle. The piezo sensor could not be flush mounted with the interior part of the combustion chamber due to constraints on the engine cylinder head. However, the sensor was mounted by drilling a 1.0 mm size hole in the cylinder head, and a 40 mm long aperture communicated between the sensor and the combustion chamber. This therefore introduced a time lag between the actual pressure changes in the combustion chamber and the pressure sensed by the sensor (due to 40 mm long passage). The time lag is estimated to be of the order of 0.4° CA. In addition to this, the error in TC identification (explained in the following section) is about 0.2° CA, which adds to a total of 0.6° CA in terms of accuracy of pressure-crank angle data recorded. This aspect is considered while interpreting the results.

3.2.3.2 Accuracy of TC Identification

The Top center (TC) has been identified in accordance to the procedure discussed by Lancaster et al [1975]. To locate TC within accuracy of 0.1° CA, the authors have identified a systematic procedure, wherein multiple readings are required to be taken on either sides of TC (at 40° CA). The above-mentioned procedure has been adopted for TC identification and therefore accuracy in the current case should be well within 0.1° CA.

3.2.3.3 Emission Measurement

The emissions and exhaust temperature were measured in the exhaust manifold; the temperature was measured using K-type (Chromel-Alumel) thermocouple. Adequate provision was made to condition the flue gas sample prior to measurements. The flue gas composition was analyzed using a multi-component analyzer, which are based on infrared and chemical cell technique. The substances analyzed were nitrogen

oxide (NO), carbon monoxide (CO), carbon dioxide (CO_2) and oxygen (O_2) on an intermittent basis. Since the input feed was gas with particulate matter averaging about 60 mg/Nm^3, this would amount less than 25 mg/Nm^3 (some particulate matter would burn) in the exhaust (air-to-fuel gas ratio ~1.3). Therefore particulate measurement was not envisaged.

3.2.3.4 Air/Gas Flow Measurement

The air and gas flow (in the case of gas engine) were separately measured using calibrated venturimeters. The venturimeters were subjected to primary calibration by adopting standard pitot tube measurement procedure.

3.2.3.5 Power Output Measurement

The engine output was measured by recording the voltages across the three phases of the alternator and the current drawn by the load bank. The load bank consisted of a number of resistor coils of 1.0 and 0.5 kWe each, totally to about 25 kWe. Digital frequency meter was employed to the record the frequency of the output.

3.2.4 Instrumentation on the Gasifier

The producer gas constituents were measured using on-line gas analyzers on a continuous basis. The sample gas was analyzed using a multi-component analyzer comprising of hydrogen (H_2), carbon monoxide (CO), methane (CH_4), carbon dioxide (CO_2) and oxygen (O_2) detecting sensors. The measurements of CO, CH_4 and CO_2 fractions are based on infrared technique, H_2 on thermal conductivity technique and the O_2 on chemical cell. Calibration gas of a composition similar to that of a producer gas was used for calibrating the gas analyzer prior to start and close of every test run. Random calibration was also performed between the runs in order to reduce the errors. The commercially sourced calibration gas (from Bhoruka gases Ltd, Bangalore) has been primarily calibrated using gas chromatography. The sample producer gas was conditioning prior to commencement of measurements. This was achieved in two stages using moisture and particulate matter filtering system. The data obtained from gas analyzers in terms on gas constituents/composition was further used for estimation of calorific value of producer gas and this provided an input for estimation of energy density of producer gas-air mixture.

3.2.5 Experimental Procedure

As mentioned earlier, the well-researched, tested and industrial version of the gasifier of 75 kg/hr rating formed the gas generator. The system has qualified for long hours of continuous operation in meeting the industrial requirements in terms of generation of consistent quality gas. The system comprised of a reactor, gas cooling and cleaning system, flare and ducting to the gas engine. The reactor and cooling system are similar to the discussed in Chapter II. However, in the gas cleaning system instead of using chilled water for scrubber a diesel wash was provided. The chilled water scrubbing system is a later development in gasification system and is the part of the

system for the medium power level engine (MPE) experiments. The details of these individual sub-systems have been discussed earlier in Chapter II, however an overall schematic of 75 kg/hr is shown in Fig. 3.3.

3.2.5.1 Commencement of Testing

The gasification process was initiated by lighting the reactor with an open flame at the air nozzles. The gas drawn by the blower was ducted to the flare. Within about ten to fifteen minutes, combustible gas was generated, with oxygen level in the product gas falling close to zero. This event marked the completion of gasification process, further to which the gasifier is operated in flare mode until the system reached steady state of operation. Typically this was about 2-3 hours from the cold start. The producer gas composition was monitored during this period and at the time of start of the gas engine the composition was typically be 19$\pm$1% H_2, 19$\pm$1% CO, 2$\pm$0.5% CH_4, 12$\pm$1% CO_2 and the rest, N_2, which corresponded to energy content of 5.20 – 5.50 MJ/Nm^3. Standard biomass namely, causurina with moisture content of 12-15% on dry basis (sun-dried biomass) was used as the feedstock to obtain consistent quality gas.

Once the gas composition stabilized, the engine was operated for few minutes at 1500 rev/min under no-load condition. Subsequent operations on load were also conducted at 1500 $\pm$ 50 rev/min. The throttling for speed control and air-to-fuel proportioning was achieved using manually operated valves (without carburetor). Experiments were conducted at CRs of 17.0, 14.5, 13.5 and 11.5. The CR values are based on cylinder's geometric measurements. The engine was tested at different ignition timing settings to determine the optimum ignition timing, referred as MBT (Minimum Advance for Brake Torque) at different CRs. With set ignition timing, the air and fuel were tuned to achieve maximum power. Measurements were initiated 10 to 15 minutes after attaining stable operation. The in-cylinder pressure data with a resolution of one-degree crank angle was acquired on a computer for consecutive cycles.

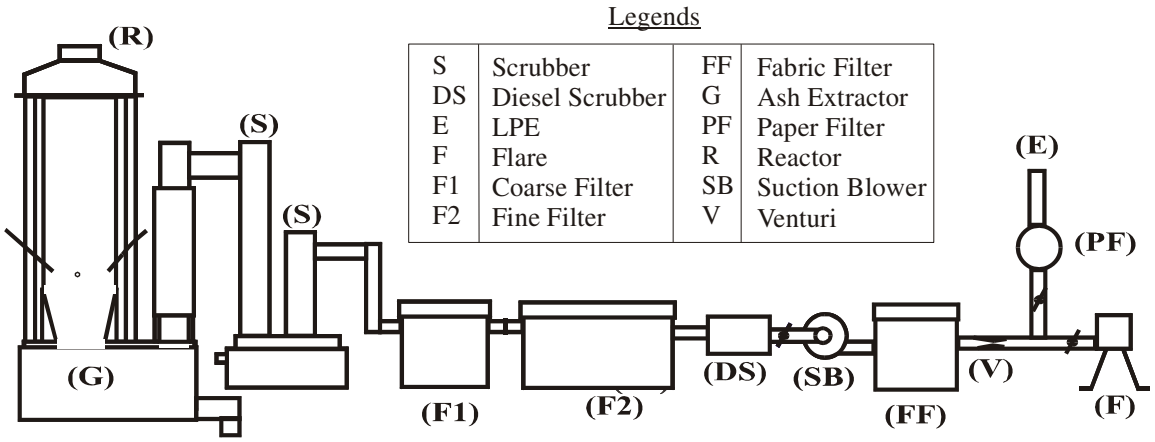

Fig. 3.3 Schematic of Open Top Re-burn Gasifier Connected to SPE

3.2.5.2 Morse Test

Morse test was conducted to assess the power loss due to friction and mechanical efficiency of the engine. In the Morse test, individual cylinders are cut out from firing, and the reduction in net brake power is determined while maintaining the rated engine speed and the air-to-fuel ratio. The difference between the brake power delivered with all cylinders firing and the brake power with one cylinder cut off provides an estimate of gross indicated power of the cut-off cylinder. Therefore cutting off individual cylinders in a sequence provides an estimation of the indicated power of complete engine. This procedure was adopted to estimate the gross indicated power and thereof the mechanical efficiency. These values are in turn compared with mechanical efficiency values obtained from the integration of p-θ data.

3.2.6 Results and Discussion

3.2.6.1 Performance

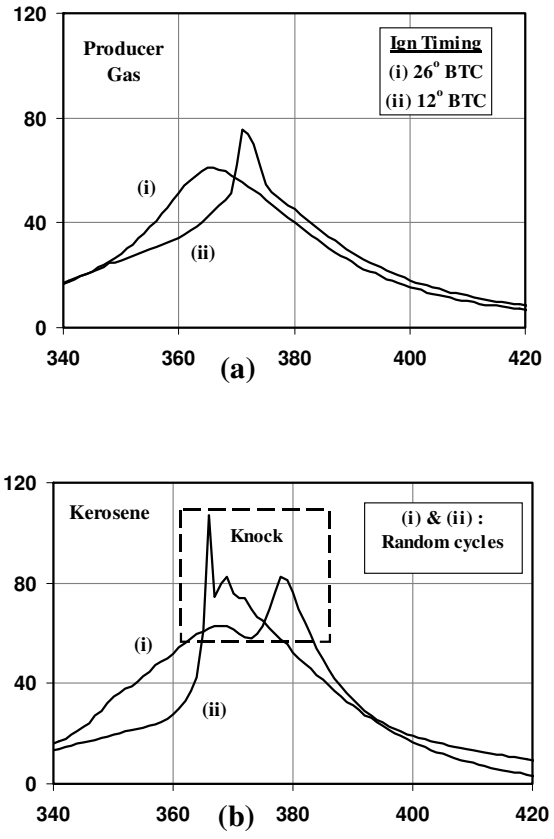

Fig. 3.4 (a) Normal Combustion under Wide Open Throttle Condition with Producer Gas at Different Ignition Timings at CR=17, (b) Incipient Knock with Kerosene at No-Load Condition with Ignition Timing of 30° BTC at CR=16.5.

The first and the foremost result of these tests is that the engine worked smoothly without any sign of knock at the CR of 17. There was no sign of audible knock during the entire load range. Moreover, the absence of knock is clear from the pressure-crank angle (p-θ), which does not show any pressure oscillations, either at part load or at full load (wide open throttle) conditions. A comparison of normal and abnormal (due to knock) combustion is shown in Fig. 3.4. The normal performance (without pressure oscillations) shown as (i) and (ii) in Fig. 3.4 (a) corresponds to two firing cycles at ignition advance of 26° and 12° BTC respectively. These correspond to operations with producer gas on LPE at CR=17 under wide open throttle conditions. Whereas, performance with incipient knock (with pressure oscillations) shown as (i) and (ii) in Fig. 3.4 (b) corresponds to two random firing cycles. These correspond to operations with kerosene fuel on a single cylinder SI engine (converted from a diesel engine) at CR=16.5 under no-load conditions. The piezo sensor employed for p-θ recording was the same in either case.

The results of the power output with producer gas are shown in Table 3.3. At CR=17, the engine delivered a maximum net brake output of 20 kW (17.5 kWe) at an efficiency of 30.7% compared to 24 kW (21 kWe) brake output at 33% efficiency with diesel (compression ignition mode). The efficiency calculation is based on the ratio of net brake output to the energy content of the air and gas mixture. The useful output and efficiency decreased with the lowering of CR. A maximum net brake output of 17.6 kW (15.3 kWe) at an efficiency of 27.5% was obtained at CR of 11.5. The power output at intermediate CR of 14.5and 13.5 were 18.8 and 18.6 kW respectively and with efficiencies around 29%. The efficiency at CR = 13.5 was comparable to that at 14.5 probably due to relatively leaner operation. The extent of de-rating in brake power was about 16.7% at CR = 17 and increased to as high as 26% at CR = 11.5 compared with baseline operations in diesel mode.

Table 3.3: Maximum Net Engine Output at Varying CR

CR	IGN, BTC	Φ	Net Elec. Power, kWe	Net Brake Power (BP_{Net}) , kW	Mixture Energy Density, MJ/kg	Efficiency : Gas-to-Shaft, %
17.0	06	1.10	17.5	20.0	2.20	30.7
14.5	10	1.10	16.4	18.8	2.20	29.0
13.5	14	1.06	16.2	18.6	2.10	29.3
11.5	15, 17	1.07	15.3	17.6	2.20	27.5

Φ =Equivalence Ratio: (Actual fuel- to- air ratio)/(Stoichiometric fuel- to- air ratio)

Table 3.4: Maximum Net Engine Output as a Function of Ignition Timing at Varying CR

IGN, BTC	Φ	BP_{net}, kW*	η : Gas–to-Shaft, %	IGN, BTC	Φ	BP_{net}, kW*	η : Gas–to-Shaft, %
CR=17.0				CR=14.5			
06	1.10	20.0	30.8	08	1.20	18.6	25.0
12	1.00	19.8	31.0	10	1.10	18.8	29.0
17	1.09	18.4	29.0	16	1.11	17.9	27.5
22	1.03	17.9	28.0	20	1.11	17.7	27.2
26	1.10	16.2	25.3				
33	1.25	14.0	19.0				
CR=13.5				CR=11.5			
08	1.05	18.2	28.6	06	1.07	17.0	27.0
14	1.06	18.6	29.0	15,17	1.07	17.6	27.5
18	1.07	17.0	27.8	27	1.09	15.6	25.5
25	1.06	17.0	28.0	38	1.07	13.3	20.0

* Excluding Radiator Fan Power

The net brake output with producer gas at varying ignition timing for the four different CRs tested is shown in Table 3.4. It is evident from the above data that ignition timing had to be retarded with the increase in CR in order to obtain higher output. This is because the thermodynamic conditions in terms of pressures and temperature are more severe at higher CR and thereof the combustion is faster thus calling for the optimum ignition timing to be located close to TC. The maximum output was recorded at an ignition advance of 6° BTC at CR=17 and increased to about 15 - 17° BTC at a CR=11.5. At intermediate CR of 14.5 and 13.5 the ignition advance was 10 and 14° BTC respectively. The fuel-air equivalence ratio was about 1.06 $\pm$ 0.5 in most of the cases, with efficiency of 30.7 and 27.5% corresponding to maximum output at higher and lower CRs respectively. An isolated case of efficiency at 31% was seen corresponding to ignition setting of 12° CA, probably due to relatively leaner operation. In the above data presented, the air-to-fuel ratio was tuned from the viewpoint of deriving maximum output and therefore the efficiency figures are necessarily not the maximum that can be obtained. The incremental gain in maximum power and efficiency per unit CR is shown in Table-3.5. The gain in power was between 2.2 and 2.6 per unit CR, but the gain in efficiency was marginally lower. However, these figures are well within the range of 1 to 3% gain per unit increment of CR reported by Heywood [1988].

Table 3.5: Incremental Gain in Power and Efficiencies

Range in CR	Gain in power/CR, %	Gain in efficiency/CR, %
14.5 to 17.0	2.60	2.3
13.5 to 17.0	2.20	1.4
11.5 to 17.0	2.50	2.1

Next, the variation of mechanical efficiency (ratio of net brake power to gross indicated power), η_{mech} with CR is shown in Table 3.6. These values are deduced from indicated power measurements (based on integration of pressure-volume diagram) and net output measured, also values obtained from standard multi-cylinder Morse test are shown in Table.3.6. The η_{mech} of the engine at CR of 17 is about 80% and increased to as high as 87% at CR of 11.5. The increase in η_{mech} is attributed to the reduction in rubbing friction [Gish et al, 1958] due to lower cylinder pressures encountered at lower CRs. A break-up of the components leading to total losses is further discussed in Table 7.3 of Chapter VII.

Table 3.6: η_{mech} Measurements

CR	η_{mech} from $\int pdV$	η_{mech} from – Morse test
17.0	80-82	81 $\pm$ 1
14.5	84-86	84 $\pm$2
13.5	85-88	86 $\pm$2
11.5	88-90	88 $\pm$1

3.2.6.2 Pressure – Crank Angle Data

The pressure-crank angle (p-θ) recording is shown in Fig 3.5 to 3.8 at different CRs, none of these show any trace of knock for all ranges of load inclusive of peak. These figures contain ensemble average data over thirty consecutive cycles.

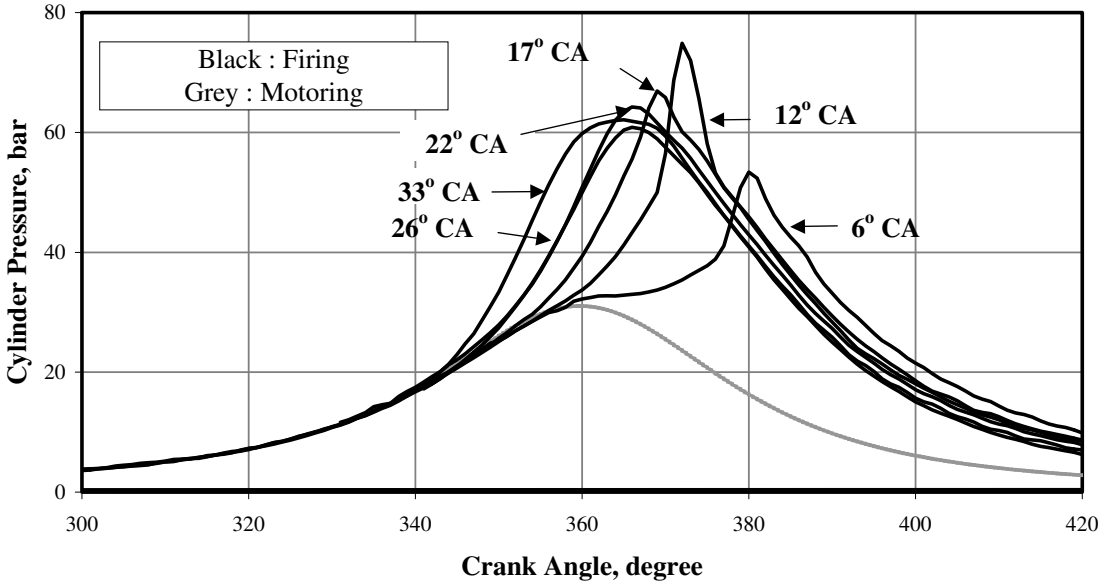

Fig. 3.5 p-θ Recording Corresponding to Maximum Brake Output at Varying Ignition Advance at CR=17. Ensemble-Averaged Data Over 30 Consecutive Cycles.

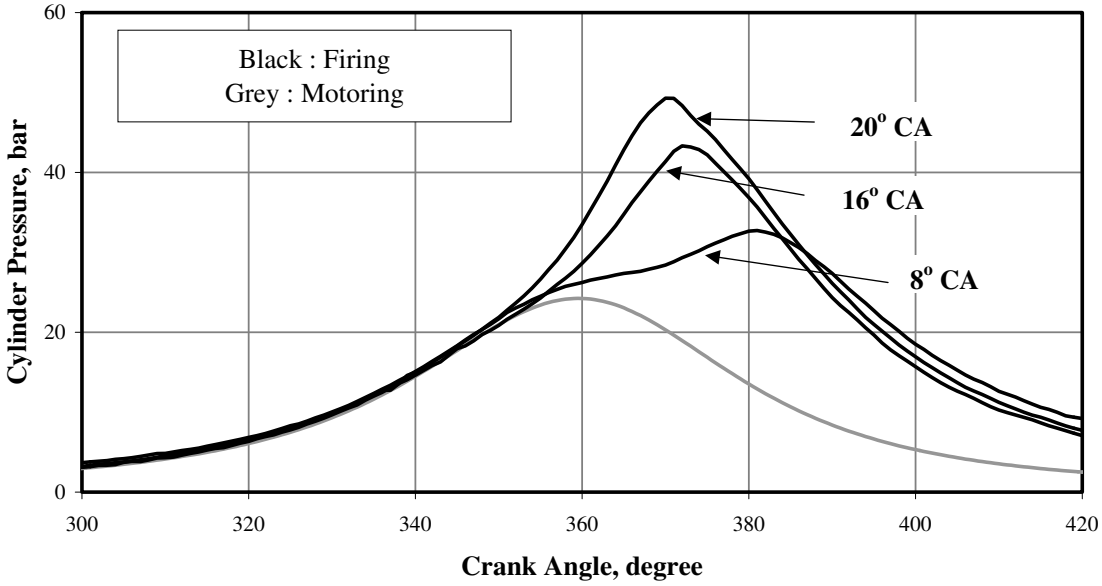

Fig. 3.6 p-θ Recording Corresponding to Maximum Brake Output at Varying Ignition Advance at CR=14.5. Ensemble-Averaged Data Over 30 Consecutive Cycles.

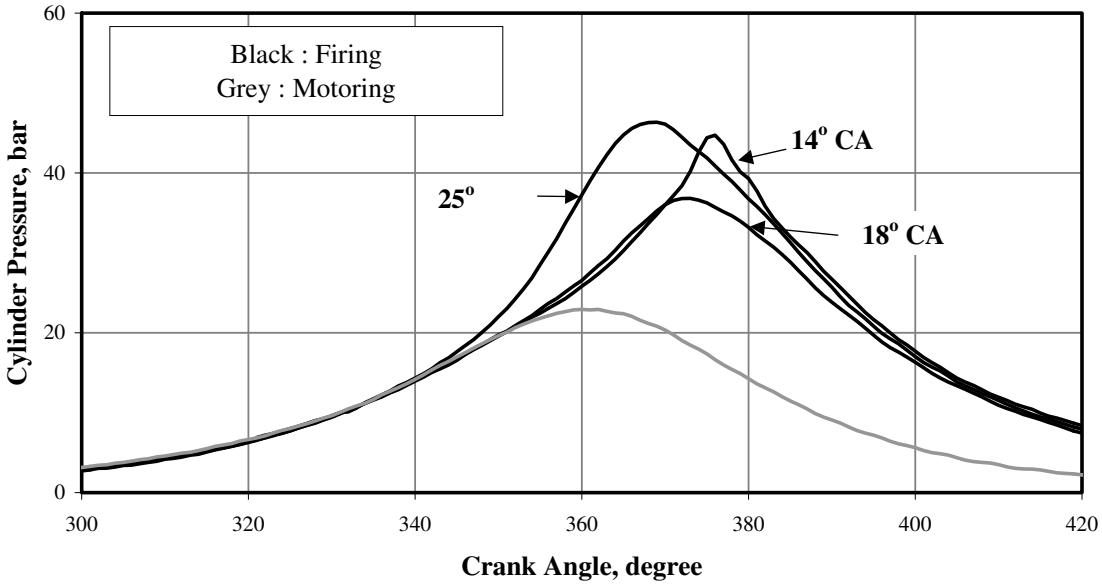

Fig. 3.7 p-θ Recording Corresponding to Maximum Brake Output at Varying Ignition Advance at CR=13.5. Ensemble-Averaged Data Over 30 Consecutive Cycles.

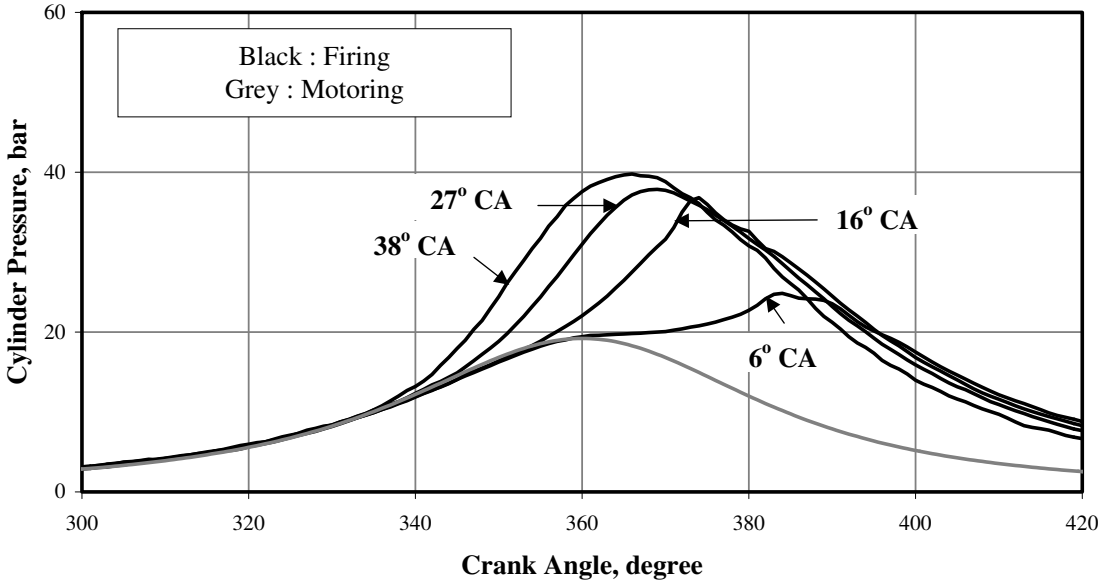

Fig. 3.8 p-θ Recording Corresponding to Maximum Brake Output at Varying Ignition Advance at CR=11.5. Ensemble-Averaged Data Over 30 Consecutive Cycles.

It is clear from these curves that smooth and normal combustion seemed to occur even at advanced ignition timing of 33° CA corresponding to CR of 17. Faster burn rate due to presence of hydrogen in the fuel gas could be the principal factor for the no-knock performance. The effect of the ignition advance on the pressure history is evident

from the above curves. There are substantial differences in the maximum cylinder pressure and their point of occurrence. The ratio of maximum cylinder pressure between the highest and the lowest CR at corresponding ignition timing is about 2.

The net work delivered over a complete cycle can be found by integrating the pressure-volume (p-v) data over the four processes. This also helped in identifying the optimum ignition timing for a given CR - commonly referred as MBT. The net indicated mean effective pressure (IMEP) obtained from the integrated p-v data is a measure of effectiveness with which an engine of a given volumetric displacement converts the input energy into useful work. The IMEP obtained from ensemble average p-v data (~ 30 cycles) at varying CR as a function of ignition timing is shown in Figure 3.9. At CR=17, the maximum IMEP recorded is 5.98 bar corresponding to a ignition timing of 6° CA and this declined to 4.85 bar with ignition timing being 15° CA at CR of 11.5. These values are obtained at $\Phi = 1.08 \pm 0.2$ and fall within the anticipated value of $\Phi = 1.0$ to 1.1 [Heywood, 1988]. It is also evident from the plot that variations in the IMEP values are modest between ignition timings of 6 and 12° CA corresponding to CR=17.

Exploring further the p-θ data, the peak pressure and the point of occurrence at ignition timings close to MBT are listed in Table 3.7. These measurements are accurate within – 1.0° CA (due to possible lag in the signal and error in TC identification). It is evident from the data that peak pressure seemed to occur between 17 and 19° ATC (After Top Centre) at all CRs. In the case of CR=13.5, the peak pressure seemed to occur at the optimum value (17° ATC) identified in the literature [Heywood, 1988; Wu et al, 1993]. In the case of CR=11.5, the peak pressure occurred at 17 and 12° ATC for an ignition timing of 15 and 17° BTC respectively. The difference in the IMEP between the two ignition timings was found to be 3%. However, for CR of 17 and 14.5 the ignition timing identified in the Table 3.7 seemed to be marginally deviating from the optimum value. The variation of IMEP within this close range would be marginal as it is well acknowledged that the relative torque delivered has a flatter characteristic around MBT [Heywood, 1988].

Table 3.7: Cylinder Peak Pressures and Their Occurrence

CR	Ign. advance ° CA	Peak pressure, bar	Occurrence ° ATC
17.0	6	55.00	20
14.5	10	43.30	19
13.5	14	45.00	17
11.5	15, 17	33.00, 38.00	17, 12

The coefficient of variation of the IMEP at all CRs and ignition settings occurred well within 3-3.5%, as shown in Fig. 3.10 implying low cycle-to-cycle variation. The reason for low cyclic variation is the faster rate of combustion occurring inside the engine cylinder. The faster rate of combustion is attributed to higher flame speeds due to the presence of hydrogen in the gas and also to the combustion chamber design.

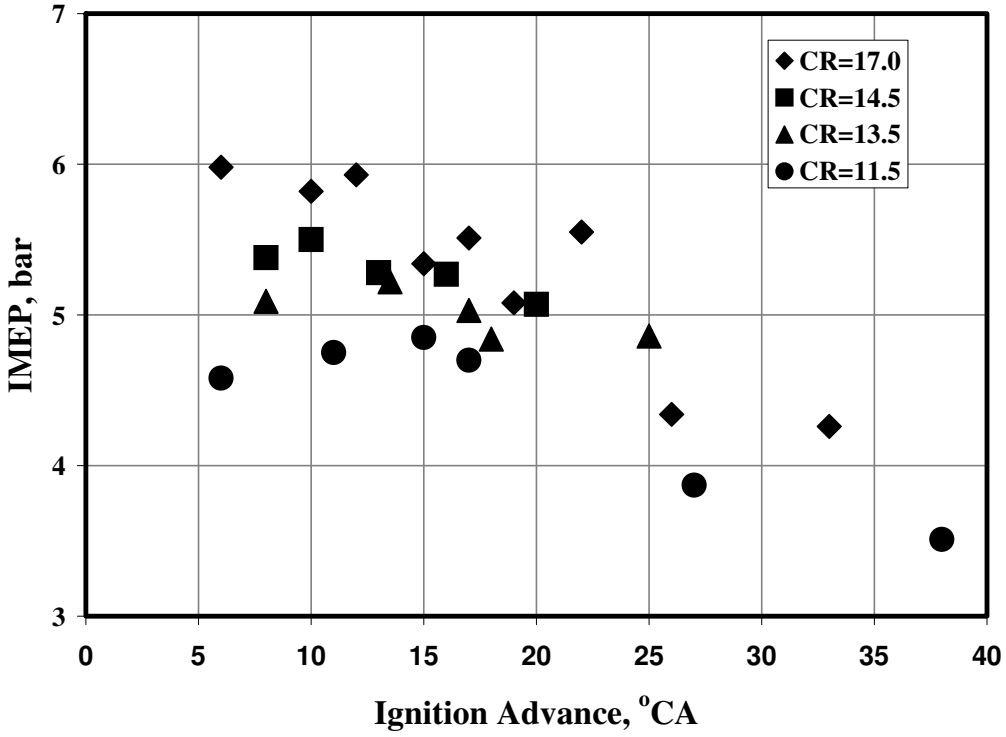

Fig. 3.9 Variation of IMEP (Net) with Ignition Advance at Various CRs

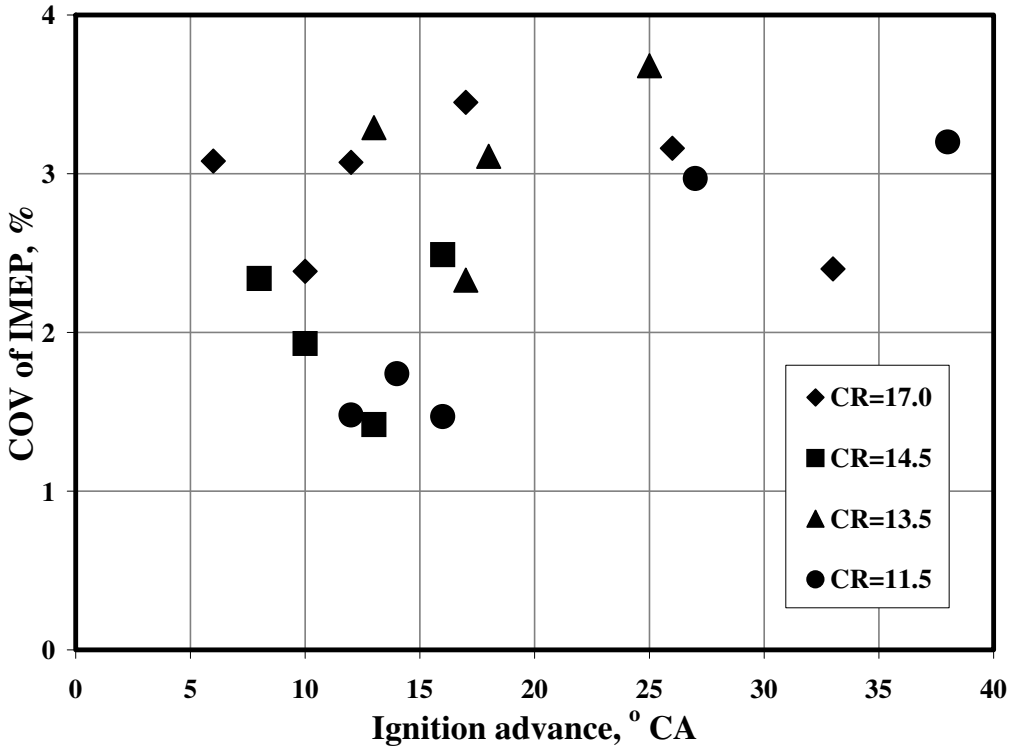

Fig. 3.10 COV of IMEP (Net) with Ignition Advance at Various CRs

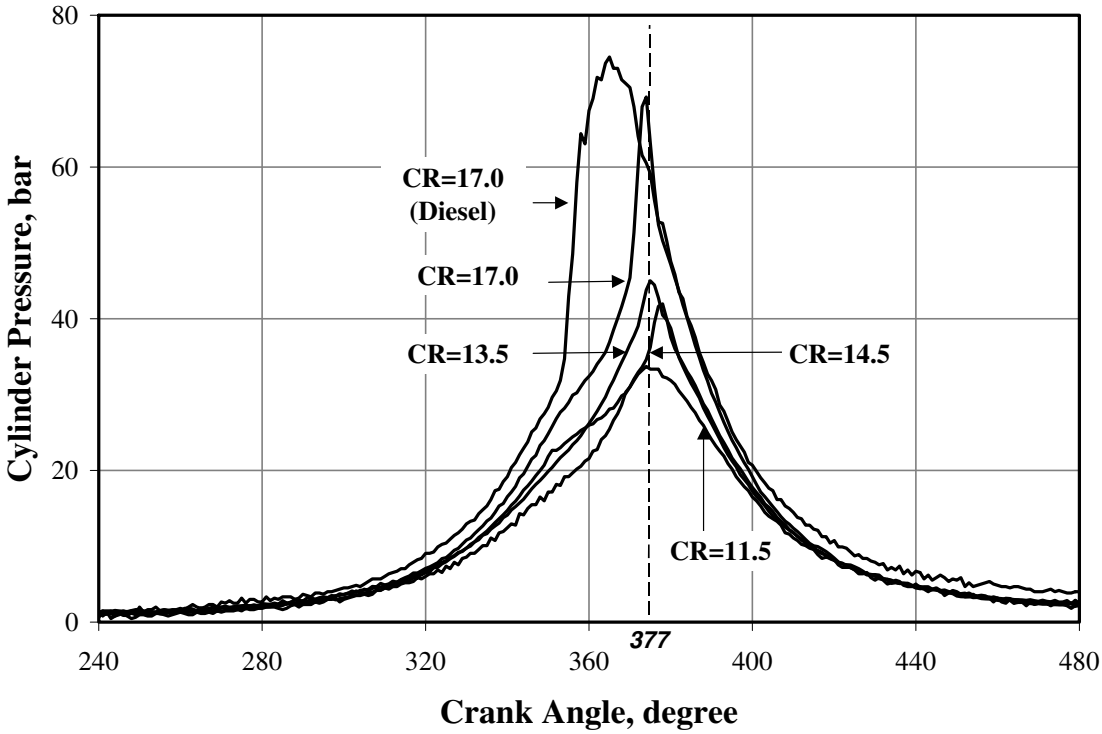

Fig. 3.11 Comparison of p-θ Curves at Different CR; Ignition Timing is at MBT or Close to MBT (Within MBT + 2° CA). The p—θ curves correspond to ignition setting of 10°, 10°, 14° and 15° BTC for CR of 17, 14.5, 13.5 and 11.5 respectively. Operation in Diesel Mode at 90% of rated Load (at Optimum Injection Timing - 34° BTC). All are Ensemble-Averaged Data Over 30 Consecutive Cycles.

Fig. 3.11 shows the comparison of p-θ curves for different CR around MBT in gas mode of operation. In case of the ignition timing close to MBT, the peak pressure is observed to occur around 16 -17° ATC. The ratio of maximum cylinder pressure between the highest and the lowest CR is about 2. The p-θ curve in diesel mode at MBT shows a maximum pressure of 85 bar to occur at 10°ATC. The point of occurrence of peak pressure is consistent with the data (5 -10° ATC) available in literature [Heywood, 1988]. The observed difference in the p-θ curves between diesel and gas mode is attributed to the nature of combustion. In case of diesel mode, combustion occurs in a diffusion mode, wherein fine droplet combustion occurs in an atmosphere of vitiated air. The pressure rises rapidly to a peak at 10° ATC since the initial rate of burning is fast. Whereas in gas operation (which is essentially in spark ignition mode of operation), combustion occurs in a pre-mixed mode, wherein there is a definite flame front traveling across the pre-mixed fuel - air mixture. Therefore the pressure rise in this case is not as rapid as seen with compression ignition mode of operation. It is also evident from these curves the magnitude of pressure rise is lower in case of gas operation.

Summarizing, the MBT for producer gas fuel is identified to be in the following crank angle intervals. 6-10° BTC for CR=17.0, 10-12° BTC for CR=14.5, 12-14° BTC for CR=13.5 and 15 –17° BTC for CR=11.5. This range is identified keeping in view the modest variation in the net power output.

3.2.6.3 Energy Balance

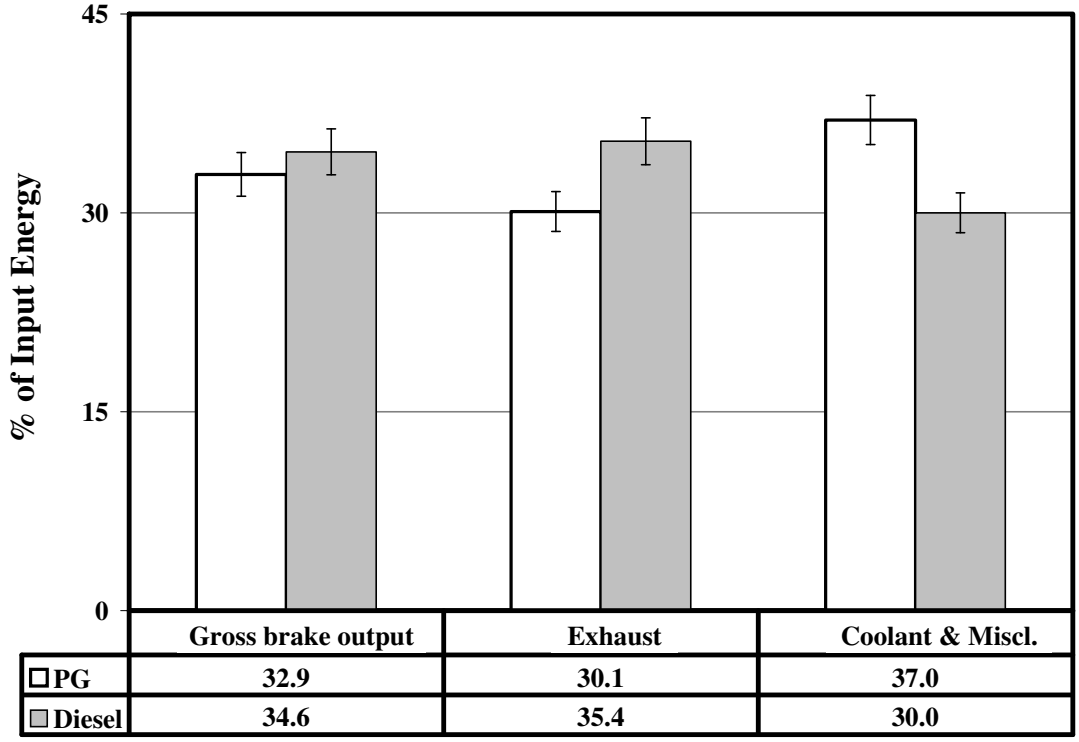

	Gross brake output	Exhaust	Coolant & Miscl.
PG	32.9	30.1	37.0
Diesel	34.6	35.4	30.0

Fig. 3.12 Energy Balance Comparison in Diesel and Producer Gas Mode at Maximum Brake Output. The Marker Refers to the Error Band.

Figure 3.12 represents the overall energy balance at CR =17. The energy balance is based on gross brake power output. The gross brake output is sum of net shaft output and power consumed by engine accessories (water pump/fan, dynamo and FIP = 1.4 kW). The energy balance in gas mode corresponding to maximum brake output (at 6° CA) showed a useful output (Gross brake power) of 32.9%, about 30% is lost through exhaust (sensible and chemical enthalpy - CO) and remaining 37% to the cooling water (inclusive of frictional and radiative losses). Figure 3.12 also compares the energy balance in gas and diesel mode (at rated output of 24kW) at CR of 17, the energy loss to the coolant and miscellaneous is about 37% compared to 30% in diesel and whereas, energy loss through exhaust is lower by about 5% in gas mode. Overall the brake thermal efficiency is lower by about 1.5% in gas.

The energy balance as a function of CR is shown in Figure 3.13. There is an increase in energy loss through exhaust with the reduction in the CR, where as the loss through the coolant is higher at higher CR. The increased amount of heat loss to the cooling water in gas operations is attributed to engine combustion chamber design. Heywood [1988] indicates that engine geometries such as bowl-in-piston would experience 10% higher heat transfer. The heat transfer to the coolant in the current case falls well within this range (7-10%). The influence of engine geometry on heat loss could

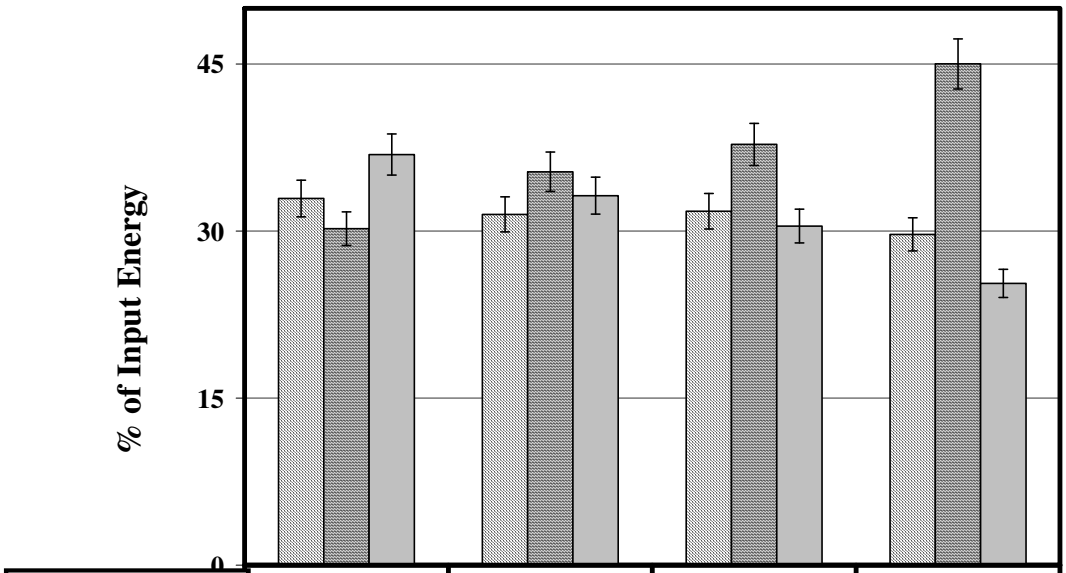

CR	17	14.5	13.5	11.5
Brake output	32.9	31.5	31.8	29.7
Exhaust	30.2	35.3	37.8	45.0
Coolant & Miscl.	36.9	33.2	30.4	25.3

Fig. 3.13 Comparison of Energy Balance at Various CRs with Producer Gas Corresponding to Maximum Brake Output. The Marker Refers to the Error Band.

be more in gas mode compared to diesel because of basic difference in the nature of combustion. In the case of compression ignition engine, combustion is heterogeneous and essentially occurs at multiple ignition sites in a diffusion mode. Therefore, there is no definite flame front propagation and combustion does not occur close to the wall unlike that in a spark-ignition engine. This is one of the prime reasons for increased heat loss to the coolant in spark-ignition engine, which is so in the current study in gas mode.

With the increase in CR, it can be seen that there is marginal improvement in the conversion efficiencies. However, in reality the gain in efficiency is much larger at higher CR and consistent with the thermodynamics. The gross indicated efficiency (including pumping losses) at CR=17 (39%) is higher by about 18% compared to that at CR=11.5 (33%). However, the gain is reduced due to lower mechanical efficiency at higher CR as shown in Table - 3.6. Similarly, energy loss to the coolant is higher at higher CR due to higher cylinder temperature (as a consequence of higher cylinder pressure) and increased frictional losses (refer Table 7.2 and discussion therein) and energy loss through exhaust decreases with the increase in CR due to increased thermal efficiency.

3.2.6.4 Emissions

The emissions measured are Nitric oxide (NO) and Carbon Monoxide (CO). The variation of NO in gas mode at varying CR with ignition advance is shown in Fig. 3.14. NO_2 was not accounted as it forms small part (~5%) of NOx generated [Heywood, 1988]. The NO level has been represented as an emission index in units of gram per unit MJ of input energy. These results are compared with the CPCB norms (equivalent to EURO I norm) meant for diesel engine powered vehicle, as there are no existing CPCB norms for stationary engines. Similarly, there are no norms existing for small power level (< 2.0 MW) stationary engines, therefore, existing diesel vehicular norms of CPCB are stated for comparison. Also the data is compared with the Swiss emission norm, as it is generally understood that their norms are stringent. The NO level reduced with the retardation of ignition timing and this feature is observed for all CRs. The NO level is observed to be maximum at the highest CR with advanced ignition timings, whereas in the MBT range of 6 to 20° BTC the NO is lower and comparable in almost all the cases. It is well known that NO generation is strongly dependent on the temperature, oxygen availability and residence time in the combustion chamber. With the flame speed of the gas mixture being high, the ignition setting is retarded whereby the residence time in the high temperature combustion chamber is automatically reduced. Therefore the low NO levels at retarded ignition setting are an expected and consistent behavior. The above results match well with those quoted by Heywood [1988], which show small to modest variation of NO with CR. The NO emissions are lower than the CPCB and Swiss norm for all cases around MBT.

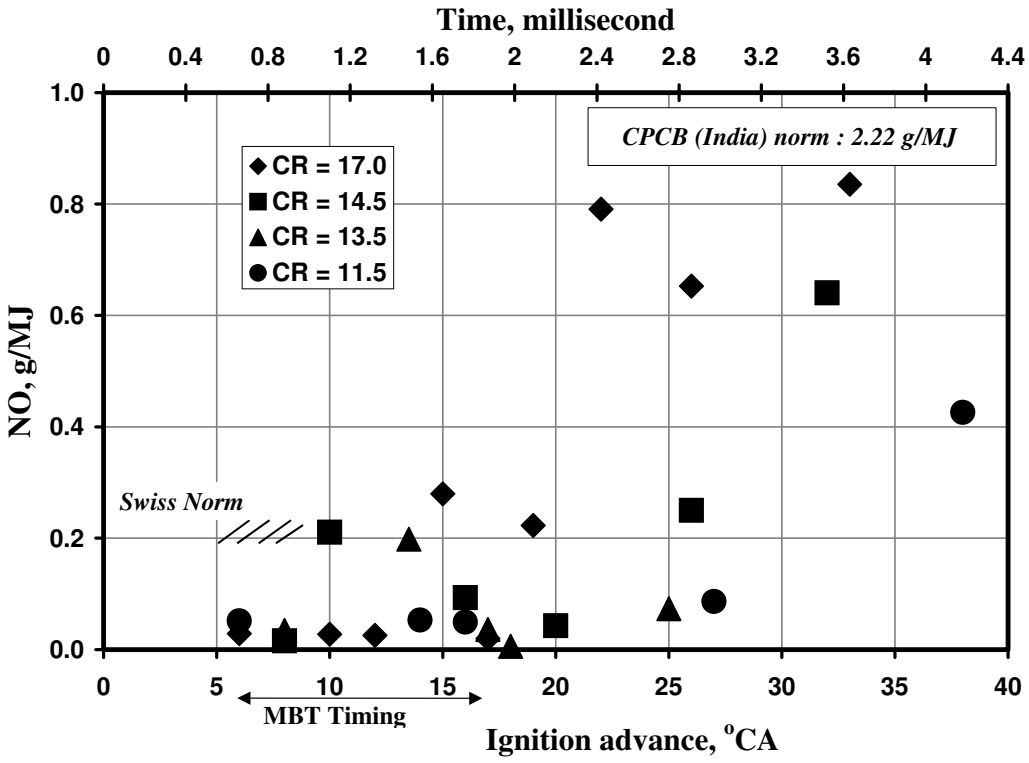

Fig. 3.14 Variation of NO with Ignition Advance at Various CRs

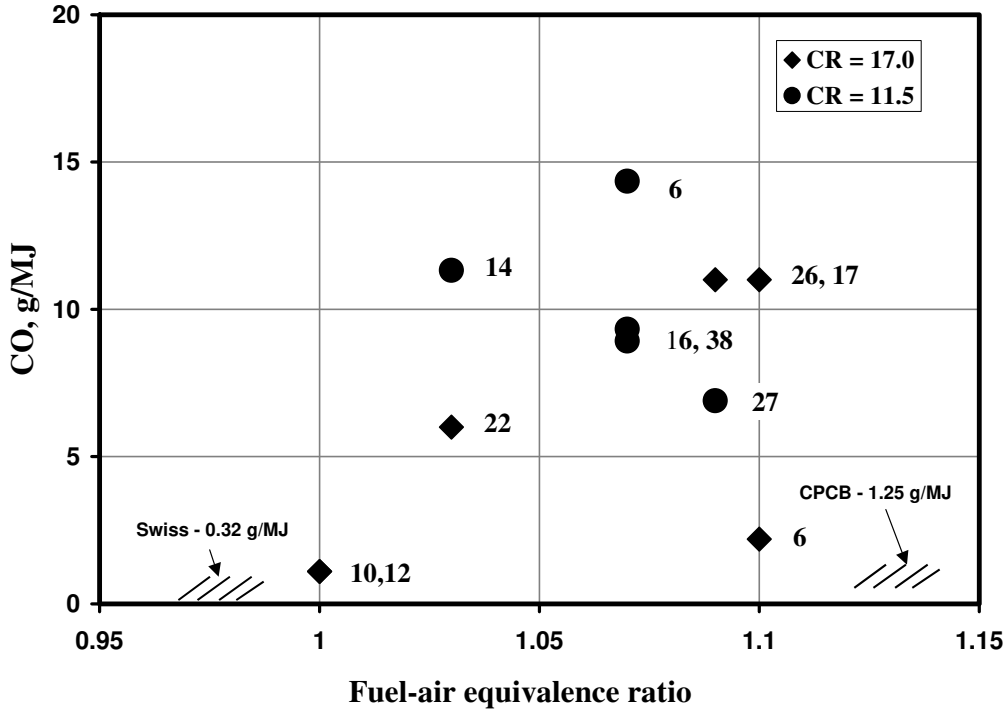

Fig. 3.15 Variation of CO with Fuel-Air Equivalence Ratio. The Number Next to the Legend Indicates the Ignition Advance in ° CA, BTC.

The variation of CO with equivalence ratio (Φ) is shown in Figure 3.15. The CO levels are represented in grams per MJ of input energy. The trend of CO with Φ is clear from the figure. The CO levels were lower at the highest CR as well as fuel lean conditions, and this could be attributed to higher temperatures, leading to relatively complete combustion. Overall, the levels are found to be much higher than the CPCB and Swiss norm. It appears that the engine can meet CPCB and other emissions norms (Table 3.11) if the engine is operated at fuel lean conditions without the need for a catalytic convetor.

3.2.7 Concluding Remarks

Performance of the engine at higher CR is smooth and it has been established that operating engines using producer gas in SI mode at CR up to 17 is feasible. This is obvious from the p-θ curve, which shows smooth rise in pressure without any pressure oscillations. A shorter duration of combustion has been observed with producer gas fuel, requiring retardation of the ignition timing to achieve MBT. These faster burning cycles are corroborated by low cyclic pressure fluctuations with coefficient of variation ~ 3%. The faster burning process has been identified to be due to higher flame speed of the fuel - air mixture and this is attributed to the hydrogen content in the gas. The MBT arrived from this study is much retarded than claimed by the earlier researchers. The MBT in the current case are in the range between 6 and 17° CA for CR range between 17 and 11.5 against 30 - 45° CA (for a CR of 11.5 and below) claimed by the earlier researchers. This change in ignition advance in the present study can only be attributed to the improved producer gas composition. The hydrogen content in the present case is about 18-20% against 11-12% claimed by Parke et al [1981] and 10% (theoretical) by

Martin et al [1981]. However, it is difficult to comment on the retarded MBT of 35° CA claimed by Shashikanta et al [1999] with hydrogen content of 24%.

The maximum de-rating in power is observed to be 16.7% in gas mode compared to diesel operations at comparable CR. The extent of de-rating is much lower when compared to any of the previous studies [Parke et al 1981, Ramachandra, 1993, Martin et al, 1981]. This value matches with a similar kind of de-rating reported with natural gas operation by Das et al [1997]. However, the brake thermal efficiency drops down by 5% compared to normal diesel mode of operation. This is related to excessive heat loss to the coolant at all CRs, resulting in engine overheating within 30-40 min of operations at full load. The emission in terms of NO is found to be much lower than the stipulated norms of CPCB and Swiss. However, the CO levels are found to higher. These observations are consistent with the results of Giordano [1999] on a producer gas engine powered with a IISc gasifier. Lastly, the information that is relevant to biomass gasifier coupled to a gas engine is the specific fuel (biomass) consumption. The specific biomass works out to about 1.15 –1.25 per kWh electric energy generated that corresponds to an overall efficiency (biomass to electricity) of 21 and 19% at 17 and 11.5 CR respectively.

3.3 Medium Power level Experiments

3.3.1 Description of the Engine

The understanding gained from the experimental work on the SPE engine is translated on to the medium power level engine (MPE) and its performance accessed on producer gas. The gas engine chosen for experiments is a 12 cylinder (V-configuration), turbo-charged – after cooler engine, supplied originally to operate on dilute natural gas (biogas fuel). These brand engines are marketed as bio-gas engines and are serving as base load power plants in many parts of India. This engine is adopted to operate on producer gas along with a specially designed gas carburetor. The detailed specification of the engine is given in Table 3.8. This engine is basically built from a diesel engine frame (model no. TBD4V12, rated at 444 kW at CR of 15) at a modified CR of 12, to operate on gaseous fuels in a spark-ignited mode. The other modifications implemented on the engine are with respect to turbo-charger (model K-28 in place of K-36) and combustion chamber (simple cylindrical bowl in place of torroidal shape). The K-36 and K-28 turbo-charger are designed to generate a pressure ratio of 2.2 and 1.5 - 1.6 respectively. Therefore, the estimated power rating of the modified engine in diesel is between 290 - 310 kW (with the modified turbo-charger and lower CR ~ 2% reduction in power per unit CR assumed from Heywood [1988]). The modified engine (to operate as a SI engine) was initially equipped with double sparking ignition system, where in a redundant spark occurred during the exhaust process. Itso happened that whenever the engine was operated with an ignition timing coinciding with the valve overlap period, a backfire occurred into the engine intake. This therefore limited the available range of ignition timing for testing purposes. The problem was subsequently resolved by replacing with a single sparking ignition system, which permitted engine operation over a wider range of ignition timing.

Table 3.8 Medium Power level Engine Configuration Details

Parameter	Specification
Make and Model	Greaves, Coupled to a 300 kVA Alternator
Engine Type	12 Cylinder, 'V' Configuration Gas Engine, Turbo-Charged with After Cooler
Rated Output - Diesel	290 – 310 kW (Estimated) @ 1500 Rev/Min
Rated Output – Diluted Natural Gas (Bio-Gas)	250 - 270 kW @ 1500 Rev/Min (Achieved)
Type of Cooling	Water Cooled with Radiator
Bore x Stroke	128 x 140 mm
Swept Volume	1.8 Litre
Compression Ratio	12:1
Bumping Clearance	1.6 mm
Combustion Chamber	Flat Cylinder Head and Bowl-in Piston
Squish Area	68%
Ignition System	Gill Instruments – Single Sparking Unit with Individual Coil for Each Cylinder
Governor	GAC Make
Spark Plug Type & Location	Cold, Offset – Located in the Vertical Plane Close to the Outer Edge of the Bowl
Intake Port	Directed Type
Valve Timing	Inlet Valve Opening – 12° BTC Inlet Valve Closing – 55° ABC Exhaust Valve Opening – 44° BBC Exhaust Valve Closing – 15° ATC
Firing Order	A1, B5, A5, B3, A3, B6, A6, B2, A2, B4, A4, B1
SFC, m^3/kWh – Bio-Gas	0.3
Alternator Efficiency	92%

BTC: Before Top Center, ABC: After Bottom Centre, BBC: Before Bottom Centre, ATC: After Top Centre

The combustion chamber is formed of a flat cylinder head and a bowl-in piston. The bowl is cylindrical in shape and has a squish area of 68% (percentage of piston area closely approaching the cylinder head at the smallest spacing). The spark plug is located at an offset in the vertical plane close to the outer edge of the bowl. The single spark type electronic ignition unit comprised of a controller, Hall effect sensor, and individual ignition coils, wiring harness and spark plugs. The ignition timing was precisely controlled by interfacing with a computer to within one-degree crank angle. The engine coupled with a standard alternator was connected to a load bank (resistor coils) to facilitate load tests. The mixture (air + gas) intake system comprised of an air filter, turbo-compressor, after cooler, mixture controller – gas governor, manifold and runner to each cylinder head.

A 250-kg/hr-biomass gasifier formed the gas generator with the system elements in terms of gas cleaning system different compared to the 75- kg/hr system. The details of the 250-kg/hr gasifier system has been dealt in Chapter II. Plate 3.4 shows the view of the gasifier.

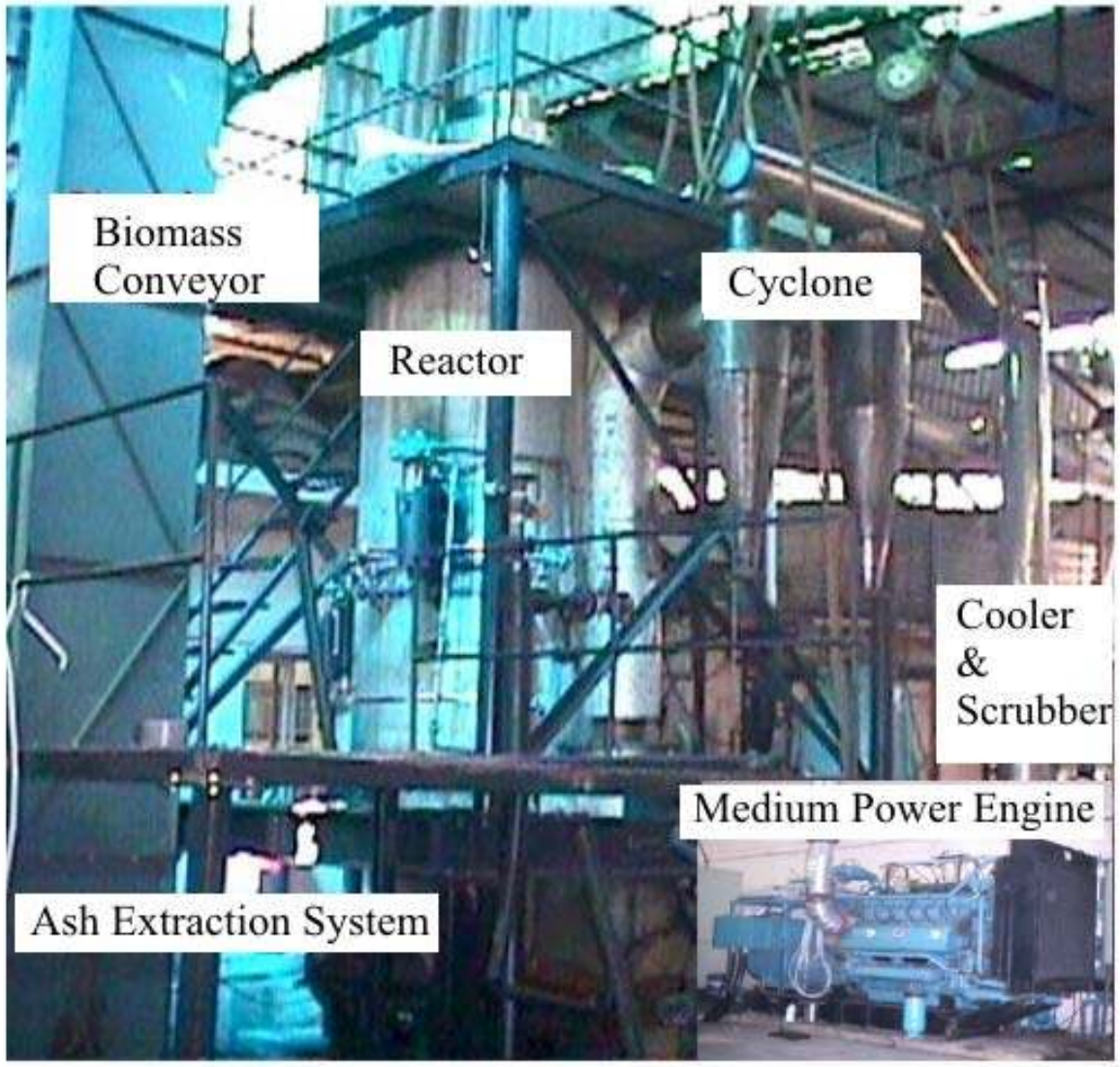

Plate 3.4: A View of a 250 kg/hr Open-Top, Re-Burn Down Draft Gasifier to Supply Gas to MPE. Major Sub-Systems of the Plant Identified. The Inset on the Right Shows the Gas Engine

Since the engine is of reasonably higher power level, the air-to-fuel control due to load variation assumed a major proposition. This called for design and development of a gas carburetor for producer gas application, as carburetors are not available for producer gas fuel. The carburetors available for other gaseous fuel, namely the natural gas, biogas and landfill gas are unsuitable due to widely different stoichiometric air-to-fuel requirement. The stoichiometric air-to-fuel ratio varies between 10 to 6 (on volume basis) for fuels such as natural gas and bio-gas/land fill gas based on methane content in the gas. However, stoichiometric air-to-fuel ratio for producer gas is about 1.2 to 1.4 (on volume basis) based on the constituents of the gas.

3.3.2 Producer Gas Carburetor

The essential features in the gas carburetor are

- Ability to maintain the required air-to-fuel ratio (1.2 to 1.5:1) with load or throttle variation
- Smooth operation with minimal pressure loss
- Shut off the fuel in case of engine tripping or shut-down
- On-line provision for air/fuel tuning during testing

The above-mentioned feature was incorporated in the development of a gas carburetor and is shown in Fig. 3.16. The carburetor is simple in design and does not have moving components. It has a separate port for air and fuel, where the individual ports could be modified or tuned to achieve the required air-to-fuel ratio. The carburetor is designed to operate in conjunction with the zero-pressure regulator. The combination of pressure regulator and gas carburetor was located between the gasifier and the engine intake system as shown in Fig. 3.16. The zero pressure regulator ensures a gas pressure (downstream of the pressure regulator) identical to that of air pressure and this is achieved by connecting the air pressure line (down stream of air filter) to the upper chamber of the regulator. This arrangement ensures the regulator to maintain the gas pressure close to that of air pressure (~ a few mm below atmospheric pressure) and thereby the set air/fuel ratio irrespective of the total mixture flow rate.

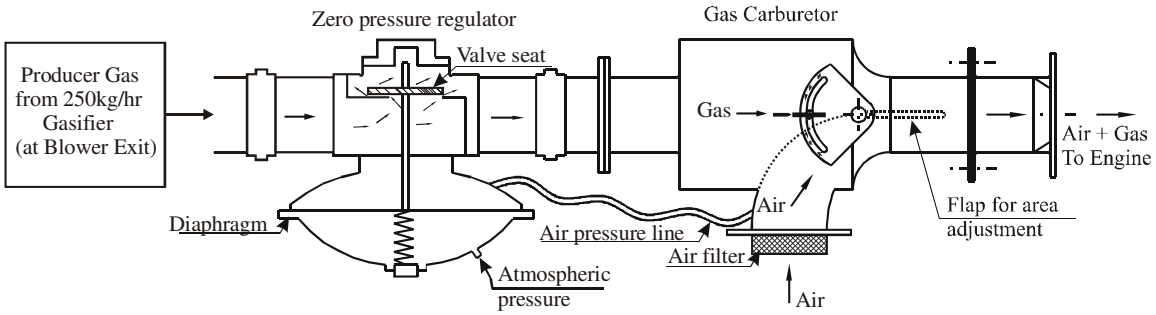

Fig 3.16 Schematic of Producer Gas Carburetor with Zero Pressure Regulator in the Gas-Air Line Circuit

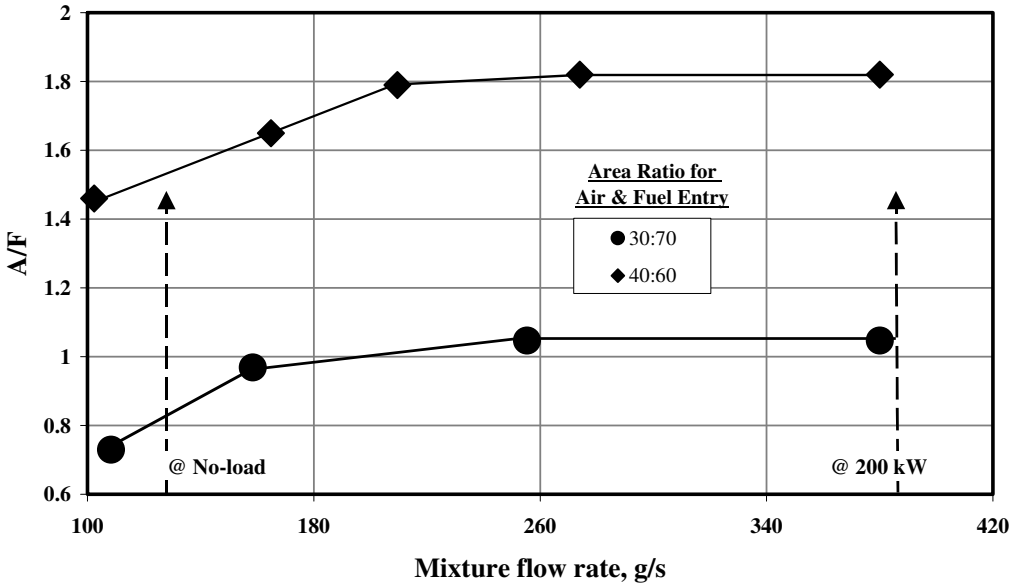

Fig. 3.17 Flow Tests with Gas Carburetor at Varying Area Ratio for Air and Fuel Entry

Flow tests performed with zero-pressure regulator and the gas carburetor showed reasonable functioning in terms of air-to-fuel ratio control against total or mixture flow rate variations as shown in Fig. 3.17. Flow test was conducted using a blower to simulate the engine suction. The air and fuel flow rates were individually measured over a range of engine's operating conditions. The two cases shown in the above figure correspond to area ratios for the air and fuel entry. These cases are possibly the extreme limits and the required operation point for the engine operation could lie in between them. The A/F ratio was reasonably constant beyond a specified mixture flow rate, with relatively rich mixture at low mixture flow rates. This characteristic is desirable from the viewpoint of engine operation – rich mixture for engine start-up and no-load operations, relatively leaner mixture during part load operation. However, for peak load operation – stoichiometry or rich mixture is desired calling for the adjustment of the carburetor flap. Considering gas engine operation at the field level, the carburetor is designed in such a manner that in the event of load throw-off the flap of the carburetor could move to full air flow (by motorizing) condition thus ensuring safety of the engine.

3.3.3 Experimental Procedure

The scheme of operation up to the exit of gas from the gasifier system was on lines similar to that mentioned for SPE. However, instead of engine drawing the gas, the gas was drawn using a blower and made available for the engine operation. The gas was made available at a higher pressure, typically 3000 to 5000 Pa, above the atmospheric pressure. The gas pressure had to be reduced for proper functioning of the gas carburetor, and this was achieved using a pressure regulator placed with the blower outlet and the entry to the carburetor. Relevant parameters as dealt in the SPE tests were measured and in addition, the turbocharger pressure was also recorded.

Experimental procedure as identified in Section I was adopted for preparation and subsequent evaluation of the engine. The engine was started directly using producer gas and allowed to stabilize for about 5 minutes; subsequently the load was applied and gradually increased. Data relating to energy input – in terms of gas flow rate and gas composition, power delivered and emission were recorded. Similarly for combustion diagnostics, pressure-crank angle data was obtained in and around MBT.

3.3.4 Results and Observations

A trace of the gas composition and the calorific value is shown in Fig. 3.18. The gas composition in these experiments was found to be lower than obtained in the earlier instances. The LCV in these experiments is about 4.8 - 5.0 MJ/Nm^3 at the time maximum output from the engine. The reason this fact is brought out explicitly because the reduction in the mixture density has an implication on the maximum shaft output delivered and this is discussed subsequently.

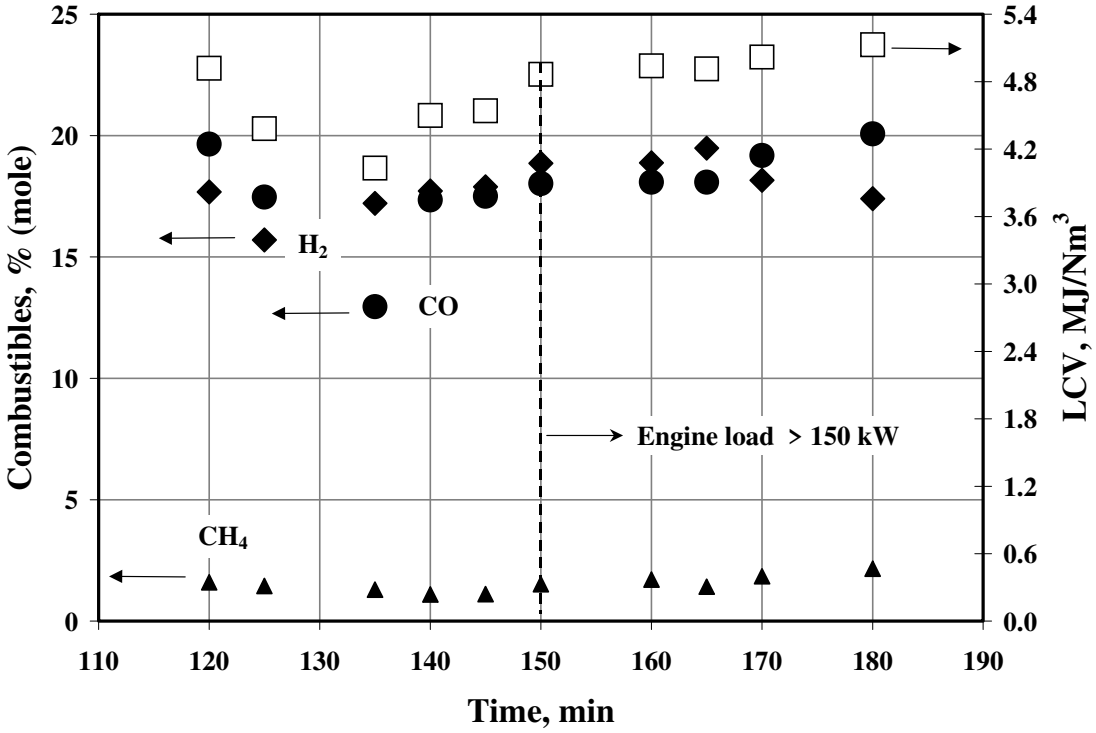

Fig 3.18 An on-Line Trace of Producer Gas Composition and LCV

The performance results presented below pertain to CR of 12 and at various ignition settings. A maximum gross brake output of 194 kW (including 12 kW consumed by the radiator fan) was recorded with an ignition advance between 12 and 14° CA at $\Phi = 0.94$. The value of Φ was lower in the current case because of limitation coming from the gasification system. In fact, the gas composition in terms of combustibles deteriorated with increased supply of the gas to the engine. This therefore limited the input energy to the engine. The maximum net brake output of the engine at various ignition timings is shown in Table 3.9.

Table 3.9: Maximum Net Brake Power at Varying Ignition Timings

IGN, BTC	Φ	Net Elec. Power, kWe	Net Brake* Power, kW	Efficiency : Gas-to-Shaft, %
24	0.97	154	167	27.4
18	0.96	160	174	27.6
14	0.94	165	182	28.3
12	0.94	165	182	28.3

* Excluding Radiator Fan Power

The maximum net brake output was obtained at an ignition advance between 12 and 14° CA with gas-to-shaft efficiency being 28.3%. At relatively advanced ignition timing, the output was observed to reduce. The p-θ could not be acquired during this set of experiments; however, it was acquired in the subsequent tests at two ignition settings as shown in Fig. 3.19. The p-θ curve does not correspond to maximum output obtained at that particular setting in the earlier experiments. However, these correspond to a net brake output of 148 and 149 kW at 19 and 12° CA respectively, obtained under wide throttle open condition at Φ = 0.91. The peak pressure and the point of occurrence at 19 and 12° CA are 65 bar, 7° ATC and 55 bar, 16° ATC respectively. Therefore, the MBT on this particular engine with producer gas should be between 12 and 14° CA. However, it is not clear as to why the brake outputs are almost identical when the ignition timings are vastly different. The point to be noted here the optimum timing; the maximum power output is obtained at slightly retarded ignition timing as compared to the SPE engine at comparable CR. This could probably be due to faster combustion due to higher turbulence (mean speed of the piston is 7.0 m/s against 5.8 m/s in SPE) and higher cylinder pressure and temperature due to turbo- charging.

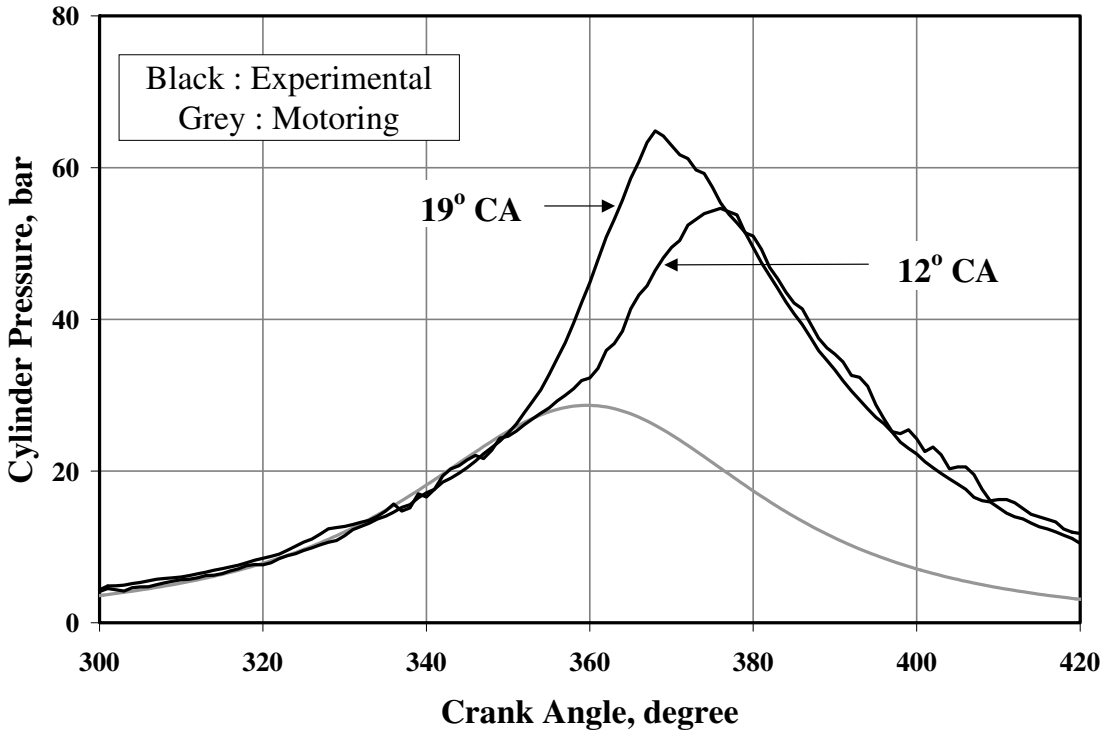

Fig. 3.19 p-θ Recording at Varying Ignition Advance. Ensemble- Averaged Data Over 30 Consecutive Cycles

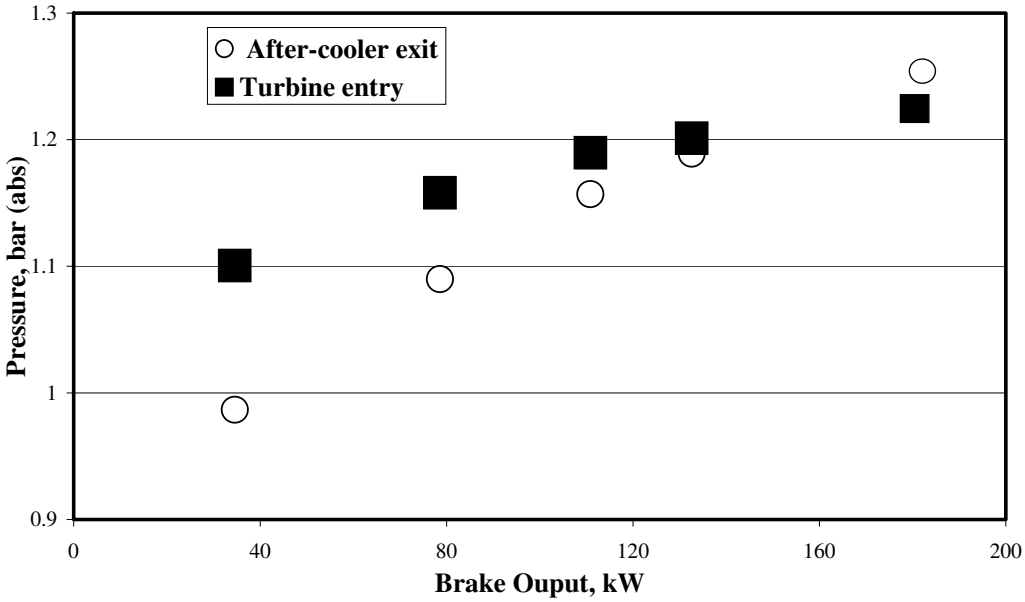

Fig. 3.20 Turbo-Charger Pressure at the Exit of After-Cooler and Turbine Entry.

The integrated p-θ data for the suction and exhaust processes, which is termed as pumping losses showed negative values in the range of –1 to –4 kW depending on the ignition advance, though positive values are normally expected for a turbo-charger engines. The reason for turbo-supercharger incurring this pumping loss is evident from Fig. 3.20, which shows the variation of turbo-charger pressure with brake output. The pressure into the inlet manifold i.e after-cooler exit is lower than the turbine entry pressure till a load of 140 kW. Even at this load the pumping losses will be negative because of the additional pressure loss occurring in the intake and exhaust valves. The intake manifold pressure becomes sufficiently higher than the turbine entry pressure at a load of 180 -185 kW. This essentially means the engine incurred pumping losses till a large part of the load range (till about 60-70% of the rated load – 290 kW) and gain in terms of positive pumping work could be expected only beyond 185 kW (when intake manifold pressure is higher than exhaust pressure). This, therefore, identifies the necessity for matching of the turbocharger commensurate with the engine demand. This point is particularly relevant when operated with low energy density fuels where the engine output is derated to an extent of about 25% or more.

The overall energy balance at different values of ignition advance corresponding to peak output delivered is shown in Fig, 3.21. The energy balance shows that at MBT about 30% was realized as gross brake output (including fan power = 12 kW), with the remaining 70% lost to exhaust and coolant. There is a re-distribution of energy pattern at advanced and retarded ignition settings, wherein the loss to the coolant increases with ignition advancement and similarly loss to the exhaust increases with delayed ignition.

Further, the performance of the engine is represented in terms of normalized value of brake specific fuel consumption (bsfc) in Fig 3.22. The bsfc at various ignition timing is normalized with bsfc at MBT, with all values corresponding to full throttle condition. A change in two degrees in ignition timing appeared to have modest effect on the fuel consumption, however with 5 to 10 degree change, the impact was much more significant.

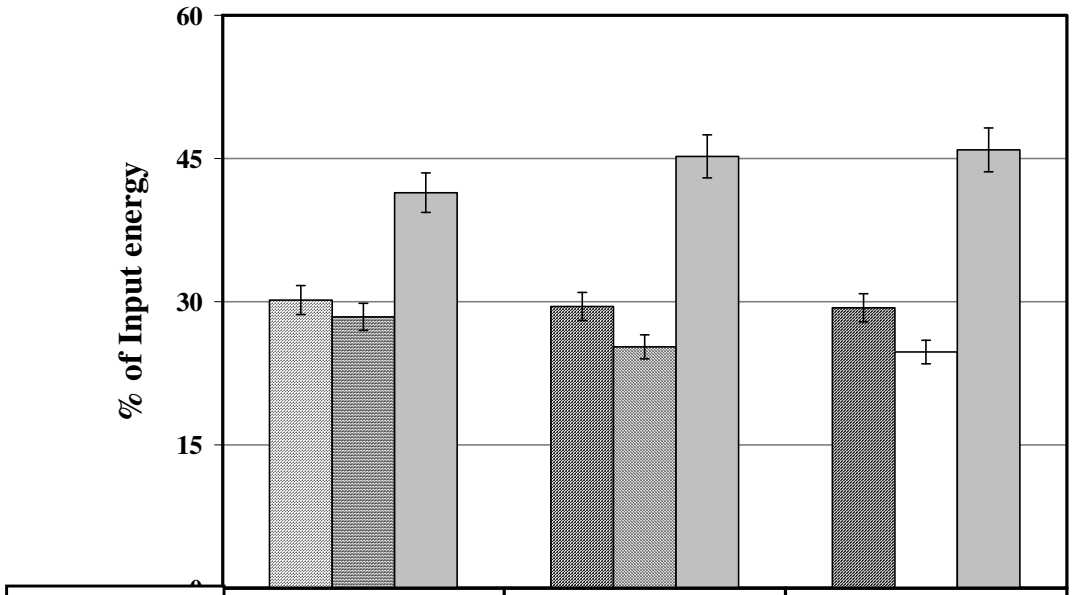

Ign., ° BTC	12	18	24
Brake output	30.2	29.5	29.4
Exhaust	28.4	25.3	24.7
Coolant & Miscl.	41.4	45.2	45.9

Fig. 3.21 Energy Balance at Varying Ignition Timing

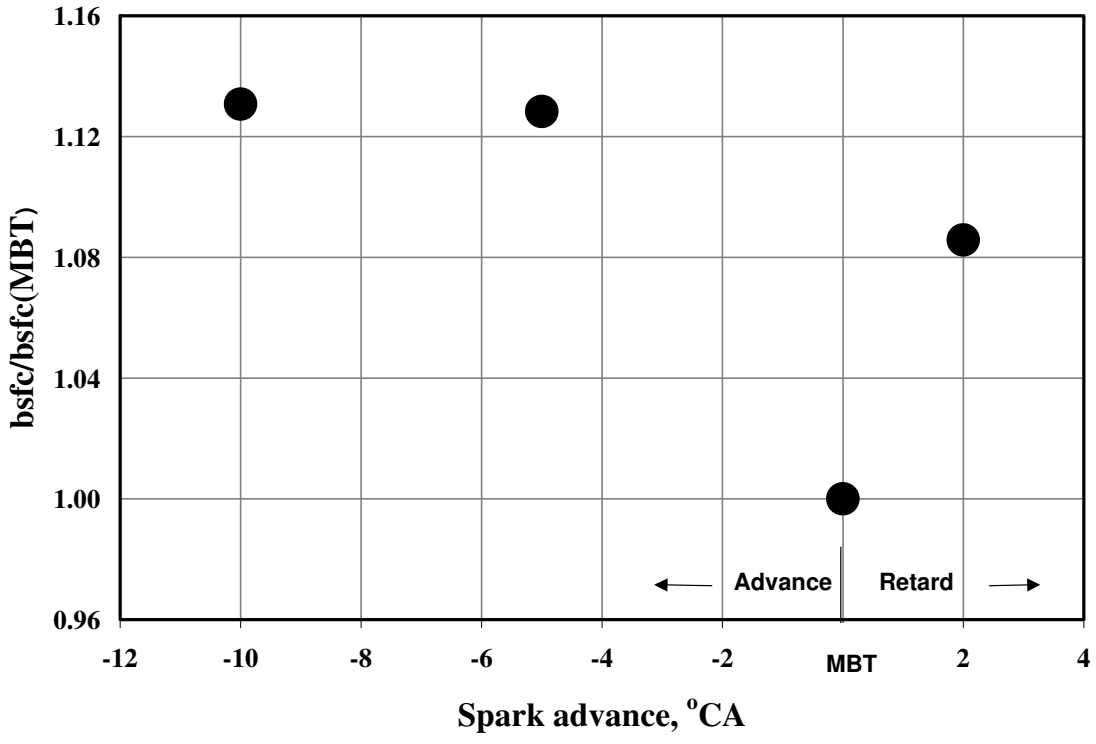

Fig. 3.22 Variation of bsfc with Ignition Advance. bsfc (MBT – 12° BTC) is 1.05 kg of Biomass or 2.8 kg of gas per kWhr

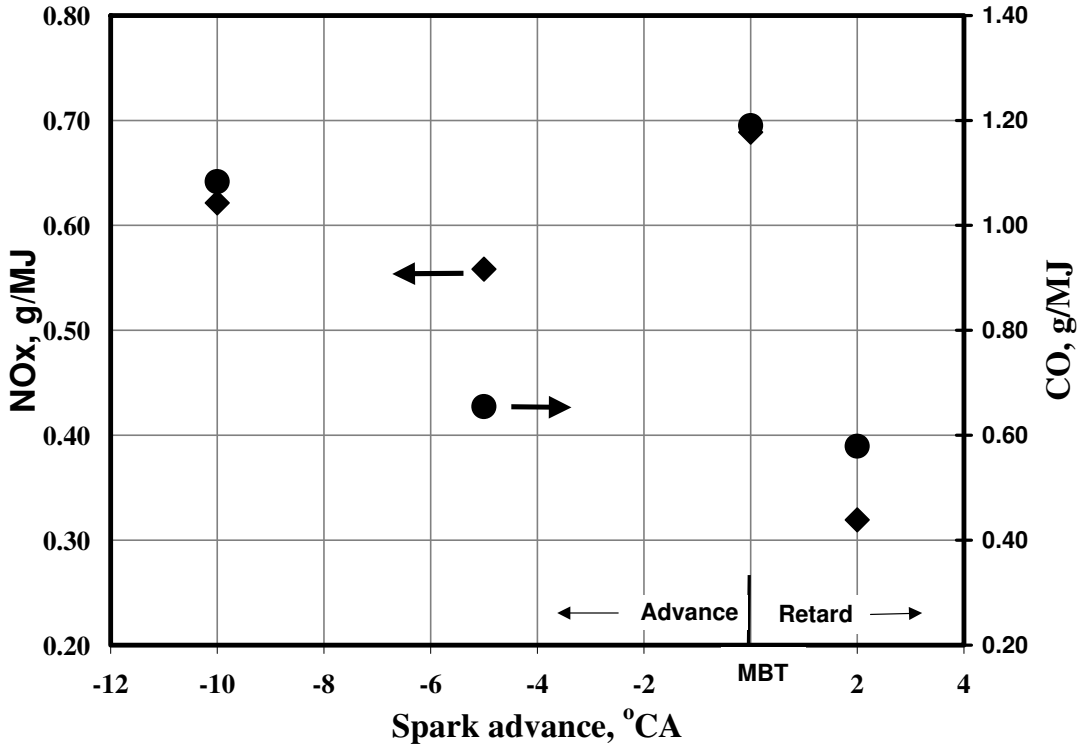

Fig. 3.23 MPE Emissions at Varying Ignition Setting Corresponding to Peak Output.

The variation of emission in terms of NO and CO is shown in Fig 3.23 as a function of ignition advance. There was a reduction in NO emission observed with retardation of ignition timing and this is attributed to reduction in residence time as in the earlier case. Similarly, there was also reduction in CO seen with retardation of the ignition setting implying completion of combustion even at MBT of 12° BTC.

3.3.5 Concluding Remarks

Like in the case of SPE, operation with producer gas is found be smooth with no indications of knock whatsoever from the p-θ curves. The engine and the gas carburetor system responded positively to the load changes. In addition, the carburetor was able to maintain the required air-to-fuel ratio with load changes. A gross brake output of 194 kW was obtained at an ignition advance of 12-14° CA, with Φ = 0.94. This ignition advance is found to be consistent with the earlier results on SPE where a MBT of 15 -17° CA was arrived at a CR of 11.5. The marginal retardation could probably be related to faster combustion because of higher turbulence (mean speed of the piston is 7.0 m/s against 5.8 m/s in SPE) and higher cylinder pressure and temperature due to turbo-charging. Table 3.10 shows the comparison of delivered power on MPE using producer gas and diluted natural gas. The data with diluted natural gas (biogas) has been recorded on a field system comprising of a Greaves engine (identical to MPE) at UGAR Sugars Ltd, Belguam, Karnataka, India.

Table 3.10: Summary of MPE Results at MBT

Fuel gas	Power (kW)* & Efficiency (%)	MBT, ° BTC	Mixture energy density, MJ/kg	Pressure- boost (turbo-charger)
Diesel (Estimated)	290 – 310 kW *(Base-line data)*	-	-	1.5 –1.6
Diluted Natural gas (75% CH_4)	270 kW; 34%	28-30	2.48	1.5 - 1.6
PG	194 kW; 30 %	12 -14	1.90	1.47
PG (Estimated)	*214 kW (with 10% increase in LCV)*	*12 -14*	*2.10*	*Possibly > 1.47*

* Including Radiator Fan power

With the boost pressure of the order of 1.47 measured against an expected pressure of 1.5 to 1.6 in diesel, the de-rating of power with producer gas is about 32-37%. This de-rating appears to be higher when compared to the results of SPE (26% at CR=11.5). However, as indicated earlier the mixture density in the experiments with MPE were about 4.8 to 5.0 MJ/Nm^3, which is about 10% lower than what has been measured on similar class gasifier. This also would shift the operations from the currently achieved lean ($\Phi < 1.0$) towards richer limits. If an increment of 10% in the mixture density is considered (which is actually so with respect to the tests on SPE – Table-3.3) the de-rating is reduced to 26-30% and compares closely with the SPE results. The performance of producer gas against diluted natural gas ($\Phi=0.97$) fares slightly better with de-rating at 28%, and the de-rating further narrowing down to about 20% at the expected output of 214 kW with producer gas (LCV ~ 5.3 MJ/Nm^3).

The energy balance in case of MPE showed higher fraction of the energy loss through coolant compared to SPE results at comparable CR. In case of SPE, heat loss through exhaust is higher due to unburned CO in the exhaust. However, the gross brake thermal efficiency is marginally higher than SPE. The emission in terms of NO and CO are found to be lower than the CPCB limits. However, NO levels are found to higher and CO levels lower compared to SPE results and this attributed to lean operation with MPE.

Further, the emissions with producer gas operation are compared against existing emission standards of various countries in Tale 3.11. The standard given for Indian conditions correspond to that of diesel powered vehicle (Euro I) for gross vehicle weight > 3.5 tons [http://terin.org/urban/standard.htm]. As stated earlier there are no standards existing for stationary engine (< 2 MW), a suggestion made by Indian diesel engine manufacturers association [http://www.kirloskar.com/html/sw/emissions] is pending for approval with CPCB. These are is in the brackets in Table 3.11 under India column.

The emissions with producer gas operation correspond to that measured under steady state conditions, using pre-calibrated instruments. However, the standards of various countries correspond to a specific procedure (steady state test cycle) meant for commercial engines. Therefore, the exact procedure might not have been followed in the current study, but measurements were made under steady-state conditions.

Table 3.11: Comparison of Emissions (g/MJ) with Producer Gas Operation against Existing Emission Norms in Various Countries

Parameter/Country*	USA	EU	Japan	India
CO	3.06	1.4 - 1.8	1.67	1.25 (3.9)
NOx	2.56	2.56	2.6 - 3.06	2.22 (5.0)
HC	0.36	0.36	0.4 - 0.56	0.3 (0.98)
PM	0.15	0.15 - 0.24	-	0.1 –0.2 (<3.5 Bosch)
SPE results between 6 to 20° CA for all CRs (min & max values) at Φ = 1.0 – 1.2				
Parameter/CR	17.0	14.5	13.5	11.5
CO	1.1 – 11.0	11.0 – 15.0	4.0 –16.0	9.0 –14.0
NOx	0.03 – 0.28	0.02 – 0.22	0.03 –0.20	0.05
PM	< 0.014			
MPE results between 12 to 24° CA for CR=12.0 at Φ = 0.94 - 0.97				
CO	0.58 – 1.2			
NOx	0.32 – 0.7			
PM	< 0.0005			

* Source: http://app10.internet.gov./scripts/nea/cms/htdocs/article.asp, PM is Particulate Matter

It can be seen that NO emission with producer gas is lower than all the existing norms. The CO results with MPE are encouraging, however there is large deviations with respect to SPE results. Therefore, treatment of exhaust in terms of CO is mandatory from the viewpoint of deriving maximum output (Φ >1.0). This could be true even with respect to HC emissions. However, Particular Matter (PM) is expected to be low even though measurements were not done because the input feed is gas with particulate matter less than 2 mg/Nm^3 (with MPE experiments), which amounts to < 0.5 mg/MJ. In the case of SPE experiments PM is estimated to be less than 14 mg/MJ, with input gas containing particulate matter to the extent of 60 mg/Nm^3.

3.4 Observations

Experimental studies have revealed engine operation to be smooth at a CR of 17.0 without any trace of knock thus establishing PG as a high-octane fuel. With the SPE engine, the extent of de-rating is observed to be 16.7% and 5% in terms of power and efficiency (gas to shaft power) respectively at the highest CR of 17 and it goes down to 27% and 21% respectively at CR of 11.5. The loss in power with PG operation is partly due to reduction in calorific value and partly due to reduction in the number of moles of the products released. In the case of MPE, the extent of de-rating is observed to be higher and the reasons for this feature are brought out.

It is seen that the optimum ignition timing i.e MBT with producer gas operation more retarded when compared to gaseous fuels like natural gas (15° CA at 14.7 CR) with CH_4 > 94% [Stone et al, 1996]. This is attributed to faster combustion due to laminar burning velocity being higher for producer gas compared to natural gas. Similarly MBT is retarded when compared with earlier works on producer gas and this is again attributed to producer gas constituents. Emission in terms of NO is observed to be lower partly due to lower peak cylinder temperature

and partly due to MBT being retarded. However, CO emissions in the case of SPE are larger, which calls for slightly fuel-lean operations.

3.5 Summary

Experimental results pertaining to gas engine operations at two different power levels have been discussed. Important parameters like the MBT at different CRs for producer gas fuel have been brought out. Some of the engine pressure history data (p-θ curve) shall be compared against the zero-D predictions in Chapter VII.

The Experimental Work 25

Chapter IV

Zero-Dimensional Model Formulation

This chapter discusses the formulation of zero-dimensional (0-D) model to simulate the SI engine cycle process. Eddy entrainment and laminar burn-up model based on flamelet concept of turbulent combustion are discussed. The parameters that need to be determined for using the above model are brought out.

4.1 Introduction

It is well recognized that the processes that govern the engine operation are extremely complex in nature. While much is known about these processes, there is no adequate understanding from the fundamental point of view. Therefore, it is difficult to make predictions of engine operation based on governing equations alone. Empirical relations and *ad hoc* approximations are being used to bridge this gap and these seem to be appropriate till better understanding prevails over the underlying physics. An advantage of such empirical models is that they can put to immediate use in areas of engine design and analysis.

Therefore, thermodynamic or 0-D model still continues to be popular [Maly, 1994] among the engine designers because (i) what is of interest in many cases is the overall efficiency with power and (ii) it can be calibrated to appreciable accuracy by comparing against a wide set of experimental data on overall performance. They are also very useful in parametric studies of the effects of changes in engine operating variables on engine power and efficiency. Emissions can be captured only to a limited extent. These phenomenological models have been thoroughly discussed in the review paper by Blumberg et al [1979].

4.2 Sub-models of 0-D Model

The zero-dimensional models are based on First Law of Thermodynamics, where time is the only independent variable. The model comprises of sub-models to simulate the processes of an engine cycle namely, intake, compression, heat release followed by expansion and exhaust. Depending upon the objective of the model, the sub-models are generally chosen. Since the objective of the present work is to simulate heat release, well-proven sub-model for turbulent combustion is chosen and relatively simpler sub-model is considered for the gas exchange process. However, pollutant formation is not modeled and heat transfer based on empirical relation is used. The various sub-models and empirical relation used in the present work are

- Filling and emptying technique (FET) for intake and exhaust processes as outlined by Heywood [1988].
- Eddy entrainment and laminar burn-up (EELB) model for simulation of heat release as derived by Keck [1982]
- Heat loss due to convection based on Annand's heat transfer correlations as discussed by Baruah [1986].

4.2.1 Gas Exchange Process – FET Model

In this model, the manifold is represented by finite volume where the mass of gas could increase or decrease with time. The mass and energy conservation equations coupled with mass flow rates into and out of the control volume – determined by equation of flow through a restriction are used to define the state of the gas in the control volume. The model also accounts for backflow of exhaust products into the intake manifold, but characterizes the contents of the manifold with a single gas temperature, pressure and composition. No wave action for charging during the intake and exhaust processes is accounted for.

In this work, the engine is modeled as three open systems comprising of the intake system, the cylinder and the exhaust system. The FET has been proved to be an accurate tool [Heywood, 1988] for intake and exhaust processes for engines with small and compact manifold (ratio of exhaust system volume to displaced/swept volume ~ 1.2) by the earlier researchers [Janota et al, 1967]. Therefore, it has been taken appropriate to consider the above model for the present work since the engine that is being examined falls under such category (ratio of exhaust system volume to displaced/swept volume ~ 1.1). The output of this sub-model (in terms of pressure and temperature) serves as an initial condition for the subsequent in-cylinder process.

4.2.2 Heat Release Process - EELB Model

The concept of wrinkled flame or flamelet regime of turbulent pre-mixed combustion in a homogenous charged spark-ignition engine has been discussed in Chapter I. Based on these well conducted experimental investigations that include schlieren, shadowgraph and laser scattering measurements, an empirical equation for calculating burn rate, namely EELB has been derived by Keck [1982]. In this model, the flame propagation (or heat release) is modeled as a two-zone model, where a thin wrinkled multi-connected laminar flame separates the burned and the unburned mixture. The EELB model as formulated by Keck is represented in a pictorial form in Fig. 4.1

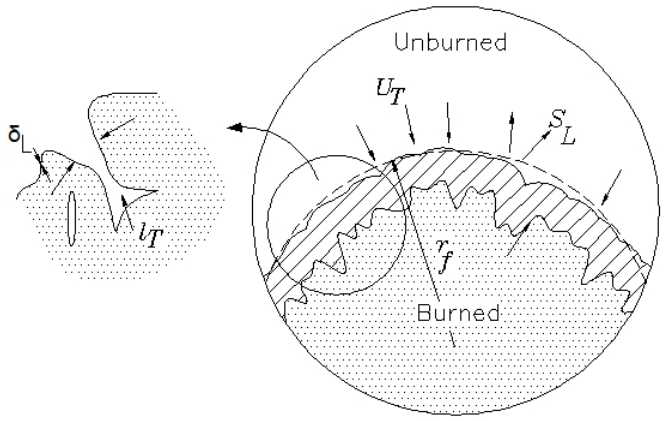

Fig 4.1 Schematic of Turbulent Premixed Spark-Ignition Engine Flame. Here u_T is Characteristic Speed, l_T is Characteristic Length Scale, S_L is Laminar Burning Velocity, ρ_u is Unburned Gas Density and δ_L is Reaction-Sheet/Flame Thickness, From Heywood [1988].

It is mathematically stated in the form of two equations, namely

$$\frac{dm_b}{dt} = \rho_u A_f S_L + \frac{\mu}{\tau_b} \qquad \text{- (4.1)}$$

$$\frac{d\mu}{dt} = \rho_u A_f u_T - \frac{\mu}{\tau_b} \qquad \text{- (4.2)}$$

where, parametric mass $\mu = \rho_u l_T (A_\ell - A_f)$ and characteristic time, $\tau_b = l_T/S_L$. A_l and A_f are laminar and spherical flame areas respectively. The relation between flame radius r_f and burned gas radius r_b based on experimental data is suggested by Keck [1982] as follows:

$$r_f / r_b \to 1 \text{ as } r_f \to 0 \qquad \text{- (4.3)}$$

and $$\left(r_f - r_b\right) \to u_T \tau_b \text{ as } r_f \to \infty \qquad \text{-(4.4)}$$

An empirical equation, which satisfies these limiting conditions, has been suggested to be

$$r_f = r_b + u_T \tau_b \left(1 - \exp\left(-\left(r_b / u_T \tau_b\right)^2\right)\right) \qquad \text{- (4.5)}$$

Equation 4.1 represents the mass burn rate, the first term in this equation represents the laminar propagation of an approximately spherical flame front of the thick turbulent flame; the second term represents the burning of mixture already entrained with in this flame front. Equation 4.2 represents the rate of change of unburned mixture μ within the flame front, the first term represents the turbulent convection of unburned mixture across the spherical front of the flame and the second term represents the mass rate of burning of entrained but not-yet-burned mixture which is contained within the wrinkles and islands. This distortion and stretching of the thin reaction sheet is produced by the turbulent flow field [Heywood, 1988].

The four important validity limits identified [Keck, 1982] and Heywood [1988] for equation 4.1 and 4.2 are as follows:

1. For a quiescent mixture, $u_T \to 0$ or $l_T \to \infty$

$$S_T \cong S_L \qquad \text{-(4.6)}$$

2. Initially, as $t \to 0$

$$S_T \to S_L \qquad \text{-(4.7)}$$

3. Quasi-steady state, $d\mu / dt \cong 0,$,

$$S_T \approx u_T + S_L \qquad \text{-(4.8)}$$

4. Final burning after the flame front reaches the wall, $t \geq t_w \ \ (A_f \to 0)$,

$$\dot{m}_b \Big/ \dot{m}_b(t_w) = \exp\left\{-(t - t_w)/\tau_b\right\} \qquad \text{-(4.9)}$$

Where, S_T is the turbulent burning speed. Using the above formulation, Keck's [1982] calculation of expansion speed (sum of turbulent burning speed and unburned gas speed) closely compares with the experimental results of Heywood et al [1984] for propane and hydrogen flame in an engine with simple geometry. It is reemphasized again here that Keck in his work [1982] brings out the need for validation of the above

formulation for different geometrically shaped engines, especially those with significant swirl and squish.

In these equations, there are two quantities, namely the characteristic speed and length, which could be related to the turbulence parameters namely turbulence intensity and length scale. Heywood [1988] relates the characteristic length scale to turbulent intensity u' and characteristic length scale to Taylor length scale l_M. It is also suggested that in order to use the above model, one needs to determine u' and integral length scale l_I, and subsequently l_M could be determined with the assumption of homogenous and isotropic turbulence.

These turbulence parameters can either be determined using empirical correlations or from fundamental studies. Keck [1982] has provided empirical relationship for obtaining characteristic speed and length by coupling with few other variables related to engine geometry. Similarly Borgnakke [1984] has suggested an empirical relation for estimating the value u' at the start of combustion to the mean intake flow through the valve. Similarly, l_I, at the start of combustion is considered to be proportional to a characteristic flow dimension, usually the clearance height. It further assumed that during combustion, the unburned mixture undergoes isentropic compression sufficiently rapidly that simple distortion process occurs. These are given as follows

$$u' = u_0'(\rho/\rho_0)^{1/3} \; ; \; l_I' = l_{I,0}(\rho/\rho_0)^{-1/3} \qquad \text{-(4.10)}$$

Where ρ refers to the density of the unburned gas and the suffix '$_0$' refers to the state to at the start of combustion. Some these correlations have been formulated for simpler geometries where turbulence is more dependent on the intake port design and less on the fluid-piston interaction inside the cylinder. Extending the same correlation is not appropriate for complex geometries where the flow is known to get substantially modified in the compression process. This leaves only with the other choice of estimating the turbulence parameters, namely by conducting a detailed 3-D modelling on the engine geometry under study. The computation of these turbulent parameters based on detailed CFD modelling is discussed in Chapter VI. The other important parameter set required to implement the EELB model is the laminar burning velocity for a particular fuel-air mixture, at thermodynamic conditions (pressure and temperature) encountered in an engine operation. The computation of laminar burning velocity for producer gas-air mixture is discussed in Chapter V.

4.2.3 Heat Loss Modelling – Empirical Relation

Convection is observed to be the dominant mode of heat transfer in SI engines [Heywood, 1988]. There are two sources for radiative heat transfer with in the engine cylinder: the high temperature burned gases and soot particles in the flame, if any. In a SI engine, the flame propagates across the combustion chamber from the ignition point through the previously mixed unburned mixture. Although the flame front is luminous, all the chemical intermediaries in the reaction process are gaseous and there is little

scope for soot particles in the flame. However, in a compression- ignition engine, most of the fuel burns in a turbulent diffusion flame as the fuel drops vaporize and burn with air. The flame is reported to be highly luminous, and soot particles are formed as an intermediate step in the combustion process. Therefore the radiation from soot particles in the diesel engine flame is estimated about five times the radiation from the gaseous combustion products and accounts for about 20-35% of the total heat transfer and a higher fraction of maximum heat transfer rate. Since the present study is concerned with a SI engine, only convective mode of heat transfer is accounted in the 0-D model.

Based on extensive experimental measurement over a wide range of engines empirical relations for heat transfer rate both in spark-ignition and compression ignition engines have been suggested by Annand [1963] and Woschni [1967]. The convective heat transfer flux from the gas to the cylinder wall given by Annand [1963] is as follows:

$$\frac{\dot{q}}{A_w} = \frac{ak}{D}(\mathrm{Re})^b (T_m - T_w) \qquad \text{-(4.11)}$$

Where k is the thermal conductivity of the gas, Re is the Reynolds number based on mean piston speed and the characteristic dimension is the cylinder bore D, A_w is the effective combustion chamber area, T_m the mean temperature of the burned/unburned gas and T_w the wall temperature. a and b are constants. The value of a is expressed to vary between $0.35 \le a \ge 0.8$ with the intensity of the charge motion and engine design and b = 0.7.

In the present study, empirical relation of Annand [1963] is used in the 0-D model. A constant value of b=0.7 is chosen and for a, different values are chosen depending upon the process. This is essentially arrived at by calibrating the 0-D model against one of the experimental firing cycle with the heat transfer constant a tuned in such a way that heat loss to the walls and the exhaust match with the experimental values. The Reynolds number, Re is calculated on mean piston speed, which are 5.8 and 7.0 m/s corresponding to an engine speed of 1500 rev/min for LPE and MPE respectively. One important assumption considered in the 0-D model with respect to heat transfer is the constant wall temperature. Literature [French et al, 1973] indicates varying average wall temperature in the combustion chamber, with cylinder liner in the temperature range of 120 to 180° C and piston much higher based on measurements at various locations in a SI engine at CR = 8.5. A constant wall temperature of 450 K has been assumed for all the processes in the 0-D model.

4.3 Modelling Details

Making use of the sub-models as mentioned earlier, a full cycle thermodynamic model is constructed involving the following processes.

4.3.1 Gas exchange process

The 0-D calculations commence with the intake process of the (gas + air) mixture. Suitable discharge co-efficient is chosen for the intake and exhaust valve flow based on steady flow results on engines (with similar configuration valve) available in the Literature [Bicen et al, 1985]. The gas exchange period extends from the opening of exhaust valve to the closing of the inlet valve, when either one or both valves are open. The cylinder condition at the terminating point of the gas exchange period is called the trapped condition and this gives the thermodynamic initial condition for the subsequent in-cylinder processes. The cycle of events between the intake valve closing and the exhaust valve opening are (1) compression, (2) ignition delay and flame initiation (3) flame propagation and (4) expansion processes.

4.3.2 Compression process

The compression process commences with the closure of intake valve and compression of the trapped mass. The assumptions considered in this process are: perfect mixing model with the state of gas-air-recycled mixture being homogenous, chemical reactions being absent and pressure being uniform. At appropriate crank angle the ignition is initiated, following which is there is an apparent heat release delay. Using the first law of thermodynamics stated as

$$\frac{dQ}{d\alpha} = mC_v \frac{dT}{d\alpha} + p\frac{dV}{d\alpha} \qquad \text{-(4.12)}$$

and the equation of state of gas $pV = mRT$, the equations for pressure and temperature changes with respect to crank angle or time is obtained. These are expressed as

$$\frac{dp}{d\alpha} = \left[-\left(1 + \frac{R}{C_v}\right) p\frac{dV}{d\alpha} + \left(\frac{R}{C_v}\right)\frac{dQ}{d\alpha} \right] \frac{1}{V} \qquad \text{-(4.13)}$$

and

$$\frac{dT}{d\alpha} = T\left[\frac{dV}{Vd\alpha} + \frac{dp}{pd\alpha} \right] \qquad \text{- (4.14)}$$

where, dQ is the heat loss obtained using equation 4.11. As the compression commences, the above variables are updated step-by-step using Euler's method, given by the general expression given below, where Δα is the time step in crank angle.

$$(Variable)_{n+1} = (Variable)_n + (Variable)_n * (\Delta\alpha) \qquad \text{- (4.15)}$$

4.3.3 Flame Initiation and Ignition Delay Period

The nominal ignition time is the instant when the spark occurs between the electrodes. However, there is a period of apparent delay between the time of sparking and the pressure rise due to combustion. It has been established by earlier researchers that flame propagates in a laminar mode till the flame kernel attains a critical size, beyond which the propagation becomes turbulent [Heywood 1988, Kalghatgi 1985]. In one case, Kalghatgi [1985] has identified the critical size of the flame to be around 11 mm radius for the propane and air gas mixture. This delay period is also considered as the time in which 1 to 10% of the initial unburned mass is consumed [Heywood, 1988]. Ignition delay is therefore considered to be the time required for the flame to assume a radius equivalent to 1% of the initial mixture by propagating at laminar burning velocity corresponding to the cylinder pressure and temperature. The estimated value is crosschecked by superimposing the computed motoring pressure-time curve with the experimental firing curve. In case of large differences between the two, the second method of estimation is considered. At the end of the ignition delay period, two physically distinct zones is considered to exist in the cylinder, one small part is formed by the flame kernel (at different pressure and temperature) and the rest by the unburned mixture. Further progress in computation is made by adopting the procedure, which identifies the steps for the two-zone calculations as discussed by Baruah [1986]. The procedure is of three steps, namely compression without combustion (Step I), during which the unburned mixture is considered to undergo normal compression process and this time period is same as the ignition delay period. The basis of this procedure is shown in Fig. 4.2.

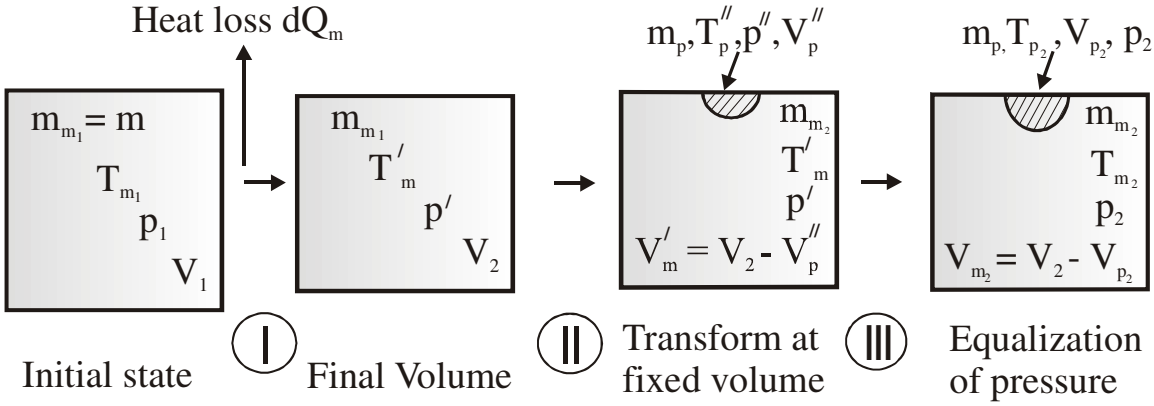

Fig. 4.2 Basis of Flame Initiation Process, From Barauh [1986]

At the end the ignition delay period, there is a definite thermodynamic state for the unburned mixture, which is calculated on lines similar to that explained in the compression process. At this instant, Step II is considered, where in a flame kernel is assumed to appear instantaneously. This process is based on the assumption that flame nucleus is formed under constant volume conditions resulting in high pressure and temperature in the products region. With the combustion taking place at constant volume, the unburned mixture zone is maintained at constant temperature and pressure T'_m and p' respectively. The pressure, p'' and temperature of products in the flame

kernel, T''_p are calculated from chemical equilibrium calculations, which are based on minimizing of Helmholtz energy. Similarly, the mass of the product is calculated corresponding to 1% of the trapped unburned mass. The total internal energy, E at the end of Step II is given by

$$E = m_m e_m + m_p e_p \qquad \text{- (4.16)}$$

The assumption of constant volume combustion in the Step II produces a pressure difference between the unburned and burned zone. Since this is physically impossible, another step, namely Step III is required for pressure equalization. In this step it is assumed that pressure equalization occurs adiabatically and at constant volume, V_2. This also implies the process is of constant internal energy, E.

4.3.4 Flame Propagation

At the completion of ignition delay period there are two distinct zones, separated by a flame front on which further computations are performed. A record is kept of the burned volume against the flame radius, and of the flame front area and flame contact with the cylinder wall and piston. With the advancement in calculations, the thermodynamic data pertaining to specific heats are accordingly updated based on the temperature in the burned and unburned zone. The principal assumptions made during this calculation are (1) the original charge is homogenous, (2) the pressure is uniform throughout the cylinder, (3) the volume occupied by the flame reaction zone is considered to be negligible, (4) the burned gas is at thermodynamic and chemical equilibrium, (5) the unburned gas is frozen at its original composition, (6) both burned and unburned gases have uniform local specific heats, (7) there is no heat transfer between burned and unburned zone, there is heat transfer between the two respective zone with the corresponding wall/piston area in contact. The total internal energy for the whole system is given by equation 4.16 and using the first law of thermodynamics the following equation is arrived at

$$\frac{dE}{d\alpha} = m_m \frac{de_m}{d\alpha} + e_m \frac{dm_m}{d\alpha} + m_p \frac{de_p}{d\alpha} + e_p \frac{dm_p}{d\alpha} \qquad \text{- (4.17)}$$

where, burn rate

$$\frac{dm_m}{d\alpha} = -\frac{dm_p}{d\alpha} = \rho_u A_f S_T \qquad \text{- (4.18)}$$

It is here that for the burn rate term (eq. 4.18), the EELB model equation 4.1 is substituted. Using equations 4.16 and 4.12, distinct equations for the change in pressure and burned and unburned gas temperatures are obtained. Using these equations along with heat loss, separate heat loss equation for the burned and unburned zones, the variables are updated with respect to time till the flame touches the wall and the entire mass of mixture is consumed.

4.3.5 Expansion

Once the combustion is complete, the variables are organized for a single zone calculation and thermodynamic properties are calculated with time. This process terminates with the commencement of opening of the exhaust valve, where by exhaust products flow out of the cylinder. With the completion of exhaust process, one cycle of operation is completed and the cycle is repeated till the results converge.

4.4 Summary

Procedure for 0-D modelling of a SI cyclic process is outlined. The sub-model required for implementing the 0-D model, namely the gas exchange sub-model and heat release sub-model are discussed. The heat release sub-model, which forms the crux of the 0-D model, is based on Eddy Entrainment and Laminar Burn up model meant for wrinkled flames in a homogenous charged SI engine. The parameters required for using the heat release sub-model, namely the laminar burning velocity (at elevated pressure and temperature as in a engine cylinder), and turbulent intensity and length scale have been identified. In addition, relevant correlations considered for estimation of heat loss due to convection are brought out.

Zero-Dimensional Model Formulation

Chapter V

Laminar Burning Velocity Calculations

This chapter discusses the calculations of laminar burning velocity of producer gas + air + recycled gas mixture at pressures and temperatures typical of unburned mixture in a reciprocating engine. The effect of varying amount of recycled gas on the burning velocity is brought out. Based on a number of calculations at varying initial pressures and temperatures, and equivalence ratio, an expression for estimating the laminar burning velocity with the recycled gas mass fraction is obtained.

5.1 Introduction

Laminar burning velocity is the important intrinsic property of a combustible fuel, air and burned gas mixture. It is the velocity with which the flame propagates into a quiescent premixed unburned mixture ahead of the flame. The additional feature of engine related flame is the presence of residual or burned gas from the earlier cycle and this causes a reduction in the laminar burning velocity [Heywood, 1988]. The study of laminar burning velocity becomes relevant for estimating the burn rate in a spark ignition (SI) engine. Laminar burning velocities at pressure and temperature typical of a reciprocating engine operation are usually measured using spherical closed vessels. Data and derived correlations are available in the literature for a wide range of premixed air and fuel that includes hydrogen, methane, propane, iso-octane, methanol and gasoline [Heywood, 1988]. However, there have been a few studies using producer gas fuel, both computational and experimental (at ambient conditions) and some of these are highlighted here. In this chapter, procedure for computing of laminar burning velocity is discussed; subsequently the results of computations at thermodynamic conditions typical of a reciprocating engine along with a generalized correlation are brought out.

5.2 Experimental - Earlier Studies

Laminar burning velocity for producer gas - air mixture has been obtained by experiments and theoretical calculations for various compositions and mixture ratios by the earlier researchers [Kanitkar et al, 1993, Chakravarthy et al, 1993 and Mishra et al, 1994]. The laminar burning velocity at ambient conditions (0.92kPa, 300 K) has been experimentally determined by Kanitkar et al [1993] by conducting experiments using standard flame tube apparatus for producer gas - air mixture for a wide range of mixture ratios. These experiments were conducted at laboratory reference conditions using producer gas generated from an on-line IISc's open top re-burn gasification system. The gas consisted of 18-23% H_2, 17-20% CO, 3-4% CH_4, 13-14% CO_2 and rest N_2. A wide range of mixture ratios were considered within the flammability limits of rich and lean mixtures, namely equivalence ratio (Φ) = 0.47 (26% fuel on volume basis) and 1.65 (56% fuel) for lean and rich limits respectively. The physical values of burning velocity varied between 0.10 to 0.13 m/s from lean to rich limits, with the peak value being 0.50$\pm$0.05 m/s around stoichiometry (45% fuel). The burning velocity for producer gas + air mixture is found to be higher by 30% compared to stoichiometric CH_4 + air mixture at ambient conditions and with comparatively higher values at the lean limit (CH_4 ~ 0.025m/s). This information is expected to help in understanding if the Minimum Advance for Best Torque (MBT) value for producer gas operation is advanced/retarded compared to MBT (about 15° CA at 14.7 CR) identified for natural gas (> 94% CH_4) operation by Stone et al [1996].

5.3 Theoretical Predictions

5.3.1 Procedure

Theoretical laminar burning velocity predictions have been made by the earlier researchers [Goyal, 1989, Lakshmisha, 1991, Chakravarthy et al, 1993 and Mishra et al, 1994] using in-house developed software called 'FLAME CODE' for one-dimensional adiabatic premixed laminar flame. The calculations involve the solution of conservation equations describing the laminar one-dimensional multi-component, chemically reacting, and ideal gas mixtures. The relevant conservation equations are,

$$\frac{\partial \rho}{\partial t} + \frac{\partial (\rho u)}{\partial x} = 0 \qquad \text{- (5.1)}$$

$$\rho \frac{\partial Y_i}{\partial t} + \rho u \frac{\partial Y_i}{\partial x} = -\frac{\partial J_i}{\partial x} + \dot{\omega}_i''', \quad i = 1, \ldots, N_s \qquad \text{- (5.2)}$$

$$\rho \frac{\partial h}{\partial t} + \rho u \frac{\partial h}{\partial x} = \frac{\partial}{\partial x}\left(\frac{\lambda}{c_p}\frac{\partial h}{\partial x}\right) - \sum_{i=1}^{N_s} \frac{\partial}{\partial x}\left[h_i\left(J_i + \frac{\lambda}{c_p}\frac{\partial Y_i}{\partial x}\right)\right] \qquad \text{- (5.3)}$$

Where x is the coordinate fixed to the laboratory normal to the flame, Y_i are the mass fractions of the species, $\dot{\omega}'''$ is the volumetric production/consumption rate of chemical species, the temperature and h is the sum of chemical and sensible enthalpies given by

$$h = \sum_{i=1}^{N_s} \left(h_i^0 + \int_{T_0}^{T} c_{pi}\, dT \right) Y_i \qquad \text{- (5.4)}$$

The corresponding boundary conditions are given by

$$\begin{aligned} x \rightarrow -\infty &: \frac{\partial Y_i}{\partial x} \rightarrow 0 \,,\ \frac{\partial T}{\partial x} \rightarrow 0 \\ x \rightarrow +\infty &: Y_i \rightarrow Y_{i,u} \,,\ T \rightarrow T_u \end{aligned} \qquad \text{- (5.5)}$$

As noted in Equation 5.5, the hot boundary contains equilibrium mass fractions of relevant species and adiabatic flame temperature and the cold boundary contains reactant mass fractions and ambient temperature. The calculations commence from a given set of initial profiles of mass fraction (Y_i) and Temperature (T), which are linearly distributed with distance, x over an assumed flame thickness. The choice of the set of kinetic studies and rate constants has been arrived by earlier researchers [Lakshmisha, 1991, Mishra et al, 1994], which is a set of elementary reactions validated for H_2-air and CH_4–air systems. The CO-air forms a subset of CH_4-air system.

With the producer gas representing CO-H_2-CH_4-0_2-N_2 system, the species and the reactions considered for calculations are given in Table 5.1. Reaction rate is defined as,

$$dC_i/dt = A_f\, e^{-E/RT} T^m \prod C_j^{\nu_j} \qquad \text{- (5.6)}$$

where, C_i is the concentration of species and ν_j the stoichiometric coefficients of the reactions listed in Table 5.1. The values of frequency factor A_f, activation energy E and coefficient m are given in Table 5.1. For each species, the NASA polynomial cure fits used to calculate the thermodynamic properties, namely specific heat, enthalpy and entropy. The transport properties such as diffusion coefficients and thermal conductivity for the mixture are evaluated using the correlations given in the report by Brokaw [1961]. The diffusive fluxes are calculated using the trace diffusion approximation neglecting the Soret and Dufour effects. The conservation equations are solved by finite difference scheme using operator-split technique. In this method the reaction equation is solved using an implicit method of the Crank-Nicholson type and the diffusion equation using the explicit forward-time central space (FTCS) scheme. The set of equations are solved at one time level and the properties at the next time level are obtained by a simple updating scheme. The burning velocities for different species are calculated and the convergence of these burning velocities as well with time of integration is used to determine the steady state. The results of burning velocity along with Y_i and T constituted the output of the solution procedure.

Table 5.1: Kinetic Scheme Used for the Present Laminar Burning Velocity Calculations [Warnatz, 1984]. A_f in cm³.s mole, E in kcal/mole

No.	Reaction	A_f	m	E
R1	$OH + O \leftrightarrow O_2 + H$	1.8E + 13	0.0	0.0
R2	$O + H_2 \leftrightarrow OH + H$	1.5E + 07	2.0	76.58
R3	$OH + H_2 \leftrightarrow H_2O + H$	1.0E + 08	1.6	33.28
R4	$OH + OH \leftrightarrow H_2 + O$	1.5E + 09	1.14	0.0
R5	$H + H + M \leftrightarrow H_2 + M^*$	9.7E + 16	-0.6	0.0
R6	$H + OH + M \leftrightarrow H_2O + M$	2.2E + 22	-2.0	0.0
R7	$O + O + M \leftrightarrow O_2 + M$	2.9E + 17	-1.0	0.0
R8	$H + O_2 + M \leftrightarrow HO_2 + M$	2.0E + 18	-0.8	0.0
R9	$H + HO_2 \leftrightarrow OH + OH$	1.5E + 14	0.0	10.80
R10	$H + HO_2 \leftrightarrow H_2 + O_2$	2.5E + 13	0.0	73.17
R11	$O + HO_2 \leftrightarrow OH + O_2$	2.0E + 13	0.0	0.0
R12	$OH + HO_2 \leftrightarrow H_2O + O_2$	2.0E + 13	0.0	0.0
R13	$HO_2 + HO_2 \leftrightarrow H_2O_2 + O_2$	2.0E + 12	0.0	0.0
R14	$OH + OH + M \leftrightarrow H_2O_2 + M$	3.3E + 22	-2.0	0.0
R15	$H + H_2O_2 \leftrightarrow H_2 + HO_2$	1.7E + 12	0.0	37.4
R16	$H + H_2O_2 \leftrightarrow H2O + OH$	1.0E + 13	0.0	36.1
R17	$O + H_2O_2 \leftrightarrow OH + HO_2$	2.8E + 13	0.0	64.35
R18	$OH + H_2O_2 \leftrightarrow H_2O + HO_2$	7.0E + 12	0.0	14.03
R19	$CO + H + M \leftrightarrow CHO + M$	6.9E + 14	0.0	17.0
R20	$CO + O + M \leftrightarrow CO_2 + M$	7.1E + 13	0.0	-45.11
R21	$CO + OH \leftrightarrow CO_2 + H$	4.4E + 07	1.5	-74.1
R22	$CO + HO_2 \leftrightarrow CO_2 + O$	1.5E + 14	0.0	24.0
R23	$CO + O_2 \leftrightarrow CO_2 + O$	2.5E + 12	0.0	48.15
R24	$CH_4 + H \leftrightarrow CH_3 + H_2$	2.2E + 04	3.0	87.61
R25	$CH_4 + O \leftrightarrow CH_3 + OH$	1.2E + 07	2.10	76.28
R26	$CH_4 + OH \leftrightarrow CH_3 + H_2O$	1.6E + 06	2.10	24.76
R27	$CH_4 + M \leftrightarrow CH_3 + H + M$	5.7E + 17	0.0	92.24
R28	$CH_3 + O \leftrightarrow CH_2O + H$	7.0E + 13	0.0	0.0
R29	$CH_3 + O_2 \leftrightarrow CH_2O + O$	1.5E + 13	0.0	29.7
R30	$CH_2O + H \leftrightarrow CHO + H_2$	2.5E + 13	0.0	40.40
R31	$CH_2O + O \leftrightarrow CHO + OH$	3.5E + 13	0.0	35.38
R32	$CH_2O + OH \leftrightarrow CHO + H_2O$	3.0E + 13	0.0	12.03
R33	$CH_2O + CH_2 \leftrightarrow CHO + CH_4$	1.0E + 11	0.0	61.64
R34	$CH_2O + M \leftrightarrow CHO + H + M$	1.4E + 17	0.0	76.85
R35	$CH_2O + M \leftrightarrow CO + H_2 + M$	2.0E + 16	0.0	38.0
R36	$CHO + H \leftrightarrow CO + H_2$	2.0E + 14	0.0	0.0
R37	$CHO + O \leftrightarrow CO + OH$	3.0E + 13	0.0	0.0
R38	$CHO + O \leftrightarrow CO_2 + H$	3.0E + 13	0.0	0.0
R39	$CHO + OH \leftrightarrow CO + H_2O$	5.0E + 13	0.0	0.0
R40	$CHO + O2 \leftrightarrow CO + HO_2$	3.0E + 12	0.0	0.0

* M represents the third body, which is chaperon efficiency weighed total concentration

The burning velocity is calculated from

$$S_{Li} = \frac{\int_{-\infty}^{+\infty} \dot{\omega}'''_i \, dx}{\rho_u (Y_{i,u} - Y_{i,b})}, i = 1,2,....., N_s \quad \text{- (5.7)}$$

$$S_{LT} = \frac{\int_{-\infty}^{+\infty} \sum_{i=1}^{Ns} \dot{\omega}'''_i h^o_i \, dx}{\rho_u (H_u - H_b)} \quad \text{- (5.8)}$$

where, H_u and H_b is the total enthalpy of the unburned mixture and burned gases respectively.

5.3.2 Predictions – High Pressure

In one of the earlier studies [Chakravarthy et al, 1993] conducted using the above code for producer gas+ air mixture at ambient conditions, the theoretical predictions compared well within the error band of experimental data. In one of the subsequent studies [Mishra et al, 1994], predictions at higher pressures indicated the burning velocity of producer gas to reduce from 0.4 m/s at 1 atm (300 K) to 0.04 m/s at 40 atm (300 K). Such a drastic reduction in burning velocity at high pressure was attributed to the drastic reduction in the radical pool due to suppression of dissociation. This drastic reduction in burning velocity at higher pressure has relevance in the field of internal combustion engine because of similar pressures encountered during operation. However, this effect can be expected to be completely modified by the corresponding increase in temperature on account of compression in a reciprocating engine.

5.3.3 Current Work – High Pressure and Temperature Along with Recycled Gas

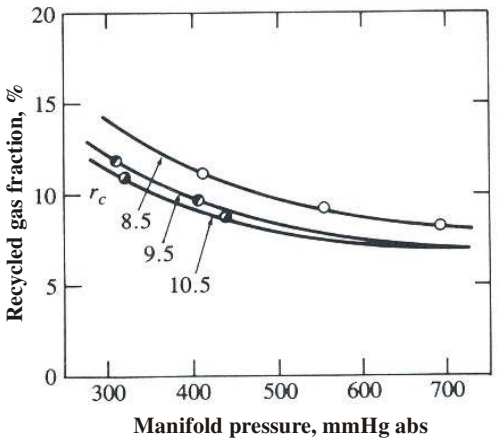

Fig. 5.1 A Trace of Recycled Gas (RG) Variation with CR Recorded on a SI Engine at 1400 rev/min [see Heywood, 1988]

The zero–dimensional calculations required input in the form of laminar burning velocity at pressure and temperature prevalent in the engine cylinder at the time of initiation of ignition. Therefore, producer gas + air mixture compositions comparing closely with the experimental data at varying mixture ratios was considered. In an actual reciprocating engine operation, there is some amount of burned product that is trapped in the clearance volume from the previous cycle, as also there is some amount of the reverse flow of burned products from the cylinder into the intake manifold. The extent or fraction of recycled

gas in the fresh mixture depends upon the compression ratio (CR) and the valve overlap period. The data on recycled mass fraction from literature [see Heywood, 1988] as a function of CR is shown in Fig. 5.2. In order to simulate the mixture conditions close to an actual SI engine operation, varying amounts of recycled gas fraction (0 to 10%) are considered for the calculations and these are well within the recycled gas mass fraction for engines with CR between 17 and 11.5:1. The fuel considered is of nominal composition with 20 % each of H_2 and CO, 2% CH_4, 12% CO_2 and rest N_2. Calculations are made at varying equivalence ratio (Φ), initial temperature and pressure and with *varying amounts of recycled gas 0, 5 and 10%*. The results of these computation are shown in Table-5.1 for two identified producer gas + air mixture and at two equivalence ratios.

Table 5.2: Computational Laminar Burning Velocity at Varying Initial Conditions of Mixture – Pressure, Temperature and Recycled Gas (RG) Mass Fraction.

Pressure, bar (abs)	$T_{unburned}$, K	S_L, cm/sec						
		Case I*	Case II#					
		Φ =0.90	Φ =1.07			Φ =0.90		
		0% RG	0% RG	5% RG	10% RG	0% RG	5% RG	10% RG
5	630	105	143	130	112	122	110	92
10	746	132	179	162	139	154	144	113
15	821	151	205	183	159	176	151	132
20	876	163	217	196	169	189	166	141
25	920	173	229	205	176	200	174	148
30	954	178	236	207	180	206	180	152
35	995	191	249	213	186	221	190	164
40	1028	202	259	231	189	227	198	176
45	1056	207	268	238	200	235	208	181
50	1082	215	275	245	204	243	214	190

* Case I Corresponds to H_2 = 20%, CO= 18%, CH_4 =2%, CO_2 = 12% and rest, N_2
\# Case II Corresponds to H_2 = 20%, CO= 20%, CH_4 =2%, CO_2 = 12% and rest, N_2
Recycled Gas for Case I and II is H_2O =12%, CO_2 =15% and rest, N_2

It is clear from the above data that burning velocities decrease substantially with dilution at all initial mixture pressure conditions and Φ. This essentially occurs due to reduction in the adiabatic flame temperature due to dilution. The effect of dilution on the burning velocity is shown in Fig. 5.2 for rich and lean fuel +air mixture at different initial mixture pressures. The proportional reduction in laminar burning velocity is essentially independent of the unburned mixture equivalence ratio, initial pressure and temperature over the range of computation conducted. This effect is consistent with studies conducted by Rhodes et al [1985] using gasoline fuel at initial pressure of 1 and 2 atmosphere.

A least-square curve fitting done using the data of Case II resulted in an expression for laminar burning velocity in terms of cylinder pressure and is as follows.

$$S_L\ (\mathrm{cm/s}) = 94.35\left(\frac{p}{p_0}\right)^{0.2744}\ (0.96 + 1.2(\Phi - 1))(1 - 2.4\psi) \qquad \text{- (5.9)}$$

where, p is the cylinder pressure in bar (abs), p_o the reference pressure (1.0 bar), Ψ the recycled gas mass fraction and Φ the fuel-air equivalence ratio. The burning velocity dependence upon the initial temperature is built into the pressure term in Equation 5.8. The above correlation is correct within $\pm$ 6% for the data of Case II. This correlation fits for the data in Case I by including a correction factor due to lower CO content, which is explained below.

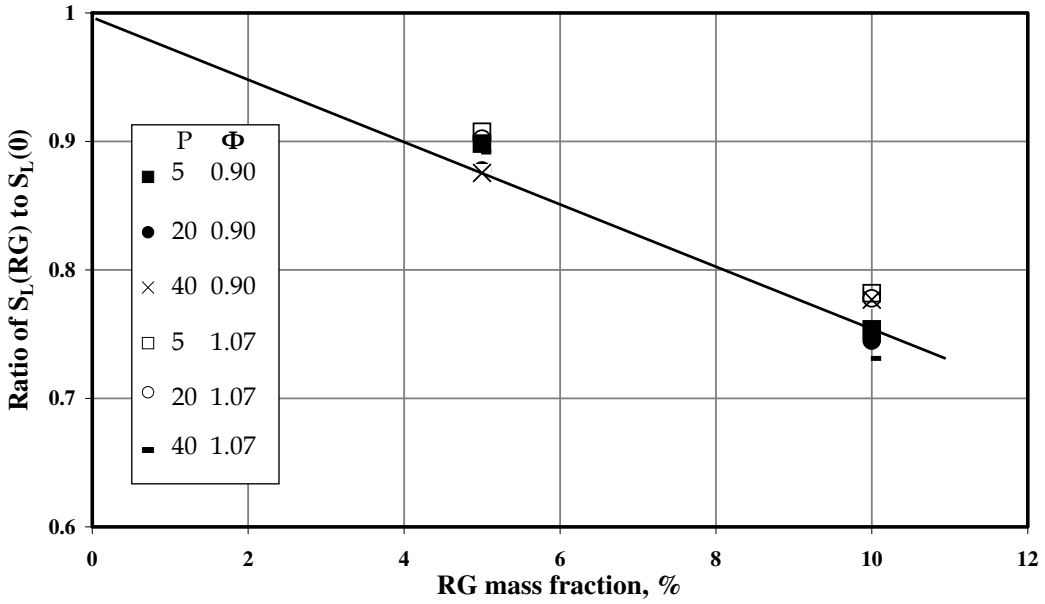

Fig. 5.2 Effect of Variation of Recycled Gas (RG) on the Laminar Burning Velocity at Rich and Lean Mixtures and Different Initial Pressures.

It has been brought out in Chapter III that laminar burning velocity for producer gas is about 30 % higher than natural gas at ambient conditions. The burning velocity of producer gas is quite sensitive to the variations in fraction of H_2 and CO and this is quite possible in the process of gasification. A sensitivity analysis of variation in CO and H_2 content towards laminar burning velocity at a equivalence ratio of about 0.9 revealed the burning velocity to reduce by about 7% for reduction of every 1% in H_2 or CO content. To further explore the behaviour seen above, the heat lease rate is examined at six varying conditions. The conditions examined correspond to 40 and 20 bar (abs) initial pressure with *0, 5 and 10%* recycled gas fraction. The two pressures listed above are the typical working pressure at the highest and lowest CR dealt in this thesis. The heat release rate across the flame is plotted as a function of non-dimensional temperature for six conditions in Fig. 5.3. The initial unburned gas temperature and the corresponding

adiabatic flame/burned gas temperatures are given in Table 5.3. It is very much evident from the plot the influence of RG on the heat release rate at both initial mixture pressures.

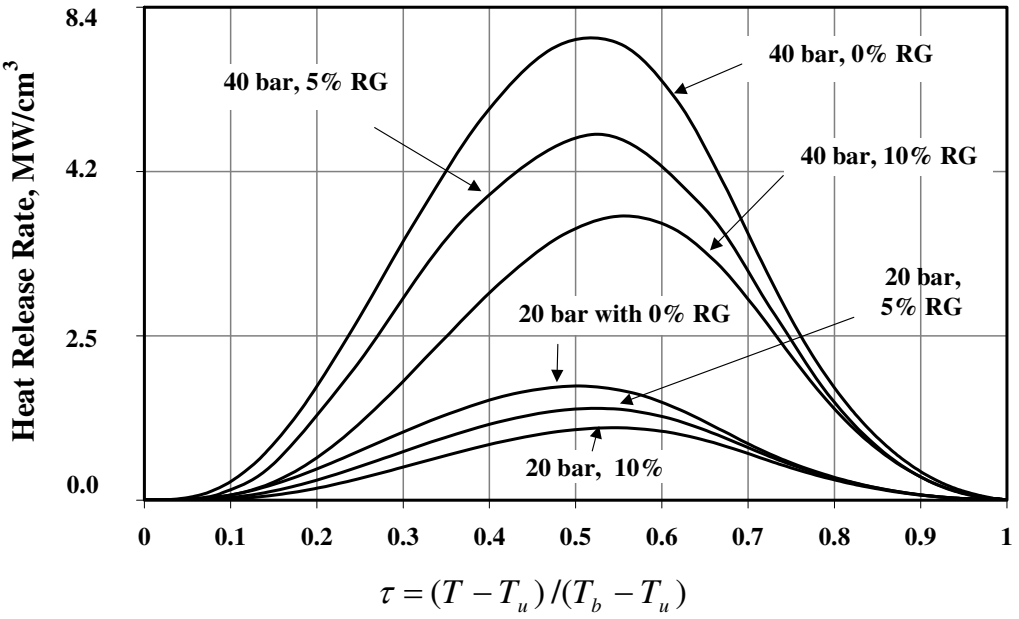

Fig. 5.3 Heat Release Rate Profile vs. Non-Dimensional Temperature across the Flame at Two Initial Mixture Pressure of 20 and 40 bar (abs), with and without Recycled Gas (RG).

Table 5.3: Laminar Burning Velocity and Laminar Flame Thickness at Φ =1.07 for Different Pressures and Recycled Gas (RG)

Pressure	20 bar (abs)			40 bar (abs)		
RG, %	0	5	10	0	5	10
T_u, K	876	876	876	1028	1028	1028
T_b, K	2330	2275	2200	2450	2395	2345
S_L, cm/s	217	196	169	259	231	189
δ_L, mm	0.23	0.21	0.19	0.092	0.13	0.09

The distance between positions of 1% (initial temperature, T_u) and 99% (adiabatic flame/burned gas temperature, T_{ad} or T_b) temperature rise is used for the estimation of the flame thickness, δ_L and is shown in Table 5.3. The δ_L is about 0.21 $\pm$ 0.02 mm and 0.1 $\pm$ 0.01 mm at 20 and 40 bar (abs) pressure respectively. The order of flame thickness is well within the values measured experimentally by Smith [1982] ~ 0.2 mm for propane fuel under engine conditions. Similarly the flame thickness according to the procedure of Abraham et al [1985] (ratio of thermal diffusivity to laminar burning velocity) works out about 0.8 microns. The kolmogorov length scale, l_k for the engine under study is about 4 microns (for a Re_T =2100 and l_I =1.2 mm, assuming isotropic and homogenous turbulence: $l_k = l_I\, Re_T^{-3/4}$). Therefore, the ratio of $l_k/\delta_L \approx 5.0$ implying flame can be treated

as negligibly thin in the context of wrinkled flame structure relevant to SI engine [Abraham et al, 1985].

5.4 Summary

A correlation for estimation of laminar burning velocity as a function of initial pressure and recycled gas fraction is obtained. This expression is used in the 0-D model to estimate the burn rate for a wide range of operating conditions.

Laminar Burning Velocity Calculations. 68

Table 5.1: Kinetic Scheme Used for the Present Laminar Burning Velocity Calculations [Warnatz, 1984]
Table 5.2: Computational Laminar Burning Velocity at Varying Initial Conditions of Mixture – Pressure, Temperature and Recycled Gas (RG) Mass Fraction.
Table 5.3: Laminar Burning Velocity and Laminar Flame Thickness at Φ =1.07 for Different Pressures and Recycled Gas Fraction

Chapter VI

CFD Modelling

This chapter discusses the detailed three-dimensional modelling of a reciprocating engine geometry comprising of a flat cylinder head and a bowl-in-piston combustion chamber, simulating the motoring or non-firing conditions. The turbulence is modelled using standard $k-\varepsilon$ model and the results are compared against experimental results from the literature. Relevant turbulence parameters and velocities extracted from the modelling study are used in the 0-D model whose predictions are discussed in the next chapter.

6.1 Introduction

Turbulence in reciprocating engines is considered important because of its large influence on the combustion characteristics. In order to find optimum conditions in a combustion system, it is essential to get a good approximation of the in-cylinder turbulence. From this viewpoint, multi-dimensional modelling using CFD codes is pursued and involves simulation with and without combustion. One of the major challenges of CFD in the recent times is that several models need to be combined in order to simulate a complete engine cycle. The $k-\varepsilon$ model is the most commonly used turbulence model in CFD, even though its deficiencies are known [Versteeg et al, 1995], indeed $k-\varepsilon$ model is still considered to the best compromise between computational time and precision. However, in the recent times, second-moment closure models are being pursued in engine modelling [Lebrere et al, 1996; Watkins et al, 1996], with the increased validity of the model. But complex numerical approaches such as Direct Numerical Simulation (DNS) are difficult to implement on engine like situation, because of enormous pre-requisites such as high mesh density and exorbitant CPU time. This is also the case with Large Eddy Simulation (LES), where accurate sub-grid models are required, and research in this field is still in progress [Lebrere et al, 1996]. For implementing CFD model, mesh density assumes primary importance; some of the earlier studies on engine geometry using different mesh densities are summarized in Table 6.1.

Table 6.1: CFD Studies on Engine Geometries with Different Mesh Densities

Researcher	Summary of The Work	Geometry & Mesh
Schapertons et al [1986]	Cold flow studies in two different bowl-in piston geometries of a diesel engine	Engine cylinder, 0.02 million cells
Haworth et al [1990]	Cold flow studies with different intake valves and limited comparison with experimental results.	Intake pipe and engine cylinder, 0.023 million cells
Trigui et al [1994]	Cold flow studies using STAR-CD code; experimental flow field data used as initial conditions.	Engine cylinder, 0.06 million cells
Jones et al [1995]	Cold flow in a four valve pent roof SI engine through two complete cycles using SPEED code. Predictions compared qualitatively and quantitatively (one case) with the experimental results.	Engine cylinder, 0.03 million cells
Strauss et al [1995]	Simulation of combustion in a indirect combustion chamber geometry of diesel engine using SPEED code	Engine cylinder, 0.0425 million cells
Reuss et al [1995]	Cold flow studies compared against Particle Image Velocimetry results using KIVA and GMTEC code	Engine cylinder, 0.06 million cells
Khalighi et al [1995]	Flow and combustion modelling in a four-valve SI engine. Cold flow results compared with water-analog flow studies. Numerical inaccuracies discussed.	Engine cylinder, 0.023 - 0.12 million cells
Lebrere et al [1996]	Cold flow using $k-\varepsilon$ and second-order closure turbulence model. Predictions compared against LDA measurements.	Engine cylinder, 0.072 million cells
Bauer et al [1996]	Flow through intake system of a SI engine using STAR-CD code. Predictions of instantaneous pressure and temperature in the intake system compared with the experimental results.	Intake system and engine cylinder, 0.12 million cells
Duclos et al [1996]	Simulation of SI engine combustion using KIVA – II code and compared with the experimental results.	Intake pipe and engine cylinder, 0.12 million cells

From the above Table 6.1, it is evident that the computational mesh densities have increased with the enhancement in the computational speed over the period of two decades. Reasonably good qualitative (a few cases quantitative) comparison have been claimed by the some of the researchers listed above with mesh density less than 0.12 million cells, by using turbulence models such as $k-\varepsilon$ in most cases and second order closure model in one case [Lebrere et al, 1996]. They claim the grid independent solution based on global balances in momentum and kinetic energy, with mesh refinement to have little effect on the results.

In the present work, a detailed 3-D cold flow study is conducted on piston-engine geometry with a mesh density of 0.2 million cells to simulate the engine cold flow condition. CFD simulation is conducted over two complete motoring cycles involving intake, compression, and expansion and exhaust processes on a bowl-in piston engine geometry at two CRs, namely 17.0 and 11.5. Data on the turbulence parameters, and reverse squish velocities (referred as the reverse squish period during the beginning of expansion process) derived from the above study are used as input in the 0-D modelling. Similarly, a hypothetical path for the flame kernel movement is obtained from the CFD results. This is estimated by tracking the velocity of a particle along a streak line, in and around the point of ignition. The simulation is conducted using a commercial CFD code CFX - 4.3. The grid is generated using a pre-processor called CFX-build. The numerical solution is obtained using CFX-solver, which is based on finite volume technique. The results are analysed using a post-processor known as CFX-Analyse.

6.2 Problem Definition

The geometry considered for modelling is identical to the combustion chamber geometry of Small Power level Engine (SPE). The combustion chamber comprises of a flat cylinder head and an eccentrically located hemispherical bowl. The geometric details of the engine are given in Table 3.1. The piston, which is one of the moving boundaries, simulates the reciprocating movement of an engine. The minimum clearance between the piston and the cylinder head as the piston approaches its uppermost point of travel is about 1.5 mm for a CR of 17.0 and increases to 5.2 mm at CR of 11.5. The other moving boundary is formed by the intake valve (non-swirl type) to allow fluid flow into the cylinder geometry. The geometry is also provided with an exhaust port that is opened at appropriate time to simulate the exhaust process. Since the simulation does not involve combustion, simplifying the geometry with a port in place of a moving exhaust valve is taken not to influence the accuracy of the results. The geometry described above is relatively complex, involving a time dependent grid to simulate the piston and intake valve movement. This is achieved by writing additional fortran programmes to simulate the transient grid in the present study. Simulation is also conducted on a flat piston (without the bowl) at a CR=17.0 in order to assess the magnification of turbulence intensity caused by the presence of bowl.

6.2.1 Grid Generation

The geometry described in Cartesian co-ordinate system is required to simulate the reciprocating engine operation. This is achieved using a multi-block grid methodology, in which a set of unstructured blocks is glued together, and on each of them is a structured grid. In the resulting geometry with a three-block structure, it is found that there is a mismatch of the grids at the interfacing planes. These are resolved by identifying the interfacing nodes of the adjacent blocks as ‘unmatched’ and thereby allow the solver to adopt appropriate methodology for data transfer between the adjacent blocks. Also suitable regions are identified as ’patches’ in order to define the boundary conditions. The type of grid adopted for this geometry is ‘two-way bias’. In this approach, the grid density increases from the central region towards the walls. The

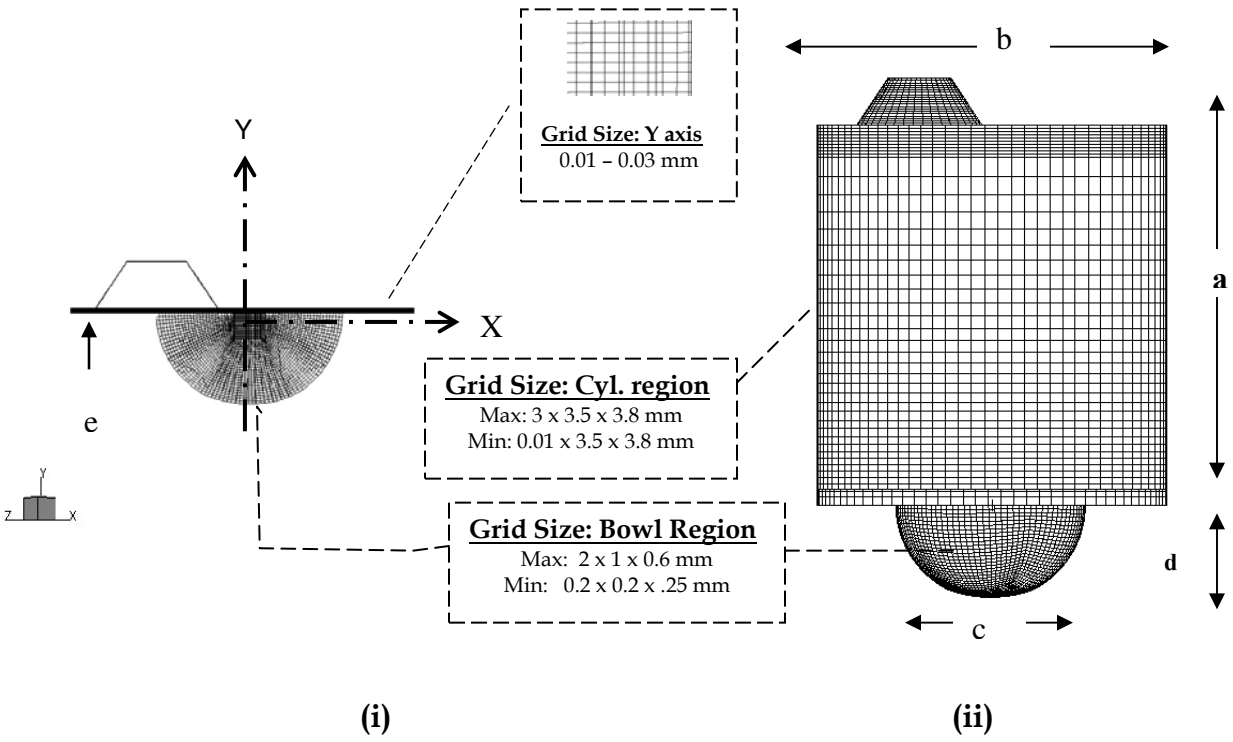

Fig. 6.1 Grid Distribution (i) with the Intake Valve Fully Closed and Piston at TC (ii) with Intake Valve Fully Open and Piston at BC. The Physical Dimensions of the Geometry are: a=116 mm, b=110 mm diameter, c=60 mm diameter, d=30 mm and e=1.5/5.2 mm for CR=17.0/11.5 Respectively.

grid distribution with the piston at extreme positions is shown in Fig. 6.1. When the piston is at BC, the minimum and maximum grid sizes are 0.01 mm and 3.0 mm in the axial direction and 3.5 mm in the radial direction and azimuthal spacing about 4.0 degree.

Similarly, when the piston is at TC, the change in the grid size occurs only in the axial direction and corresponds to a minimum and maximum of 0.01 mm and 0.03 mm respectively. This grid pattern corresponds to a mesh density of 0.2 million computational nodes. The geometry is created with the piston at TC and the intake valve fully closed as shown in Fig. 6.1 (i). Further, the intake and the piston move in accordance to the engine cycle operation to simulate different processes.

6.2.2 Boundary and Initial Conditions

The flow domain considered for simulation is downstream of the engine intake manifold. Therefore, flow through intake manifold is not modelled. However, the transient flow condition in the intake manifold is accounted by introducing time-varying boundary condition (pressure) at the intake valve. The manifold pressure profile is generated from the actual pressure measurements on the experimental engine (SPE). These are obtained using a strain gauge transducer mounted on the intake manifold, very close (upstream) to the intake valve of the cylinder, with the engine operating at rated speed (1500 rev/min). Similarly, intake valve

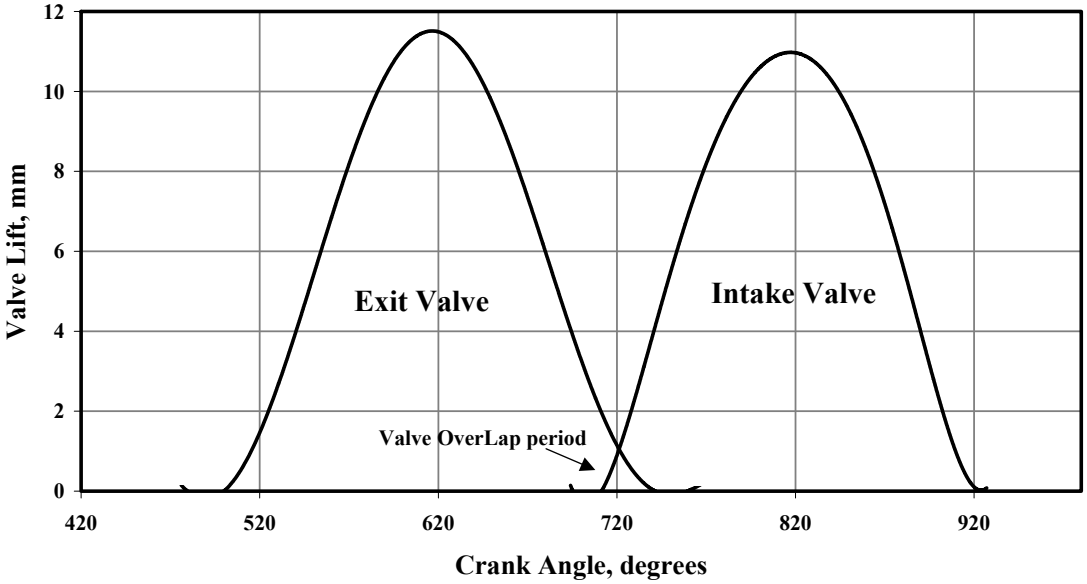

Fig. 6.2 Valve- Lift Profile of the Engine (SPE)

movement is simulated using the actual valve lift profile of the engine as shown in Fig. 6.2. In the computations, a minor change in the intake valve opening timing is introduced in order to simply the grid movement. The intake valve opens at TC instead of actually opening a few degrees (26° CA) earlier. Similarly, the closure of the exhaust port occurs at TC. The valve overlap period is thus not simulated and it is anticipated not to effect the predictions since the simulation does not involve combustion. The complete closure of the intake valve is simulated by making the grid size at the valve region to low value (< 0.25 mm) and imposing wall condition subsequently.

The computations commence with the induction process in which a set of initial conditions is assumed for the first cycle. Initial conditions for some of the variables are obtained from motored 0-D results, namely, initial pressure and temperature. The initial conditions correspond to a pressure of 920 kpa (corresponding to atmospheric pressure at Bangalore) and a temperature of 300 K for the working fluid (air). However suitable assumptions are made of the remaining variables. The three components of velocity are taken as 0.001 m/s; similarly, initial low values for turbulence kinetic energy and dissipation rate are assumed at 0.001 m^2/s^2 and 0.001 m^2/s^3 respectively. A constant wall temperature of 450 K is considered through out the simulation. The working fluid is treated as a single gas since combustion is not considered. These computations are repeated over two complete cycles in order to obtain results independent of the initial conditions.

6.2.3 Aspects of Modelling

The CFD code solves the 3-D, ensemble-averaged Navier-Stokes and enthalpy equations governing turbulent and compressible gas flow along with heat transfer for the geometry described above. To simulate the turbulence parameters, standard $k-\varepsilon$ model has been chosen without and with compressibility effects due to velocity dilatation. The working fluid is treated

as a single gas since combustion is not simulated. The algorithm employed for spatial and temporal discretisation are 1st order accurate hybrid and backward difference schemes respectively. The governing equation set includes the continuity equation, three momentum equations, the enthalpy equation and two turbulence equations.

For flow calculations with a moving grid, the transport equations are suitably modified [Hawkins et al, 1991]. There are two main changes: the transient term allows for the change in volume and the advection terms include the grid velocity. The complete sets of equations are as follows:

$$\frac{1}{\sqrt{g}}\frac{\partial\sqrt{g}\,\rho}{\partial t}+\nabla.(\rho(U-\frac{\partial x}{\partial t}))=0 \qquad \text{- (6.1)}$$

$$\frac{1}{\sqrt{g}}\frac{\partial\sqrt{g}\,\rho U}{\partial t}+\nabla.(\rho(U-\frac{\partial x}{\partial t})\otimes U)=B+\nabla.\sigma \qquad \text{- (6.2)}$$

$$\frac{1}{\sqrt{g}}\frac{\partial\sqrt{g}\,\rho H}{\partial t}+\nabla.(\rho(U-\frac{\partial x}{\partial t})H)-\nabla.(\lambda\nabla T)=\frac{\partial p}{\partial t}-\nabla\rho.\frac{\partial x}{\partial t} \qquad \text{- (6.3)}$$

where, g accounts for the expansion and compression of the grid, x is the grid position, U is the velocity, H is the total enthalpy, B is the body force, λ is the thermal conductivity and σ the stress tensor. Similar transformation is applied for the turbulent transport equations. The transport equations for turbulence kinetic energy, k and turbulence dissipation rate, ε are as follows:

The equation for k is given by

$$\frac{\partial\rho k}{\partial t}+\nabla.(\rho Uk)-\nabla.((\mu+\frac{\mu_T}{\sigma_k})\nabla k)=P-\rho\varepsilon \qquad \text{- (6.4)}$$

Where, P is the shear production defined as,

$$P=\mu_{eff}\nabla U.(\nabla U+(\nabla U)^T)-\frac{2}{3}\nabla.U(\mu_{eff}\nabla.U+\rho k) \qquad \text{- (6.5)}$$

The equation for ε without compressibility effect is given by

$$\frac{\partial\rho\varepsilon}{\partial t}+\nabla.(\rho U\varepsilon)-\nabla.((\mu+\frac{\mu_T}{\sigma_\varepsilon})\nabla\varepsilon)=C_1\frac{\varepsilon}{k}P-C_2\rho\frac{\varepsilon^2}{k} \qquad \text{- (6.6)}$$

The equation for ε with compressibility effect is given by

$$\frac{\partial\rho\varepsilon}{\partial t}+\nabla.(\rho U\varepsilon)-\nabla.((\mu+\frac{\mu_T}{\sigma_\varepsilon})\nabla\varepsilon)=C_1\frac{\varepsilon}{k}P-C_2\rho\frac{\varepsilon^2}{k}+C_3\rho\varepsilon\nabla.U \qquad \text{- (6.7)}$$

where, μ is molecular viscosity, μ_T the turbulence viscosity and σ the Prandtl number. The values of constants are $C_1 = 1.44$, $C_2 = 1.92$, $C_3 = -0.373$. The constants C_1 and C_2 are the standard constants used in $k-\varepsilon$ model. The value considered for C_3 is same as that of Jennings [1992].

Since the flow is considered compressible, the equation of state is the ideal gas law given by

$$P = \rho RT \qquad \text{- (6.8)}$$

6.3 Numerical Scheme

The numerical scheme of CFX solver is based on finite volume technique, and involves the following steps

- Integration of the governing equations of fluid flow over all the control volumes of the solution domain.

- Discretisation involves substitution of the terms in the integrated equation representing flow processes such as convection, diffusion and sources with finite-difference type approximation and thereby converting into algebraic equations. In the present modelling, the algorithm employed for spatial discretisation is hybrid scheme and is 1st order accurate. Similarly, a 1st order accurate backward difference scheme is employed for temporal discretisation.

- Solution of the algebraic equations is obtained by an iterative method.

6.4 Computational Procedure

Computations have been made for an operational speed of 1500 rev/min, with time step of the order of 0.5° CA (50 micro seconds). The calculations commence with the piston at TC, with the intake valve and exhaust port closed. Using the initial and boundary conditions as mentioned earlier, the computation proceeds with the piston descending downwards and the intake valve beginning to open so as to allow fluid to enter the flow domain i.e. cylinder. The closure of the intake valve (the passage between the valve and cylinder head is reduced to less than 0.25 mm) takes place in accordance with the actual valve timing of the engine. The intake valve closes at 64° ABC (After Bottom Centre), at which time the boundary condition at the intake valve is changed from 'pressure' to 'wall' to prevent fluid escaping from the cylinder. The valve closure is halted with a cell size of less than 0.25 mm to prevent collapse of the grid. In this transitional period a lower time-step of the order of 0.01° CA (1 micro second) is adopted to so as to prevent divergence in the solution. Further upward movement of the piston results in compression of the fluid till the piston reaches TC, beyond which fluid expansion occurs. The exhaust port opens at 38° BBC (Before Bottom Centre) by introducing a pressure boundary condition at the exhaust port. The exhaust process continues till the piston reaches TC, which completes one cycle of operation. Using the results of the first cycle as the initial condition, the second cycle is computed. This procedure is repeated to simulate operations at two CRs namely,

17 and 11.5. On the flat piston geometry computations are attempted at CR = 17. Calculations are done with a grid density of 0.2 million cells. For a time step of 0.5° CA, the number of iterations employed to get converged solution is about 70. The time step independence of the calculations has been verified (shown in Fig. 6.4 – 6.6). The principal results extracted from these calculations are velocities at the intended location of spark plug and turbulence parameters namely, turbulence intensity, u' and integral length scale, l_I.

6.5 CFD Results

It is clear from the current experimental investigations that optimum ignition timing for producer gas fuel is close to TC. At this particular setting, the major part of the combustion occurs during reverse squish regime, it was thought prudent to focus the CFD results in the later part of the compression (around the time of piston approaching TC) and early part of expansion process (retreating from TC). Heywood [1988] indicates to the induction system and the piston geometry having significant effect on the in-cylinder flow characteristics. The initial in-cylinder flow pattern set up during the induction process is observed to modify in the subsequent process in a few geometries, as also observed in the present study. In this section, schematic diagram derived from the velocity profile across selected plane is discussed. Further, two-dimensional velocity vectors and contour plot of scalar variable at time intervals close to TC are presented. The flow field related to bowl-in piston geometry is mainly discussed, and at important juncture, the result of flat piston geometry is brought out in order to highlight the features of geometry under investigation. Turbulence intensity is calculated using the correlation – Turbulence kinetic energy = $3/2\ u'^2$.

6.5.1 Velocity Distribution

The flow during the induction is observed to be transient, highly turbulent and fluctuating. The evolving flow pattern as a function of time is schematically shown in Fig. 6.3, these are derived from the velocity profiles across the axial plane passing through the centre of the geometry, the schematic shown in the circumferential plane is in below the cylinder head (1.2 mm), in the plane of intake valve opening. The flow field is observed to be as follows. During the initial stages of suction process, there are two major rotating flow patterns established in the cylinder as a consequence intake jet interacting with the walls of the cylinder. One flow pattern is termed as swirl (rotating mass about the cylinder axis) and occurs as the flow is discharged tangentially towards the cylinder wall, where it is deflected sideways and downward in a swirling motion. The other flow pattern occupying major part of the domain is observed in the transverse direction and is termed as tumble (rotating mass normal to the cylinder axis). Apart from these, there are recirculating flows in local regions in the vicinity of cylinder head/bore interface and these occur due to flow separation. These are evident from Fig 6.3 (at 30° CA) that shows the separation of the jet at the intake port and setting up of strong re-circulating pattern at the corner of the geometry and also the commencement of tumbling flow vortices. The tumble flow is constituted by two-barrel type vortices, which are observed to be asymmetric against symmetric vortices observed by Ekchian et al [1979] in water-analogy experiments.

Fig. 6.3 Schematic Diagram of the Evolving Fluid Flow during Intake, Compression and Early Part of Expansion in a Bowl-In Piston Engine Geometry. The Central Figure Shows the Tangential Velocity Plot in the Circumferential Plane, 1.2 mm below the Intake Valve. The Axial View Corresponds to the Velocities along Section –DD. 'S' denotes Separation Zone and 'T' denotes Tumbling Vortices. 360° CA Corresponds to TC and 250° CA Flow After Intake Valve Closure.

This difference in the flow pattern is due to off-axis valve location in the current case against axisymmetric in-flow with Ekchian et al [1979]. The flow pattern in the case of off-axis valve is much more complex even though a similar structure is observed and this is due to uneven flow distribution over the intake port cross section.

The flow pattern at 60° CA corresponds to the piston approaching the maximum instantaneous speed. There are two vortices visible with different centres of rotation. The vortex away from the wall (right side) is rotating in the clockwise direction, with the center of rotation close to the top of piston. The second vortex is close to the wall (left side) and rotating in the counter-clockwise direction, with the center of rotation at a higher plane beneath the intake port. In addition, there is distinct flow pattern visible in the bowl region. These vortices are continually convected with the fluid as evident from the location of centre of rotation of the left vortex corresponding to a piston position at 120° CA. It is also evident that the sense of rotation of the right side vortex is reversed and is same as the left side vortex. These vortices further disintegrate and merge into a single vortex by the time the piston reaches the bottom centre (BC) – 180° CA. Further, during ascendance of the piston in the compression process, single vortex in the cylindrical region is visible after the closure of the intake valve corresponding to 250° CA. The intensity of the swirling and the tumbling motion are normally quantified in terms of swirl and tumble ratio. These are defined as follows:

$$\text{Swirl ratio} = 60\,H_y \big/ 2\pi M_y\, N \quad \text{and Tumble ratio} = 60\,H_{x,z} \big/ 2\pi M_{x,z}\, N$$

Where $H_{x,,\,y,\,,z}$ and $M_{\,x,,\,y,\,,z}$ is the angular momentum and moment of inertia about x, y, z axis respectively and N is the speed of the engine in rev/min. These ratios change with the evolving flow pattern and are shown in Table 6.2 at particular crank angles. Tumble ratio is specified in x and z planes about the instantaneous fluid center of rotation where as swirl ratio is computed about the y-axis of the geometry or bowl axis. The swirl ratio is quantified at regular time intervals, however the tumble ratio is quantified in the event of single tumble present in the flow domain and this only occurs in the last stages of intake and early part of compression process.

Table 6.2: Computed Parameters at Specific Crank Angles

° CA	Swirl Ratio* (Y-axis)	Swirl Ratio+ (Bowl-axis)	Tumble Ratio (X-axis)	Tumble Ratio (Z-axis)
180	1.00	1.60	1.35	1.35
250	0.85	1.41	1.50	1.50
270	0.90	1.45	1.40	1.40
300	0.82	1.63	1.20	1.20
330	0.50	1.10	NC	NC
360	0.30	0.40	NC	NC

* Complete Domain, + Bowl Region, NC: Not Calculated – Regime of Two Tumble

As the piston ascends upwards during the compression process, the fluid from the cylindrical region is pushed into the bowl region thereby increasing the angular velocity of the fluid in the bowl. The fluid flow pattern till the commencement of later part of compression process is found to be same for both CRs. However, as the piston approaches TC (> 330° CA), the squish effects fluid movement into the bowl and the squish velocities are found to be vastly different with either CRs. Due to the squish effect (becomes dominant); the fluid in the cylindrical portion is pushed into the bowl leading to formation of two vortices in the bowl. The peak squish effect is observed to occur around 350° CA, shown in Fig. 6.4, where in the local velocities are as high as 20 m/s around the edge of the bowl corresponding to CR=17. There is a slight asymmetry in the velocity distribution probably due to eccentricity of the bowl. The velocity vector plot in the axial plane at the same crank angle shows the evolution of counter rotating toroidal vortices. At TC (360° CA) the counter-rotating vortices continue to survive and get displaced downwards in the bowl. These results are qualitatively compared with some of the experimental observations of Arcoumanis et al [1983]. These researchers have experimentally measured the mean and turbulence velocities on an axi-symmetric engine of CR = 6.7 at a speed of 200 rev/min using three piston geometries, which include the bowl-in piston geometry under motoring conditions.

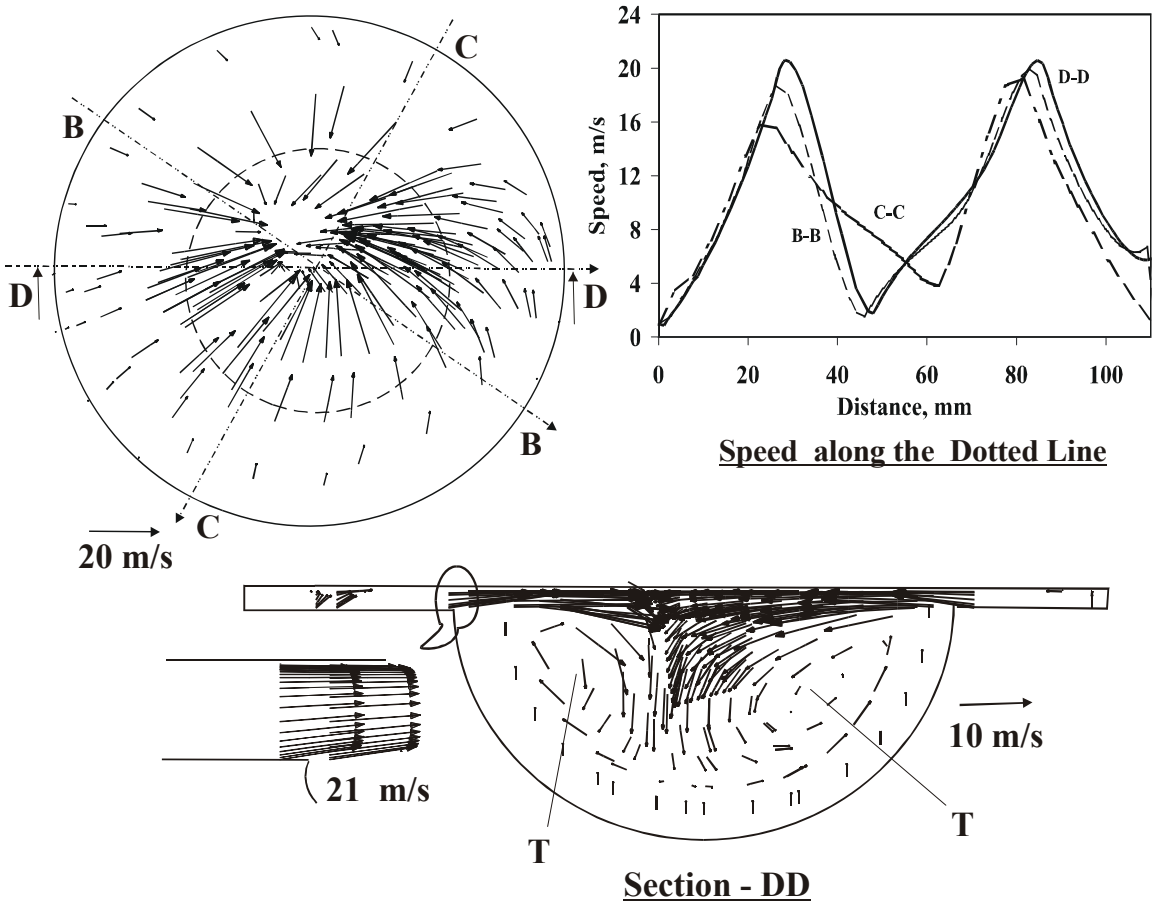

Fig. 6.4 Vector Plot in the Axial Plane (Section –DD) during Squish Period Corresponding to 350° CA – CR=17.0. Vector Plot in the Circumferential Plane is at a Distance of 1.2 mm below Cylinder Head, the Dotted Circle in Circumferential View Represents the Edge of the Bowl.

Measurements are reported to have been done in the presence and absence of swirl so as to access its influence on the mean and turbulence velocities. The results from the Arcoumanis et al [1983] are compared with the CFD results in Fig. 6.5. The predicted flow field pattern compares favourably (in the sense of vortex rotation) with the experimental results observed in the absence of intake swirl. However, CFD result shows the existence of swirl during intake (peak swirl ratio ~ 2.1 @ 50° CA) process. Further comparison with the experimental flow field in the presence of intake swirl (opposite sense of rotation of vortex, shown as Fig 6.5v) would not appropriate because the mean piston speed in either case is widely different (experiments is 0.63 m/s against 5.8 m/s in CFD) and with squish velocity being linearly dependent on piston speed [Heywood, 1988], it is conjectured that the behaviour would be vastly different in either case.

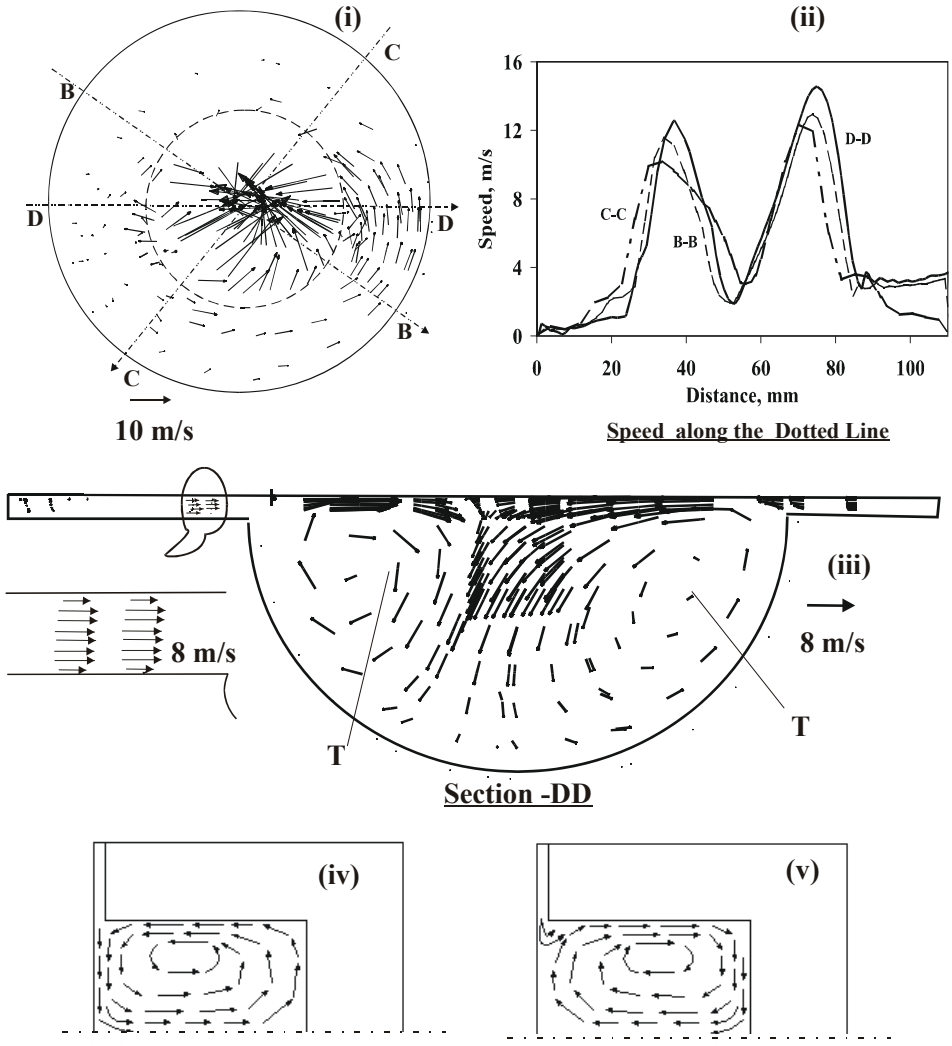

Fig. 6.5 (i) Vector Plot in the Circumferential Plane is at a Distance of 1.2 mm below the Cylinder Head corresponding to 360° CA (TC) –CR=17.0, (ii) Speed along the Dotted Line, (iii) Velocity in the Axial Plane – Section DD, (iv) and (v) Experimental Results about the Symmetry Plane from Arcoumanis et al [1983] at 360° CA (TC) in the Absence and Presence of Intake Swirl Respectively. Dotted Circle Represents the Edge of the Bowl.

The swirl ratio at the end of the compression process is quantified as 0.3; this reduction in swirl could be due to interaction of swirl with the squish. Further, as the piston descends downwards from TC the effect of reverse squish sets in where the fluid begins to flow out of the bowl into the cylindrical region and in the process the counter-rotating vortices are displaced upwards. Here, it is necessary to emphasize that reverse squish effect is vastly different with either CRs and these are brought out later in this section. The fluid movement further intensifies with the piston descending downwards as shown in Fig. 6.6, maximum reverse squish effect becomes evident at about 370-372° CA, where in the velocities are as high as 31 m/s with asymmetry in velocity distribution.

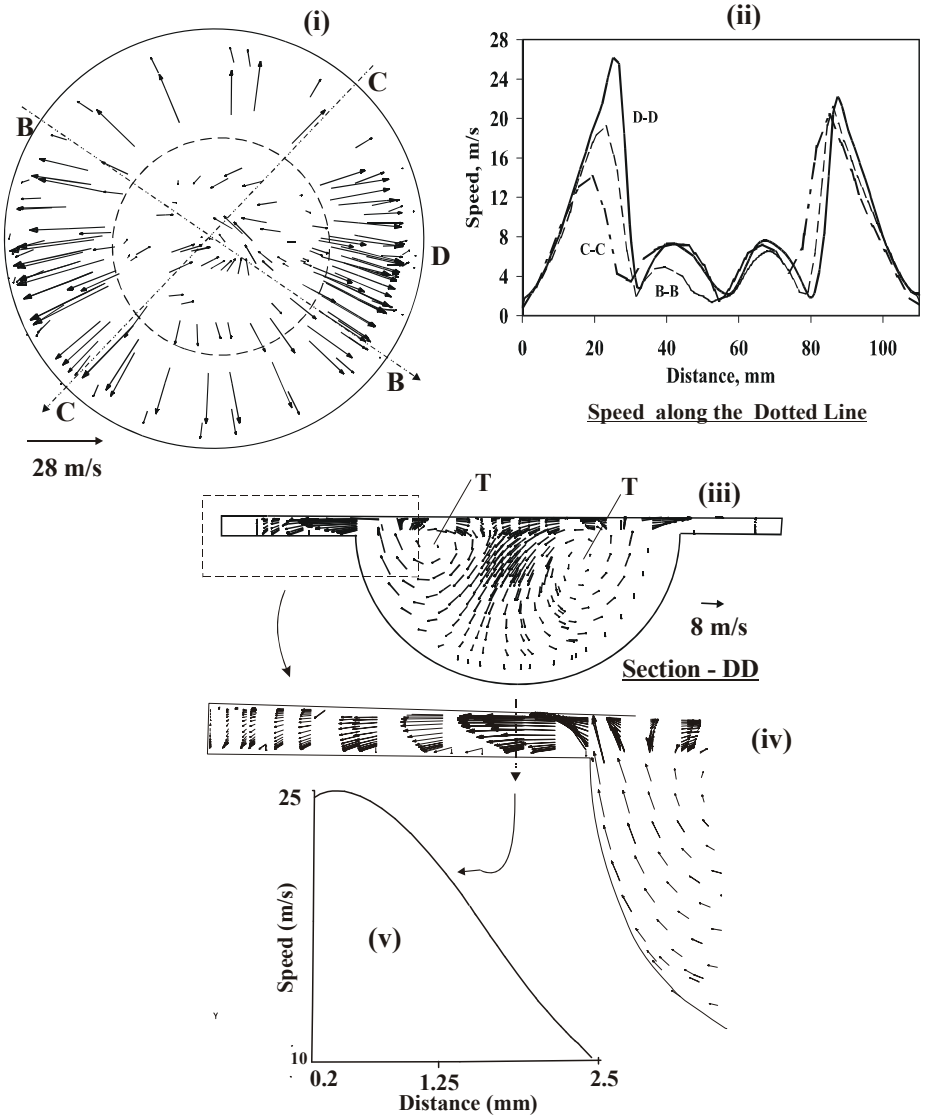

Fig. 6.6 (i) Vector Plot in the Circumferential Plane at a Distance of 1.2 mm below the Cylinder Head corresponding to 370° CA – CR=17.0, (ii) Speed along the Dotted Line, (iii) Velocity in the Axial Plane – Section DD, (iv) Enlarged View of the Velocity Plot Near the Edge of the Bowl and (V) Speed in the Axial Direction – along the Dotted Line Shown in (iv). Dotted Circle Represents the Edge of the Bowl.

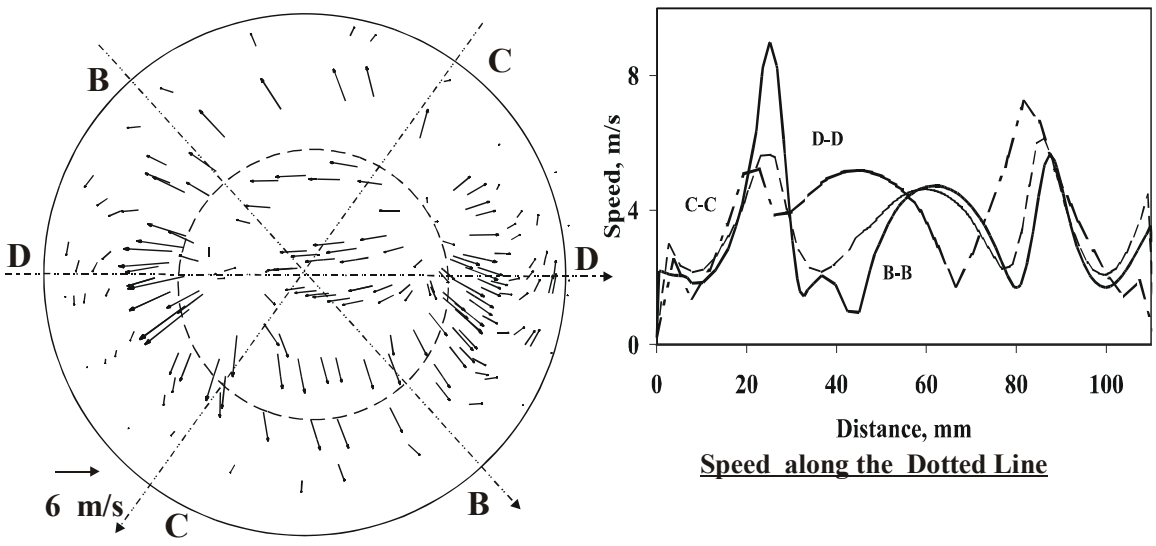

Fig. 6.7 Vector Plot in the Circumferential Plane at a Distance of 1.2 mm below the Cylinder Head corresponding to 370° CA - CR=11.5. Dotted Circle Represents the Edge of the Bowl.

At CR = 11.5, the observed flow field is similar to that at 17.0 CR However, the squish and reverse squish velocities are lower corresponding to CR=17.0. The peak squish velocities are in the range of 8 m/s at 350° CA. Similarly the fluid movement out of the bowl during the reverse squish period is not intense and maximum velocity at the edge of the bowl is of the order of 5 - 6 m/s with asymmetry in distribution as evident from Fig. 6.7.

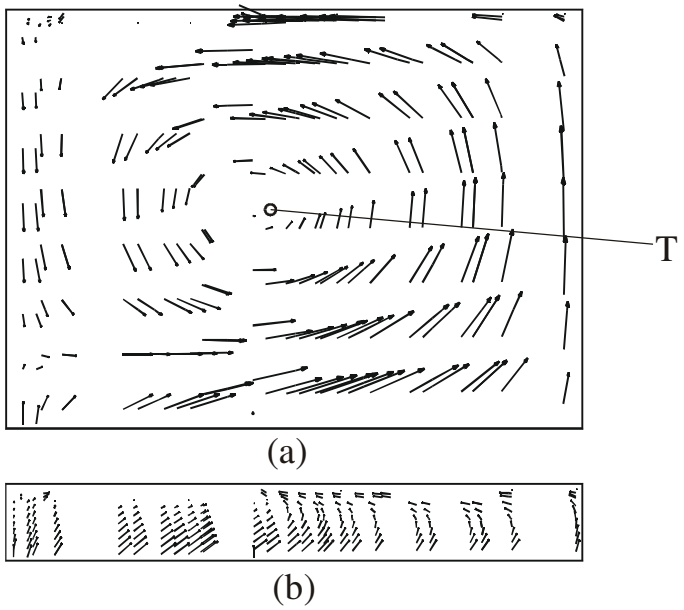

Fig. 6.8 Vector Plot in the Axial Plane with Flat Piston Geometry (CR=17.0) (a) 250° CA, (b) 330° CA

With regard to the flat piston geometry, the fluid flow indicates the presence of single vortex as shown in Fig. 6.8 (a) at the completion of valve closure with swirl and tumble ratio being 0.85 and 1.3 respectively, comparing closely with the bowl geometry. However, in the later part of the compression process there is no evidence of tumbling flow as shown in Fig. 6.8 (b). The resultant flow field close to TC has an influence on the turbulence intensity that is discussed subsequently.

Summarizing the flow field results, the jet-like character of the intake flow interacting with the cylinder walls and the moving piston, creates large scale rotating flow pattern within the cylinder. The flow field is observed to undergo large-scale changes during intake and subsequently in the compression process. Between the two CRs with bowl-in piston geometry, it is observed that there is no distinct change in the fluid flow pattern in the intake and early part of the compression process. However, in the last stages of compression and early part of expansion, the fluid velocities near the edge of the bowl are largely different, the high CR creating large shear zones near to the edge of the bowl.

Between the flat head and bowl-in-piston geometries, the swirl and tumble ratio are about the same during intake process. During compression the swirl ratio is found to be higher in the bowl region due to increase in the angular velocity of the fluid. However, there is one distinct difference observed between the two geometries, in the case of bowl-in piston geometries there is evidence of formation of two tumbling vortices and these survive till TC. In the flat piston geometry, there is evidence of a single tumbling vortex during early part of the compression and is dissipated much earlier to the completion of compression process. The effect of these flow pattern on the turbulence generation is discussed subsequently.

6.5.2 Turbulence Distribution

The variation in turbulence intensity (u') and integral length scale (l_I) is firstly discussed. Further insight is provided by examining the spatial distribution of turbulence kinetic energy in and around TC, which is relevant from the combustion viewpoint. Figure 6.9 shows the CFD results of u' values for the bowl-in piston geometry in the diametric plane (4 mm below the cylinder head). The computed results are shown with and without the compressibility effects in the ε - equation. Examination of the computed results reveals large variation in u' right through the induction and compression process. Initial high turbulence is set in due to shear in the high velocity jet entering the cylinder. The turbulence fluctuation, u' goes to as high as 22 m/s and this approximately coincides with the point of maximum piston speed and the valve lift, further to which there is fall in turbulence intensity with commencement of intake valve closure. The turbulence fluctuation, u' again increases post beyond intake valve closure due to increased fluid movement and peaks at about 30° CA prior to TC, subsequent to which there is decline. These results are comparable with and without accounting for the compressibility effect in the ε- equation.

Further, the results are compared with the experimental results of Catania et al [1996] as shown in Fig. 6.9. These experiments are conducted on a production diesel engine of CR = 18.0, with slightly re-entrant bowl-in piston geometry using hot-wire anemometer at varying speed ranging between 600-3000 rev/min. The comparison is made considering the results at two

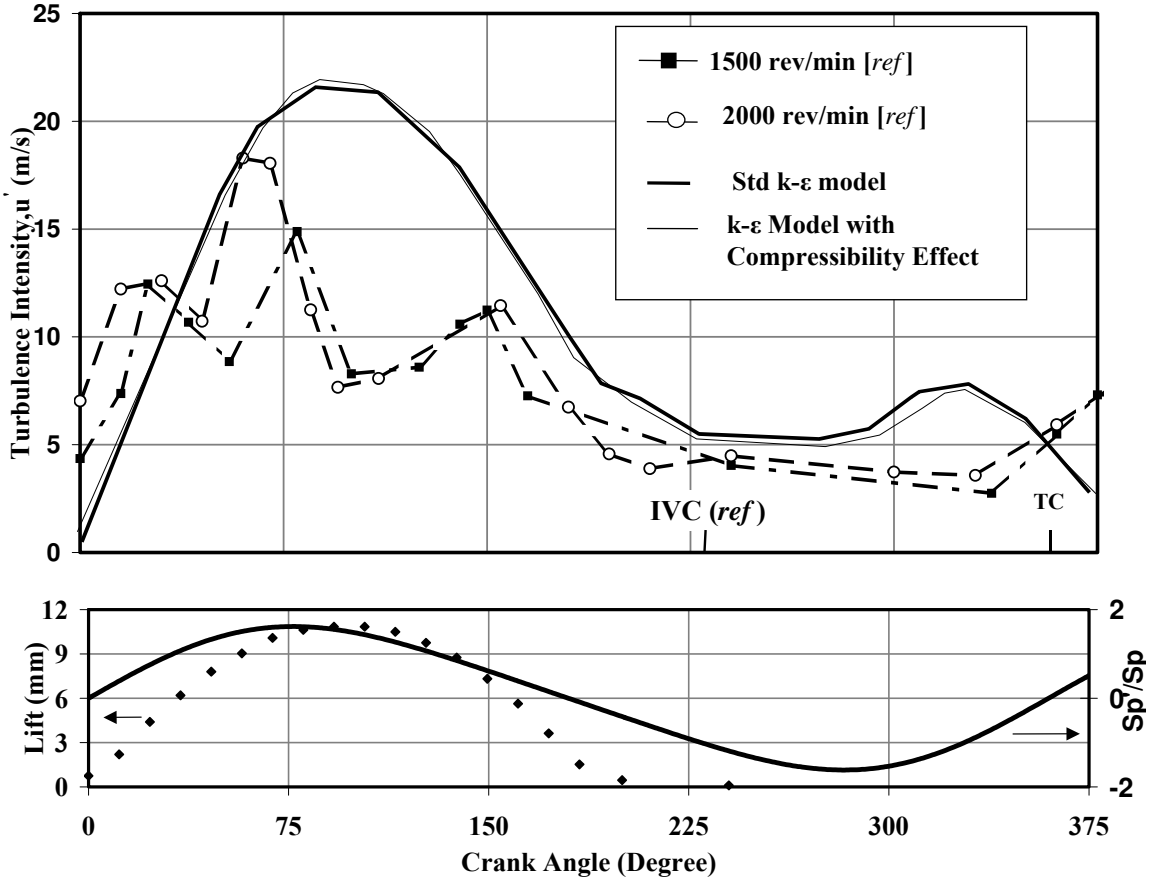

Fig. 6.9 Top Plot is the CFD Result Using k-ε Model (with and without Compressibility Effect) as a Function of Crank Angle. *ref* is the Experimental Result of Catania et al [1996] on a Similar Configuration Engine. The Bottom Plot (solid line) Shows the Variation of Instantaneous Piston Speed Normalized with the Mean Piston Speed (5.8 m/s) – for the CFD Geometry and Corresponding to 2000 rev/min of *ref*. The Dotted Line is the Intake Valve Lift Profile of the CFD Geometry. Maximum Intake Valve Lift for *ref* is 8.1 mm.

engine speeds, namely 1500 and 2000 rev/min, which correspond to two mean piston speeds of 4.3 and 5.8 m/s. The comparison of the u' between the two results appears fair (considering the fact that the geometries are similar, but not identical) till about inlet valve closure. In this time period, the location of the peak value is different by about 30 to 40° CA and this is attributed to differences in intake valve timing/valve lift profile. Beyond the intake valve closure one finds opposing trends in the variation of u' with CA. As the piston starts compressing the fluid, there is an increase in u' and peaks at 30° BTC beyond which there is a decline in u' against continuous decline in the measured values. In the post - TC region, there is again a contradictory trend in comparison to experimental results. This feature is unaltered even when compressibility effect is accounted by choosing a constant of -0.373 [Jennings, 1992] for the velocity dilatation term in the ε-equation. In the work of Han et al [1995], using RNG $k-\varepsilon$ model on Mexican hat piston top where the effect of velocity dilatation and kinematic viscosity are accounted in the ε equation, similar qualitative behaviour of u' declining in the post-TC period as noted here has been observed. Similarly, other experimental studies in the

literature suggest the trend of increase in u' for certain bowl-in piston geometries, namely the re-entrant configuration compared to simpler cylindrical configuration in the post-TC period [Corcione et al, 1994] and this is inferred as due to higher shear zones with re-entrant geometries.

Next the mass-averaged u' and l_I as a function of CR are shown in Fig. 6.10, the location corresponds to mid 3-D zone in the bowl region of the geometry. It is clear from the figure that variation of u' with time is close to being independent of CR; these are consistent with the observations made by Lancaster [1976] and Ikegami et al [1987]. Similarly, the variation of l_I calculated using k and ε are also shown in Fig. 6.10, which indicates l_I to be higher at lower CR compared to higher CR and is qualitatively consistent with the experimental results of Ikegami et al [1987].

Fig. 6.11 shows the comparison of u' for both the piston geometries. The variation in u' with time is about the same until early part of the compression process. In the later part of the compression process, it is evident that decline in u' is faster in the case of the flat geometry. This declining behaviour could be due to following reasons (i) absence of squish generating mechanism with flat geometry (ii) absence of tumbling vortices in the later part of compression process. The absence of turbulence generating mechanism like squish in the case of flat geometry is evident. However, it is important to recognize the role of the tumbling vortices taking note of the literature. Floch et al [1995] have studied

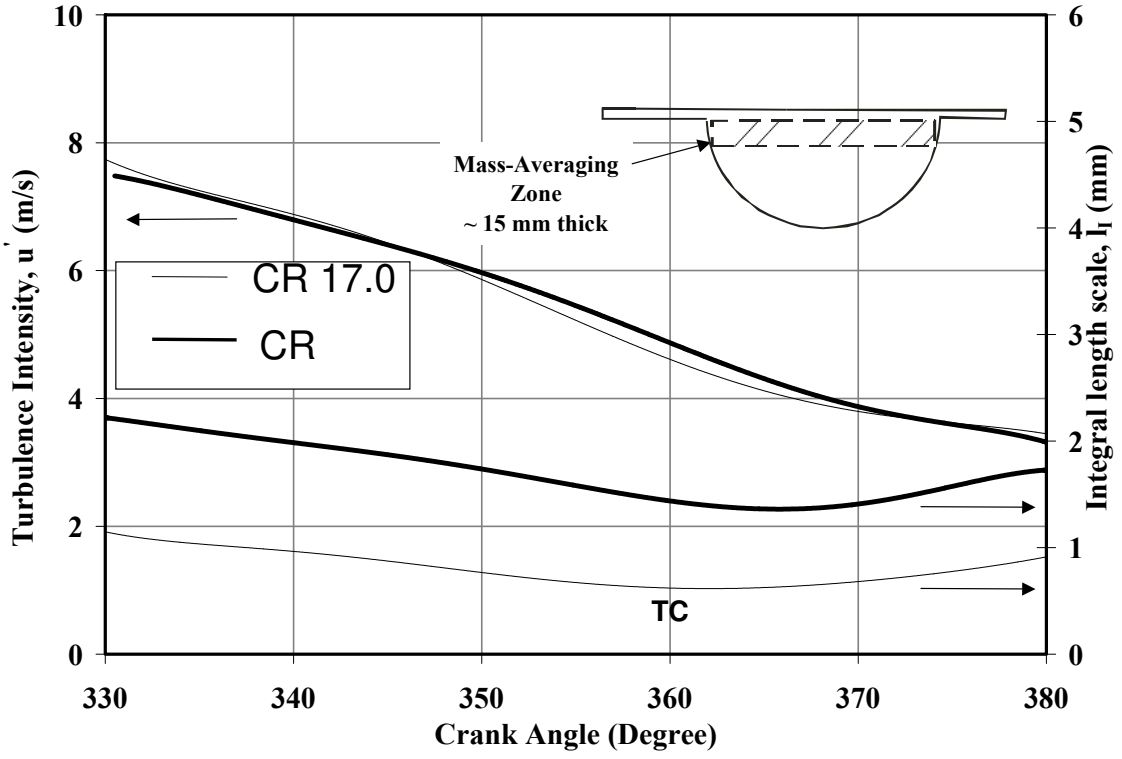

Fig. 6.10 Variation of Mass Averaged u' and l_I across a 3D Zone Shown in the Inset at Varying CRs.

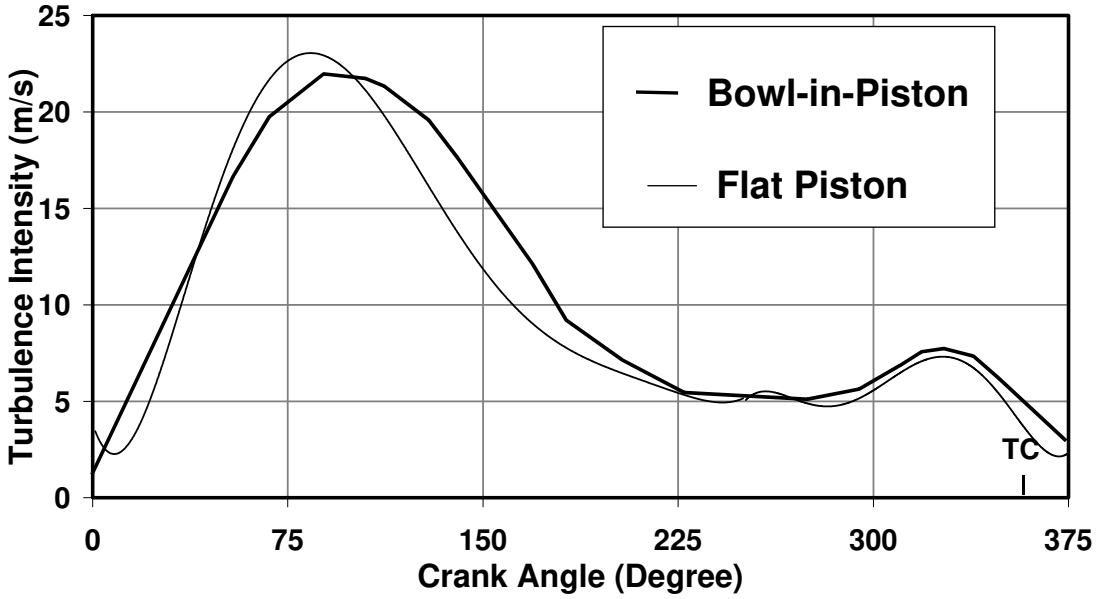

Fig. 6.11 Comparison of u' for the Two Piston Geometries – 4 mm below Cylinder Head.

the influence of swirl and tumble on the turbulence intensity and combustion in a SI engine. Their study indicates the breakdown of the tumbling vortices (prior to TC) to be responsible for enhancement of turbulence along with decline in the tangential velocities. It is conjectured that tumble contributes to higher turbulence due to the dissociation of the main vortex into turbulence as a result of piston movement. It is further observed that in the case of swirl, the rotating motion is conserved during compression process thereby contributing to turbulence generation to a lesser extent (due to lesser swirl dissociation). Similarly Urushihara et al [1995] observe that tumble flow generates turbulence in combustion chamber more effectively than swirl flow does, and that swirling motion reduces the cycle-by-cycle variation of mean velocity which tends to be generated by the tumbling motion. In the current study, there is evidence of tumble vortex breakdown with flat piston geometry much earlier to TC, this apart from the absence of squish appears to be responsible for the faster decline in u'.

Next, the spatial distribution of turbulence kinetic energy (TKE) at crank angles close to TC and for both CR and for the flat piston geometry is shown in Fig. 6.12. The contour plots in the axial plane reveal spatial variation in TKE and this is consistent with the experimental observations of Schapertons et al [1986]. A general observation at all time steps indicates the TKE to be of high intensity in the central region of the bowl decreasing towards the walls. Another revealing information from the contour plot is the shifting in the distribution of TKE with time and this is caused due to changes in the flow pattern occurring in the bowl region due to squish and reverse squish effects. It is also observed that the TKE is marginally lower (5%) at higher CR probably due to enhanced dissipation of kinetic energy on account of increased fluid movement during squish and reverse squish period. Lastly, the comparison of TKE of the two-piston geometries reveals substantial enhanced TKE for bowl-in piston geometry compared to the flat piston. In case of flat geometry, the turbulence kinetic energy is more or less uniform through out the combustion chamber.

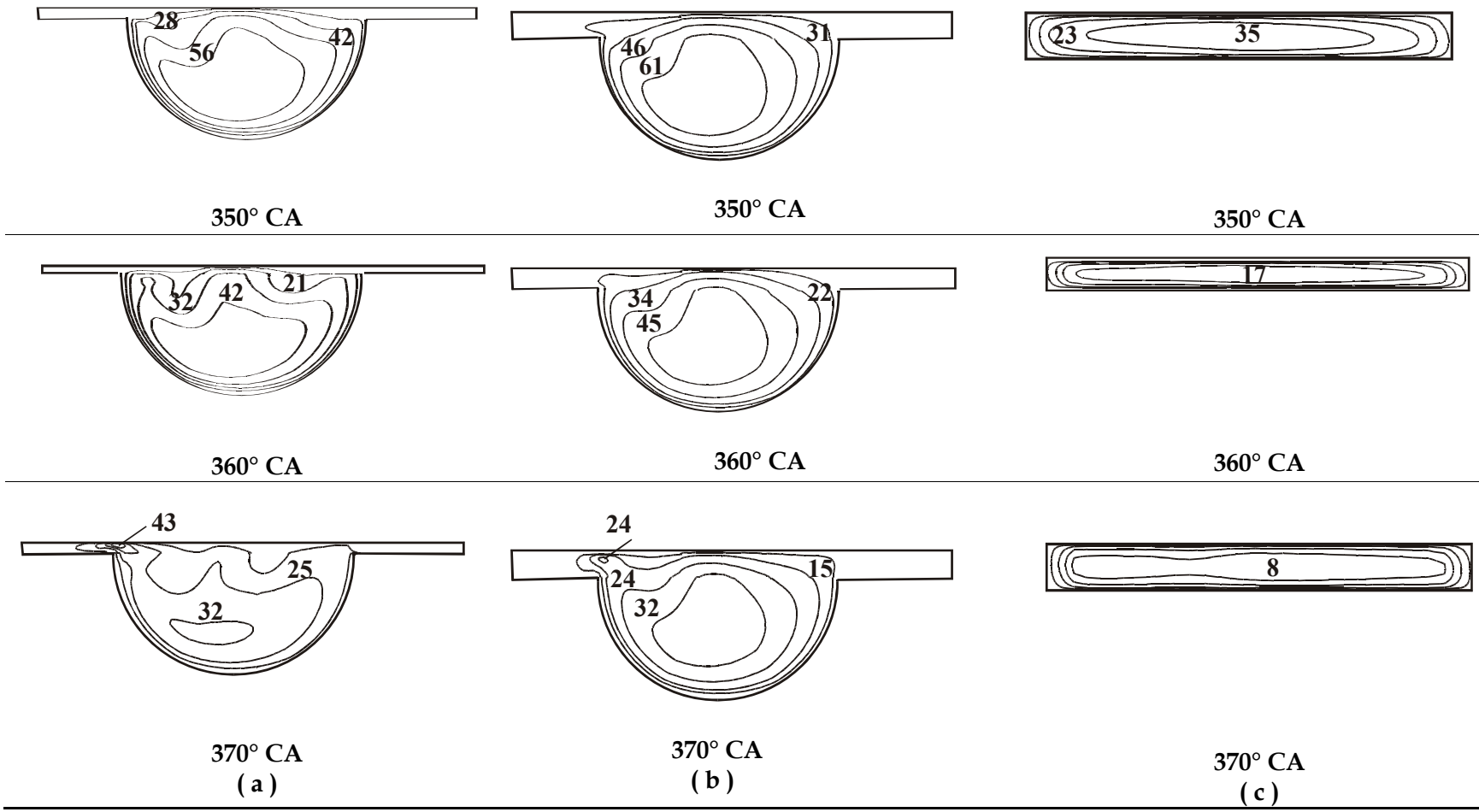

Fig. 6.12 CFD results: Contour Plot of Turbulence Kinetic Energy (m^2/s^2) on an Axial Plane Through the Centre of the Geometry (a) Bowl Geometry – CR = 17.0 (b) Bowl Geometry – CR = 11.5 (c) Flat Geometry – CR = 17.

6.6 Other Inputs for the 0-D Model

Other than the turbulence parameters, the velocity (normal component) in the region of the ignition source (spark plug) is required in order to allow for the possible flame movement during the process of ignition delay and subsequent flame propagation. This data is extracted from the CFD data by plotting streak line. A streak line is drawn for a zero mass particle originating at a point near to the ignition source into the bowl region and it is shown in the inset of Fig. 6.12. The normal component of velocity obtained at location nearest to the streak line is considered for flame displacement/movement and is shown in Fig. 6.13 for both CRs 17.0 and 11.5. It is evident from the plot that there is flow reversal due to reverse squish effect (in the path of streak line) subsequent to TC in the case of CR=17.0 and not so with CR=11.5 (in the path of streak line) due to lower reverse squish velocities. These velocities are considered for flame displacement in the 0-D model.

Other than the turbulence parameters, the velocity in the region of the ignition source (spark plug) is required in order to consider for the possible flame movement during the process of ignition delay and subsequent flame propagation. The existence of higher squish/reverse squish velocities in the case of higher CR is evident from Fig. 6.14, which shows velocities at the edge of bowl in the time period around TC. It is not so in the case of lower CR. The CFD data is further compared with the values obtained from correlation discussed by Heywood [1988]. It must be brought out that the squish velocities obtained from the correlation are in the absence of combustion and without effects like gas inertia, friction, gas leakage past piston rings and heat transfer. The predicted velocities from CFD qualitatively match with the correlation data, with some real time effect like heat transfer included in the simulation the CFD results are considered appropriate as an input for the 0-D model.

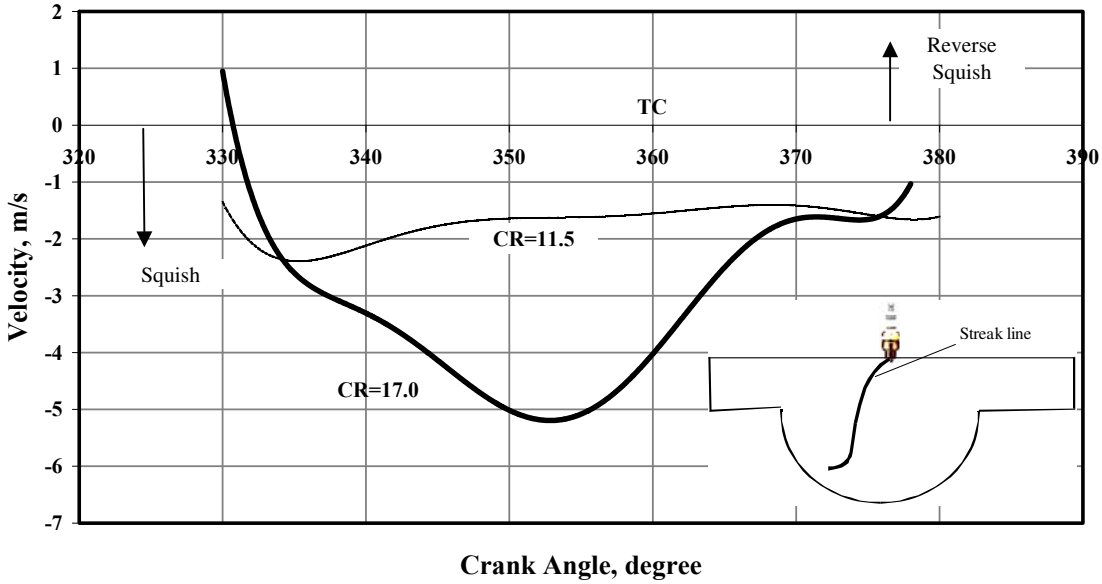

Fig. 6.13 Normal Component of Velocity along a Streak Line from the Point of Ignition at Two CRs from CFD Studies

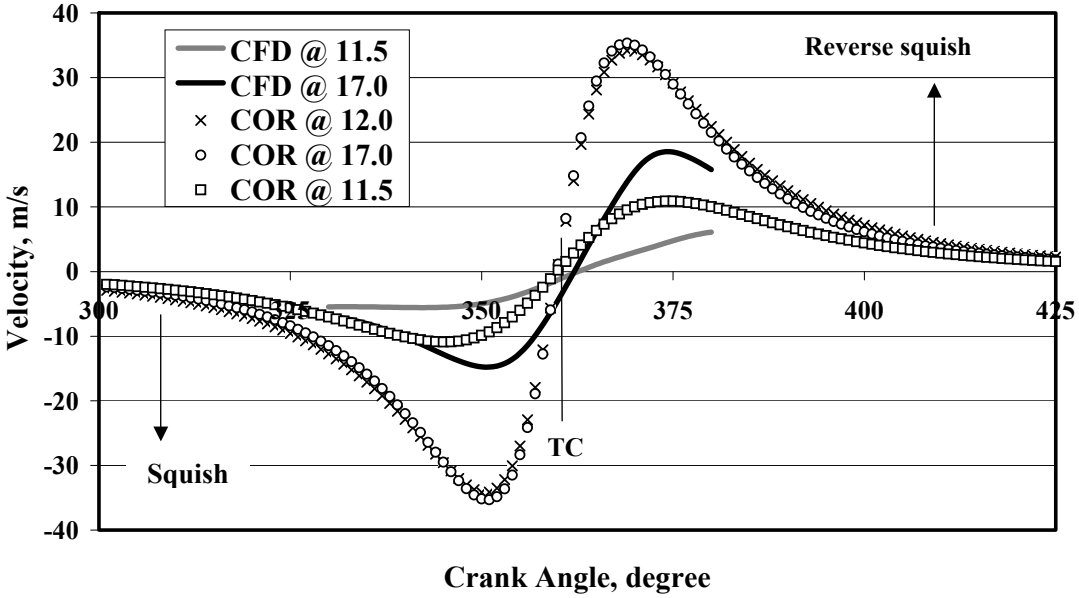

Fig. 6.14 Comparison of Squish and Reverse Squish Velocities from CFD and using an Empirical Correlation – COR [Heywood, 1988] for SPE Geometry (CR=17.0 and 11.5) and MPE Geometry (CR=12.0).

6.7 Observations

3-D computations on engine geometry are able to capture the generic features of fluid flow in a reciprocating engine and are consistent with some of the experimental observations available in the literature. The presence of high shear zones near to the edge of the bowl during squish/reverse squish is evident, more so in the case of higher CR with bowl-in piston geometry. The standard $k-\varepsilon$ model predicts trends in TKE in and around TC different from experiments and this is reasoned to be due to limitation of the $k-\varepsilon$ model to capture transient effects due to squish/reverse squish phenomenon. The difference in the fluid flow pattern compared bowl-in piston during the later part of the compression process appears to the cause for u' to be lower in the case of flat piston geometry.

6.8 Summary

Three important results have been extracted from the motored 3-D computations to be used in 0-D model to predict p-θ curves and these are (i) mass-averaged turbulence parameters, namely turbulence intensity and integral length scale, (ii) velocity (normal component) for flame kernel movement/displacement, (iii) extent of velocities near to the edge of the bowl in the reverse squish regime.

CFD Modelling

Fig. 6.14 Comparison of Squish and Reverse Squish Velocities from CFD and using an Empirical Correlation –COR [Heywood, 1988] for SPE Geometry (CR=17.0 and 11.5) and MPE Geometry (CR=12.0).

Table 6.1: CFD Studies on Engine Geometries with Different Mesh Densities
Table 6.2: Computed Parameters at Specific Crank Angles

Chapter VII

Predictions of Zero-D Model

This chapter discusses the Zero-D (0-D) predictions, where in the pressure-crank angle curves are predicted on two engine geometries at different compression ratios. Full cycle thermodynamic analysis is dealt with both engine geometries.

7.1 Introduction

The basis of this chapter is the thermodynamic model that has been described in Chapter IV. The heat release that forms the primary part of the model is based on eddy entrainment and laminar burn-up models. Two important parameters have been identified to implement this model. One of these is the laminar burning velocity at pressures and temperatures typical of unburned mixture in a reciprocating engine; this has been numerically computed as brought out in Chapter V. The other parameter set is related to turbulence characteristics and fluid velocities at the time of ignition and subsequent flame propagation. These have been quantitatively derived from the CFD analysis conducted on the SPE geometry and since the combustion chamber of MPE also involves a bowl-in-piston, the results of SPE geometry are extended to the MPE geometry for 0-D predictions. Using these data, the heat release part of the engine cyclic process is predicted, prior to which the initial thermodynamic conditions are established using the gas exchange sub-model. For the heat release sub-model, the details of the combustion chamber geometry with respect the shape and size of the bowl and the location of the spark plug are considered. 0-D predictions are attempted on the combustion chamber geometry of SPE at varying CR and ignition advance; similarly predictions are attempted at a fixed CR at two ignition settings for the MPE geometry. The energy balance results obtained from the full-thermodynamic cycle are further compared with the experimental results.

7.2 Engine Combustion Chamber Geometry

7.2.1 Small Power level Engine

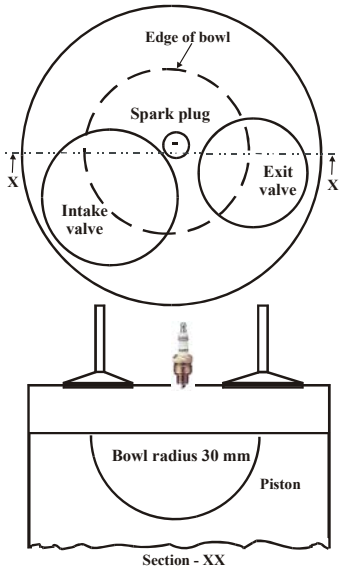

Fig. 7.1 Combustion Chamber of SPE

The combustion chamber comprises of a flat cylinder head and hemispherical shaped bowl as shown in Fig. 7.1. The bowl is eccentrically located on the piston top with a shift of about 3 mm from the axis. The bowl measures 30 mm in radius, with a volume of 55 $\pm$ 1 cc. The flat portion of the piston top provides a squish ratio of 0.7 with respect to the cylinder head. The bumping clearance between the cylinder head and flat portion of the piston measures 1.5, 3.4 and 5.2 mm at 17.0, 13.5 and 11.5 CR respectively. The spark plug is located close to center (offset of 8 mm from the axis of the cylinder), with the spark plug electrode flush with cylinder head. There is one intake valve and one exit valve of directed type measuring 39 and 33 mm diameter respectively to allow flow into and out of the cylinder. The valve has a maximum lift of 11 mm as shown in the Fig. 6.2 of Chapter VI.

7.2.2 Medium Power level Engine

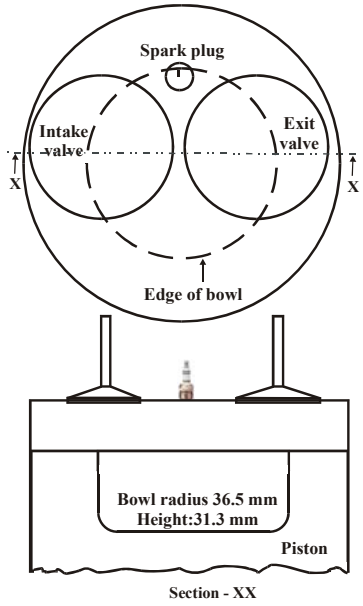

Fig 7.2 Combustion Chamber of MPE

In this case, the combustion chamber is formed of the flat cylinder head and a centrally located cylindrical shaped bowl as shown in Fig. 7.2. The bowl measures 73 mm in diameter and 31.3 mm in height with a volume of 131 cc. The squish ratio is about 0.68 with a minimum bumping clearance of 1.6 mm. There is also additional volume in the form of small depression on the piston top for valve accommodation. However, in this geometry, the spark plug is not centrally located but placed at a point, which is close to the outer edge of the cylindrical bowl and could have additional influence on the flame kernel movement. The chamber is provided with one intake and exit valve of directed type measuring 46 mm diameter with a maximum lift of 14

mm with opening and closure in accordance to the valve-lift profile as shown in the Fig. 7.3.

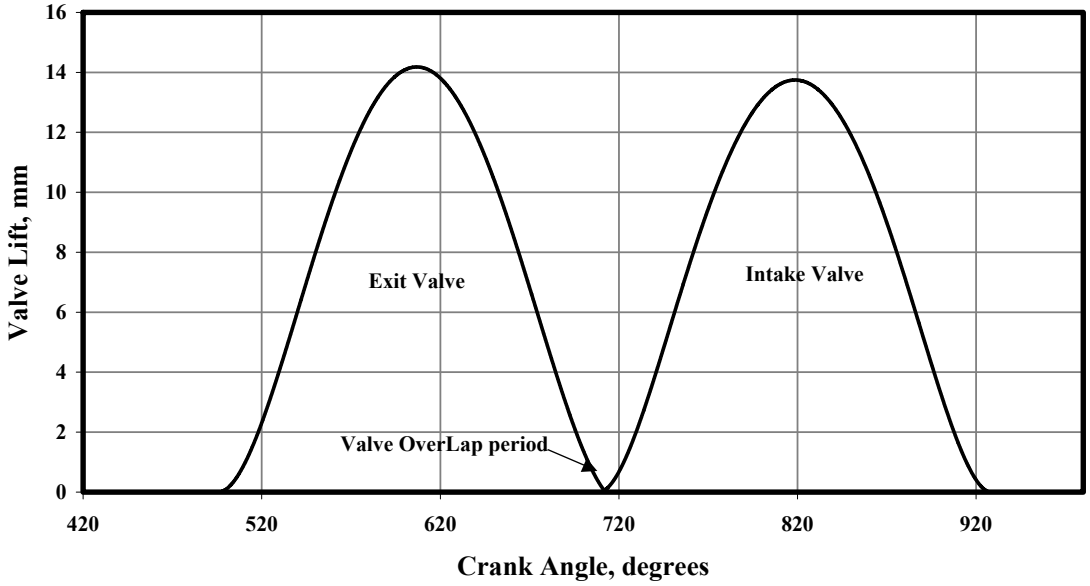

Fig. 7.3 Valve-Lift Profile of MPE

7.3 Validation of Motoring Curve

Prior to proceeding with the prediction of firing p-θ curves, computations under motoring conditions are validated by comparing with the in-cylinder motoring curve recorded on the engines. The experimental motoring curve is recorded on an engine operating under wide-open throttle condition and with the engine operating at the rated speed. p-θ curve is recorded by conducting a "grab" motoring test where the instrumented cylinder of the engine is switched rapidly from firing to motored operation as outlined by Heywood [1988]. This is achieved by cutting-off the spark to the instrumented cylinder and subsequently recording the pressure history. The data used in 0-D simulation is shown in Table 7.1. An important outcome of this motoring simulation is the estimation of charge trapped inside the cylinder at the closure of the intake valve, along with an estimation of recycled gas mass fraction at the beginning of a fresh cycle. In order to arrive at these conditions, it is required to properly account for the charge-flow into and out of the cylinder by choosing appropriate values for discharge coefficients (C_d) for the intake and exit valves. For the present work, values of C_d, of 0.32 and 0.55 are chosen for the intake and exit valves respectively. C_d value chosen for the exit valve is consistent with the steady flow studies quoted in the literature [Bicen et al, 1985], whereas C_d for the intake valve is lower (around 0.5 quoted in the literature) and this is assumed because of additional pressure drop upstream of the intake manifold (200 mm of water against 30 - 40 mm in diesel mode of operation) caused due to long passage from the gas source.

The valve lift profiles have been appropriately considered along with the valve overlap period as shown in Figs. 6.2 and 7.3. The pressure variations in the intake and

the exit manifold are also a part of the simulation, and therefore a constant boundary condition is chosen upstream and downstream of intake (90 kPa and 300 K) and exit manifold (92 kPa and 300 K). Heat transfer is neglected for the manifold part of the flow.

Table 7.1: Data for 0-D Simulation

Wall Temperature		450 K	
Simulation Speed		1500 rev/min	
Annand Coefficient for Heat Transfer - a			
Suction	**Compression & Expansion**		**Exhaust**
0.2	0.8		0.4
Annand Coefficient for Heat Transfer - b		0.78	
Recycled Gas Mass Fraction (%) with CR			
17.0 CR	**13.5 CR**	**11.5 CR**	**12.0 CR**
6.5	7.5	8.5	8.5
Boundary Condition			
Intake Manifold		90 kPa and 300 K	
Exit Manifold		92 kPa and 300 K	
$C_{d,}$ - Intake and Exit valve		0.32 and 0.55	

However, for the in-cylinder computations Annand's heat transfer correlation [Annand et al, 1963] is used with varying heat transfer co-efficient as shown in Table 7.1 (values for 'a' in Eq. 4.11 discussed in Chapter IV). The above coefficients are established by trial-and-error procedure using one test case corresponding to an ignition advance of 26° CA at CR = 17.0. 0-D cycle predictions are made by tuning the above coefficients till the predicted overall energy balance approximately match with the corresponding experimental data. The value chosen for the compression process is higher due to the engine geometry [Annand et al, 1963]. In fact the values chosen for the suction and compression process match with the heat transfer data obtained the cold-flow CFD studies. For the expansion and exhaust processes of the firing cycle, the values for the coefficient are chosen in accordance with the information available in the literature [Annand et al, 1963]. A constant wall temperature of 450 K has been chosen throughout the analysis.

The motored pressure history is simulated using producer gas and air mixture and validated against the experimental p-θ curve in order to arrive at the realistic initial thermodynamic conditions. This validation procedure is followed for SPE at all CRs. The possible error in pressure matching is well within 0.5% for all the cases. However, for the MPE, validation could be possible at a slightly different operating condition (at lower intake charge pressure), because of difficulty in getting experimental motoring curve at corresponding operating condition. During experimentation it was observed that cutting off spark to one cylinder lowered the engine output and thereby affected the turbo-charger performance in terms of charge pressure to the cylinders. Therefore validation is done with the experimental motoring curve at charge pressure of 1.1 bar (abs) and the required thermodynamic conditions corresponding to higher brake output is obtained by changing the charge pressure in the intake manifold (1.25 bar at a gross brake output of 160 kW).

7.4 Assumptions and Features for the 0-D Model

The assumptions and features for the 0-D model are listed below

1. The gas exchange process is simulated Filling and Emptying technique. The details are discussed in section 4.2.1 of Chapter IV. The intake and exit boundary conditions, and C_d for the valves are given in Table 7.1.

2. All the four processes, namely gas exchange, compression, heat release and expansion are simulated with heat loss, and mixture/product gas considered as perfect gas. The heat transfer coefficients used for different processes are listed in Table 7.1. A constant wall temperature of 450 K is considered for all processes.

3. Subsequent to ignition occurring a preset time, there is an apparent time delay in cylinder pressure rise due to combustion called the ignition delay. During the ignition delay period the flame kernel is displaced from its point of formation.

4. The combustion is considered to occur under constant volume conditions, with products and mixture at different pressures. At the end of ignition delay period the pressure in the combustion chamber equilibrates in accordance to the procedure discussed in section 4.3.3 of Chapter IV.

5. With further movement of the flame, the heat release is simulated using EELB sub-model as outlined in section 4.2.2, wherein a spherical flame front (reaction zone) is assumed to propagate into the unburned mixture using two zone model. Heat transfer is considered between individual zones and the combustion chamber walls.

6. The other assumptions on the heat release model are that the original charge is homogenous, with burned gas at full thermodynamic equilibrium and unburned gas at its original composition. Similarly, pressure is considered to be uniform throughout the cylinder with uniform local specific heats for burned and unburned gas.

7. For the EELB sub-model, the laminar burning velocity, turbulence parameters and flame movement as discussed in Chapter IV and V are used.

7.5 Presentation of Experimental Data

Among the experiments conducted on SPE and MPE, thirteen test cases are chosen representing the engine operation at different ignition settings. These experiments correspond to the maximum brake output obtained at a particular ignition setting under full throttle conditions. Some of the experimental data such as the gas composition and fuel-air equivalence ratio are used as an input in the 0-D model. The output of the 0-D model, which is p-θ data, is compared against the experimental p-θ

curve. Another such comparison is the overall energy balance. Some of the terminologies relevant to energy balance are identified as follows.

Gross Indicated Power (IP_G) – Net Brake Power (BP_N) = Total Losses (L_T)

Where,

Total Losses (L_T) = Pumping Loss (F_L) + Power consumed by accessories i.e fan (F_A) + Friction Loss (F_R)

The experimental energy balance is available as

Input energy (IE) = Net Brake Power (BP_N) + Power consumed by the fan (F_A) + Energy loss through exhaust + Energy loss through coolant.

The coolant contains thermal energy on account of heat loss + a part of total loss (L_T) i.e equivalent to F_R. Similarly the exhaust loss contains sensible heat + chemical heat (unburned CO) + pumping loss.

Table 7.2 Break-Up of L_T Components, Deduced from Experimental Results.

Ign, ° CA	IP_G, kW	BP_N, kW	L_T, kW	F_L, kW	F_A kW	F_R, # kW	F_R/cyl kW	Peak Pr, bar	Friction Index *
26	20.6	16.2	4.4	1.1	1.4	1.9	0.64	60	1.07
22	22.4	17.9	4.5	1.1	1.4	2.0	0.66	65	1.02
17	23.4	18.4	5.0	1.1	1.4	2.5	0.84	68	1.24
12	25.2	19.8	5.4	1.1	1.4	2.9	0.97	77	1.26
6	25.3	20.0	5.3	1.2	1.4	2.8	0.90	56	1.61
25	21.0	17.0	4.0	1.1	1.4	1.5	0.50	45	1.11
18	21.0	17.0	4.0	1.1	1.4	1.5	0.50	37	1.35
14	22.5	18.6	3.9	1.1	1.4	1.4	0.47	45	1.04
27	19.3	15.6	3.7	1.1	1.4	1.2	0.40	37	1.08
17	21.0	17.6	3.4	1.1	1.4	0.9	0.30	37	0.81
6.0	20.5	17.0	3.5	1.2	1.4	0.9	0.30	25	1.20
19	177	148	29.0	1.0	12.0	16	1.40	65	2.00
12	177	149	28.0	4.0	12.0	12	1.00	55	1.81

estimated by difference, * Friction Index = ((F_R/cyl)*α)/Peak Pr), where α is any constant ~ 100
Data Below Dotted Line Refers to MPE

Whereas, the energy balance derived as an output of 0-D computation is of the following nature

Input energy (IE) = IP_G + F_L + Heat loss through exhaust + Heat loss to walls

where, the heat loss to the exhaust does not include the pumping loss. Similarly, the heat loss to the walls does not contain frictional loss. In order to compare data on component basis requires restating of the above data in a consistent manner. This requires an estimation of the frictional loss and is deduced from the experimental result. A break-up of total loss is given in Table 7.2; F_L is estimated from the experimental p-θ curve, with F_A actually measured (discussed in Chapter III).

In the data stated in above table, BP_N (net brake power) is the measured value as explained in Chapter III, IP_G (Gross Indicated power) is obtained by integrating the expansion and compression curves of p-θ data. F_L (Pumping loss) is obtained by integrating the exhaust and suction curve of p-θ data. F_A (Accessories power) is estimated from a separate experiment as explained in Chapter III and F_R (friction power) is calculated by difference. It can be observed from the above Table that the estimated frictional power per cylinder is comparable for both the engine geometries around the same cylinder pressure. However, the frictional power varies with the CR and this is due higher pressures encountered in the cylinder.

7.6 Comparison of FSR data

The Flame Speed Ratio (FSR) is defined as the ratio of turbulence burning velocity to laminar burning velocity. Under quasi-steady conditions, turbulence burning velocity is taken as a sum of laminar burning velocity and turbulence intensity. This ratio, which forms an input for the 0-D model, is compared with some of the engine/non-engine data available in the literature. Groff et al [1980] has established a FSR correlation obtained from the experimental and computational study conducted on a SI engine using propane fuel under varying conditions of speed, ignition timing, valve configuration and spark plug location. This author has further compared his data with the non-engine and engine data of Abdel-Gayed et al [1976] and Ballal et al [1974] respectively. Groff et al [1980] has adopted two criterions for FSR calculations, one corresponding to the flame attaining a size of 30 mm and the other corresponding to a mass burned fraction (MBF) of 50%. Where as, the data of Abdel-Gayed et al [1976] and

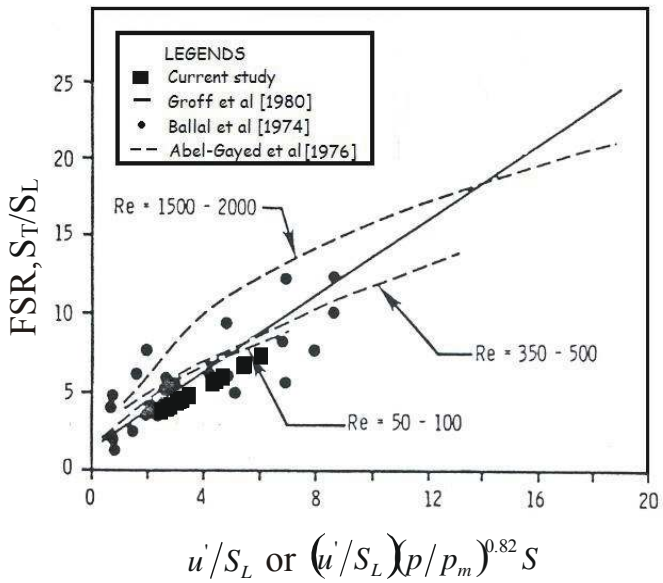

Fig. 7.4 FSR Data of the Current Study in Comparison with Engine/Non-engine Data, From Groff et al [1980]. *S* refers to spark advance and p_m is the motoring pressure

Ballal et al [1974] corresponds to 50% MBF. A comparison with the current FSR data is shown in Fig. 7.4. The FSR data of the current study corresponds to 50% MBF, this criterion is chosen because in some of the cases (at CR=17.0) the 50% MBF occurred much earlier to the flame attaining 30 mm size. All the cases shown in Fig. 7.4 correspond to the one with spherical flame assumption. For u'/S_L < 4.0, the current FSR data agrees favorably with the correlation of Groff et al [1980] and the non-engine data in the Reynolds number range of 50 – 100. However, at 7. 0 > u'/S_L > 4.0 it is lower than Groff et al [1980] and Abdel-Gayed et al [1976] results in the Reynolds number range of 1500-2000, but is favorable with the data of Ballal et al [1974]. The Turbulence Reynolds number of the current results is in the range of 2000 - 2200. One reason attributed for the FSR value to be lower in the current study is the higher laminar burning velocity with producer gas compared to propane, in the case of Groff et al [1980].

7.7 Procedure for 0-D Computations

In these computations, appropriate fuel-air mixture recorded during experiments constitutes the input energy (IE). Dilution in terms of recycled gas fraction as depicted in Table 7.3 is considered at corresponding CRs. The computational procedure is summarized as a flow-chart in Fig. 7.5. The blocks indicated in the center of the flow-chart represents the sequence of four thermodynamic processes constituting one complete cycle. The necessary inputs for the heat release process are indicated, which are derived from discrete computations highlighted in Chapter IV and V. Similarly, the equilibrium calculations for computing products and the adiabatic flame temperature are obtained using SP-273 code of NASA [Gordon et al, 1975]. The criteria for converge is also highlighted, it is the stabilization of the peak cylinder pressure value, which needs to be within about 1.0% in the successive cycles.

Coming to actual values used in the 0-D computations, in the case of turbulence parameters, variation in turbulence intensity is considered to be same at all CRs (Fig. 7.6) for SPE test cases, whereas appropriate integral length scale at CR of 17.0 and 11.5 as depicted in Fig. 7.6 is considered. The velocities considered for flame kernel movement are shown in Fig. 7.7. For CR=13.5, the velocities are taken the same as at CR = 11.5 and for integral length an intermediate valve (between CR = 17.0 and 11.5) is assumed. For the MPE geometry, the turbulence intensity is considered at a higher value than the SPE geometry because the mean piston speeds of the two engines are different. The mean piston speed of SPE is 5.8 m/s against 7.0 m/s for the MPE. According to the experimental study conducted by Catania et al [1996] at varying speeds, corresponding to different mean piston speeds, the turbulence intensity is observed to increase with the increase in mean piston speed. For instance, for the increase in engine speed from 1500 rev/min (mean piston speed = 4.3 m/s) to 2000 rev/min (5.7 m/s) the turbulence intensity increased by about 25 – 30% between 330 to 390° CA. Similar trend is also observed in the experimental study conducted by Groff et al [1980]. Therefore, for the MPE tests cases, enhanced values of turbulence intensity to an extent of 25% is used. However, the length scale corresponding to CR = 11.5 of SPE are used.

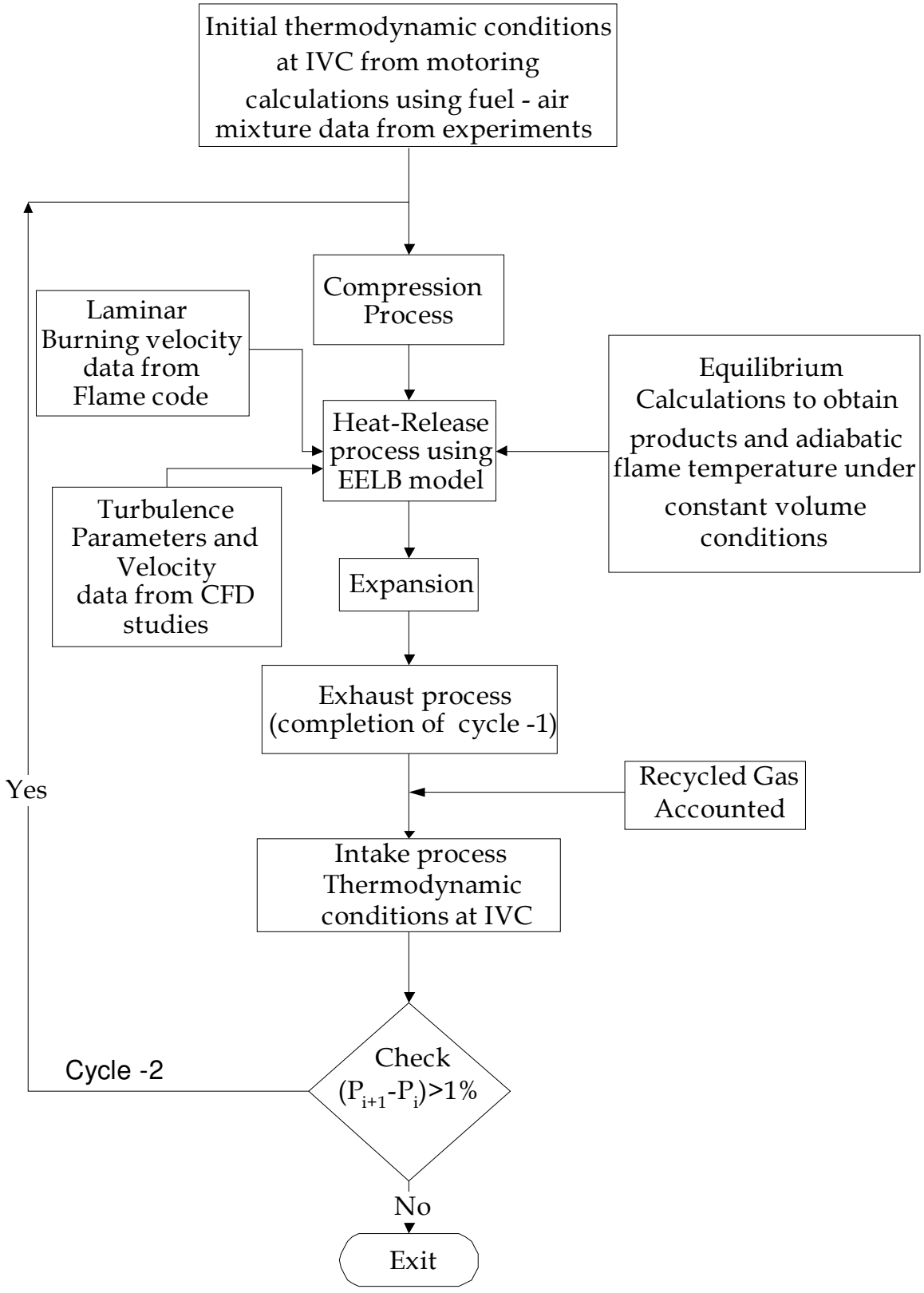

Fig. 7.5 Flow-chart for 0-D Computations

7.8 Predictions of p-θ curve

The salient features of the thirteen test cases are shown in Table 7.3, wherein the fuel gas composition, fuel-air equivalence ratio without recycled gas, recycled gas fraction, input energy per cycle, ignition advance, estimated ignition delay are highlighted.

Table –7.3: Principal Parameters of the Test Cases Used in the 0-D Predictions

No.	CR	Composition, Vol %			Φ	RG %	Input* Energy/ Cycle, kJ	Ign, °CA	Ign#. Delay, °CA	Category
		H_2	CO	CH_4						
1	*17.0*	*20.8*	*16.2*	*2.0*	*1.10*	*6.5*	*1.70*	*26*	*12*	*Simple*
2	17.0	21.0	18.6	2.0	1.03	6.5	1.70	22	9	Simple
3	17.0	21.5	16	2.5	1.09	6.5	1.69	17	9	Complex -I
4	17.0	2.10	19.2	2.0	1.00	6.5	1.69	12	9	Complex -I
5	17.0	20.0	20.0	2.0	1.10	6.5	1.73	6	6	Complex -I
6	13.5	20.0	15.0	2.5	1.06	7.5	1.62	25	9	Simple
7	13.5	20.0	15.0	2.5	1.07	7.5	1.63	18	9	Simple
8	13.5	20.0	15.7	2.5	1.06	7.5	1.63	14	9	Complex -I
9	11.5	18.0	18.0	2.5	1.09	8.5	1.63	27	9	Simple
10	11.5	21.0	20.0	2.0	1.07	8.5	1.70	17	9	Complex -I
11	11.5	19.5	20.0	2.0	1.07	8.5	1.66	6	6	Complex -I
12	12.0	19.5	19.0	0.6	0.91	8.5	3.25	19	8	Complex -II
13	12.0	18.5	19.0	0.5	0.91	8.5	3.25	12	5	Complex -II

* Input energy = Mass of mixture in the cylinder at the closure of intake valve * LCV of the fuel-air- recycled gas (RG) mixture; # Ignition delay estimated by considering the point of deviation of the firing curve with **the** motoring curve at their respective CR; Cases 12 & 13 refer to MPE

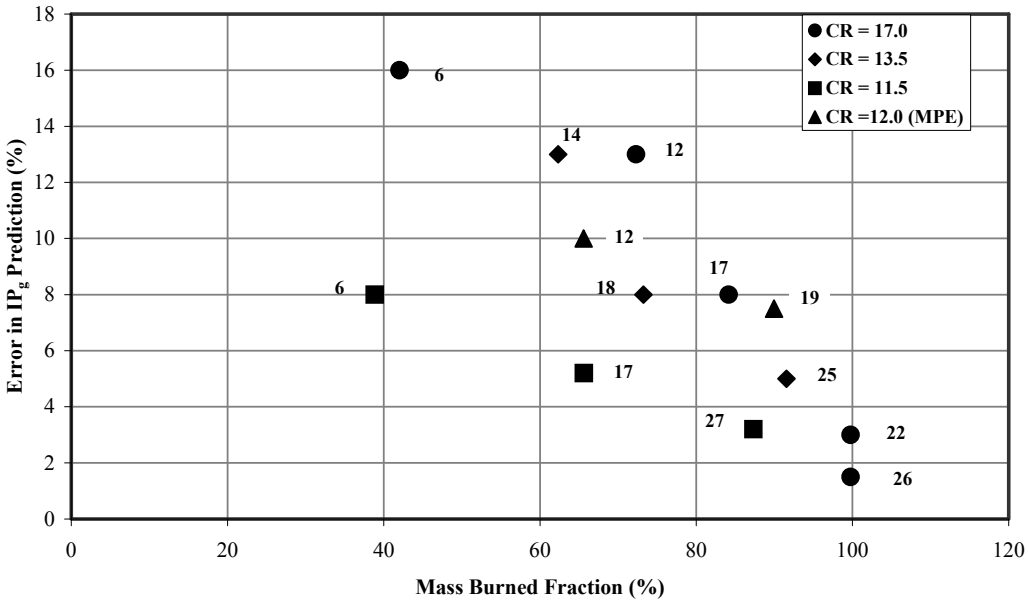

Fig. 7.6 Plot of Error in the Predicted Indicated Power (IP_G) vs. Mass Burned Fraction (MBF). Numbers Next to the Legend Refers to the Ignition Setting in °CA

These thirteen cases are further categorized into simple and complex using the following criteria. The error in the indicated power obtained from the 0-D prediction (compared to experimental indicated power) is plotted against Mass Burned Fraction (MBF) corresponding to 372° CA in Fig. 7.6. This particular crank angle is chosen because the reverse squish effect is observed to assume its peak at this value from the CFD studies. These predictions are made by assuming spherical flame propagation through out the combustion period. It is evident from the Fig. 7.6 that in the case of advanced ignition setting (> 19° BTC) the MBF is in excess of 87% and the maximum error in IP prediction is about 7.5%. Among such five cases, four cases of SPE are categorized as simple, where as the case of MPE corresponding to 19° CA is categorized under Complex – II due to its offset ignition (spark plug) location and moreover, due to large deviations observed in the predicted cylinder pressures. The case pertaining to CR = 13.5 at 18° CA is categorized under Simple because the predicted pressures are marginally deviating from the experimental results even though the MBF is low at 73%. All other cases relating to SPE with lower MBF (< 85%) are categorized under Complex – I category. Similarly, the MPE case at 12° CA is classified under Complex – II category. These aspects are further discussed for individual categories in the subsequent sections. Further, the physics behind this classification is as follows.

- Simple: These are related to advanced ignition setting, wherein flame propagation is assumed to occur in a spherical manner, the fluid dynamics during this period is not dominant (inferred from CFD analysis) enough to alter the flame shape.

- Complex – I and II: These are related to retarded ignition setting wherein major part of the flame propagation occurs at a time when the fluid dynamics becomes dominant due to reverse squish effect. The increased fluid flow out of the bowl region of the combustion chamber is assumed to alter the flame shape from spherical to flat shape and this occurs in the later part of heat release. In addition to this, the flame kernel is assumed to undergo larger initial displacement due to offset location of the ignition source in the case of Complex – II.

In the Table 7.3, Case No. 1 (in italics) corresponding to an ignition advance of 26° CA at CR=17.0 is used as a trial case for choosing the coefficients for the heat loss equation (Equation 4.11 of Chapter IV). The coefficient chosen for the four processes of the engine cycle is given in Table–7.1. The predicted p-θ curve and the overall energy balance for this particular case are discussed subsequently.

7.9 Estimation of Ignition Delay

The ignition in all cases is followed by an ignition delay period, wherein there is an apparent time delay till appreciable change is observed in the cylinder pressure. During this time delay, 1% of the initial mass is assumed to have been consumed, which works to a sphere of about 12 mm diameter. For example, the ignition delay for an ignition setting of 26° CA is as follows. The laminar burning velocity at these conditions (2300 kPa, 770K) is 1.5 m/s. It has been established by earlier researchers that flame propagates in a laminar mode till the flame kernel attains a critical size, beyond which

the propagation becomes turbulent [Kalghatgi, 1985]. If one were to consider laminar flame propagation during this period, the ignition delay works out to 36° CA for a flame size of 6 mm radius. But this time delay appears to be too long, which points towards burning velocity being much higher during the initial phase of combustion. As ignition delay is a complex function of fuel-air mixture ratio and fluid dynamics in the vicinity of the spark plug, it is not amenable for estimation by the simple procedure elucidated above. This therefore leaves no choice other than estimating it from the experimental data. It is estimated by superimposing the motoring curve over the experimental firing curve and taking the point of nearest deviation from the point of ignition as the delay period. This procedure is employed for estimating the ignition delay period for all the cases.

During the ignition delay period, flame kernel movement from the ignition site is considered by accounting for the velocities (normal component) in the vicinity as shown in Fig. 6.13 of Chapter VI. The enhancement in velocity due to combustion is appropriately accounted by multiplying with a factor equivalent to the ratio of burned gas temperature ($T_{burnred}$) to the unburned mixture temperature ($T_{unburned}$). Subsequent to the ignition delay, the displaced flame propagates spherically into the turbulent flow field thus consuming the unburned mixture. Computations are attempted using the turbulence intensity (u') and integral length scale (l_l) values extracted data from the CFD analysis and these are mass-averaged 3-D zone passing through the bowl center as depicted in Fig. 7.7. Typical integral length scale in the region of piston bowl is in between 1.0 and 1.5 mm during the last stages of compression process and this is typical of the characteristic length scale of wrinkled flames discussed in the literature [Keck, 1982]. Further enhancement of turbulence parameters in the unburned mixture due to combustion is accounted by considering simple rapid distortion theory (Equation 4.10 of Chapter IV) as elucidated by Groff et al [1980].

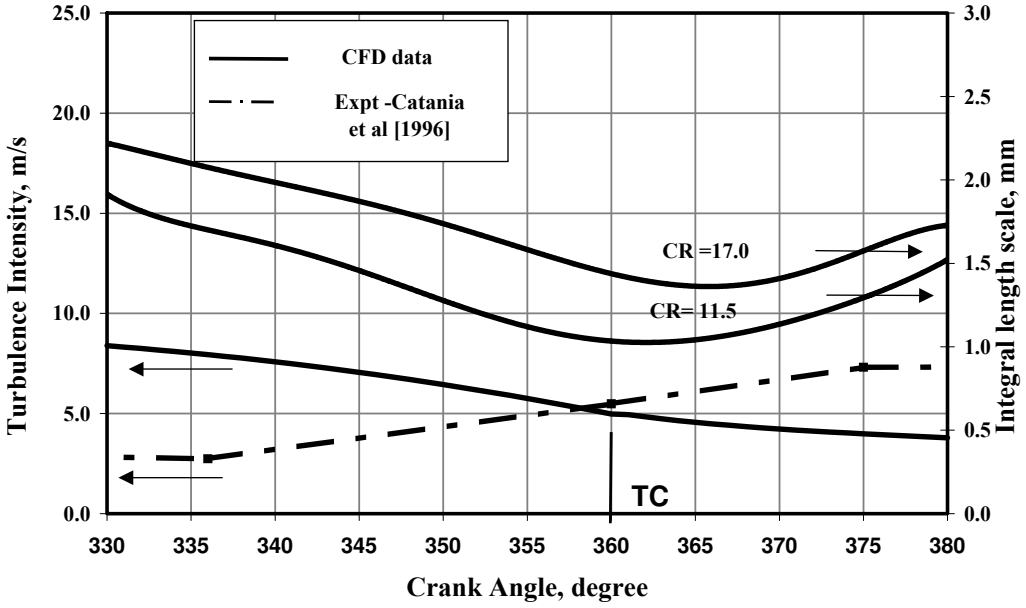

Fig. 7.7 Turbulence Parameters used in the 0-D Model

7.10 Predictions of p-θ curve – Simple Cases

Four test cases (Nos. 2, 6, 7, 9) belonging to two CRs of SPE are categorized as simple and their salient features are repeated again in the Table 7.4 for ease of reference. Case no. 1 represented in italics is essentially used as a trial case for choosing the coefficient for the heat loss equation.

Table –7.4: Principal Parameters of 'Simple' Cases

No.	CR	Composition, Vol %			Φ	RG %	Input* Energy/ cycle, kJ	Ign, °CA	Ign#. Delay, °CA	Category
		H_2	CO	CH_4						
1	*17.0*	*20.8*	*16.2*	*2.0*	*1.10*	*6.5*	*1.70*	*26*	*12*	*Simple*
2	17.0	21.0	18.6	2.0	1.03	6.5	1.70	22	9	Simple
6	13.5	20.0	15.0	2.5	1.06	7.5	1.62	25	9	Simple
7	13.5	20.0	15.0	2.5	1.07	7.5	1.63	18	9	Simple
9	11.5	18.0	18.0	2.5	1.09	8.5	1.63	27	9	Simple

* Input energy = Mass of mixture in the cylinder at the closure of intake valve * LCV of the fuel-air- recycled gas (RG) mixture; # Ignition delay estimated by considering the point of deviation of the firing curve with the motoring curve at their respective CR.

The simple cases are predicted with the following theory. A well-observed phenomenon of a spherical flame propagating into unburned mixture is considered. Groff et al [1980] have identified the ratio of the mean fluid velocities to the flame propagation velocity (sum of turbulence flame speed and unburned gas velocity) as a criterion for suitability of spherical flame assumption. Higher ratio due to higher fluid velocities is observed to distort the sphericity of the flame. In the current case this ratio works to less than 0.5 (fluid velocity ≈ 10-12 m/s and flame propagation speed ≈ 20 m/s) and therefore spherical flame assumption is considered to be valid. With the ignition occurring at the pre-set time, a flame kernel forms at the ignition site. During the ignition delay period, the flame kernel is assumed to move vertically downward due to the surrounding turbulent fluid flow. Further, the flame is assumed to be located along the axis of the combustion chamber, since the ignition source is located close to the center and moreover the flow field is close to symmetry in the bowl region (shown in Fig. 6.3 of Chapter VI). Subsequent to the ignition delay period, the EELB model of flame propagation is invoked wherein a spherical flame is assumed to propagate into the unburned mixture, with continued movement of the flame due to local fluid velocities. The spherical flame propagation model is schematically depicted in Fig. 7.8. During the flame propagation, the flame is considered to be turbulent wherein there are two components contributing to the mass burn rate in accordance with the EELB model. The first component is due to laminar propagation of the spherical flame and the second due to the burning of the entrained mixture in the wrinkled flame. This spherical flame

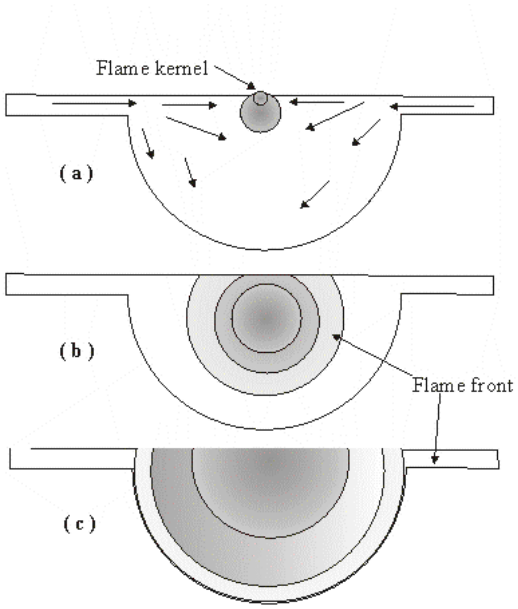

Fig. 7.8 Spherical Flame Propagation –(a) Kernel Formation, (b,c) Turbulent Flame Propagation

propagation continues till the flame encounters a wall; in this particular combustion chamber the first such instance occurs once the flame engulfs the bowl region of the combustion chamber. Once the flame front assumes the size of the bowl, flame propagation is no longer possible in the bowl region, the entrained unburned mixture in the bowl is assumed to burn exponentially (Eq. 4.9 of Chapter IV). But the spherical flame propagates further in the flat region of the combustion chamber geometry, till the flame touches the far cylinder wall. Once the flame achieves the size of the cylinder bore (radius of 55 mm) the flame is assumed to quench, with the remaining entrained mixture to burn exponentially. During the quasi-steady flame propagation, typical turbulence burning velocities are of the order of 7-9 m/s (at CR = 17.0) and time scale of the order of 0.5– 0.6 ms during the initial stages of flame propagation, and once the flame reaches the wall, time scale for exponential burning is of the order of 0.8 to 1.0 ms and somewhat similar to the value (0.6 to 1.0 ms) reported by Keck [1982].

Using the above theory, four predictions have been attempted. The producer gas fuel considered for computation is same as the recorded values during experimentation, and details for all the test cases are given in Table 7.4. The recycled gas is estimated at 6.5%, 7.5% and 8.5% for CRs of 17, 13.5 and 11.5 respectively from the motoring analysis and subsequent analysis with combustion did not show appreciable change in the value. The recycled gas considered for the analysis is the product gas, which is obtained from the equilibrium calculations. The mixture (gas + air + recycled gas) is estimated to have a lower calorific value between 1.9 and 2.0 MJ/kg. The initial trapped mass at the closure of intake valve is estimated at 0.850 g, which works out to an input energy between 1.6 and 1.7 kJ per cycle. Using these initial conditions compression process is simulated without heat release till the point of ignition.

7.10.1 Results

Subsequent to the ignition delay period, flame propagation occurs in accordance with the theory discussed earlier. The simulation scheme is organized to calculate the complete engine cycle, till successive cycles converge. The first cycle simulation is done assuming a recycled gas of 12% H_2O, 14% CO_2 and rest N_2. Two more cycle simulations are subsequently attempted using the product gases obtained from the equilibrium calculations as the recycled gas. The criteria applied for converge is the stabilization of the peak pressure value, the results stabilized within 0.5% in about two cycles.

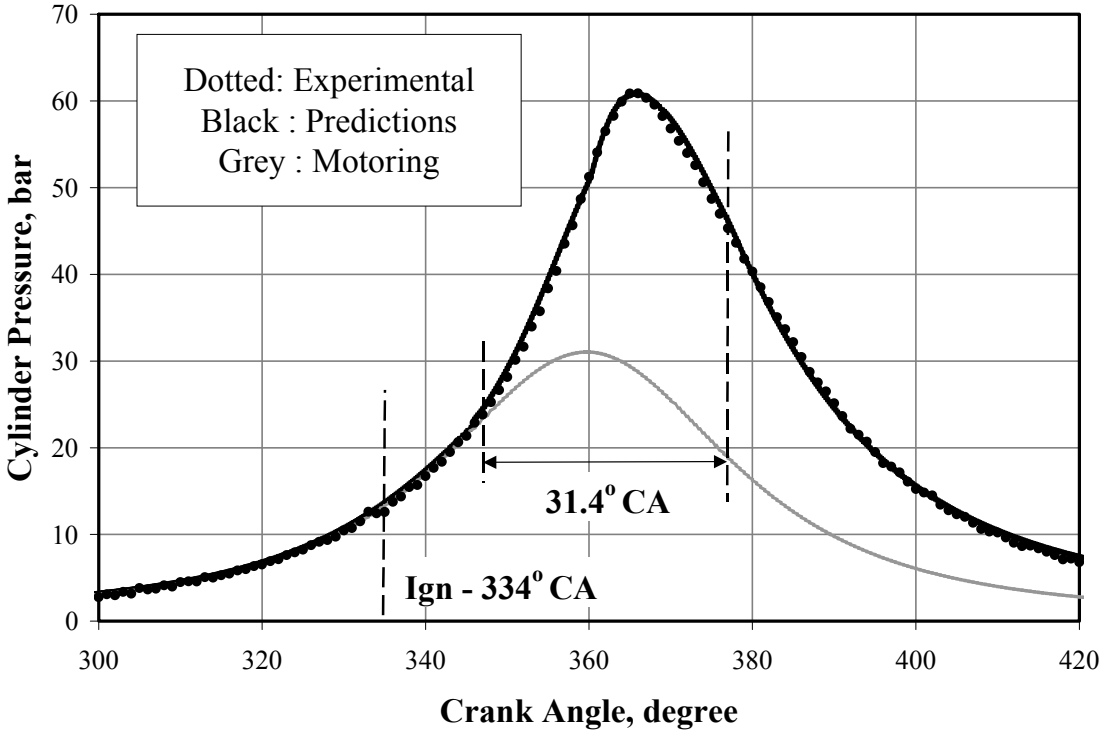

Fig. 7.9 Trial Case used for Establishing the Heat Loss Equation Coefficient at 26° CA Ignition Advance @ CR=17.0. Combustion Duration Excludes the Delay Period.

These computations are attempted with a time step of 0.2° CA (0.022 ms) and confirmed to be time step independent. Fig. 7.9 shows the prediction for the trial case used for choosing the coefficient for the heat loss equation. This heat loss equation parameter once established is subsequently held unchanged for all the twelve predictions, which include simple, complex-1 and II cases. The predictions for the four Simple category cases are shown in Figs. 7.10-7.13. The principal results are given in Table –7.5. It is evident that MBF is higher than 85% in four cases except that with CR = 13.5 corresponding to ignition advance of 18° CA. The computed results at CR=17.0 corresponding to an ignition advance of 22° CA match excellently with the experimental data, with marginal variation in the peak pressure and its point of occurrence. The total combustion duration (100% mass fraction burned) is lower by about four degrees in case of 22° CA than 26° CA due to higher burn-rate.

Table –7.5: Principal Results of 'Simple' Cases. MBF. Mass Burned Fraction (MBF) corresponds to 372° CA

CR	Ign, ° CA	Experiment		Prediction			
		Peak Pressure, bar	Occurrence, ° CA	Peak Pressure, bar	Occurrence, ° CA	Duration, ° CA	MBF, %
17.0	*26*	*60.9*	*366*	*60.8*	*365.8*	*43.4*	*100*
17.0	22	64.4	366	63.0	366.4	39.6	100
13.5	25	46.3	368	44.8	367.2	60.0	92
13.5	18	36.9	372	36.8	371.0	56.0	74
11.5	27	38.0	368	35.2	367.6	68.0	87

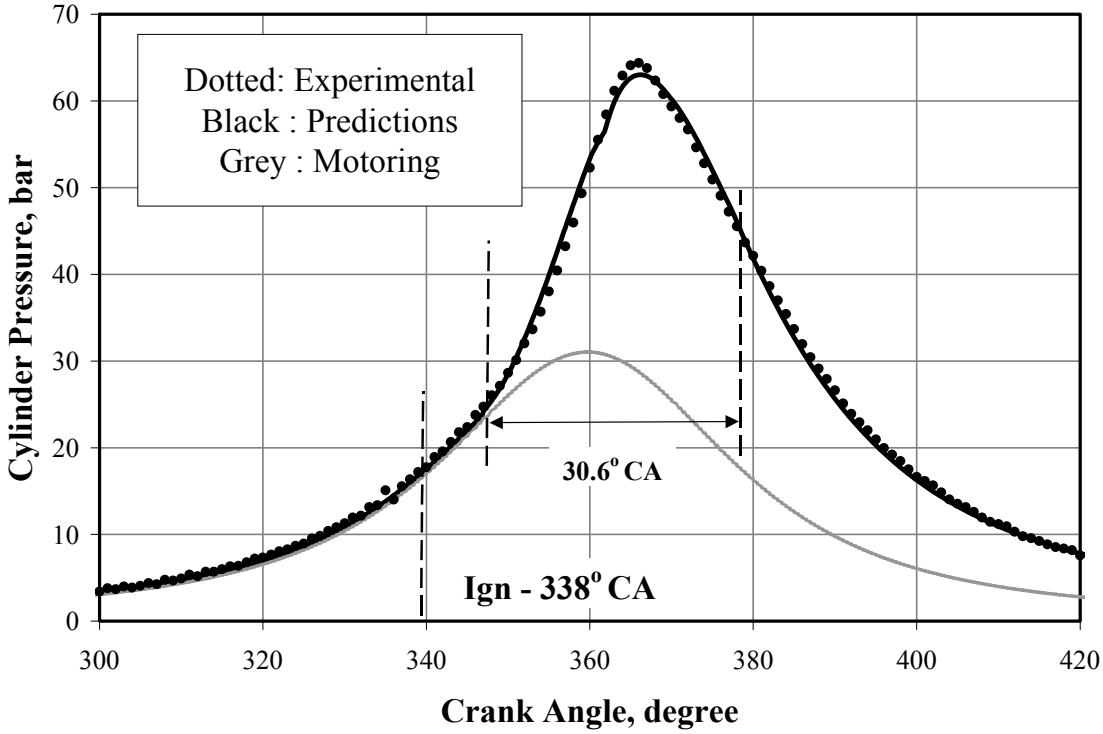

Fig. 7.10 p-θ Prediction at 22° CA Ignition Advance @ CR=17.0. Combustion Duration Excludes the Delay Period.

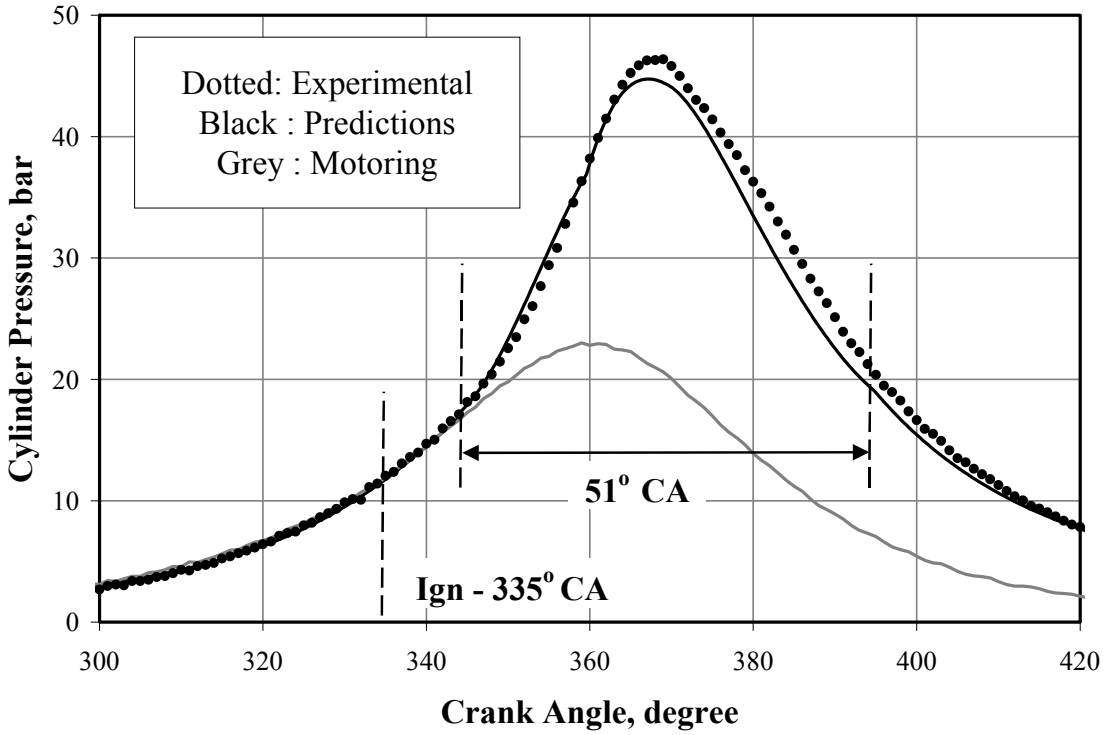

Fig. 7.11 p-θ Prediction at 25° CA Ignition Advance @ CR=13.5. Combustion Duration Excludes the Delay Period.

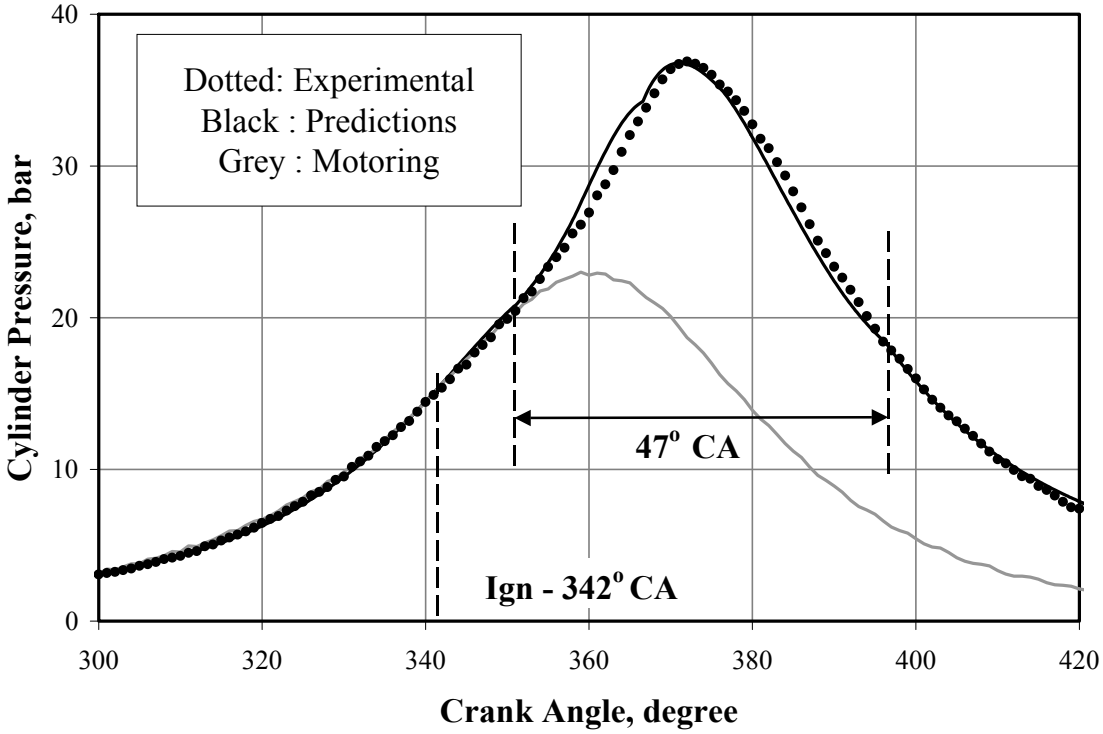

Fig. 7.12 p-θ Prediction at 18° CA Ignition Advance @ CR=13.5. Combustion Duration Excludes the Delay Period.

In the predictions at CR=13.5 at an ignition advance of 25° CA, the pressures are marginally higher right at the commencement of heat release, with peak pressure falling short of the experimental value by about 1.5 bar and as a consequence the expansion pressures are lower. However, prediction at 18° CA match reasonably well with the experimental data even though the predicted pressure deviates after about 356° CA, the duration of combustion is again shorter at retarded ignition setting. In the predictions at CR=11.5 at an ignition advance of 27° CA, the pressures are marginally higher right at the commencement of heat release, with peak pressure falling short of the experimental value by about 3.0 bar and as a consequence the expansion pressures are lower. The duration of combustion is much longer when compared to corresponding ignition setting at CR=17.0. The pressure-volume data is integrated to determine the gross indicated power (IP_G) and the pumping losses – incurred with respect to the suction and exhaust processes. The data obtained from the single cylinder analysis is considered to be a reasonable representative of the remaining two cylinders of SPE and therefore reported for the complete engine (three cylinders). These values are compared with the respective experimental energy balance as shown in Table 7.6.

In the Table 7.6, experimental results are presented in two ways; the first row (Ex-org) contains the original set of results. The second row contains the redistributed experimental results (Ex-red), presented in a manner discussed in Section 7.2 for one-to-one comparison with the 0-D results presented in the third row. The energy balance corresponding to 26° CA at CR=17.0 is the trial case wherein the coefficients for heat loss were arrived at, it is shown in italics in the Table.

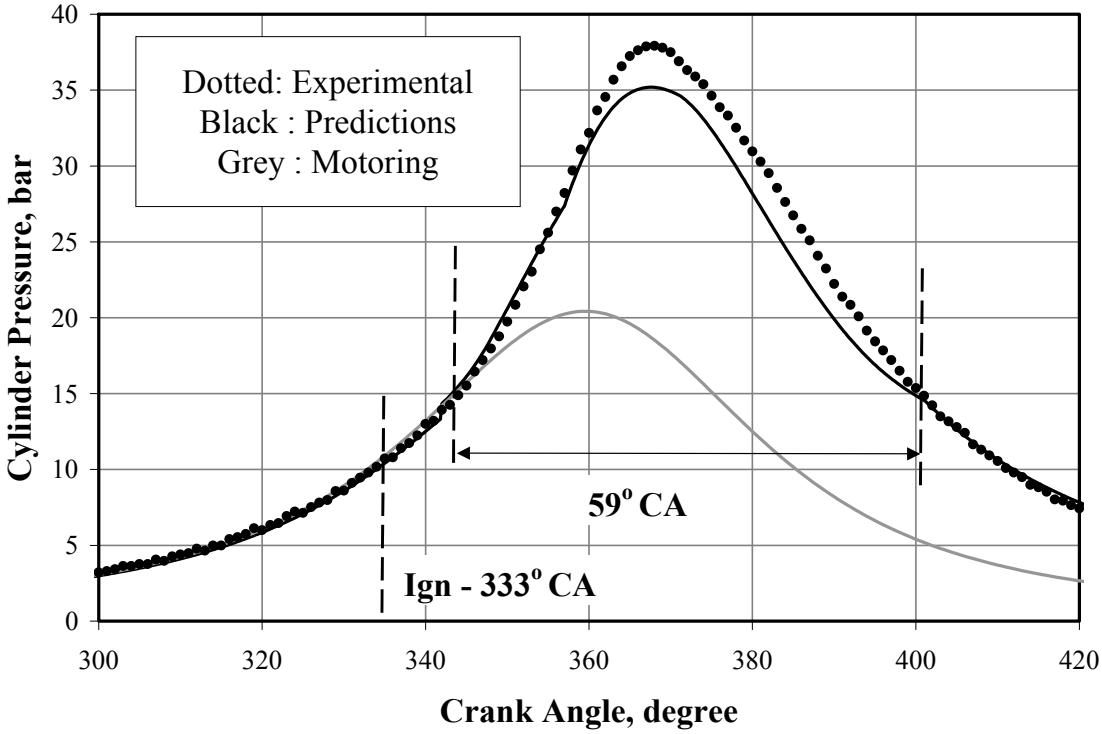

Fig. 7.13 p-θ Prediction at 27° CA Ignition Advance @ CR=11.5. Combustion Duration Excludes the Delay Period.

Table – 7.6: Comparison of Energy Balance (kW) of 'Simple' Cases

Mode	IE	IP_G	F_L	BP_N	F_A	F_R	Exhaust	Coolant/Wall
				CR=17.0, 26° CA				
Ex-org	*64.0*	*20.6*	-	*16.2*	-	-	*22.0*	*25.8*
Ex-red	*64.0*	*20.6*	*1.1*	*16.2*	*1.4*	*1.9*	*20.9*	*22.5*
0-D	*64.0*	*20.3*	*1.2*	*NC*	*NC*	*NC*	*21.8*	*20.7*
				CR=17.0, 22° CA				
Ex-org	64.0	22.4	-	17.9	-	-	20.3	25.8
Ex-red	64.0	22.4	1.1	17.9	1.4	2.0	19.2	22.4
0-D	64.0	21.8	1.2	NC	NC	NC	19.7	21.3
				CR=13.5, 25° CA				
Ex-org	60.7	20.7	-	17.0	-	-	25.0	18.7
Ex-red	60.7	20.7	1.1	17.0	1.4	1.5	23.9	15.8
0-D	60.7	19.7	1.3	NC	NC	NC	20.7	19.0
				CR=13.5, 18° CA				
Ex-org	61.0	21.0	-	17.0	-	-	30.0	14.0
Ex-red	61.0	21.0	1.1	17.0	1.4	1.5	28.9	11.1
0-D	61.0	19.4	1.3	NC	NC	NC	22.0	18.3
				CR=11.5, 27° CA				
Ex-org	61.0	19.3	-	15.6	-	-	19.0	26.4
Ex-red	61.0	19.3	1.1	15.6	1.4	1.2	17.9	23.8
0-D -I	61.0	18.7	1.3	NC	NC	NC	22.0	19.0

Ex-org: original experimental results, Ex-red: redistributed results NC: Not Computed

The heat loss through coolant as well as exhaust compares reasonably well with the experimental data, also the error in IP_G is about 1.5%. Marginal variation in heat loss to walls and exhaust is due to computed cylinder pressure (as a consequence, temperature) being higher in the later part of the expansion process, and is attributed to the choice of fixed heat transfer coefficient for the entire process**.**

Get ting back to the predictions, in the case of CR=17.0, the predicted IP_G is lower by 3.0% for an ignition setting of 22° CA. The heat loss through exhaust and coolant also compare reasonably. However, with CR=13.5 the predicted IP_G is lower by 5 and 8% at an ignition setting of 25° and 18° CA respectively. Similarly the predictions are different with respect to the heat loss. In the case of experimental results, there is large fraction of heat loss through exhaust and this is due to large amount of unburned CO in the exhaust, constituting nearly 40% of energy in both the cases. In the case of CR=11.5, the predicted IP_G is lower by 3%, with overestimation of exhaust losses and an underestimation of coolant losses, and the argument stated earlier with respect to choice of heat transfer coefficient holds good.

7.11 Predictions of p-θ curve – Complex – I Cases

Six test cases belonging to two CRs of SPE are categorized under Complex - I and their salient features are repeated in the Table 7.7 for ease of reference. Predictions are initially attempted using simple spherical flame propagation model, the difference observed between the predicted and the experimental results is lowered by assuming certain hypothesis, formulated on the basis of fluid flow phenomenon occurring inside the engine cylinder. This behavior is established from the cold flow CFD studies.

Table –7.7: Principal Parameters of 'Complex – I' Cases

No.	CR	Composition, Vol, %			Φ	RG %	Input* energy/ cycle, kJ	Ign, °CA	Ign#. Delay, °CA	Category
		H_2	CO	CH_4						
3	17.0	21.5	16	2.5	1.09	6.5	1.69	17	9	Complex -I
4	17.0	2.10	19.2	2.0	1.00	6.5	1.69	12	9	Complex -I
5	17.0	20.0	20.0	2.0	1.10	6.5	1.73	6	6	Complex -I
8	13.5	20.0	15.7	2.5	1.06	7.5	1.63	14	9	Complex -I
10	11.5	21.0	20.0	2.0	1.07	8.5	1.70	17	9	Complex -I
11	11.5	19.5	20.0	2.0	1.07	8.5	1.66	6	6	Complex -I

7.11.1 Results

The methodology adopted for computation remains the same as in the earlier case. The results of the six predictions are shown in Figs. 7.14 to 7.20. Predictions using spherical flame assumption are shown for all the six test cases as Case I in these figures. For instance, it is evident from the Fig. 7.14 that there is deviation in the computed pressures beyond a crank angle (CA). It is not immediately obvious as to why there is a deviation beyond a certain point. The deviation in pressure might be occurring as a result of increased burn rate either due to enhanced surface burning area or the enhanced entrainment. Higher surface area for burning is possible provided the flame

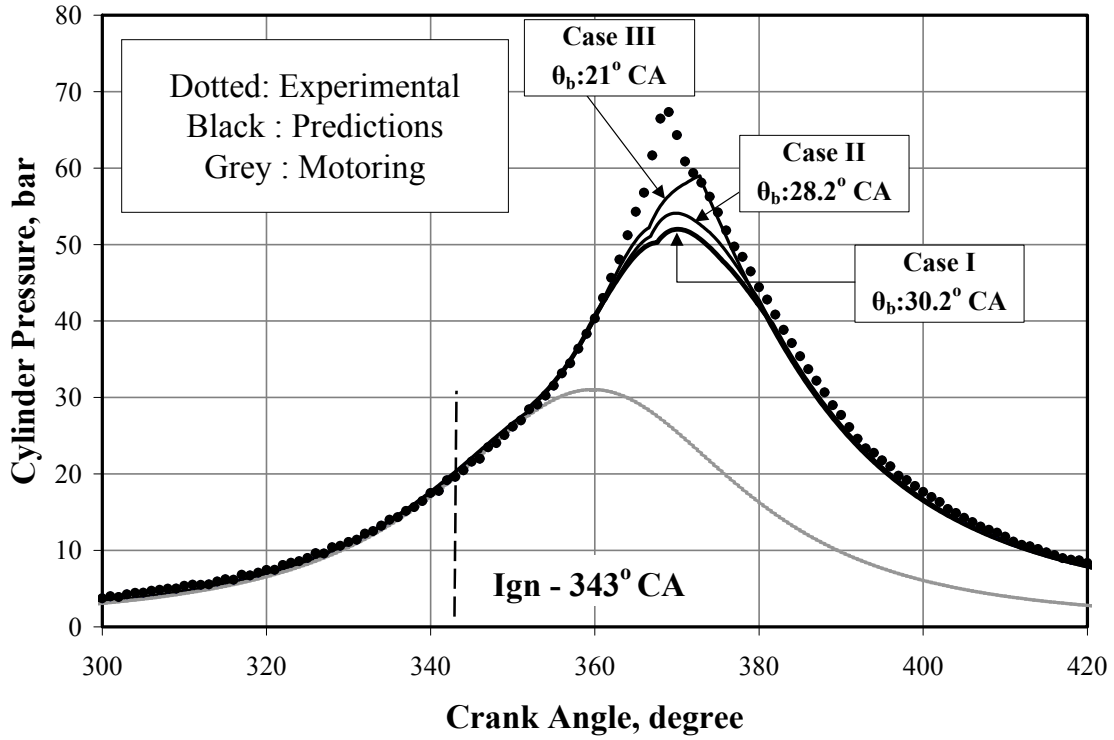

Fig. 7.14 p-θ Prediction at 17° CA Ignition Advance @ CR=17.0. Combustion Duration Excludes the Delay Period.

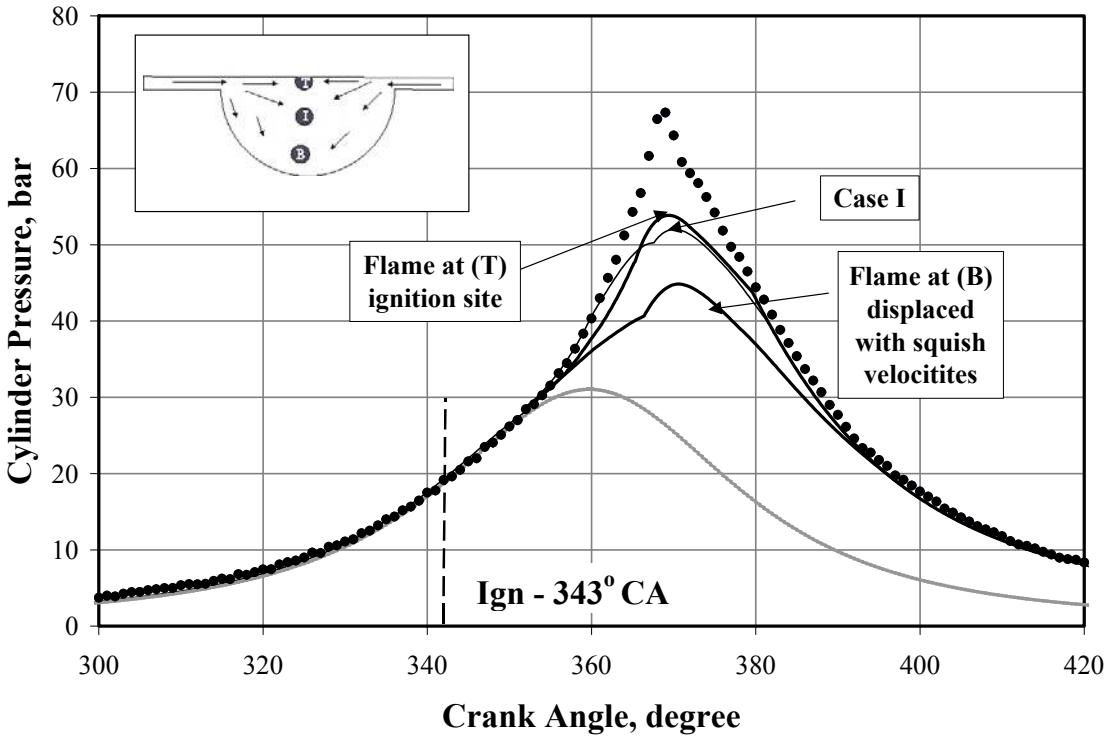

7.15 p-θ Prediction at 17° CA with Flame Kernel at Different Locations. Inset Shows the Possible Locations of Flame Kernel at the End of Ignition Delay

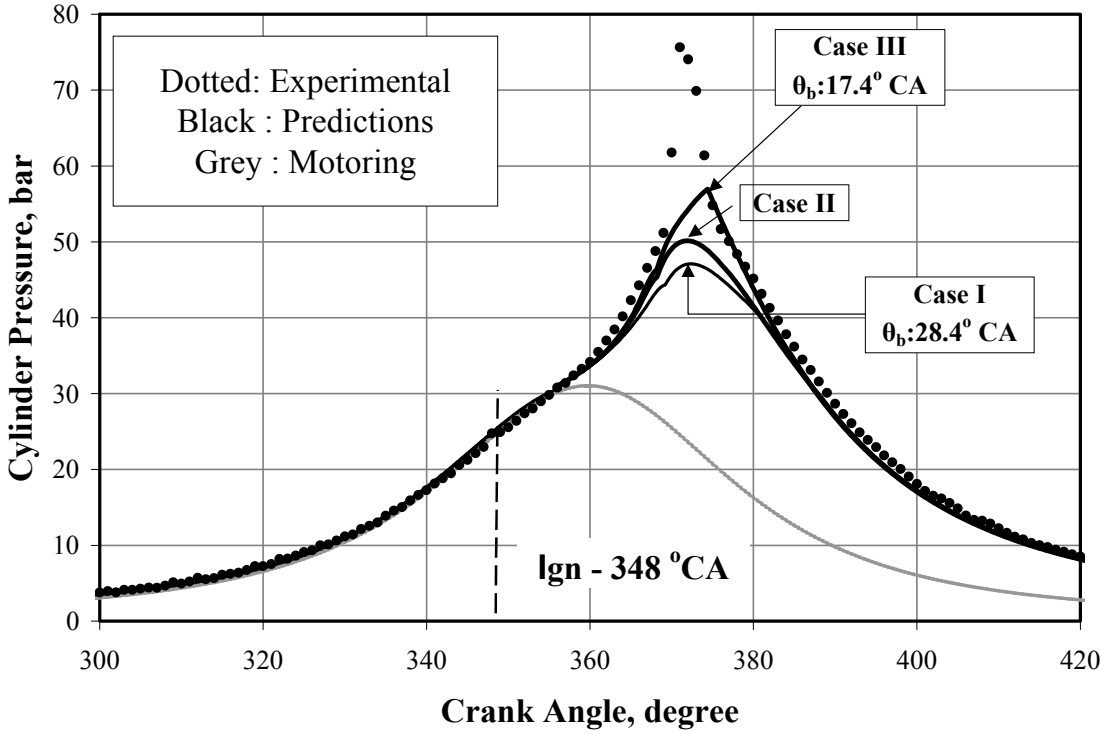

Fig. 7.16 p-θ Prediction at 12° CA Ignition Advance @ CR=17.0. Combustion Duration Excludes the Delay Period.

does not quench the surrounding walls and the flame remains afloat. This calls for the displacement of the spherical flame in a more complex manner than what has been accounted in this analysis. Using the test case of CR=17.0 at an ignition advance of 17° CA, computation are attempted with the flame kernel at various locations at the end of ignition delay period. These locations correspond to (1) at the ignition site and (2) with flame displaced deeper into the bowl on account of squish as shown in the inset of Fig. 7.15.

Predictions with flame kernel displaced deep into the bowl are poorer than Case I as shown in Fig. 7.15, where as the one at the ignition site is marginally better. But this assumption does not appear feasible considering the local fluid dynamics at the ignition site. However, it is evident that at advanced ignition settings (26 and 22 °CA), the computational results are excellent with flame movement based on velocities derived from CFD studies as noted earlier. If one were to consider that flame movement being adequately represented in the model, the increase in pressure could only be attributed to enhanced entrainment rate. This therefore called for a reexamination of the turbulence intensity values from the CFD studies. The computed CFD results showed a decline in turbulence kinetic energy beyond TC (Fig. 7.6); where as experimental results from the literature [Catania et al, 1996] suggested enhancement in turbulence intensity during the reverse squish period (after TC).

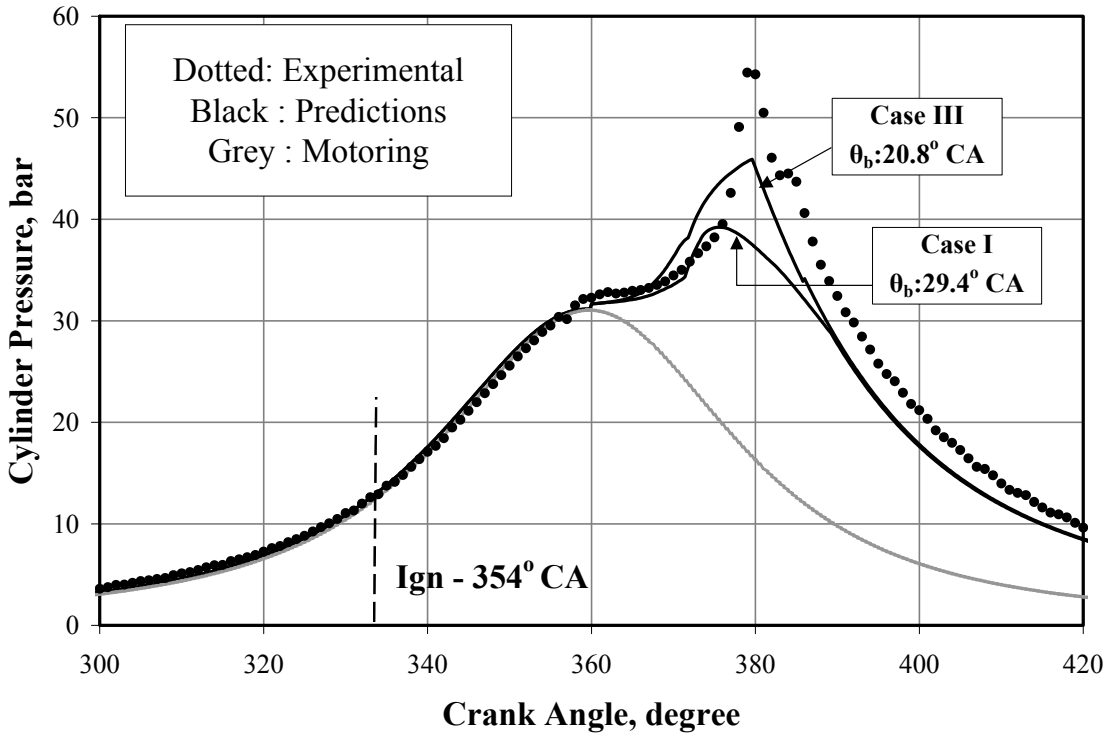

Fig. 7.17 p-θ Prediction at 6° CA Ignition Advance @ CR=17.0. Combustion Duration Excludes the Delay Period.

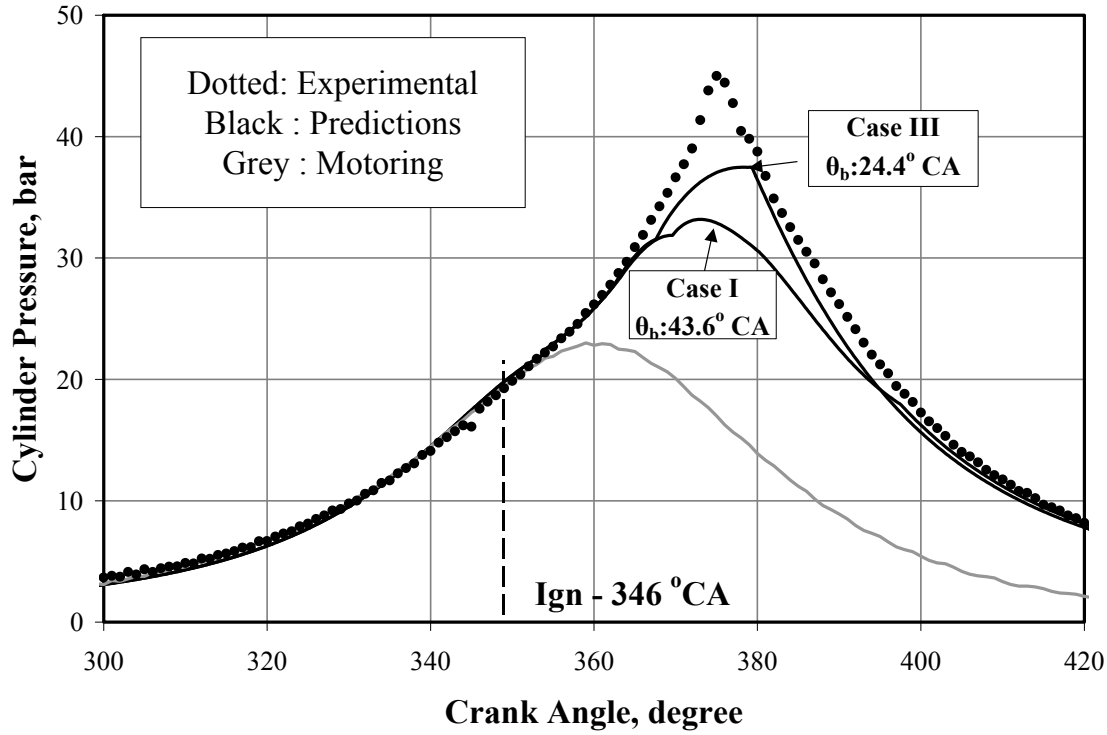

Fig. 7.18 p-θ Prediction at 14° CA Ignition Advance @ CR=13.5. Combustion Duration Excludes the Delay Period.

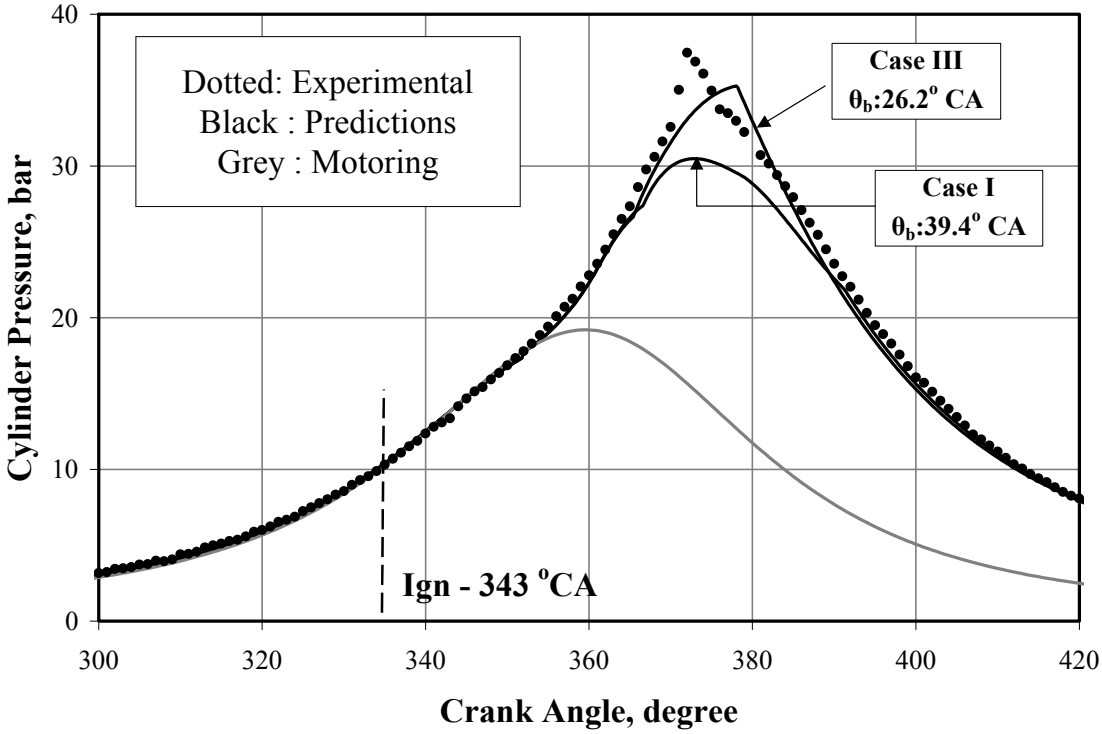

Fig. 7.19 p-θ Prediction at 17°CA Ignition Advance @ CR=11.5. Combustion Duration Excludes the Delay Period.

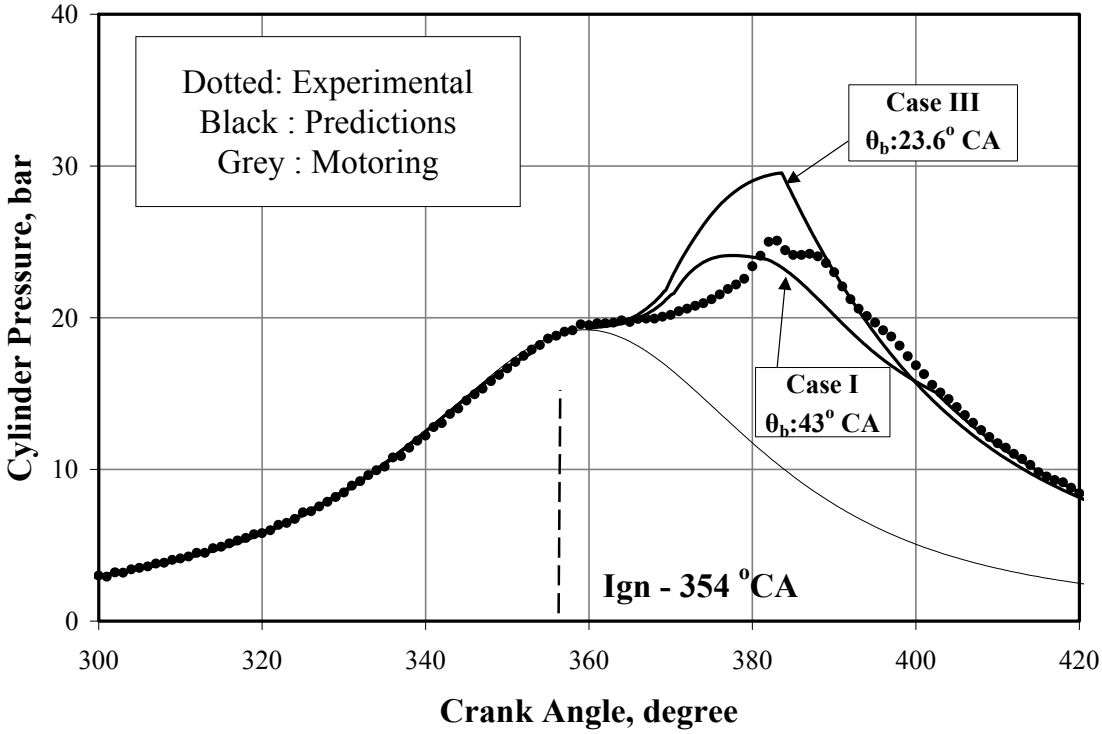

Fig. 7.20 p-θ Prediction at 6° CA Ignition Advance @ CR=11.5. Combustion Duration Excludes the Delay Period.

It is evident from CFD studies the presence of high shear zone (particularly close to the edge of the bowl) during the reverse squish period, it appears the k-ε turbulence model is unable to capture the transient effects except for small region at the edge of the bowl. Further computations are attempted with the hypothesis that turbulence intensity values from CFD studies are under-predicted during reverse squish period (post TC). The turbulence intensity considered for the pre-TC period is based on CFD results, for the post-TC period experimental trends of Catania et al [1996] shown in Fig. 7.6 is adopted. The results corresponding to ignition setting of 17 and 12° CA at CR=17.0 are shown as Case II in Figs. 7.14 and 7.16. The computed values show marginal improvement, but still the under-prediction appears to be large. Similarly the variation is found to be marginal in other four cases.

Upon further exploring the 0-D results (Case I) it became evident that in all the six test cases, major part of the combustion occurred during the reverse squish period wherein fluid dynamics within the combustion chamber is dominant. This point seems to indicate that the flow field during reverse squish period is enhancing the burn rate. This could well be so since there is steep increase in the cylinder pressure after a certain time, with a sharp pointed peak unlike a rounded peak at advanced ignition setting (Simple case). This called for a careful examination of the flow field generated from the CFD studies. The flow during the reverse squish period (366° CA) is shown in Fig. 7.21, wherein mean and peak velocities are in the range of 8-12 m/s and 20 m/s respectively. The variation of squish velocity (from CFD) as a function of CA at the edge of the bowl is shown in Fig 7.22. This part has been discussed in Section 6.6 of Chapter VI. Under reacting conditions (with combustion) these velocities would be much higher, by an order of 2.0 –2.5 consistent with the ratio of T_{burned} to $T_{unburned}$).

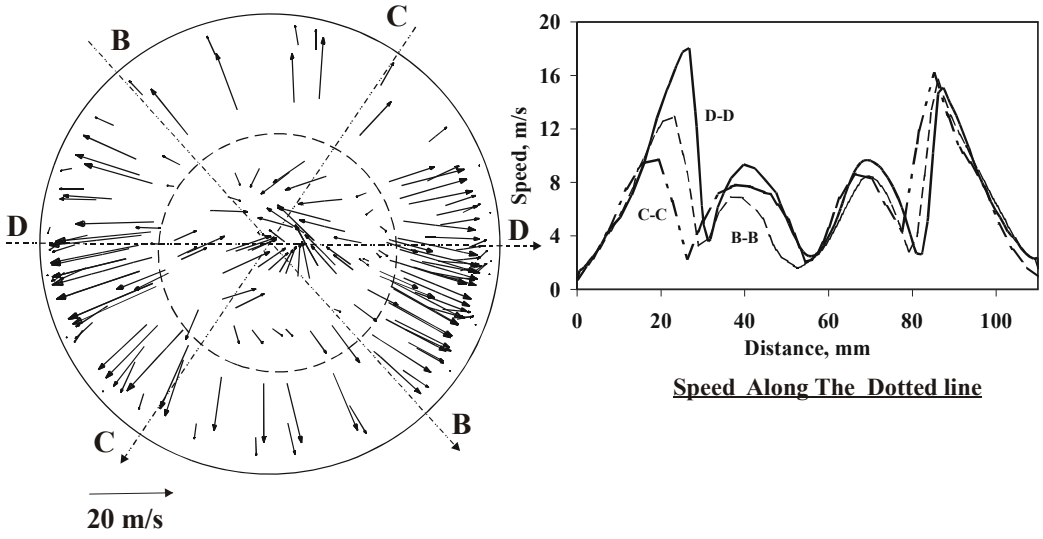

Fig. 7.21 Vector Plot in the Diametric Plane at a Distance of 0.2 mm Below Cylinder Head at 366° CA. Dotted Circle Represents the Edge of the Bowl.

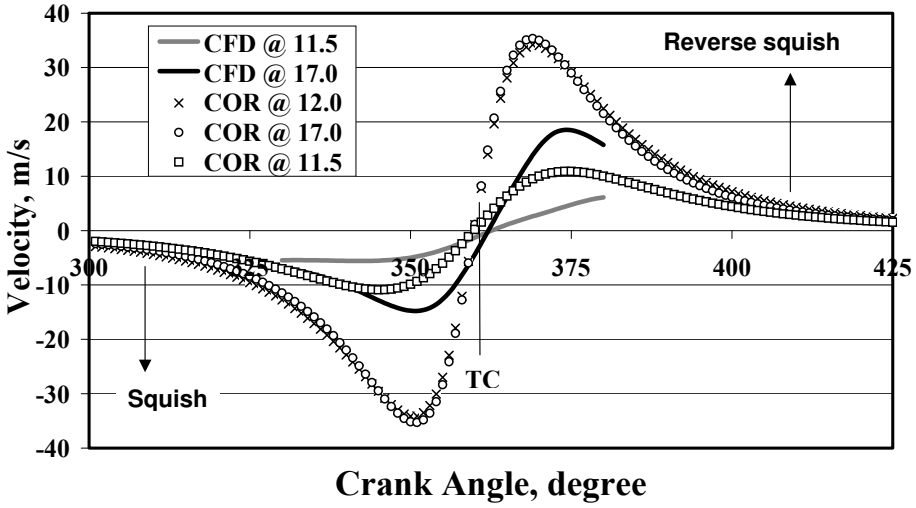

Fig. 7.22 Comparison of Squish Velocities from CFD and using an Empirical Correlation –COR [Heywood, 1988] at for the SPE Geometry (CR=17.0 and 11.5) and the MPE Geometry (CR=12.0).

Taking the fluid dynamics during reverse squish into account, a hypothesis is formed for flame propagation beyond the bowl region: the flame penetrates the flat section at the top with enhanced (depending upon the squish velocities around that time period) velocities, and then propagates into the unburned mixture at the same velocities in an annular cylindrical manner from the cylinder head downwards. This Reverse Squish Flame (RSF) hypothesis is pictorially depicted in Fig. 7.23. With the RSF hypothesis computations are re-attempted, where in a flat annular flame is assumed to travel outwards subsequent to spherical flame engulfing the bowl. The flat annular flame is assumed to travel at a rate dictated by the local outgoing fluid velocities as shown in Fig. 7.21.

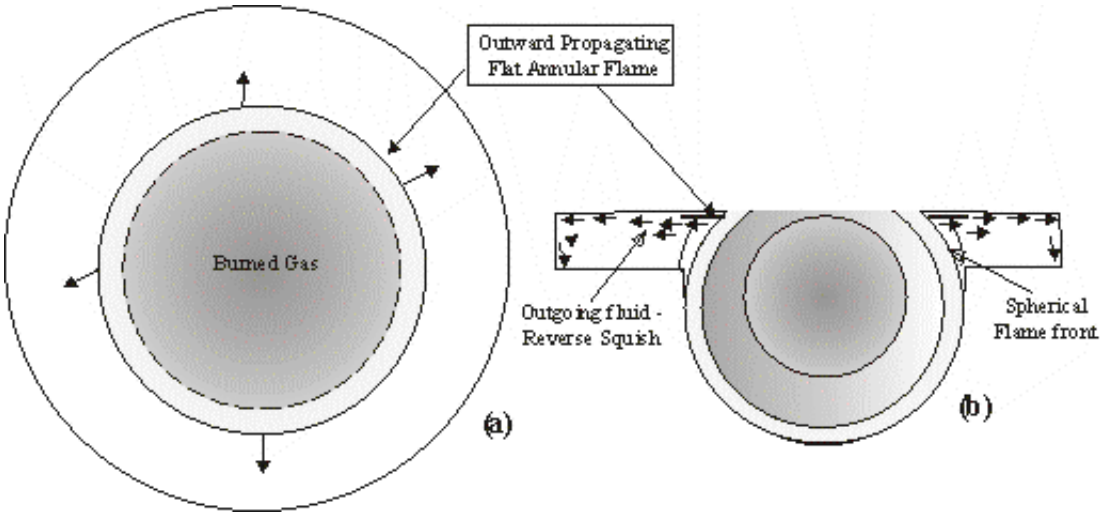

Fig. 7.23 Reverse Squish Flame (RSF) Hypothesis. (a) Flat Annular Flame Propagating Outward along the Cylinder Head (b) Axial View Showing Flat Flame Propagation Due to Outward Flow of Fluid. The Dotted Circle Shows the Trace of Spherical Flame on the Cylinder Head.

Under reacting conditions, these velocities assume higher value in commensurate with the ratio $T_{burned}/T_{unburnted}$ All features of EELB flame propagation

are taken valid except that flame shape is considered 'Flat'. With these assumptions the predictions are better, shown as Case III for all test cases in Figs. 7.14 to 7.20. The principal results are given in Table –7.8. It is evident that combustion duration is lower with RSF hypothesis compared to entirely spherical flame assumption.

Table –7.8: Principal Results of 'Complex - I' Cases. Mass Burned Fraction (MBF) corresponds to 372° CA.

Case	Experiment		Prediction			
	Peak Pressure, bar	Occurrence, °CA	Peak Pressure, bar	Occurrence, °CA	Duration, °CA	MBF, %
CR=17.0, 17° CA						
I	67.4	369	52.0	370.8	37.2	84
III	67.4	369	59.0	372.8	30.0	100
CR=17.0, 12° CA						
I	75.6	371	47.1	372.4	37.4	72
III	75.6	371	57.0	374.4	26.4	92
CR=17.0, 6° CA						
I	54.5	379	39.2	375.0	35.4	42
III	54.5	379	43.7	380.8	26.8	56
CR=13.5, 14° CA						
I	45.0	376	33.2	373.2	52.6	62
III	45.0	376	37.5	379.2	33.4	80
CR=11.5, 17° CA						
I	37.5	372	30.5	373.0	48.4	66
III	37.5	372	35.8	378.4	35.2	88
CR=11.5, 6° CA						
I	25.0	383	24.0	377.6	52.0	39
III	25.0	383	25.5	383.6	23.6	52

The mass burned fraction (MBF) – including the entrained mass at the time of peak reverse squish effect (Case I – with spherical flame assumption) is given in Table – 7.8, which shows large variation in MBF for a given ignition setting at different CR's. This clearly indicates that there is substantial amount of unburned fuel in the combustion chamber and all that is required is a mechanism to trigger the rapid energy release apart from normal flame propagation. One such theory proposed in this thesis is the RSF hypothesis; the predicted pressures with RSF hypothesis are better than entirely spherical flame assumption for all the six cases. The unburned fuel corresponding to 372° CA is relatively lower with RSF compared to spherical flame assumption according to Table 7.8. However, the peak pressures are lower, with point of occurrence at a later point compared to experiments. The predictions still do not simulate the steep rise in pressure; this therefore points towards fluid dynamics being too complex during reverse squish period and appears to wield a major influence in altering the burn rate. Here the author would like to reemphasize that this sudden act of rapid energy release is not an abnormal combustion, namely knock or surface ignition. This is argued not to be so because if it were to be so then it should have been evident at advanced ignition setting, wherein conditions are more favorable. Moreover, this sharp rise in pressure is not desirable because of its contribution to higher power output. Therefore, in the current context it is difficult to perceive the exact mechanism by which there is a sudden

increase in burn rate, nevertheless the data point towards that. In addition to what has been proposed in the RSF hypothesis it is quite possible that the hot burned products flowing out of the bowl during reverse squish period are mixing with the unburned mixture in the flat region, which is followed by nearly instantaneous burning due to the thin tongue igniting. The change in the velocity distribution pattern in the flat part of the piston geometry as evident from Fig. 7.24 (a) could result in large velocity gradient under reacting conditions. Such a situation could lead to formation of vortices, wherein the burned gas emerging out of the bowl (during peak of reverse squish period) could mix with the unburned mixture above the flat part of the piston geometry. The hypothesis is schematically depicted in Fig. 7.24 (b). This mechanism appears to be strongly dependent on the local fluid dynamics caused due to engine geometry and the piston movement. The factors that appear to dictate pressure rise in the later part of combustion are, the time of the spherical flame engulfing the bowl (whether coinciding with the reverse squish effect becoming dominant) - the magnitude of reverse squish velocity, amount of unburned mixture in the flat region of the combustion chamber and relative magnitude of energy release rate to cylinder volume changes. This argument appears to be consistent with the experimental p-θ data, wherein at an ignition timing of 17° CA (CR = 17.0), there is a sharp rise in the cylinder pressure, occurring over 2-3° CA, where as at 6° CA this is observed to occur over 7-8° CA. Further analyzing, at a less retarded ignition setting (17° CA), the amount of unburned mixture is lower; therefore mixing would be rapid, thus resulting in instantaneous burning.

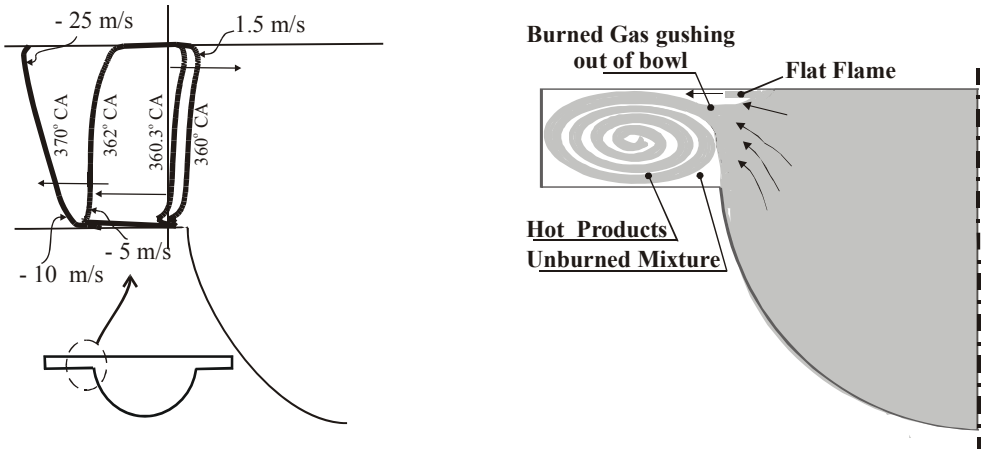

Fig. 7.24 (a) Velocity distribution close to the edge of the bowl (u component) - above Flat Region of the Piston at the end of squish period and in the Reverse Squish period (b) Hypothesis Depicting Burned Gas Outflow from the Bowl Into the Cylindrical Region During Reverse Squish Period. The Mixing of the Burned Gas with the Unburned Gas in the Presence of a Flat Flame Could Result in Rapid Burn Rate.

However, at retarded ignition setting (6° CA) the fraction of unburned mixture is relatively larger, thus requiring more time for mixing and as a consequence the heat release rate is gradual. Moreover, the thermodynamic conditions at less retarded ignition setting is favourable for steep rise in cylinder pressure. These observations are not that evident at low CR probably due to lower reverse squish velocities.

A comparison of energy balance on similar lines to the earlier case is shown in Table 7.9. The predicted IP_G improves with the RSF hypothesis at all ignition settings and CRs.

Table – 7.9: Comparison of Energy Balance (kW) of 'Complex –I' Cases

Mode	IE	IP_G	F_L	BP_N	F_A	F_A	Exhaust	Coolant/Wall
CR=17.0, 17° CA								
Ex-org	63.5	23.4	-	18.4	-	-	19.0	26.1
Ex-red	63.5	23.4	1.1	18.4	1.4	2.5	16.9	22.2
0-D - I	63.5	21.7	1.3	NC	NC	NC	21.6	18.9
0-D -III	63.5	21.9	1.3	NC	NC	NC	21.3	19.0
CR=17.0, 12° CA								
Ex-org	63.6	25.2	-	19.8	-	-	17.0	26.8
Ex-red	63.6	25.2	1.1	19.8	1.4	2.9	15.9	22.5
0-D -I	63.6	22.0	1.3	NC	NC	NC	21.6	18.7
0-D -III	63.6	22.7	1.3	NC	NC	NC	20.9	18.7
CR=17.0, 6° CA								
Ex-org	65.0	25.3	-	20.0	-	-	18.5	26.5
Ex-red	65.0	25.3	1.2	20.0	1.4	2.8	17.3	22.3
0-D -I	65.0	21.1	1.3	NC	NC	NC	24.6	18.0
0-D -III	65.0	22.4	1.3	NC	NC	NC	23.2	18.0
CR=13.5, 14° CA								
Ex-org	63.0	22.5	-	18.6	-	-	24.5	19.9
Ex-red	63.0	22.5	1.1	18.6	1.4	1.4	23.4	17.1
0-D- I	63.0	19.5	1.3	NC	NC	NC	23.5	18.6
0-D -III	63.0	19.9	1.3	NC	NC	NC	22.8	19.0
CR=11.5, 17° CA								
Ex-org	64.0	21.0	-	17.6	-	-	27.6	18.8
Ex-red	64.0	21.0	1.1	17.6	1.4	0.9	26.5	16.5
0-D - I	64.0	19.9	1.3	NC	NC	NC	24.2	18.6
0-D -III	64.0	20.3	1.3	NC	NC	NC	23.4	19.0
CR=11.5, 6° CA								
Ex-org	63.0	20.5	-	17.0	-	-	25.2	20.8
Ex-red	63.0	20.5	1.2	17.0	1.4	1.0	24.0	18.4
0-D- I	63.0	18.9	1.3	NC	NC	NC	24.8	18.0
0-D- III	63.0	19.8	1.3	NC	NC	NC	23.3	18.6

Ex-org: original experimental results, Ex-red: redistributed results NC: Not Computed

The predicted heat loss through exhaust and coolant/wall compares reasonably with the experimental data and any marginal variation in these values is again attributed to the selection of the heat transfer coefficient. However, 17° CA corresponding to CR=11.5 is an exceptional case wherein the experimental heat loss is higher due large fraction of unburned CO (40%) constituting the exhaust energy.

7.12 Predictions of p-θ Curve – Complex –II Cases

Two test cases at a fixed CR of 12.0 belonging to MPE are categorized under complex - II and their salient features are repeated in the Table 7.10 for ease of reference.

Table –7.10: Principal Parameters of 'Complex – II' Cases

No.	CR	Composition, Vol, %			Φ	RG %	Input* Energy/ cycle, kJ	Ign, °CA	Ign#. Delay, °CA	Category
		H_2	CO	CH_4						
12	12.0	19.5	19.0	0.6	0.91	8.5	3.25	19	8	Complex -II
13	12.0	18.5	19.0	0.5	0.91	8.5	3.25	12	5	Complex -II

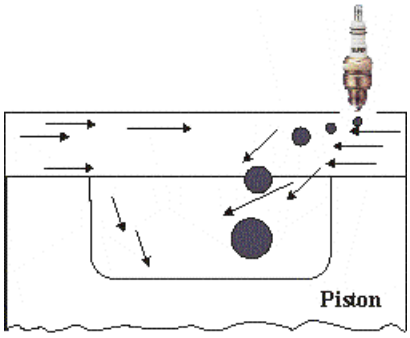

Fig. 7.25 Flame Kernel Displacement into the Bowl Due to the Effect of Squish

Predictions are initially shown using simple spherical flame propagation model, followed by RSF hypothesis. An important aspect to be noticed in the combustion chamber is the location of ignition source i.e. spark plug. The spark plug in this particular geometry is located at an offset, which lies on a plane above the flat part of the piston. In the event of flame kernel formation after ignition, the flame kernel is bound to be exposed to higher velocities and there by get displaced deeper into the bowl as shown in Fig 7.25. Displacement of the flame as a consequence of squish phenomenon could be much more complex than what is accounted in the model. This could also be one of the reasons for ignition delay to be shorter compared to SPE test cases at corresponding ignition setting, despite fuel-air mixture being lean. Considering offset spark plug location, higher velocity is considered for the initial flame kernel movement, which is of the order of squish velocity (20 –25 m/s). At the end of the ignition delay period the flame kernel is assumed to be along the axis of the combustion chamber due to symmetry in the flow field. The methodology adopted for computation is the same as discussed earlier. The turbulence intensity considered in the model is higher by 25% than that of SPE, the length scale employed corresponds to that employed in CR=11.5. This part has been bought out in Section 7.7. For the flame movement, squish velocities obtained from CFD corresponding to CR=17.0 are used *since bumping clearance in MPE is nearly same as that of SPE at the highest CR*. All other geometric parameters with respect to the combustion chamber of MPE are adopted and the valve profile shown in Fig. 7.4 is considered. All other parameters relating to C_d, and heat transfer coefficients adopted in the earlier predictions are taken valid for MPE. No additional resistance in the gas exhaust line caused due to the presence of the turbo-charger is considered, which essentially means flow through the turbo-charger is not modeled. However, for the purpose of calculations, the recorded charge pressure (experimental data) downstream of the turbo-charger is used as the intake manifold pressure. There the intake manifold pressure is assumed to be constant (1.25 bar) through the suction process of the calculations, since the variation in the manifold pressure could be marginal with a twelve-cylinder engine.

7.12.1 Results

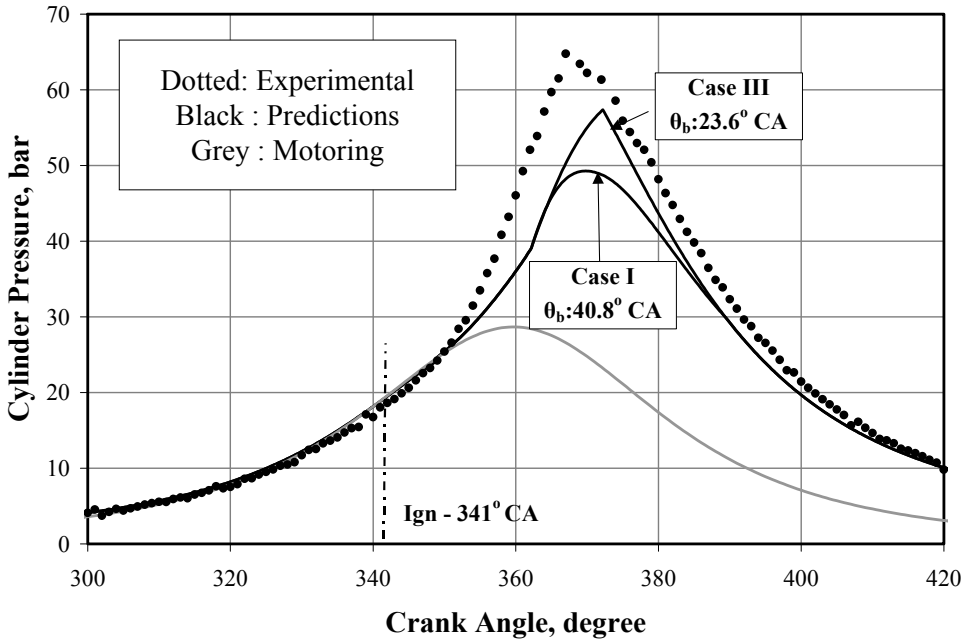

Fig. 7.26 p-θ Prediction at 19° CA Ignition Advance with MPE Geometry. Combustion Duration Excludes the Delay Period.

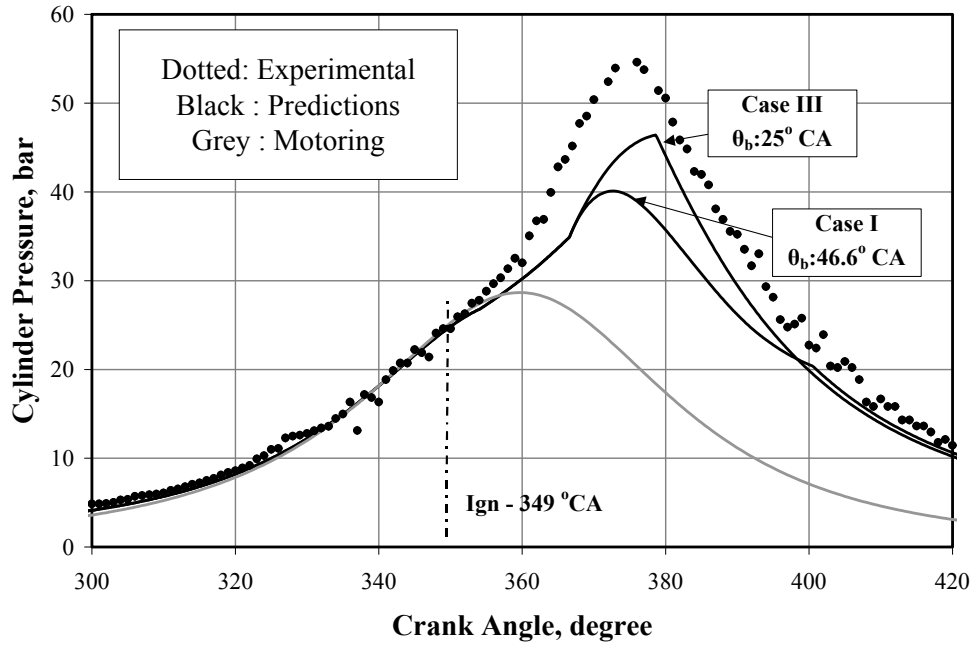

Fig. 7.27 p-θ Prediction at 12° CA Ignition Advance with MPE Geometry. Combustion Duration Excludes the Delay Period.

Table –7.11: Principal Results of 'Complex - II' Cases. Mass Burned Fraction (MBF) Corresponds to 372° CA

Case	Experiment		Prediction			
	Peak Pressure, bar	Occurrence, ° CA	Peak Pressure, bar	Occurrence, °CA	Duration, ° CA	MBF, %
CR=12.0, 19° CA						
I	65.0	367	49.3	369.8	48.8	90
III	65.0	367	56.7	372.6	31.6	100
CR=12.0, 12° CA						
I	55.0	376	40.1	37.8.0	46.6	66
III	55.0	376	46.0	379.0	30.0	69

The predictions for the two test cases are shown in Figs. 7.26 and 7.27 with spherical flame and RSF hypothesis as Case I and Case III respectively. It is evident from Figs. 7.25 and 7.26 that there is departure in the computed pressure right at the commencement of heat release and the peak pressures are also under-predicted. With RSF hypothesis, the predicted pressure is better but falls short of the experimental values. *Hence these predictions can be taken as indicative and not yet predictive.* In the case of 12° CA, the amount of unburned fuel at the time when reverse squish velocity becomes significant is larger as shown in Table 7.11. Therefore similar such mechanism as stated earlier is perceived to be occurring at retarded ignition setting, wherein burned gas flowing out of the bowl mixes with the unburned fuel contributing towards rapid burn out (Fig. 7.24). To establish the final results, the pressure-volume data is integrated to determine the indicated power (IP_G) and the pumping losses – incurred with respect to the suction and exhaust processes. The data obtained from the single cylinder analysis is considered to be a reasonable representative of the remaining eleven cylinders of MPE and therefore reported for the complete engine. These values are compared with the respective experimental energy balance as shown in Table 7.12.

Table – 7.12: Comparison of Energy Balance (kW) of 'Complex –II' Cases

Mode	IE	IP_G	F_L	BP_N	F_A	F_A	Exhaust	Coolant/Wall
CR=12.0, 19° CA								
Ex-org	490	177	-	148	-	-	190	152
Ex-red	*490*	*177*	*1.0*	*148*	*12.0*	*16.0*	*189*	*124*
0-D- I	490	164	11.0	NC	NC	NC	176	139
0-D -III	490	169	11.0	NC	NC	NC	165	145
CR=12.0, 12° CA								
Ex-org	490	177	-	149	-	-	195	146
Ex-red	*490*	*177*	*4.0*	*149*	*12.0*	*12.0*	*191*	*122*
0-D- I	490	157	12.0	NC	NC	NC	190	130
0-D -III	490	164	12.0	NC	NC	NC	179	135

Ex-org: original experimental results, Ex-red: redistributed results NC: Not Computed

The predicted IP_G is lower by 7.5 and 12% respectively for the above two cases with spherical flame propagation model. The predications in terms of the indicated power are better with RSF hypothesis. The overall energy balance compares reasonably well with the experimental data, however the computed pumping losses are higher compared to experimental results. The uncertainty in the discharge coefficients of the valves of this engine is possibly the reason for this discrepancy. Further refinement is

not attempted because the error in experimental measurement of pumping loss is fairly large, as it is obtained as the difference between two nearly equal quantities while integrating the p-v curve.

7.13 Sensitivity Analysis

Among the assumptions considered for 0-D predictions as stated in section 7.4, heat transfer coefficients for different processes were essentially obtained by matching one of the test cases against its corresponding result. The overall energy balance comparison is found to be reasonable in most cases. Similarly value of C_d for the gas exchange process was obtained by matching against motoring curve. This leaves apart the combustion wall temperature, which is considered at a fixed value of 450 K for all the processes. A sensitivity analysis considering 25° C variation in the wall temperature does not influence the results significantly (IP variation by < 0.5%). Further sensitivity analysis is considered in terms of varying the laminar burning velocity ($\pm$ 10%), turbulence intensity ($\pm$10%) and ignition delay ($\pm$3° CA). Test case belonging to CR=17.0 corresponding to an ignition timing of 22° CA is considered as reference and results are shown in in Figs. 7.28 to 7.30. The predicted pressures are marginally lower with the reduction in the laminar burning velocity and turbulence intensity. However, the rate of heat release seems to be different with different ignition delay periods. Any variation in the predicted pressure should ultimately impact the indicated output. From the results summarized in Table 7.13, it is clear that 10% variation in laminar burning velocity and turbulence intensity has very little influence on the IP_G, similarly variation in the ignition delay period lowers the output by about 3%.

Table- 7.13: Sensitivity Analysis towards IP_G (kW) Prediction at 22° CA

Exp IP_G	0-D nominal	S_L, m/s		u', m/s		θ_{delay}, ° CA	
		-10%	+10%	-10%	+10%	-2	+2
22.4	21.8	21.75	21.71	21.70	21.73	21.0	21.2

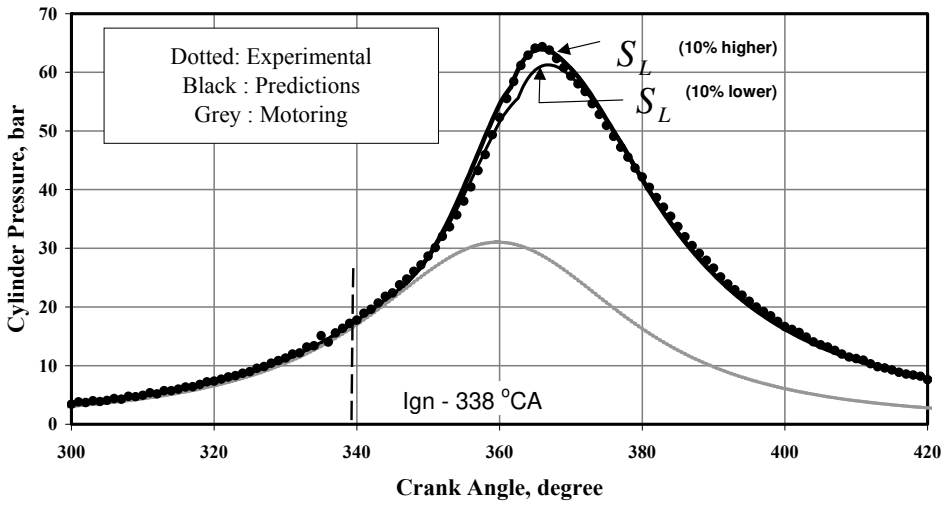

Fig. 7.28 p-θ Prediction at 22° CA Ignition Advance with $\pm$ 10% Variation in S_L

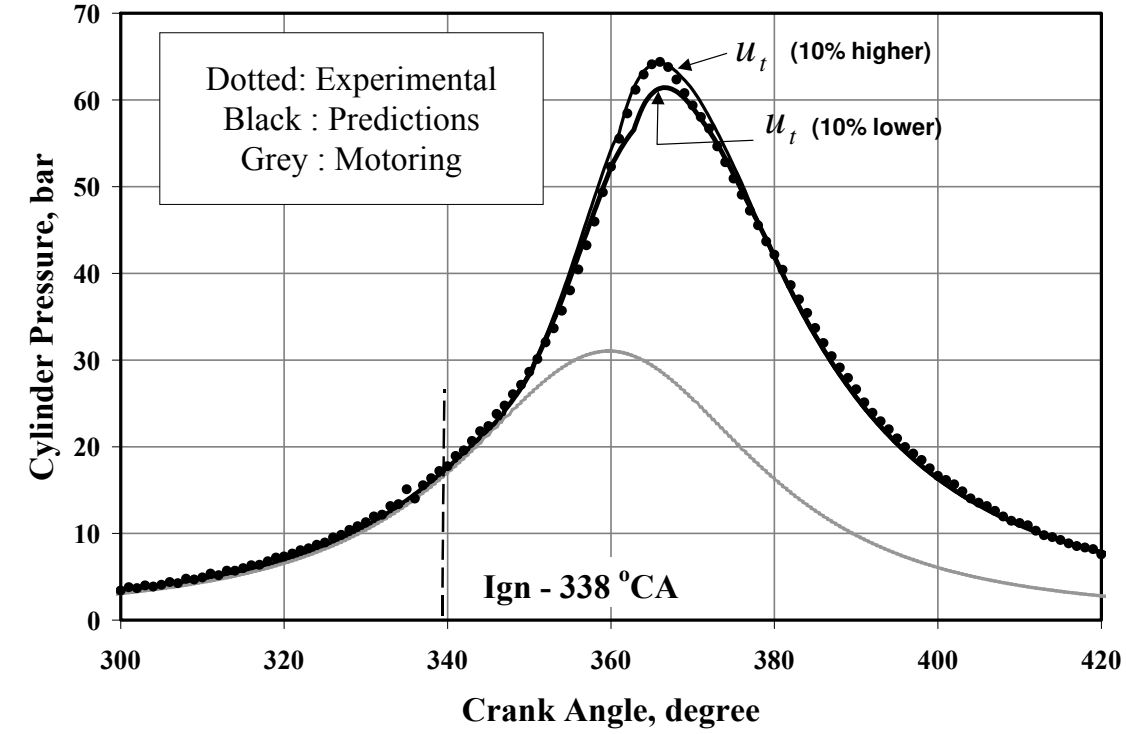

Fig. 7.29 p-θ Prediction at 22° CA Ignition Advance with ± 10% Variation in *u′*

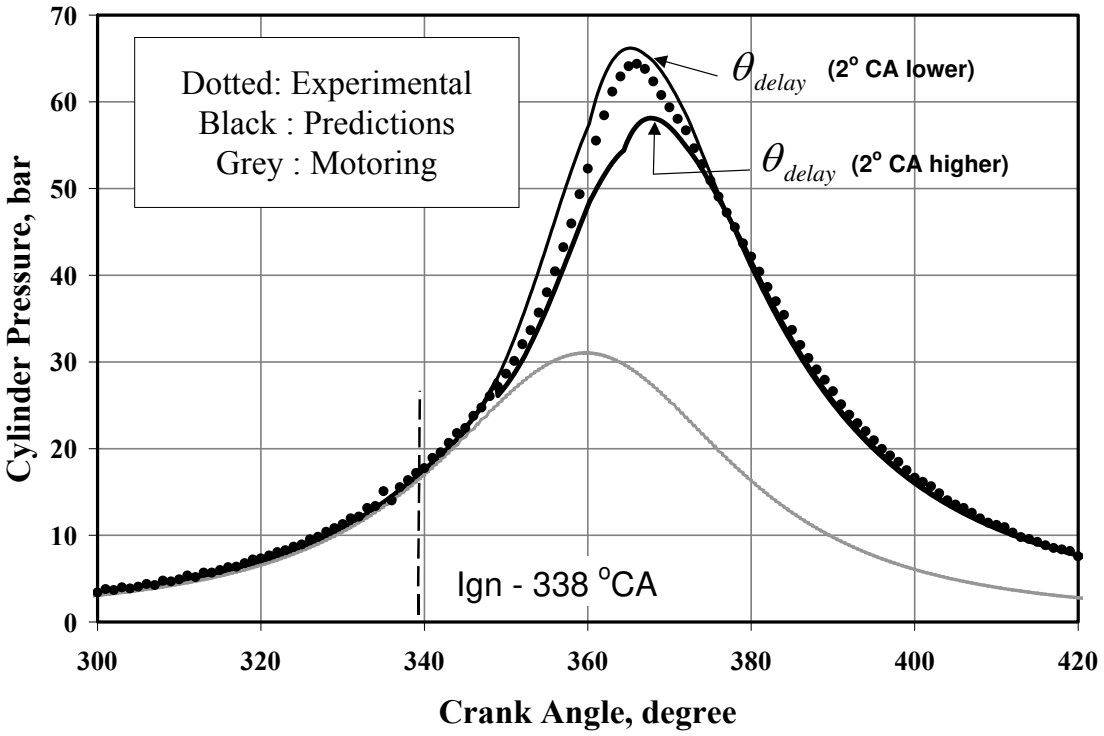

Fig. 7.30 p-θ Prediction at 22° CA with Different Ignition Delay Period

7.14 Observations

The findings of 0-D model are summarized in Table 7.14. In the four simple cases identified, the 0-D model is able to make reasonably good predictions by assuming the conventional spherical flame propagation model. The accuracy in IP prediction is around 3% for CR=17.0 and 11.5, and between 5 and 8% for the other two cases at CR=13.5. Among the six cases dealt under complex-I category, predictions appear to be better by assuming the RSF hypothesis. In fact the accuracy in the IP computation improves in all the six cases. Similar is the trend with Complex – II cases.

Table 7.14: Summary of 0-D Predictions for Different Test Cases. Turbulence Intensity Results from CFD Analysis and *ref* - Experimental Results on an Engine with Similar Configuration [Catania et al, 1996]. The Flame Shape Accounted in the Prediction both Inside and Outside the Bowl is Also Given.

Case No.		Flame Shape - Region		u'		0-D# Error, %
		Inside Bowl	Outside Bowl	Pre-TC	Post-TC	
Simple						
1		Spherical		CFD		1.5
2		Spherical		CFD		3.0
6		Spherical		CFD		5.0
7		Spherical		CFD		8.0
9		Spherical		CFD		3.2
Complex – I & II						
3	Case I	Spherical	Spherical	CFD	CFD	8.0
	Case III	Spherical	Flat	CFD	*ref*	6.0
4	Case I	Spherical	Spherical;	CFD	CFD	13.0
	Case III	Spherical	Flat	CFD	*ref*	10.0
5	Case I	Spherical	Spherical	CFD	CFD	16.0
	Case III	Spherical	Flat	CFD	*ref*	11.4
8	Case I	Spherical	Spherical	CFD	CFD	13.0
	Case III	Spherical	Flat	CFD	*ref*	11.5
10	Case I	Spherical;	Spherical	CFD	CFD	5.2
	Case III	Normal	Flat	CFD	*ref*	3.3
11	Case I	Spherical	Spherical	CFD	CFD	8.0
	Case III	Spherical	Flat	CFD	*ref*	3.0
12	Case I	Spherical	Spherical	CFD	CFD	7.5
	Case III	Spherical	Flat	CFD	*ref*	4.5
13	Case I	Spherical	Spherical	CFD	CFD	10.0
	Case III	Spherical	Flat	CFD	*ref*	7.3

Error is defined as the ratio of computed IP_G to Experimental IP_G

Summarizing the 0-D prediction qualitatively, the 0-D model is able to make reasonably accurate predictions at advanced ignition settings (above 17° BTC) using classical EELB heat release sub-model. However, at retarded ignition setting (< 17° BTC) the enhanced fluid dynamics due to reverse squish flow modifies the burn rate to such an extent that

there is a steep rise in cylinder pressure. By making use of the insight obtained from the cold flow CFD studies a hypothesis namely, Reverse Squish Flame (RSF) has been formulated wherein the outgoing fluid is assumed to modify the flame shape from spherical to flat. With this hypothesis the predictions are better but still differs from the experimental values both qualitatively and quantitatively. An interesting point to be brought is the large fraction of unburned fuel at such a point beyond which there is rapid release of energy. The exact mechanism by which rapid energy release is occurring is not clear, however a few indicators towards such possibility have been brought out. Therefore fluid-flame interaction is sufficiently complex and predictions with simpler techniques like 0-D model are not possible. This calls for a full-fledged 3-D modeling with combustion for further understanding.

7.15 Summary

0-D predictions are presented for twelve test cases of two engine geometries at different CRs by categorizing them according to their intricacies. The overall energy balance has been compared against the experimental results. These show a good agreement for cases of lower compression ratio and advanced ignition timings. For other cases, additional hypothesis are invoked and ways of improving the predictions are explored.

Predictions of Zero-D Model 98

Chapter VIII

Overview

In this final chapter, the principal contributions of the present work have been highlighted. The areas in which further research could be pursued are brought out.

8.1 Contribution of the Present Work

The first principal contribution of the present work is the revelation of non-knock performance of producer gas in high compression ratio (CR) spark-ignited engine. Earlier to this work, the general perception was that producer gas would knock when operated in high CR spark-ignited engine. This perception has been proved to be incorrect by making systematic investigations on a 20 kW rating (SPE) spark ignition engine converted from a production diesel engine at varying compression ratios of 17, 14.5, 13.5 and 11.5. The engine operation was found to be smooth at the highest CR of 17.0 without any undesirable effects of knock as discerned from the pressure-crank angle (p-θ) curve, which showed smooth rise in pressure without any pressure oscillations. However, there was de-rating of the engine power, which is about 16.7% at a CR of 17.0 and increased to 26% at a CR of 11.5. Maximum net power (excluding power consumed by fan and accessories) is recorded at a fuel-air equivalence ratio of 1.08 ± 0.2, with gas to useful shaft power conversion efficiency being 30.7 and 27.5% respectively for the highest and lowest CR. The reduction in power output with producer gas is attributed to reduction in the net calorific value of the fuel gas and air mixture, and to the net reduction in number of molecules as the mixture goes to product gases. In terms of emissions, the NOx level are well below the emission norms in India and abroad, the CO level is found to be higher when operated at slightly fuel rich conditions where maximum power is delivered. However, the CO levels will be within norms when the engine is operated at stoichiometry or slightly leaner condition. The second level of testing attempted on the 250 kW (MPE) gas engine revealed smooth

operations at the designed CR=12.0. The de-rating on this engine was found to be about 21% compared with diluted natural gas operation on similar engine. The emission in terms of NOx and CO is well below than all existing emission norms. The lower CO content with this engine is attributed to better air-to-fuel ratio control. Another important outcome from this experimental work is that the optimum ignition timing for producer gas operation is retarded compared to natural gas operation at comparable CR. This is attributed to higher laminar burning velocity of producer gas compared to natural gas. The high laminar burning velocity contributed to faster combustion as a result, there is low cycle-to-cycle variation in the indicated mean effective pressure (IMEP) at all CRs and ignition timings.

In the modelling part, a zero-dimensional (0-D) model is constructed to simulate the processes of a spark-ignition engine operation. The heat release part, which is key to the modelling, is based on the well-postulated Eddy Break-up and Laminar Burn-up model meant for turbulent pre-mixed wrinkled flames. The two key input parameter sets for the heat release sub-model are derived from further computations. The laminar burning velocity data, at pressures and temperatures encountered in an engine combustion chamber is obtained from computations based on a one dimensional flame code. The turbulence parameters, namely, turbulent intensity and integral length scale are obtained from three-dimensional CFD computations for engine combustion chamber geometry, involving bowl-in piston arrangement at CR of 17.0 and 11.5. These turbulence parameters are further assumed to undergo variations under reacting conditions by using simple rapid distortion process as stated in the literature. The variation of motored turbulence parameters under reacting condition need to be further explored using techniques such as Large Eddy Simulation.

One experimental firing case is used as a test case in tuning the 0-D model in terms of constants required for computation of heat loss. Subsequently, keeping these parameters fixed 0-D predications are made for twelve test cases involving combustion chambers of SPE and MPE at varying CRs and ignition settings. These are further categorized under three sub-groups, namely Simple, Complex I and Complex II depending upon the intricacy involved in the predictions. Under the Simple sub-group four test cases of SPE are dealt, wherein the predictions match very well with the experimental p-θ curve. These computations are attempted assuming simple spherical flame propagation model. Whereas, under Complex-I and II sub-group eight cases are dealt, wherein the cylinder pressures are under-predicted with simple spherical flame propagation model. It is observed that in most of these cases, a major part of the combustion occurred during the reverse squish period, wherein the enhanced fluid movement could be modifying the burn rate to substantially high values. The exact mechanism by which it is occurring is not clear, nevertheless an indicator towards that has been formulated, which is termed as 'Reverse Squish Flame'. Under this hypothesis the enhanced fluid movement is assumed to modify the burn rate. Predictions with this hypothesis are better but falls short of experimental results. An interesting point to be brought is the large fraction of unburned fuel at such a point beyond which there is rapid release of energy. The exact mechanism by which rapid energy release is occurring is not clear, but full computation of reacting flow field is expected to reveal this.

At this stage one might like to ask about the usefulness of the 0-D model in a general way. The answer to this is as follows. Most of the engines built for gaseous fuel like the natural gas are of CR 12.0 and below. And moreover, most of the gas engines are designed for lean-burn operation and therefore adopt complex shaped geometries (eg. bowl-in piston), supported with a centrally located spark plug to enhance the burn-rate. The optimum ignition advance for these fuels is between 24 – 28° BTC. These conditions permit a flow-field that would have marginal role of reverse squish in modifying the burn-rate. In all such cases the methodology developed here would provide 'good' predictions (within a few percent).

8.2 Scope for Future Work

To understand the complex fluid flow-flame interaction under reverse squish conditions requires a detailed 3-D modelling under reacting conditions. This is essential in order to establish some of the theories proposed with respect to Reserve Squish Flame hypothesis in this work. Understanding these features and incorporating them in the Eddy Entrainment and Laminar Burn-up model in some form would extend the applicability of 0-D model.

Appendix - I

Open Top Re-burn Gasifier

The Solar Energy Research Institute [SERI, 1979] document has in it a description of several systems and statements indicating the difficulty of building reliable gasification systems at small power. These relate to the quality of the gas in terms of energy and the particulate and tar content of the gas. Though the poor energy conversion of solid fuel to the gas was acceptable, the higher particulate and tar caused difficulties in using the gas for engine application. Even though a limited amount of research and development was attempted during the early forties, many interesting aspects have been documented by SERI. Most of the reporting in SERI has been on closed top gasification system. Several groups, all over the world, continued the work on the closed top system and have been improving the engineering and the control system with a limited extent on the basic research towards the understanding of the process; involving a large amount of financial support from various agencies.

Initially, the gasification systems were built with wood chips as fuel. Much later, the work attributed to the Chinese origin, an open top system, for rice hulls in as received-mode was developed and several systems based on these concepts have been built in India and Thailand. Consequently, several problems were reported with this design – high tar level in the gas and unconverted carbon in the ash.

Understanding the reasons of the issues involved called for fundamental studies. These studies as well as design and developmental work with extensive experimentation have resulted in a reactor design at IISc that could be used for any bio-residue. This evolution resulted in abandoning nearly all concepts evolved in the closed top system for a user-friendly, modern gasification technology. The concept of closed and open top design and their comparison is discussed below.

Closed vs Open Top Design

The closed top gasifier belongs to the World War II era, with modest improvements in technology in the recent times. It basically consists of a cylindrical reactor with a closed top and a narrow throat at the bottom as shown in Fig. A.1. The required air for gasification is drawn through the surrounding air nozzles/tuyers provided at the oxidation zone. The reactor top is removable and the charcoal/biomass is charged from the top. At the time of gasifier operation the top is kept closed, which essentially means the system operates in a batch mode and once the charge is consumed, the operations are halted and fresh biomass is charged. The char/ash is removed at the bottom.

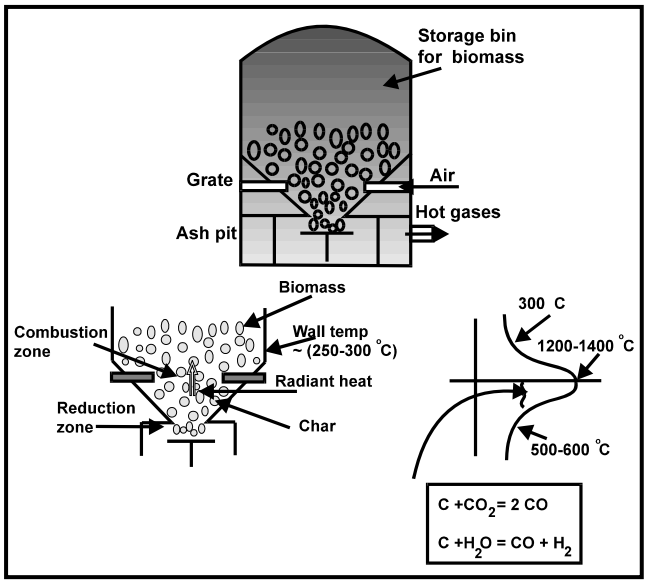

Fig A.1 Conventional Closed Top Reactor

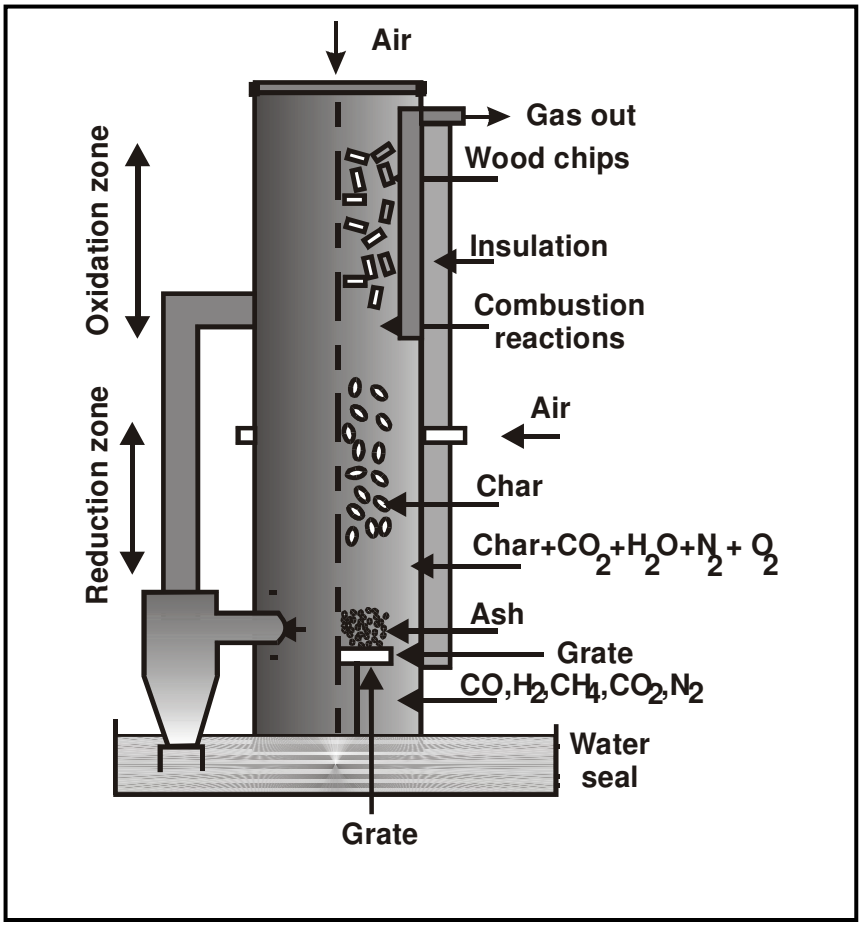

Fig A.2 Modern Open Top Re-burn Downdraft Reactor

The Open top system is a design evolved over a decade. The design at one of the stages of development shown in Fig. A.2 and has a grate at the reactor bottom. The subsequent design is with a screw based char/ash extraction system as discussed in Chapter II. The reactor is essentially built in two parts; the bottom has a ceramic lining to withstand higher temperature and top a stainless steel annular shell, which is used for heat recovery. A duct forms the passage for the hot gas from the reactor bottom to the top annular shell. The annular shell recovers some of heat from the hot flowing gas is utilized for drying of biomass residing in the reactor. The reactor top is always kept open during the gasifier operation and biomass is charged as and when it consumes. Therefore the operation of the gasifier is continuous without intermediate halting.

The prominent difference between the two designs is in the (i) L/D ratio (ii) and the air intake for gasification. The Principal physical and operational features are compared in Table A.1.

Table A.1. Comparison of Closed and Open Top Re-burn Reactor

Design/Parameter	Closed Top	Open Top
L/D	7- 8	3 – 4
Air Intake	Single point; Oxidation zone	Twin; Oxidation zone and Top (~ 2.0:3.0)
Top Region	Biomass + Volatiles > fuel rich region	Biomass + Air + Partial products > Fuel lean region
Regions of Fuel-Rich zone	Many	Few
Air/temperature Distribution	Non-uniform, regions of high and low across reactor	Relatively uniform
Tar Cracking	Low	High

In the case of open top design, the choice twin air entry provides the necessary conditions for stratification – a feature helping in movement of the reaction front into the fuel. This promotes establishing a temperature profile inside the reactor favouring cracking of tar. Induction of air from the top causes what is termed as stratification of the fuel charge. The volatiles are released at some stage in the downward path of wood chips. Mixing with air from the top causes initiation of exothermic reactions and the rise in temperature becomes steep in this zone. The transfer of heat to the upper zone causes an earlier initiation of the release of volatiles. This would mean an isotherm, say at 700K, slowly creeps upwards and the gasifier never attains a steady state during the few hours of its operation in terms of the thermal profile both in the reactor and in the annular space, as long as air is drawn from the top. If the supply of air from the top is cut off, the temperatures inside the gasifier and the annular space would attain a steady state about an hour after the cut off. It is important to note that the gas quality is not affected by the non-attainment of a thermally steady state in the gasifier. It is possible that there is some shift in gas composition, but it does not seem to have any significant effect on the calorific value of the gas. The choice of having higher L/D ratio also promotes more uniform distribution at the level of oxidation zone for a given cross-section of the reactor. This results in having a few fuel-rich regions and more uniform temperature

across the reactor. This feature of uniform temperature distribution across the reactor provides a higher possibility of tar cracking. Thus the possibility of resultant gas from the open top design with minimal tar is higher than the closed top design. The merit of the open top system as compared to the closed-top design lies in the thermal profile of the reactor and the same is evident in Fig. A.3, the temperature distribution can be found to be steeper in the closed-top as compared to open-top design.

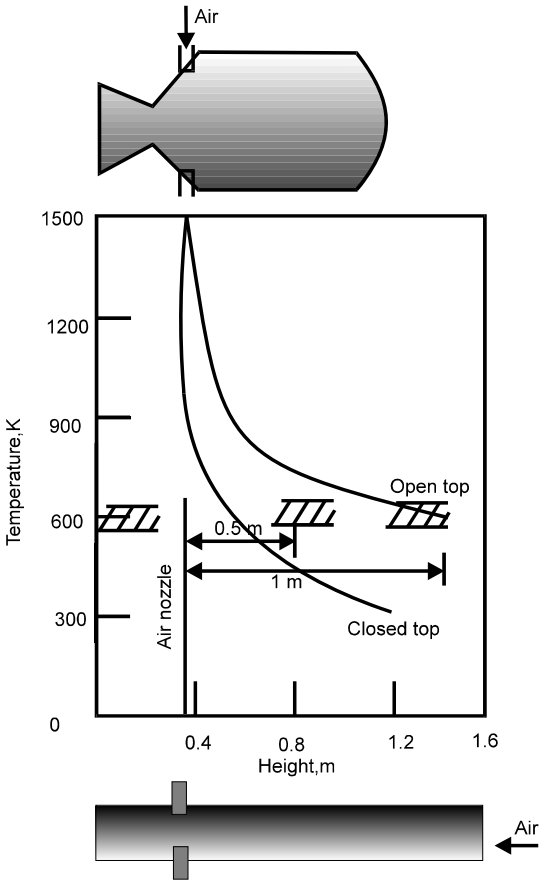

Fig A.3 Thermal Profile in a Gasifier Reactor – Closed and Open Top Re-burn Design

Appendix – II

Data and Terminology

SPE data at CR=17.0

Ign, °CA	Net shaft O/P, kW	Composition, Vol %			Input energy, kW	Φ	Ext. Temp, C	Emission	
		H_2	CO	CH_4				CO, %	NO, PPM
33	14.0	21.0	16.6	2.0	65.0	1.25	434	5.8	980
26	16.2	20.8	16.2	2.0	64.0	1.10	449	2.0	700
22	17.9	21.0	18.6	2.0	64.0	1.03	458	1.1	850
17	18.4	21.5	16	2.5	63.6	1.09	446	0.8	21
12	19.8	2.10	19.2	2.0	63.6	1.00	460	0.2	27
06	20.0	20.0	20.0	2.0	65.0	1.10	495	0.4	31

Total mixture flow rate: 30-33 g/s

SPE data at CR=14.5

Ign, °CA	Net shaft O/P, kW	Composition, Vol %			Input energy, kW	Φ	Ext. Temp, C	Emission	
		H_2	CO	CH_4				CO, %	NO, PPM
20	17.7	19.0	18.8	2.0	65.0	1.11	436	2.0	46
16	17.9	19.4	20.6	2.0	65.1	1.11	444	2.75	600
10	18.8	19.1	20.6	2.0	64.8	1.10	454	2.0	226
08	18.6	19.7	22.5	1.9	74.4	1.20	456	5.8	17

Total mixture flow rate: 30-33 g/s

SPE data at CR=13.5

Ign, °CA	Net shaft O/P, kW	Composition, Vol %			Input energy, kW	Φ	Ext. Temp, C	Emission	
		H_2	CO	CH_4				CO, %	NO, PPM
25	17.0	20.0	15.0	2.5	63.6	1.06	465	2.8	75
18	17.0	20.0	15.0	2.5	64.2	1.07	437	4.6	6
14	18.6	20.0	15.7	2.5	61.2	1.06	482	1.8	211
08	18.2	20.0	15.6	2.5	60.7	1.05	506	0.8	37

Total mixture flow rate: 30-33 g/s

SPE data at CR=11.5

Ign, °CA	Net shaft O/P, kW	Composition, Vol %			Input energy, kW	Φ	Ext. Temp, C	Emission	
		H_2	CO	CH_4				CO, %	NO, PPM
38	13.3	18.2	19.9	2.5	66.5	1.07	438	1.5	421
27	15.6	18.0	18.0	2.5	61.2	1.09	446	1.1	81
17, 15	17.6	21.0	20.0	2.0	64.0	1.07	482	2.0	55
06	17.0	19.5	20.0	2.0	63.0	1.07	483	2.6	55

Total mixture flow rate: 30-33 g/s

MPE data at CR=12.0

Ign, °CA	Net shaft O/P, kW	Composition, Vol %			Input energy, kW	Φ	Ext. Temp, C	Emission	
		H_2	CO	CH_4				CO, %	NO, PPM
24	167	17.7	19.5	2.4	611	0.97	505	0.204	1170
18	174	16.3	23.1	1.6	630	0.96	531	0.125	1066
14	182	20.1	17.4	2.2	633	0.94	560	0.19	1117
12	182	18.6	21.0	1.8	633	0.94	588	0.11	600

Total mixture flow rate: 310 - 315g/s

1. Basis for calculation of Energy Balance

- Input energy = Gas flow rate (g/s) x LCV of PG (MJ/kg)

- Gross brake output is the gross shaft power available at the engine crankshaft and is inclusive of the net brake power (useful output) and the power consumed by engine accessories (water pump/fan, dynamo and fuel injection pump). Here, the net shaft output was estimated by measuring the voltage and current across the alternator terminals and accounting the alternator efficiency. The power consumed by the engine accessories was measured separately by conducting a motoring test – wherein the engine accessories namely the water pump/fan, dynamo and fuel injection pump were driven using an external AC motor at rated engine speed and power estimated. Gas-to-shaft efficiency is defined as the ratio of net shaft output to input energy in the form of gas.

- The energy lost through exhaust includes the sensible heat – measured using K – type thermocouple and chemical enthalpy, CO percentage - measured using exhaust analyzer.

- The energy lost to coolant and miscl. is taken as a difference between the input energy and sum of gross brake output and energy loss through exhaust.

2. Ensemble Averaging for Experimental p-θ data

A. Ensemble averaging is an established statistical procedure for analyzing time varying data like that in IC engines and is therefore not explicitly brought out in the thesis. Since there could be fluctuations in pressure from cycle-to-cycle, a mean data in the form of ensemble average pressure has been represented. The ensemble averaging is done as follows:

$$p(\theta) = \frac{1}{N_c} \sum_{i=1}^{N_c} p(\theta, i)$$

where p : cylinder pressure, θ : crank angle, i : a particular cycle, N_c : total no. of cycles,

3. Choice of Cylinder Wall Temperature for 0-D Calculations

For the 0-D model an average cylinder wall temperature is required to estimate the heat losses. This value was chosen based on the Literature information (French et al, 1973) as cited in the thesis. The literature states a mean cylinder liner temperature of 120 – 180 C, and cylinder head temperature between 170 to 210 C, based on the coolant temperature. Since major part of the heat transfer is occurring during the combustion process, wherein the heat transfer areas are the cylinder head and the piston a mean temperature, which is closer to the cylinder head/piston i.e 450 K has been considered.

4. Equation for Angular Momentum and Moment of Inertia

The component of mean angular momentum H_b and Moment of Inertia M_b, for a control volume of fluid $V(t)$ about a specified point Q = (x, y, z) in a direction specified by a unit vector $\underline{b}$ are calculated as,

$$\boldsymbol{H_b = \int_{V(t)} (\rho) \underline{r} \times \underline{\tilde{U}} . \underline{b} \, d\tau}$$

$$\boldsymbol{M_b = \int_{V(t)} (\rho) \left| \underline{r} \times \underline{b} \right|^2 d\tau}$$

where $\underline{r}$ is a position vector from Q [Haworth et al, 1990].

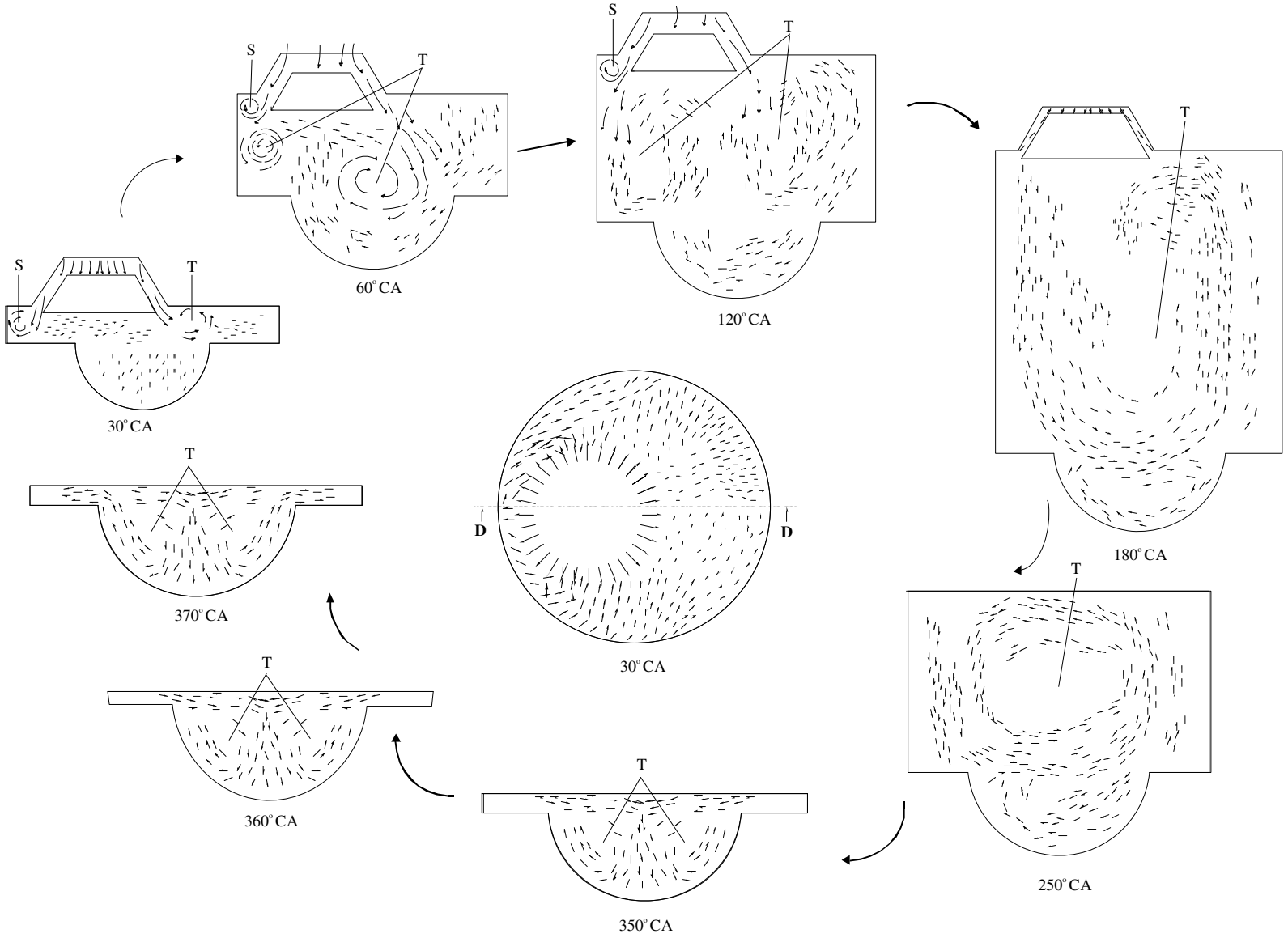

Fig. 6.2 Schematic diagrams of the evolving fluid flow during intake, compression and early part of expansion in a bowl-in piston engine geometry. The central figure shows the tangential velocity plot in the circumferential plane, 1.2 mm below the intake valve. The axial view corresponds to the mean velocities along Section –DD. 'S' denotes separation zone and 'T' denotes tumbling vortices. 360° CA corresponds to TC and 250° CA flow after intake valve closure.

References

1. Abdel-Gayed R. G. and Bradley B. (1976): "Dependence of Turbulent Burning Velocity on Burning Velocity to RMS Turbulent Velocity", Proceedings Sixteenth International Symposium on Combustion, The Combustion Institute, pp-1725-1735.
2. Abraham J., Williams F.A. and Bracco F.V. (1985): "A Discussion of Turbulent Flame Structure in Premixed Charges", SAE 850345, Vol. 94, pp. 128-143.
3. Annand W. J. D. (1963): "Heat Transfer in the Cylinders of Reciprocating Internal Combustion Engines", Proceedings Institution of Mechanical Engineers, Vol. 177, pp. 973-990.
4. Anon (1986): "Wood gas as engine fuel", A Report of the Mechanical Wood Products Branch of FAO Forestry Paper No. 72, Food and Agriculture Organization of United Nations, Rome.
5. Arcoumanis C., Bicen A.F. and Whitelaw J.H. (1983): "Squish and Swirl-Squish Interaction in Motored Model Engines", Journal of Fluid Engineering, ASME, Vol. 105, pp. 105-112.
6. Arcoumanis C. and Whitelaw J.H. (1987): "Fluid Mechanics of IC Engines: A Review", Proceedings Institution of Mechanical Engineers, Vol. 201.
7. Ballal D. R. and Lefebvre A.H. (1974): "Turbulence Effects on Enclosed Flames", Acta Astronautica, Vol. 1, pp. 471-483.
8. Baruah P.C. (1986): "Combustion and Cycle Calculations in Spark Ignition Engines", in the Thermodynamics and Gas Dynamics of Internal Combustion Engines, Vol. 2, pp. 823-865.
9. Bauer W, Heywood J.B., Avanessian O. and Chu D. (1996), "Flow Characteristics in Intake Port of Spark Ignition Engine Investigated by CFD and Transient Gas Temperature Measurements", SAE 961997, Vol. 105, pp. 2110-2117.
10. Bicen A.F., Vafidis C., and Whitelaw J.H. (1985): "Steady and Unsteady Air Flow Through the Intake Valve of Reciprocating Engine", Journal of Fluid Engineering, ASME, Vol. 107, pp. 413-426.
11. Blizard N. C. and Keck J.C. (1974): "Experimental and Theoretical Investigation of Turbulent Burning Model for Internal Combustion Engines", SAE 740191, Vol. 83, pp. 846-864.
12. Blumberg P.N., Lavoie G.A. and Tabaczynski R.J. (1979): " Phenomenological Models for Reciprocating Internal Combustion Engines", Proceedings Energy Combustion Science, Vol. 5, pp. 123-167.

13. Borgnakke C. (1984): "Flame Propagation and Heat Transfer in SI Engines", J Hillard and GS Springer (Eds), Fuel Economy in Road Vehicles Powered by SI Engines, Chapter 5, Plenum press, pp. 183-224.

14. Brokaw R.S. (1961): "Alignment Charts for Transport Properties, Viscosity and Diffusion Coefficients for Non-polar Gases Mixtures at Low Density", Technical Report TRR-81, NASA.

15. Caris D.F. and Nelson E.E. (1959): "A New Look at High Compression Engines", SAE Transactions, Vol. 67, pp. 112-124.

16. Catania A. E. and Spessa E. (1996): "Speed Dependence of Turbulence Properties in a High-Squish Automotive Engine Combustion System", SAE 960268, Vol. 105, pp. 313-334.

17. Chakravarthy P., Mishra D.P., Paul P.J. and Mukunda H.S. (1993): "The Theoretical Calculations of the Limits of Flame Propagation for Producer Gas Mixture", Proceedings Fourth National Meet on Biomass Gasification and Combustion, Vol. 4, pp. 28-37.

18. Corcione F.E. and Valentino G. (1994): "Analysis of in-Cylinder Flow Processes by LDA", Combustion and Flame, Vol. 99, pp. 387-394.

19. Das A. and Watson H.C. (1997): "Development of a Natural Gas Spark Ignition Engine for Optimum Performance", Proceedings Institution of Mechanical Engineers, Part D, Vol. 211, pp. 361-378.

20. Duclos J.M., Bruneaux G., Baritaud T.A. (1996): "3D modelling of combustion and pollutants in a 4-valve SI engine; Effect of fuel and residuals distribution and spark location", SAE 961964, Vol. 105, pp. 2048-2062.

21. Einewell P. and Johansson B. (1997): "Combustion Chambers For Supercharged Natural Gas Engines", SAE 970221, Vol. 106, pp. 408-433.

22. Ekchian A. and Hoult D.P. (1979): "Flow Visualization Study of Intake Process of an Internal Combustion Engine", SAE 790095, Vol. 88, pp. 383-399.

23. Fanslar T.D. (1985): "Laser Velocimetry Measurements of Swirl and Squish Flows in an Engine with a Cylindrical Piston Bowl", SAE 850124, Vol. 94, pp. 1.747-1.763.

24. Fleischer F., Grosse W. and Zapf H. (1981): "Fuels From Biomass and Their Rational Utilisation in Internal Combustion Engines", Proceedings International Conference - New Energy Conversion Technologies and Their Commercializations, Vol. 2, pp. 1334-1340.

25. Floch A, Franck J.V. and Ahmed A. (1995): "Comparison of the Effects of Intake Generated Swirl and Tumble on Turbulence Characteristic in a 4-Valve Engine", SAE 952457, Vol. 104, pp. 2239-2255.

26. French C. C. J, Atkins K.A. (1973): "Thermal Loading of a Petrol Engine", Proceedings Institution of Mechanical Engineers, Vol. 187, 49, pp 561-573.

27. Gatowski J.A., Heywood J. B. and Deleplace C. (1984): "Flame Photographs in a Spark-Ignition Engine", Combustion and Flame, Vol. 56, pp. 71-81.

28. Giordano P. (1999): "Experience on Running a Wood Based Co-generation Power Plant with The IISc-Dasag Gasifier", Biomass Users Network (BUN-India), Vol. 3.2, p. 2.

29. Gish R.E., McCullough J.D., Retzloff J.B. and Mueller H.T. (1958): "Determination of True Engine Friction", SAE Transactions, Vol. 66, pp. 649-661.

30. Gordon and McBride (1975): "Method of Calculating Equilibrium Composition, Adiabatic Flame Temperature, Rocket Performance and Detonation", NASA SP 273.

31. Goyal G. (1989): "Development and Application of an Efficient Implicit-Explicit Method for One-Dimensional Premixed Flames", Ph.D. Thesis, IISc.

32. Groff E.G. and Matekunas F.A. (1980): "The Nature of Turbulent Flame Propagation in Homogenous Spark-Ignited Engines", SAE 800133, Vol. 89, pp. 740-763.

33. Groff E.G. (1987): "An Experimental Evaluation of an Entrainment Flame – Propagation Model", Combustion And Flame, Vol. 67, pp. 153-162.

34. Han Z. and Reitz R.D. (1995): "Turbulence Modeling of Internal Combustion Engines Using RNG k-ε Model", Combustion Science and Technology, Vol. 106, pp. 267-295.

35. Hawkins I.R. and Wilkes N. S. (1991): "Moving grids in HARWELL-FLOW3D", AEA-InTec-0608

36. Haworth D.C., Sherif H. Tahry EI., Huebler M.S and Chang S. (1990): "Multidimensional Port-and-Cylinder for Two and Four-Valve-Per-Cylinder Engines: Influence of Intake Configuration on Flow Structure", SAE 900257, Vol. 99, pp. 647-675.

37. Heywood J.B. and Vilchis F.R. (1984): "Comparison of Flame Development in a SI Engine Fuelled with Propane and Hydrogen", Combustion Science Technology, Vol. 38, pp. 313-324.

38. Heywood J.B. (1988): "Internal Combustion Engine Fundamentals", International edition. McGraw-Hill.

39. Hirotomi T., Nagayama I., Kobayashi S. and Yamamasu M. (1981): "Study of Induction Swirl in a Spark Ignition Engine", SAE 810496, pp. 1851-1867.

40. Ikegami M., Shioji M. and Nishimoto K. (1987): "Turbulence Intensity and Spatial Integral Scale During Compression and Expansion Strokes in a Four Cycle Reciprocating Engine", SAE 870372, Vol. 96, pp. 4.399-4.441.

41. James E.H. (1990): "Further Aspects of Combustion Modelling in Spark Ignition Engines", SAE 900684, pp.1526-1543.

42. Janota M.S., Hallam A.J., Brock E.K., Dexter S.G. (1967-68): "The Prediction of Diesel Engine Performance and Combustion Chamber Component Temperature Using Digital Computers", Proceedings Institution of Mechanical Engineers, Vol. 182, pp. 58-70.

43. Jennings M.J. (1992): "Multi-Dimensional Modeling of Turbulent Pre-mixed Charge Combustion", SAE paper 920589, Vol. 101, pp. 1106 -1124.

44. Jones P. and Junds J.S. (1995): "Full Cycle Computational Fluid Dynamics Calculations in a Motored Four Valve Pent Roof Combustion Chamber and Comparison with Experiments", SAE 950282, Vol. 104, pp. 595-610.

45. Kalghatgi T.G. (1985), "Early Flame Development in a Spark-Ignition Engine", Combustion and Flame, Vol. 60, pp. 299-308.

46. Kanitkar S., Chakravarty P., Paul P.J. and Mukunda H.S. (1993): "The Flame Speeds, Temperature and Limits of Flame Propagation for Producer Gas-Air Mixtures –Experimental Results", Proceedings of Fourth National Meet on Biomass Gasification and Combustion, Mysore, India, Vol. 4, pp. 50-62.

47. Keck C.J. (1982): "Turbulent Flame Structure and Speed in Spark Ignition Engines", Proceedings Ninetieth International Symposium on Combustion, The Combustion Institute, Vol. pp. 1451-1466.

48. Khalighi B., Tahry EI. S.H., Haworth D.C. and Huebler M.S. (1995): "Computation and Measurement of Flow and Combustion in a Four-Valve Engine with Intake Variations", SAE 950287, Vol. 104, pp-611-644.

49. Lakshmisha K.N. (1991): "Computational Studies on the Flammability Limits of Premixed Gases" – Ph.D. Thesis, IISc.

50. Lancaster D.R., Krieger R.B., Lienesch J.H. (1975): " Measurement and Analysis of Engine Pressure Data", SAE 750026, Vol. 84, pp. 155-170.

51. Lancaster D.R. (1976): "Effects of Engine Variables on Turbulence in a Spark-Ignition Engine", SAE Paper 760159, Vol. 85, pp. 671-688.

52. Lancaster D.R., Krieger R.B., Sorenson S. C. and Hull W. L. (1976): " Effects of Turbulence on SI Engine Combustion", SAE 760160, Vol. 85, pp-689-710.

53. Lebrere L. and Dillies B. (1996): "Engine Flow Calculations Using a Reynolds Stress Model in The Kiva-II Code", SAE Paper 960636, Vol. 105, pp. 882-904.

54. Lewis B. and Elbe G Von (1987): "Combustion, Flames and Explosion of Gases", Academic Press Inc.

55. Maly R.R. (1994): "State of the Art and Future Needs in S.I.Engine Combustion", Proceedings Twenty-Fifth International Symposium on Combustion, pp. 111-124.

56. Martin J. and Wauters P. (1981): "Performance of Charcoal Gas Internal Combustion Engines', Proceedings of International Conference - New Energy Conversion Technologies and Their Commercialization, Vol. 2, pp. 1415-1424.

57. Mattavi J.H., Groff E.G., Lienesch J.H., Metakunas F.A. and Noyes R.N. (1978): "Engine Improvements Through Combustion Modelling", General Motors Research Laboratories Symposium on Combustion Modelling in Reciprocating Engines, Warren Michigenm.

58. Mishra D. P., Paul P. J. and Mukunda H.S. (1994): "Computational Studies on The Flame Propagation in Producer Gas-Air Mixture and Experimental Comparisons", Proceedings of the XIII National Conference on IC Engines and Combustion, Bangalore, India, Vol. 13, pp. 256-262.

59. Mukunda H.S. (1989): "Understanding Combustion", Macmillan India Limited.

60. Mukunda H.S., Dasappa S. and Shrinivasa U. (1993): "Open-Top Wood Gasifiers", Renewable Energy - Sources for Fuels and Electricity, Island press, pp. 699-728.

61. Mukunda H.S., Paul P.J., Dasappa S., Shrinivasa U. and Sharan H. (1994): "Results of an Indo-Swiss Programme For Qualification and Testing of a 300-kW IISc-Dasag Gasifier", Energy for sustainable development, Vol. 4, pp.46-49.

62. Namazian M., Hansen S., Lyford-Pike E., Sanchez-Barsse J., Heywood J and Rife J. (1980): "Schlieren Visualization of the Flow and Density Fields in the Cylinder of a Spark-Ignition Engine", SAE 800044, Vol. 89, pp. 276-302.

63. Parikh P.P., Banerjee P.K., Shashikantha and Veerkar S. (1995): "Design Development and Optimisation of a Spark Ignited Producer Gas Engine", Proceedings of XIV National Conference on IC engines and Combustion, Pune, India, Vol. 14, pp. 97-107.

64. Parke P.P., Stanley S.J. and Walawnder W. (1981): "Biomass Producer Gas Fuelling of Internal Combustion Engines", Energy From Biomass and Wastes V, Lake Buena Vista Florida, pp. 499 –516.

65. Parke P.P. and Clark, S.J. (1981): "Biomass Producer Gas Fuelling of IC Engines - Naturally Aspirated and Supercharged Engines", American Society of Agricultural Engineers, Michigan, pp. 1-35.

66. Ramachandra A. (1993): "Performance Studies on a Wood Gas Run IC engine", Proceedings of Fourth National Meet on Biomass Gasification and Combustion, Mysore, India, Vol. 4, pp. 213-218.

67. Reuss D.L., Kuo T.W., Khalighi B., Haworth D. and Rosalik M. (1995): "Particle Image Velocimetry Measurements in a High-Swirl Engine Used for Evaluation of Computational Fluid Dynamics Calculations", SAE 952381, Vol. 104, pp. 2073-2092.

68. Rhodes D. B. and Keck J.C. (1985): "Laminar Burning Speed Measurements of Indolene-Air-Diluent Mixtures at High Pressures and Temperature", SAE paper 850047, pp. 23-35

69. Schapertons H. and Thiele F. (1986): "Three Dimensional Computations for Flow Fields in DI Piston Bowls", SAE 860463, Vol. 95, pp. 135-151.

70. SERI (1979): "Generator Gas – The Swedish Experience From 1939-1945", SERI, Golden, Colorado.

71. Shashikantha, Banerjee P.K., Khairnar G.S., Kamat P.P. and Parikh P.P. (1993): "Development and Performance Analysis of a 15 kWe Producer Gas Operated SI Engine", Proceedings of Fourth National Meet on Biomass Gasification and Combustion, Mysore, India, Vol. 4, pp. 219-231.

72. Shashikantha and Parikh P.P. (1999): "Spark Ignited Producer gas and Dedicated CNG Engine - Technology Development and Experimental Performance", SAE 1999-01-3515 (SP-1482).

73. Smith J.R (1982): "Turbulent Flame Structure in a Homogenous-Charge Engine", SAE 820043, Vol. 91, pp. 150-164.

74. Smith J.R. (1982): "The Influence of Turbulence on Flame Structure on an Engine", Flows in Internal Combustion Engines, ASME, New York, pp. 67-72.

75. Stone C.R., Mendis K.J.S., Daragheh M. (1996): "Measurements and Modelling of a Lean Burn Gas Engine", Proceedings Institution of Mechanical Engineers, Vol. 210, pp. 449-461.

76. Strauss T.S., Schweimer G.W. and Ritscher U. (1995): "Combustion in a Swirl Chamber Diesel Engine Simulation by Computation of Fluid Dynamics", SAE 950280, Vol. 104, pp. 519 –530.

77. Tabaczynski R. J., Ferugson C. R. and Radhakrishnan K. (1977): " A Turbulent Entrainment Model for Spark-Ignition Engines, SAE 770647, pp. 2414-2433.

78. Tatom J. W., Colcord A.R., Williams W.M., Purdy K.R. and Beinstock D. (1976): "Development of a Prototype System for Pyrolysis of Agricultural and Forestry Wastes into Fuels and Other Products", Prepared for EPA.

79. Trigui N., Affes H. and Kent J.C. (1994): "Use of Experimentally Measured In-Cylinder Flow Field Data at IVC as Initial Conditions to CFD Simulations of Compression Stroke in I.C. Engines – A Feasibility Study", SAE 940280, Vol. 103, pp. 343-352.

80. Urushihara T., Murayama T., Takagi Y. and Lee Ki-Hyung (1995): "Turbulence and Cycle-by-Cycle Variation of Mean Velocity Generated by Swirl and Tumble Flow and Their Effects on Combustion", SAE 950813, Vol. 104, pp. 1382-1389.

81. Versteeg H.K. and Malalasekhara W. (1995): "An Introduction to CFD – The Finite Volume Method", Longman Scientific and Technical Publication.

82. Wakisaka T., Shimamoto Y. and Isshiki Y. (1986): "3-D Numerical Analysis of In-Cylinder Flows on Reciprocating Engines", SAE 860464, Vol. 95, Vol. 104, pp. 3.152-3.169.

83. Warnatz J. (1984): "Combustion Chemistry", Ed. W.C Gardiner, Springer-Vertag, New York, pp: 197-360.

84. Watkins A.P., Li S-P. and Cant R. S. (1996): "Premixed Combustion Modeling For SI Engine Applications", SAE 961190, Vol. 105, pp. 1614-1626.

85. Witze P.O. (1982): "The Effect of Spark Location on Combustion in a Variable-Swirl Engine", SAE 820044, pp. 165-175.

86. Woschni G. (1967): "Universally Applicable Equation for the Instantaneous Heat Transfer Coefficient in the IC Engines", SAE 670931, Vol.76, 1967.

87. Wu C.M., Roberts C.E., Matthews R.D. and Hall M.J. (1993): "Effects of Engine Speed on Combustion in SI Engines: Comparison of Predictions of a Fractal Burning Model with Experimental Data", SAE 932714, Vol. 102, pp. 2277-2291.

88. Yoo S.C., Lee K., Novak M., Schock H., and Keller P. (1995): "3-D LDV Measurement of in-Cylinder Air Flow in a 3.5 L 4 Valve SI Engine, SAE 950648, Vol. 104, pp. 1141-1161.